DOLB

PhD THESIS :

METAL-ORGANIC FRAMEWORKS APPLICATIONS IN PHOTOCATALYTIC REDUCTION OF CARBON DIOXIDE TO SOLAR FUELS OVER GRAPHITIC CARBON NITRIDE AND TITANIUM DIOXIDE NANOTUBES COMPOSITES

BY : RIYADH IKREEDEEGH

METAL-ORGANIC FRAMEWORKS APPLICATIONS IN PHOTOCATALYTIC REDUCTION OF CARBON DIOXIDE TO SOLAR FUELS OVER GRAPHITIC CARBON NITRIDE AND TITANIUM DIOXIDE NANOTUBES COMPOSITES

RIYADH RAMADHAN IKREEDEEGH

UNIVERSITI TEKNOLOGI MALAYSIA

UNIVERSITI TEKNOLOGI MALAYSIA

<div style="border">

DECLARATION OF THESIS / POSTGRAGUATE PROJECT REPORT AND COPYRIGHT

Author's full name : RIYADH RAMADHAN IKREEDEEGH

Date of Birth : 24/12/1991

Title : METAL-ORGANIC FRAMEWORKS APPLICATIONS IN PHOTOCATALYTIC REDUCTION OF CARBON DIOXIDE TO SOLAR FUELS OVER GRAPHITIC CARBON NITRIDE AND TITANIUM DIOXIDE NANOTUBES COMPOSITES

Academic Session : 2020/2021 -1

I declare that this thesis is classified as:

☐ **CONFIDENTIAL** (Contains confidential information under the Official Secret Act 1972)*

☐ **RESTRICTED** (Contains restricted information as specified by the organization where research was done)*

☑ **OPEN ACCESS** I agree that my thesis to be published as online open access (full text)

1. I acknowledged that Universiti Teknologi Malaysia reserves the right as follows:

2. The thesis is the property of Universiti Teknologi Malaysia

3. The Library of Universiti Teknologi Malaysia has the right to make copies for the purpose of research only.

4. The Library has the right to make copies of the thesis for academic exchange.

Certified by:

_____
SIGNATURE OF STUDENT

MKK 192004
MATRIC NUMBER

Date: 12 APRIL 2021

_____
SIGNATURE OF SUPERVISOR

DR. MUHAMMAD TAHIR
NAME OF SUPERVISOR

Date: 12 APRIL 2021

</div>

NOTES : If the thesis is CONFIDENTIAL or RESTRICTED, please attach with the letter from the organization with period and reasons for confidentiality or restriction

"I hereby declare that I have read this dissertation and in my opinion this dissertation is sufficient in term of scope and quality for the award of the degree of Master of Engineering (chemical)

Signature   :

Name of Supervisor   :   MUHAMMAD TAHIR

Date   :   12 APRIL 2021

METAL-ORGANIC FRAMEWORKS APPLICATIONS IN PHOTOCATALYTIC REDUCTION OF CARBON DIOXIDE TO SOLAR FUELS OVER GRAPHITIC CARBON NITRIDE AND TITANIUM DIOXIDE NANOTUBES COMPOSITES

RIYADH RAMADHAN IKREEDEEGH

A dissertation submitted in partial fulfilment of the
requirements for the award of the degree of
Master of Engineering (chemical)

School of Chemical and Energy Engineering
Faculty of Engineering
Universiti Teknologi Malaysia

APRIL 2021

DECLARATION

I declare that this dissertation entitled *"Metal-Organic Frameworks Applications in Photocatalytic Reduction of Carbon Dioxide to Solar Fuels over Graphitic Carbon Nitride and Titanium Dioxide Nanotubes Composites"* is the result of my own research except as cited in the references. The dissertation has not been accepted for any degree and is not concurrently submitted in candidature of any other degree.

Signature   :

Name   : RIYADH RAMADHAM IKREEDEEGH

Date   : 12 APRIL 2021

DEDICATION

This dissertation is dedicated to my father, who taught me that the best kind of knowledge to have is that which is learned for its own sake. It is also dedicated to my mother, who taught me that even the largest task can be accomplished if it is done one step at a time.

ACKNOWLEDGEMENT

In preparing this thesis, I was in contact with many people, researchers, academicians, and practitioners. They have contributed towards my understanding and thoughts. In particular, I wish to express my sincere appreciation to my dissertation supervisor, Dr. Muhammad Tahir, for encouragement, guidance, critics, friendship, advices and motivation. Without his continued support and interest, this dissertation would not have been the same as presented here.

I am also indebted to Universiti Teknologi Malaysia (UTM) for helping and supporting me during my Master study. I am also so grateful to my company; Arabian Gulf Oil Company which deserves a special thanks for its continuous support and assistance in supplying me the relevant literatures and the required information.

My wife should also be recognised for her support and patience during my study. My sincere appreciation also extends to all my colleagues and others who have provided assistance at various occasions. Their views and tips are useful indeed. Unfortunately, it is not possible to list all of them in this limited space. I am grateful to all my family members.

ABSTRACT

Photocatalytic CO_2 reduction into valuable chemicals and fuels by utilizing solar energy is an attractive approach to solve two main issues faced by the humans which are the environmental pollution caused by the greenhouse gas emissions (mainly CO_2) and the fossil fuels depletion which will result in a global energy crisis. Metal-organic frameworks (MOFs) have recently been explored as photocatalysts owing to their promising photochemical and unique textural properties. In this study, the synthesis, characterization and fabrication of two novel ternary NH_2-MIL-125(Ti) nanocomposites have been investigated for efficient photocatalytic CO_2 conversion to CH_4 and CO under visible light. The ternary photocatalysts were fabricated by coupling the amino-functionalized MOF once with g-C_3N_4 and once again with TiO_2 in the form of nanotube arrays. Graphene oxide was also used as a solid electron mediator for limiting the high recombination rate of photo-generated charges in both semiconductors. The photocatalytic experiments conducted in a fixed-bed photoreactor revealed the significant role of MOF in enhancing the optoelectronic properties and increasing the specific surface area in both composites. The novel g-C_3N_4-RGO-NH_2-MIL-125(Ti) composite exhibited the highest CO production of 383.79 μmol g^{-1} after 4 h irradiation which is 5 times higher compared to pure g-C_3N_4, while for the NH_2-MIL-125(Ti)-GO-TNTs composite, 29782.25 μmol m^{-2} of CO production was achieved compared to 23871.27 μmol m^{-2} that of pure TiO_2 NTs. However, both MOF-composites displayed lower CH_4 selectivity of 3.5 % for g-C_3N_4-MOF composite and 3.93 % for TNTs-MOF composite compared to 20 and 6.7 % that of pure g-C_3N_4 and TNTs, respectively. This was mainly attributed to the high CO selectivity of the NH_2-MIL-125(Ti) MOF. The effects of the operating parameters such as catalyst loading and CO_2 pressure have been tested. Moreover, the stability analyses for the newly synthesized MOF-composites have been investigated. Finally, the reaction mechanisms over the MOF-composites have been proposed and deliberately discussed to give clear illustrations for the constructed heterojunctions. This research provides a new and promising approach for the fabrication of MOF-composites that would be beneficial for further investigations in photocatalytic CO_2 conversion to solar fuels under visible light.

ABSTRAK

Fotokatalitik reduksi CO_2 kepada bahan kimia dan bahan api berharga dengan mengutilisasi tenaga solar merupakan satu pendekatan yang menarik untuk menyelesaikan dua masalah utama yang dihadapi oleh manusia iaitu pencemaran alam sekitar yang disebabkan oleh pelepasan gas rumah hijau (teruatamanya CO_2) dan penipisan bahan api fosil yang mengakibatkan krisis tenaga global. Kerangka logam-organik (MOF) kebelakangan ini dikaji sebagai fotomangkin kerana sifat fotokimia yang baik dan teksturnya yang unik. Dalam kajian ini, sintesis, karakterisasi dan fabrikasi dua nanokomposit NH_2-MIL-125 (Ti) telah dikaji untuk fotokatalitik pertukaran CO_2 kepada CH_4 dan CO dibawah cahaya tampak. Fotomangkin ternari difabrikasi melalui penggabungan MOF berfungsi-amino dengan g-C_3N_4 dan TiO_2 dalam bentuk nanotub arrays. Grafin oksida juga digunakan sebagai mediator elektron solid untuk mengehadkan kadar rekombinasi yang tinggi oleh foto penghasilan cas di kedua-dua semikonduktor. Eksperimen fotokatalitik dijalankan di dalam fixed-bed fotoreaktor menunjukkan bahawa MOF berperanan dalam meningkatkan sifat optoelektronik dan luas permukaan spesifik oleh kedua komposit. Novel komposit g-C_3N_4-RGO-NH_2-MIL-125 (Ti) menunjukkan pengeluaran CO yang tertinggi iaitu 383.79 μmol g^{-1} selepas 4 jam iradiasi iaitu 5 kali ganda peningkatan berbanding g-C_3N_4 tulen, sementara komposit NH_2-MIL-125(Ti)-GO-TNTs mencapai pengeluaran CO sebanyak 29782.25 μmol m^{-2} berbanding 23871.27 μmol m^{-2} oleh TiO_2 NTs tulen. Walau bagaimanapun, kedua-dua komposit MOF mempamerkan selektiviti CH_4 yang rendah iaitu sebanyak 3.5 % untuk komposit g-C_3N_4-MOF dan 3.93 % untuk komposit TNTs-MOF berbanding dengan 20 dan 6.7 % oleh g-C_3N_4 dan TNTs tulen. Hal ini terutamanya disebabkan selektiviti CO yang tinggi oleh NH_2-MIL-125(Ti) MOF. Kesan parameter operasi seperti pemuatan pemangkin dan tekanan CO_2 telah diuji. Tambahan, analisis kestabilan untuk komposit-MOF yang baru disintesis juga telah dikaji. Akhir sekali, reaksi mekanisma terhadap komposit-MOF telah diusulkan dan dibincangkan untuk memberi gambaran jelas tentang heterojungsi yang telah dikonstruk. Kajian ini memberi pendekatan baharu yang menjanjikan untuk fabrikasi komposit-MOF di mana untuk memberi manfaat bagi tujuan penyelidikan lanjut dalam bidang fotokatalitik pertukaran CO_2 kepada bahan api solar di bawah cahaya tampak.

TABLE OF CONTENTS

LIST OF TABLES

LIST OF FIGURES

LIST OF ABBREVIATIONS

MOFs	-	Metal Organic Frameworks
GHG	-	Greenhouse Gases
UV	-	Ultraviolet
RGO	-	Reduced Graphene Oxide
NT	-	Nanotube
ppm	-	Parts Per Million
CB	-	Conduction Band
VB	-	Valence Band
TEOA	-	Triethanolamine
TEA	-	Triethylamine
LED	-	Light Emitting Diode
psi	-	Pound per square inch
PSE	-	Post Synthetic Exchange
EN	-	Ethylenediamine
DETA	-	Diethylenetriamine
TETA	-	Triethylenetetramine
n/a	-	Not available
LSPR	-	Localized Surface Plasmon Resonance
DI	-	Deionized
DC	-	Direct Current
DMF	-	Dimethylformamide
XRD	-	X-ray Diffraction
FESEM	-	Field Emission Scanning Electron Microscopy
BET	-	Braunauer-Emmer-Teller
XPS	-	X-ray Photo-electron Spectroscopy
HRTEM	-	High Resolution Transmission Electron Microscopy
EXD	-	Energy-dispersive X-ray spectroscopy
PL	-	photoluminescence
DRUV-is	-	Diffuse Reflectance Ultraviolet Visible

LIST OF SYMBOLS

E_{bg}	-	Energy band gap
hv	-	Planck's constant
E_C	-	Conduction Band minimum energy level position
E_V	-	Valence Band minimum energy level position
K_B	-	Boltzmann constant
n and p	-	Concentration of the carrier
N_C and N_V	-	Effective densities of states in C_B and V_B
ΔG	-	Gibbs Free Energy
pH	-	Power of Hydrogen ion
W	-	Watt
Mg	-	Milligram
mL	-	Millilitre
M	-	Micro
H	-	Hour
^{o}C	-	Degree Celsius
K	-	Kelvin
Atm	-	Atmosphere
kPa	-	Kilopascal
CNNs	-	Carbon Nitride Nanosheets

CHAPTER 1

INTRODUCTION

1.1   Background

Environmental pollution and fossil fuels depletion have become the two major problems and the most controversial issues these days [1, 2]. Over the past decades and with the invention of the internal combustion engine, the dependence has been mostly on the fossil fuels (nearly 80 %) to fulfill energy requirements. The demand on fossil fuels utilization may rise up to 56 % by 2040, by which this sharp increase in energy demand will lead to severe shortage in fulfilling the energy requirements [3, 4]. Apart from decreasing the natural energy resources, the excessive utilization of these fuels led to a detrimental rise in the greenhouse gas (GHG) emissions; mainly CO_2, which have a crucial role in global warming phenomenon [5, 6]. Furthermore, the CO_2 gas is the primary contributor to climate change, sea level rise, the occurrence of acid rain and the loss in biodiversity [7, 8]. Thus, looking for sustainable and renewable approaches for energy production and/or environmental remediation is essential in future. Many technologies have been utilized to solve these major problems by different CO_2 utilization approaches such as carbon capturing and storage (CCS), catalytic conversion, electrochemical conversion, thermo-chemical conversion, photo-electrochemical conversion and biological fixation [9, 10]. Although, these technologies are still being used, they face significant challenges due to major relative concerns, this includes the high overall costs, low efficiency aspects, continuous monitoring and potential CO_2 leakage in some of these technologies like in the CCS technology [11].

In the last few decades, a new sustainable technology has been explored which is known as photocatalysis (photocatalytic CO_2 reduction) in which CO_2 is reduced in the presence of water into various valuable products like methane (CH_4), methanol (CH_3OH), formaldehyde (HCHO), formic acid (HCOOH) and carbon

monoxide (CO) in the presence of a photocatalyst under light irradiation. This process is carried out when the light radiations strike the photocatalyst; mainly a semiconductor, and excite the electrons to undergo a series of reduction and oxidation (redox) reactions [12, 13]. The most important discovery was explored in 1972 by Fujishima and Honda [14] with the use of TiO_2 as a photocatalyst which extensively promoted the field of solar fuel production. Since that, many successful attempts followed by other researchers for different products and over various photocatalysts such as zeolites, zirconium oxide (ZrO_2), magnesium oxide (MgO), zinc oxide (ZnO), zinc sulfide (ZnS) and graphitic carbon nitride (g-C_3N_4) [15]. However, the applications of these materials are limited since their photocatalytic performance is quite low due to some limitations such as functioning only under UV light which corresponds to only 3% of natural solar light energy [16], the high recombination rate of charge carries and the limited applications due to redox potentials and the small pore sizes in most of these materials [17].

The metal-free organic semiconductors, in particular, the graphitic carbon nitrides (g-C_3N_4) have attracted much attention in the photocatalytic CO_2 reduction field. The g-C_3N_4 is one of the best semiconductors due to many advantages such as being inexpensive, nontoxic, easy to prepare and visible light-active due to its narrower band gap ($\sim$ 2.7 eV). However, g-C_3N_4 suffers also from a high recombination of the photogenerated charges which can limit its applications. Among all the metal oxide semiconductors, TiO_2 has been also employed as one of the most proficient photocatalysts in photocatalytic CO_2 reduction, due to several benefits and some are its availability, low cost, non-toxicity, high chemical and thermal stability [18, 19]. However, TiO_2 is UV-active only and functions poorly under visible light due to its wide band gap energy (3.2 eV), which lowers its photoactivity. Furthermore, it suffers from high surface and interior charge recombination rate of electron-hole (e^-/h^+) pairs, which slows down the kinetics of photocatalytic reduction of CO_2 and hence, lowers its photocatalytic efficiency [20].

In the current development, a new promising photocatalyst materials known as metal-organic frameworks (MOFs) have attracted the researcher's attentions, mainly due to their unique properties which include crystalline porous structures;

formed by organic linkers and transition-metal nodes, extremely large specific surface area; which is beneficial for the gas (CO_2) adsorption, well-ordered structures and tunable chemical compositions [21, 22]. The MOF-composites and their modifications started to be applied increasingly in the fields of solar fuels production and environmental remediation. One of the most attractive possibilities in utilizing CO_2 is to reduce it into solar fuels by using MOF-based photocatalysts, the main reason for this attraction is their wide functionality introduced by the organic linkers and the possibility to adapt these MOFs for more specific application, particularly in contrast to TiO_2 and inorganic semiconductors [23].

In 2009, a Ti-based MOF known as MIL-125(Ti) was synthesized for first time by Férey and co-workers [24] and has received much attention for its potential applications in fields of photocatalysis and gas storage. This Ti-based MOF is not only known for its excellent adsorption properties and thermal stability but can also introduce high-density immobilized Ti sites within its porous structure. However, its wide bandgap of 3.72 eV limits its functionality only in the UV region [25]. Therefore, efforts been made to improve its optical properties and it was shifted to the visible light range by amino-functionalization through introducing the -NH_2 amine group to the organic linkers to form a very active, visible-light-responsive NH_2-MIL-125(Ti) MOF with excellent optoelectronic properties. Thus, new insights into the future development of this MOF can be proposed to improve the CO_2 photo-reduction efficiency and to increase the solar products selectivity and yield rates by coupling this Ti-based MOF with other semiconductor materials.

In this study, the amino functionalized MIL-125(Ti) MOF was used for enhancing the photocatalytic performance of the two proficient photocatalysts (g-C_3N_4 and TiO_2) which are considered as benchmarks in the field of photocatalysis. Therefore, the synthesis, characterization and photocatalytic performance of two novel MOF-composite photocatalysts were investigated and deeply discussed in this research.

1.2   Problem Statement and Hypothesis of Research

The photocatalytic CO_2 conversion to solar fuels is a promising approach for environmental remediation and energy production applications. However, the photocatalytic efficiency of the currently used photocatalyst materials is still low. It would be a very beneficial approach using MOFs with individual semiconductors like TiO_2 and $g-C_3N_4$ to achieve more visible light harvesting and to drive the photocatalytic reaction towards higher efficiency. Therefore, to gain the advantages and benefits of using MOFs in enhancing the performance of these well-known photocatalysts and come up with solutions for the future challenges, the following problems and their proposed solutions are identified:

i.   The amino-functionalized MIL-125(Ti) MOF exhibits high photo-activity under visible light irradiation. Therefore, the incorporation of TiO_2 and $g-C_3N_4$ photocatalysts with this MOF can boost the visible-light harvesting and increase the specific surface area and thus improve their photocatalytic performance.

ii. TiO_2 and suffers from a high recombination rate of photo-generated charges which results in lower yield rates. Therefore, lower TiO_2 activity can be overcome by coupling with the MOF and the low-cost graphene oxide (GO). The use of MOF will shift the TiO_2 to the visible range while the GO can limit the recombination by increasing the transfer and separation of photogenerated charges. Further improvement in photocatalytic activity can be achieved by using TiO_2 in the form of nanotube arrays which offers larger external and internal surface areas compared to that of their bulk counterparts.

iii. The NH_2-MIL-125(Ti) MOF is known for its poor photocatalytic performance alone and also with its selectivity towards CO production only. Therefore, using $g-C_3N_4$ and TiO_2 photocatalysts will increase the photocatalytic efficiency and shift the selectivity to other solar fuels such as CH_4.

iv. Reduced graphene oxide (RGO) owes several unique properties such as excellent mobility of charge carriers, high chemical stability and good mechanical strength. The combination of reduced graphene oxide with $g-C_3N_4$

and MOF can lead to limited charges recombination rate in addition to some novel properties by constructing a Z-scheme heterojunction system.

1.3   Objectives of Study

The following are the objectives of this research:

(a)   To synthesize and characterize both g-C_3N_4-RGO-NH_2-MIL-125(Ti) and NH_2-MIL-125(Ti)-GO-TNTs ternary composites.

(b)   To investigate the performances of the newly fabricated MOF-composites for photocatalytic CO_2 reduction to solar fuels under visible light irradiations.

(c)   To study the effectiveness of various parameters on the photocatalytic activity of the MOF-composite photocatalysts and to propose clear reaction mechanisms.

1.4   Scopes of Study

This study has three main scopes which are:-

1)   A combination of thermal, hydrothermal, electrochemical and sonochemical synthesis methods were used for the fabrication of the ternary composites. The MIL-125(Ti) MOF was used as a functionalized MOF in the form NH_2-MIL-125(Ti). The samples were characterized using several characterization techniques such as XRD, Raman, FTIR, FESEM, EDX, UV-visible and PL analysis.

2)   The NH_2-MIL-125(Ti) MOF was used for improving the photocatalytic efficiency by increasing visible light harvesting and the adsorption of CO_2 gas. TiO_2 was used as nanotube arrays for increasing the surface area. All the experiments were conducted for 4 h in a fixed-bed gas-phase reactor at pressure value of 0.2 bar and catalyst loading of 100 mg.

3) Different operating parameters (according to the photoreactor design) such as catalyst loading (25, 50, 100 and 200 mg), the operating gauge pressure (0.2, 0.4 and 0.8 bar), catalysts ratios (in wt. %) and irradiation time (1, 2, 3 and 4 h) were tested to increase the selectivity and yield rates. The reaction mechanisms were also studied to get a clear illustration for the fabrication of efficient heterojunction systems for photocatalytic CO_2 reduction over the novel MOF-composites

1.5   Significance of Study

This study is important for many reasons; the efficiency of CO_2 photoreaction was enhanced with the use of novel NH_2-MIL-125(Ti) MOF composites, synthesized with simple and easy methods. Moreover, most of materials used in this study are considered to be inexpensive and environmentally safe. Furthermore, only water was used as a reducing agent with no use of any other sacrificial agents compared to other studies. Finally, for maximum light harvesting, the visible light was used in this research as a light source instead of UV light (corresponding only to 3 % of solar light) which was used in many previous studies.

CHAPTER 2

LITERATURE REVIEW

2.1   Introduction

Photocatalysis has attracted the researcher's attention by being recognized as a promising solar fuel production system due to its prospective applications in both reducing carbon dioxide emissions and producing of clean solar fuels and other valuable chemicals under solar light. The photon energy can be converted into chemical energy by using MOF-based photocatalysts for CO_2 reduction with the presence of H_2O vapor in a photoreactor. Thus, for practical application of photocatalysis, the insight into understanding the fundamentals of CO_2 photocatalytic reduction and the development of MOFs as photocatalysts is necessary.

2.2   Overview and Development in CO₂ Reduction Technologies

When fossil fuels are burned, they release massive amounts of greenhouse gases (mainly CO_2) into the atmosphere which in turn trap heat in our atmosphere [7, 8]. The CO_2 gas has been increasing rapidly for the last decades and now it is considered to be the main pollutant among all other greenhouse gases and also the primary contributor to global warming, climate change and the sea level rise [26]. The combustion stoichiometry of fossil fuels as illustrated in Equations (2.1)-(2.4) gives that burning 1 ton of carbon in fossil fuels results in more than 3.5 tons of CO_2; whose accumulation in the atmosphere is now approaching 1 tera ton [27, 28].

The combustion of methane: $CH_4 + 2\,O_2 \rightarrow CO_2 + 2\,H_2O$ $\qquad\qquad$ (2.1)

(12.04 g) of C in CH_4 $\longrightarrow$ (44.01 g) of CO_2 $\qquad\qquad$ (2.2)

The combustion of ethane: $2\,C_2H_6 + 7\,O_2 \rightarrow 4\,CO_2 + 6\,H_2O$ (2.3)

(48.04 g) of C in C_2H_6 $\longrightarrow$ (176.04 g) of CO_2 (2.4)
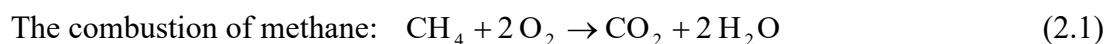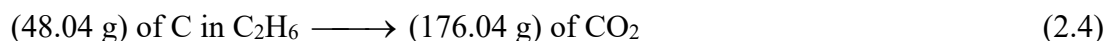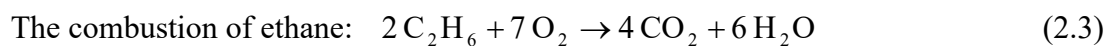
It is worth mentioning that the CO_2 emissions since the industrial revolution led to a total increase of 58.15 % (from 260 ppm to 411.2 ppm) in its atmospheric concentration as shown in Figure 2.1 (a). An attractive approach for utilizing CO_2 is by converting it into valuable fuels and/or chemicals in order to solve the problems of air pollution and fuels depletion by means of energy production and/or environmental remediation. This could be done via many technologies such as carbon capturing and storage (CCS), catalytic conversion, thermochemical conversion, electrochemical conversion, photoelectrochemical conversion, biological fixation and photocatalytic conversion. The detailed classification has been shown in Figure 2.1 (b) and discussed in the following sections:-

2.2.1 Carbon Capturing and Storage (CCS)

Rather than using a renewable energy for CO_2 reduction, the stabilization of atmospheric CO_2 concentrations can be achieved through the use of carbon capture and storage (CCS). This strategy consists of three main steps, Step 1: the CO_2 capture; where the most energy consumes, resulting in higher costs [29]. In this step, one of three common technologies might be used. Pre-combustion capture, in which fuels are converted to CO_2 and H_2 and the CO_2 produced is separated before combustion, Post-combustion capture; CO_2 is obtained and separated from the flue gases produced from the combustion, and the Oxy-fuel; where air is replaced by pure oxygen during the combustion to produce a flue gas stream with a very high CO_2 purity [30]. Step 2: the CO_2 transportation; in which the CO_2 after being captured and separated is transported to the storage site via trucks and ships when it is liquefied or by pipelines when it is in a dense phase, however, most of the transportation processes are conducted by pipelines, since they offer continuous transport and considered as a more economical way [31, 32]. Step 3: the CO_2 storage; this is the last step where CO_2 is injected in geological storages at depths of more than 1 km [33] or injected in deep ocean storages which is the less favourable option due to the
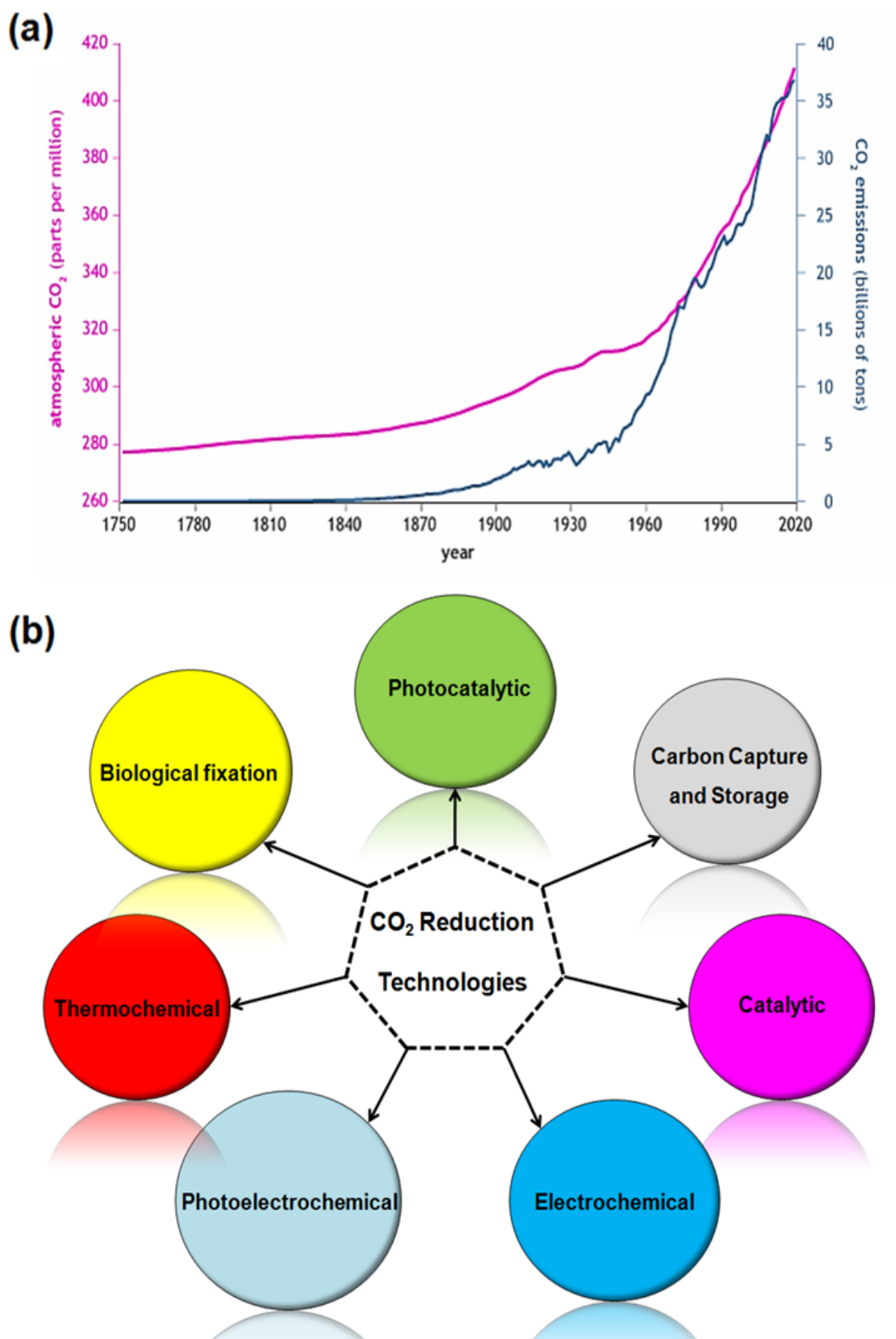
Figure 2.1   (a) The concentration of CO_2 in the atmosphere in ppm (raspberry line) and CO_2 emissions in billion tons (blue line) since 1750 [26, 34], (b) A scheme illustrating the different technologies for CO_2 mitigation and utilization.

ocean acidification and eutrophication [32]. Overall, the CCS operating cost is extremely high and all the involved processes need continuous monitoring and control. Besides, the high leakage potential risk of the stored CO_2 remains as one of its main disadvantage [11].

2.2.2 Catalytic Conversion

Catalytic conversion is one of the CO_2 utilization techniques that uses chemical means. Generally, there are two different types of this technology; heterogeneous and homogeneous catalysis. These two catalytic approaches are based on three-step process:(a) adsorption of CO_2 into the catalyst, (b) the decomposition of CO_2 and (c) the desorption of products. The CO_2 catalytic reactions basically involve the hydrogenation of CO_2 towards methane, methanol or heavier hydrocarbons. However, these reactions require high temperatures ranging from 300 to 400 °C and hence, additional CO_2 is generated for producing the energy required to provide such temperatures [35, 36].

2.2.3 Thermochemical Conversion

This technology is similar to the previous technology, however, the CO_2 chemical reduction here is achieved mainly by the thermal conversion of CO_2 into CO or CH_4 with reactions at high temperatures ranging from 500 to 1000 °C [37]. Concentrated solar radiation can also be used as an energy source to drive these highly endothermic reactions [38]. However, high initial investment costs are required for either high-temperature reactors or concentration lenses of sunlight. Furthermore, the understanding of surface chemistry, morphology, chemical and structural changes is still limited at high temperatures [37].

2.2.4 Electrochemical Conversion

The electrochemical reduction of CO_2 (ERC) dates back to 1970s [39], it is one of the most used technologies which provides possible approaches to reduce CO_2 into other chemicals or fuels with the use of electrical energy [40]. The catalytic process can be either in homogeneous or heterogeneous phase. However, understanding the reactions mechanism remains challenging due to the complexity in the chemistry of electrochemical CO_2 reduction [41, 42]. This process also requires high over-potential, moreover, the selection of the electrolyte is very important for achieving good electrocatalytic performance and to avoid poisoning and deactivation of the catalysts [35, 43].

2.2.5 Photoelectrochemical Conversion

Similar to electrocatalysis, the photoelectrochemical (PEC) route provides an opportunity for reducing CO_2 into valuable chemicals and fuels. However, they differ in the source of electrons. The applied current in electrochemical reduction provides the required electrons, whereas in the photoelectrochemical reduction, electrons come from the excitation of semiconductors by exposing them to light radiation [44]. PEC also offers broader selection for the semiconductor compared to photocatalysis. Although, photo-electrocatalytic CO_2 reduction seems to combine some of merits in both photocatalysis and electrocatalysis, it is still far away to be comparable with these technologies in terms of research and studies. Kinetics and the photoelectrode stability also remaining big challenges [39].

2.2.6 Biological Fixation

This is one of the CO_2 mitigation approaches for renewable energy production [45]. It is based on the use of microalgae, which are photosynthetic microorganisms that convert CO_2 into biomass in the presence of sunlight and water [46]. Although, great success has been made in microbial production of fuels and

other chemicals from CO_2, achieving this on an industrial scale is still not feasible due to extremely low efficiencies in CO_2 fixation [47]. Furthermore, the operating conditions for many microalgal species used in this field remain as a significant challenge for their survival. These conditions include high concentrations of CO_2, high temperatures and the pH levels which greatly influence both the growth of microalgae and the biofixation of CO_2 [48, 49].

2.2.7 Photocatalytic Conversion

The photocatalytic CO_2 reduction has attracted researcher's attention in the recent years. The concept basically simulates the general natural photosynthetic cycle, thus, no extra energy is required as the photocatalysis uses only solar light to convert CO_2 into other valuable chemicals [39]. Among all the previous technologies, photocatalysis is considered to be the most applicable and sustainable approach due to many advantages including the usage of economical reactant (water), low power requirements, room temperature reactions, considerably low pressures and no negative impacts to the environment. In addition to its superiority in terms of operating costs, productions rates and efficiencies compared to other competitors [9-11]. The CO_2 capture and conversion cycle in a typical photocatalytic system has been demonstrated in Figure 2.2.

Although, this technology needs more efforts for developing more effective photocatalysts, many researchers have already synthesized and introduced different types of photocatalysts with various composite materials. Some of these photocatalysts have shown high conversion rates under visible light irradiation, while others did not function effectively under visible light and exhibited low yield rates, however, researchers, up to date, are still trying to improve the photocatalytic properties in terms of solar fuel conversion [50]. In this review, the fundamentals of photocatalytic CO_2 reduction are discussed in details with more focusing on recent advancements in MOF-based photocatalysis.

12
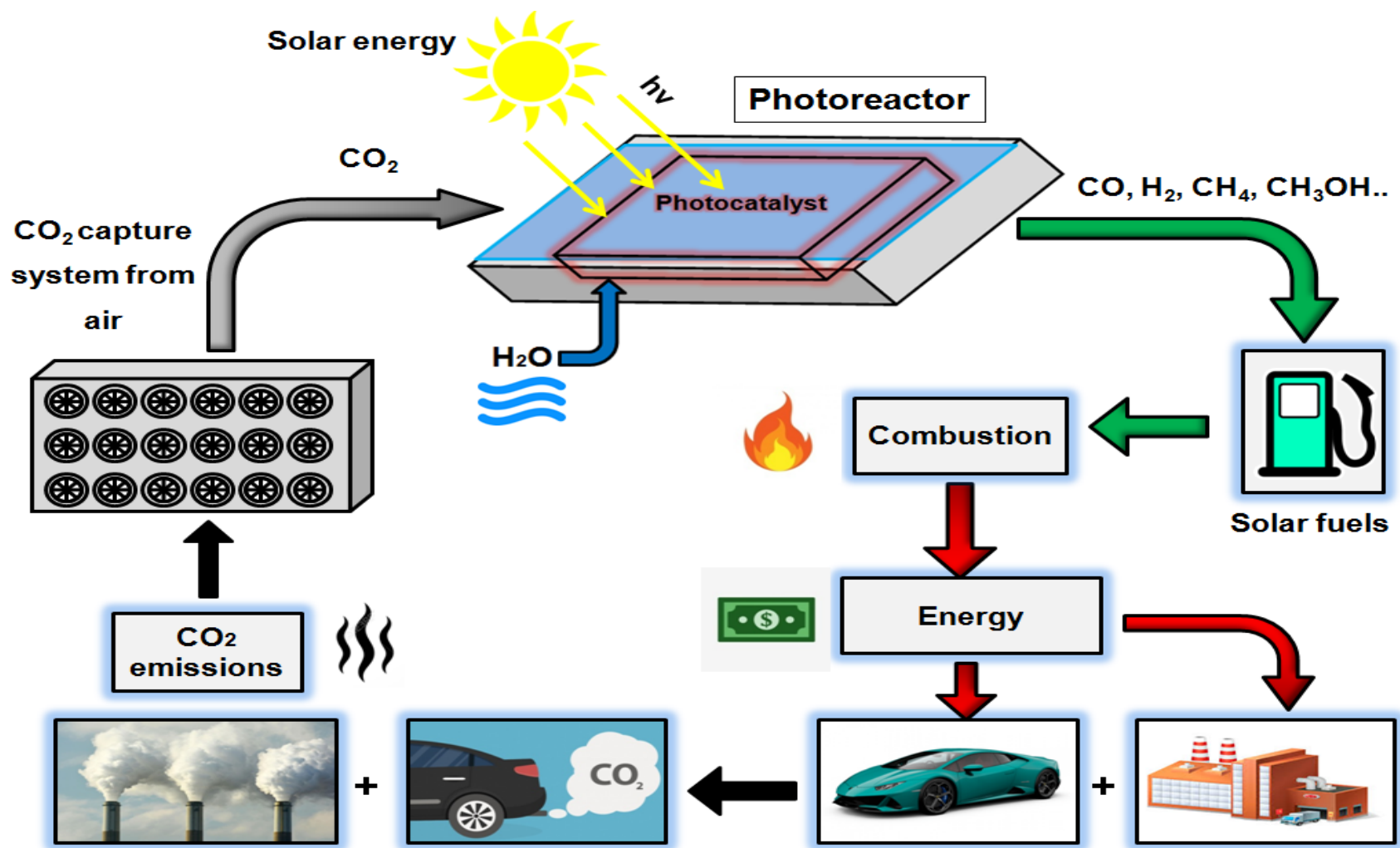
Figure 2.2   A scheme illustrating the capture and recycling of carbon dioxide into solar fuels in a typical photocatalytic system.

2.3 Fundamentals of CO₂ Photocatalytic Reduction

The good understanding of the fundamentals related to the photocatalytic CO_2 reduction process is considered to be the key for enhancing the photocatalyst efficiency and performance for obtaining higher production yields. In this section all the fundamentals including principles, thermodynamics, mass transfer and mechanisms are explained in details.

2.3.1 Principle of MOF-based Photocatalysis

MOFs are a class of porous crystalline materials that are constructed by metal ions/clusters and organic linkers [51, 52]. These materials captured widespread interest in the field of catalysis [53], gas storage [54] and separation [55], batteries synthesis [56], drug delivery [57] and other applications as shown in Figure 2.3 (a). MOFs own a lot of unique properties including large surface areas, tunable structures and high porosity [58, 59]. In recent years, MOFs have been employed for photocatalysis and extensive investigations were made for synthesizing more effective MOF photocatalysts for photocatalytic CO_2 reduction. These materials could be used either as pure MOFs (Figure 2.3 (b)) or in other several forms of MOF-based composites as illustrated in Figure 2.3 (c). The photocatalysis is known to be as a photoreaction process in the presence of a photocatalyst, in MOF photocatalysis, the process is conducted when the light radiations having energy equal to or greater than the energy band gap (E_{bg}) of MOF material are subjected to its surface to generate electron-hole pairs (e^-/h^+). When the required energy is available, the photogenerated electrons and holes undergo various oxidation and reduction processes to produce the final products. The redox reactions will either reduce acceptors (CO_2) if the MOF semiconductor donated electron (Path C) or oxidize donor species (H_2O) if holes are transferred to the surface (Path D) as shown in Figure 2.3 (d). However, if electrons fail to find any of the trapped species (e.g. CO_2 or H_2O) over the MOF surface or due to its very small energy band gap, then they generate a reverse process and recombine immediately to release unproductive energy in the form of heat [12, 13].
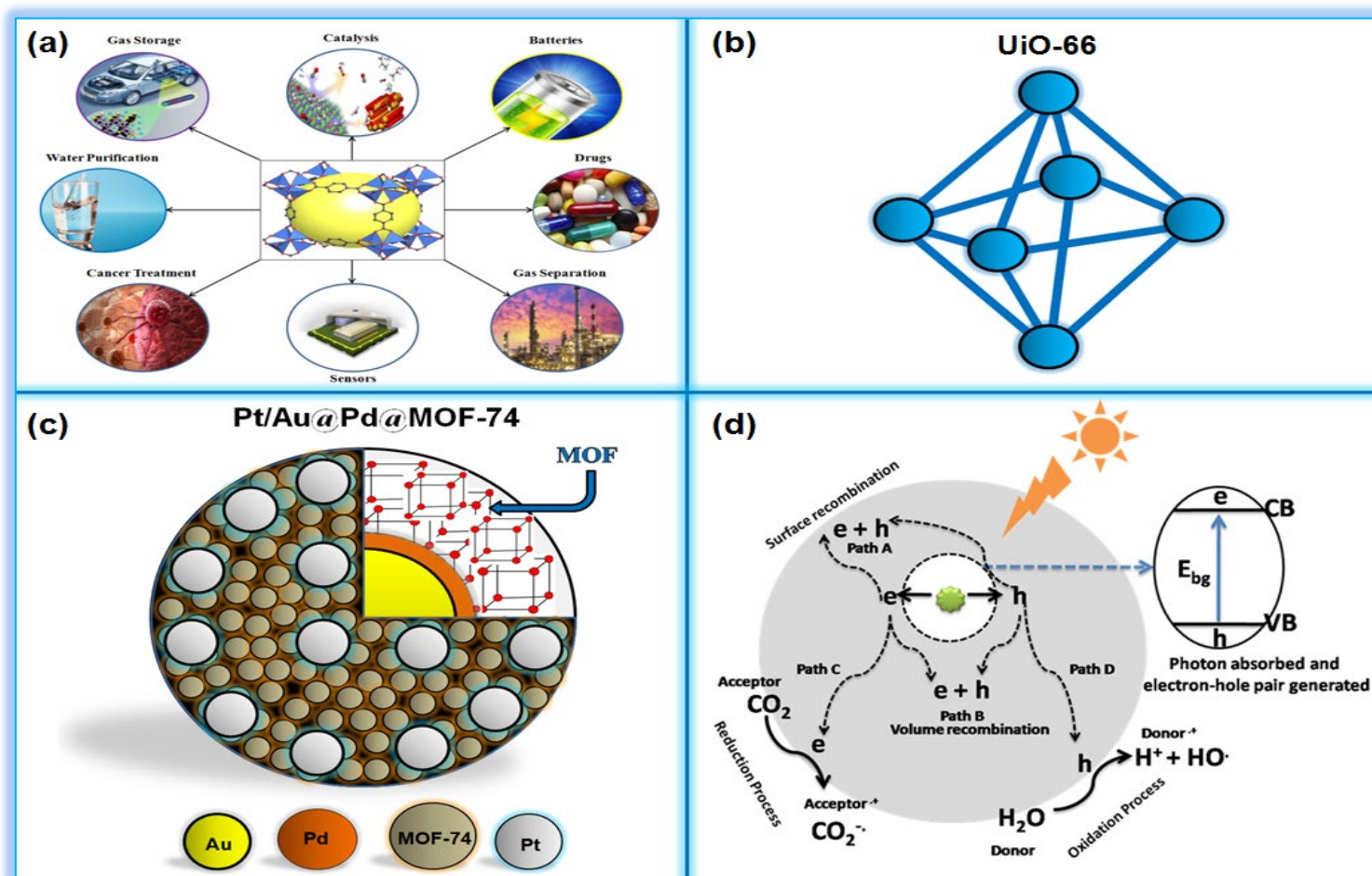
Figure 2.3 (a) A scheme illustrating the different applications of MOFs, (b) Pure Zr-based MOF (UiO-66), (c) Metal MOF-composite consisting of MOF with three different metals (Au, Pd and Pt), (d) The principle for oxidation and reduction process and pathways on the surface of a heterogeneous photocatalyst [60].

The reverse processes are either volume recombination in which separated charge carriers are recombined in the bulk of the MOF semiconductor (Path B) or surface recombination if the recombination occurs at surface (Path A). This might be represented by the Equations (2.5) and (2.6) [61].

$$\text{Photo-catalyst} \xrightarrow{\text{hv}} e^- + h^+ \tag{2.5}$$

$$e^- + h^+ \longrightarrow \text{Heat} \tag{2.6}$$

where h is the Planck's constant ($h = 6.63 \times 10^{-34}$ J.s), v is the frequency which is equal to the speed of light ($C = 2.99 \times 10^8$ m s^{-1}) over the wavelength (λ in m), e^- represents a conduction band electron, and h^+ represents a hole in the valence band. It is worth mentioning that the band gap energy is measured in (eV) where 1J is equal to 6.24×10^{18} eV.

The energy band gap of a semiconductor is formed due to the potential difference between the conduction band (CB) and valence band (VB) as illustrated in Equation (2.7), however, in MOF photocatalysis, these energy levels can also be expressed as the highest occupied molecular orbital (HOMO) and the lowest unoccupied molecular orbital (LUMO) which correspond to the VB and CB in semiconductors [62]. MOF semiconductors can be classified on this basis into two types: direct and indirect band gap semiconductors, direct band gap semiconductors; in which minimum CB level of energy and maximum VB energy level have the same angular momentum position, while in the indirect band gap semiconductors different angular momentum positions are present [13, 63].

$$E_g = E_C - E_V \tag{2.7}$$

So, both band gap and the position of the VB and CB (HOMO and LUMO) play significant roles in the photocatalytic CO_2 reduction and hence, more efforts should be exerted in the field of MOF band gap engineering for better understanding to avoid the possibility of any recombination of charge carriers.

2.3.2 Thermodynamics of CO$_2$ Photocatalytic Reduction

Oxidation and reduction processes occur when the inert compounds (CO$_2$ and H$_2$O) are activated and transformed to more reactive species called (free radicals) which then form the solar fuels and/or other valuable chemicals. CO$_2$ is considered to be thermodynamically stable and difficult to break or split into carbon monoxide and oxygen in low temperatures. Therefore, the thermodynamics of CO$_2$ photocatalysis can be discussed in terms of temperature, light, CB and VB of the semiconductors. Generally, semiconductors may have completely filled VB and empty or partially filled CB, between them, lies the forbidden energy level; band gap energy (E$_{bg}$). When light radiations with energy that is greater than the band gap strike a semiconductor, it undergoes an excitation state and disturbs a population of electrons and holes in the CB and VB, respectively. Electrons are likely to achieve internal equilibrium within energy level rather than across band gap because the relaxation time within conduction band is shorter than across the band gap as shown in Figure 2.4 (a) [63, 64]. States of electrons with internal equilibrium are known as (quasi equilibrium states) and the potential of electrons and holes in quasi-fermi levels are given by Equations (2.8) to (2.10) [65].

$$F_n = E_c + K_B T \ ln \ (\frac{n}{N_c}) \qquad\qquad (2.8)$$

$$F_P = E_V + K_B T \ ln \ (\frac{P}{N_V}) \qquad\qquad (2.9)$$

$$\Delta G = - \left| F_n - F_P \right| = - E_g - K_B T \ ln \ (\frac{nP}{N_V N_c}) \qquad\qquad (2.10)$$

where E$_C$ is the minimum energy level position (C$_B$), E$_V$ is the maximum energy level position (V$_B$), K$_B$ = is the Boltzmann constant, n and P represent the concentration of the carrier, N$_C$ and N$_V$ represent effective densities of states in C$_B$ and V$_B$.

Figure 2.4   (a) Thermodynamics and Gibbs energy of a photocatalyst when subjected to light and with no light [63], (b) The relation between the light wavelengths (λ) and the band gaps (Ebg) of semiconductors, band gaps (in eV) are calculated using the formula [$E_{bg} = 1240/(\lambda \text{ in nm})$].

18

A driving force is needed for the initiation of a photocatalytic reaction to generate electron-hole pairs. Heat is not that thermodynamic force, the required energy to start the reaction is the Gibbs free energy (ΔG) which is supplied by the light irradiations. However, it has been observed that the CO_2 photocatalytic reduction increases with the increase of temperature. This can be explained on the basis of mass transfer perspective in which the adsorption–desorption process that occurs at the photocatalyst surface strongly controls the reaction rate. Therefore, higher temperatures are more favourable for increasing the CO_2 mass transfer rate over the photocatalyst surface and thus increasing the overall reaction rate [66]. Furthermore, the temperature encourages the release of the absorbed products from the surface of the photocatalyst which improves the CO_2 photocatalytic activity and increases products yield as well [67]. Besides this, higher temperatures can also promote the reaction rate by reducing the activation energy which is required to start any chemical reaction. So, it's obvious that higher temperature is beneficial in photocatalysis, generally, to speed up the rate of the reaction.

In terms of energy, light intensity and wavelength are crucial factors in photocatalytic reactions. Energy of the excited electron-hole pairs depends upon the light wavelength, while the population of electron-hole pairs relies on the light intensity. Band gap and wavelength of light are closely related to each other; narrowing the band gap enables the semiconductor to work under visible light irradiation (wavelength = > 400 nm) as shown in Figure 2.4 (b), while UV light (100- 400 nm) is needed to activate the materials with larger band gap energy. It is noticed that the activity of CO_2 photocatalytic reduction increases with intensity, while decreases with the light wavelength. Lamps with high power emit higher number of photons and generate plenty of electron-hole pairs. However, fast recombination of photogenerated electrons and holes still able to occur even with high power lamps which lowers the photocatalytic efficiency [63]. So, when choosing a semiconductor, it is important to focus on the maximum visible light harvesting by selecting a material that can function efficiently at a wavelength ranging from 400 to 700 nm.

2.3.3 Mass Transfer of Photocatalytic CO$_2$ Reduction

The photocatalysis implies the acceleration of a photoinduced reaction by the presence of a photocatalyst and light. Photoinduced reactions start by the absorption of a photon with sufficient energy that is equal or higher than the photocatalyst band gap energy and ends up with the mass transfer of reactants in a very short time period. Generally, the processes involved in CO$_2$ photocatalytic reactions include six main steps as illustrated in Figure 2.5 with their relevant parameters. These steps are: (1) Photon absorption, (2) Excitation separation, (3) Carrier diffusion, (4) Carrier transport, (5) Catalytic efficiency and (6) Mass transfer of reactants [68, 69]. In this section the focus will be on the most two essential issues which are: photon transfer limitations and mass transfer limitations (in the case of liquid and gas phase reactions).

2.3.3.1 Photon Transfer Limitations

The light photons, acquired either from the sun or from artificial sources, travel first through the glass layer of the photoreactor then through the bulk of the fluid, depending on the type of reaction whether it is a gas phase reaction or liquid phase reaction, where in gas phase reactions the mass transfer steps are reduced to almost two steps and hence limitations of mass transfer are almost negligible. Finally, the light particles cross the boundary layer to reach the surface of the photocatalyst where the photoreaction takes place. During the penetration journey of light, a portion of the originally emitted light can be absorbed by these components before it reaches the surface of the photocatalyst as shown in Figure 2.6 (a). At steady state, the mass transfer rate to the catalyst surface is equal to the surface reaction rate which can be represented by the Equation (2.11):

$$r_{AS} = K_C \, (C_{AS} - C_{AB})$$

(2.11)

where K_C is the mass transfer coefficient, C_{AS} is the concentration of the reactants at the surface of photocatalyst and C_{AB} is the concentration of the reactants at the bulk fluid.
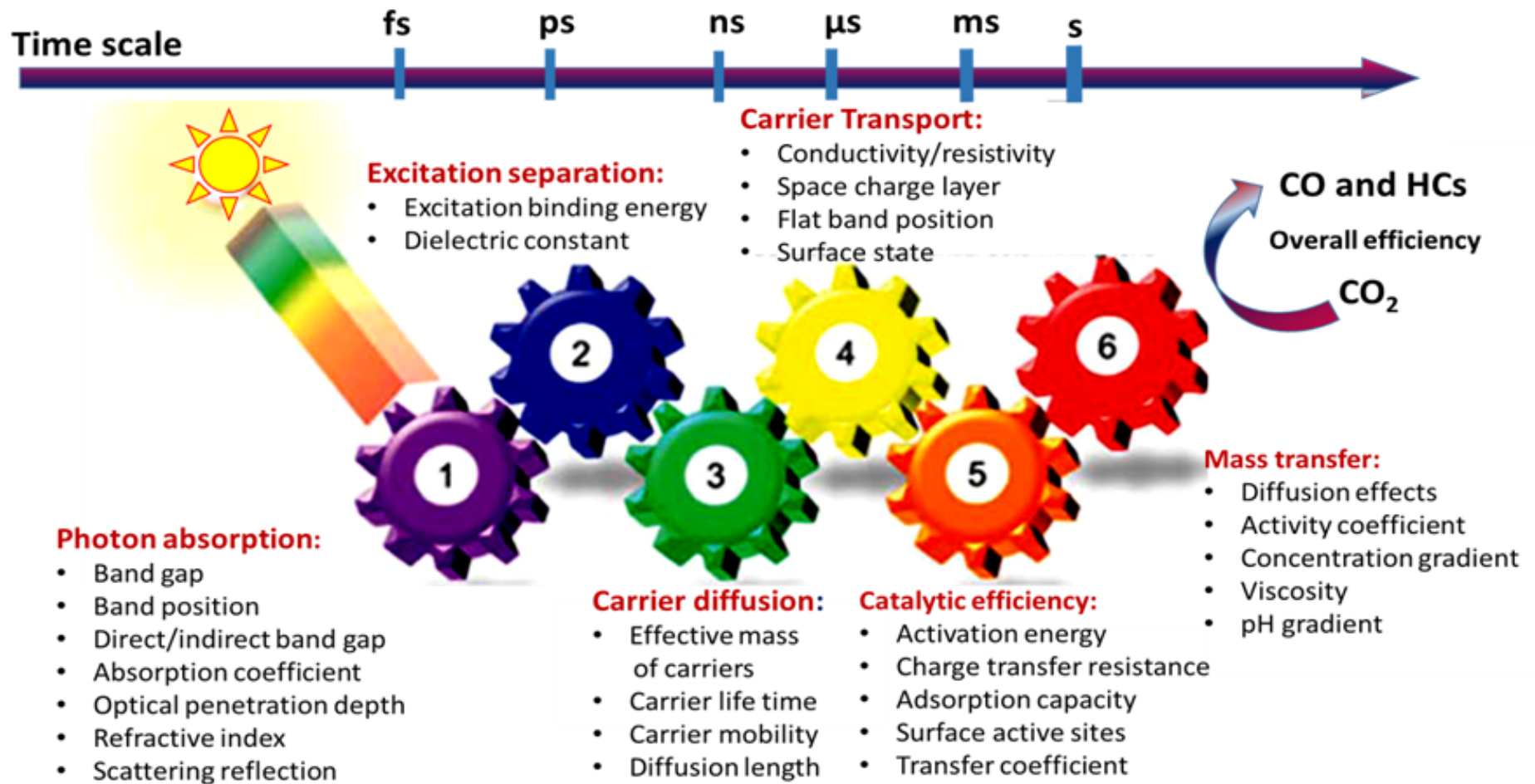
Figure 2.5   A scheme illustrating the major steps in the photocatalytic CO_2 reduction [68].
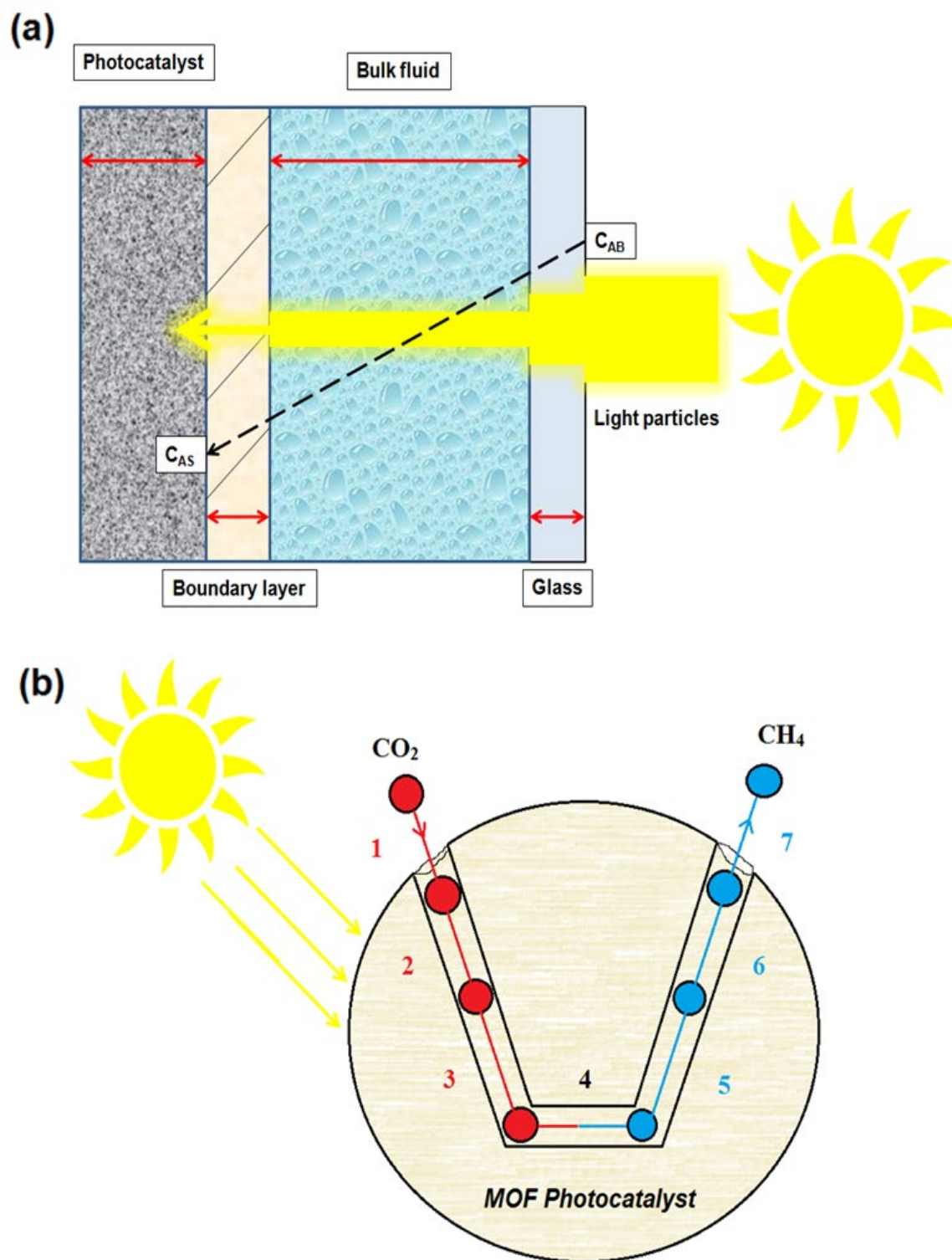
Figure 2.6   (a) A schematic diagram of the profiles of light concentrations through different mediums in a photoreactor, (b) Steps of mass transfer in photocatalytic CO_2 reduction.

2.3.3.2   Mass Transfer Steps of CO_2 Photocatalytic Reaction

The efficiency of CO_2 reduction process is in direct proportional with the rate of mass transfer, when a photocatalytic reaction is initiated, a seven-step sequence of mass transfer takes place as illustrated in Figure 2.6 (b). However, the overall reaction rate is usually controlled by one step only, and knowing the step which limits the rate is the key to understand the system and hence improve it as illustrated in the following seven steps:

1- Step 1: External diffusion of CO_2 from the bulk fluid to the external surface of the photocatalyst.

2- Step 2: Internal diffusion of CO_2 from the pore mouth to the internal surface of the photocatalyst.

3- Step 3: Adsorption of CO_2 to the photocatalyst surface.

4- Step 4: Photoreaction of CO_2 to form solar fuel.

5- Step 5: Desorption of the products (e.g. CH_4) from surface of the photocatalyst.

6- Step 6: Internal diffusion of CO_2 from the interior of the photocatalyst to the external surface.

7- Step 7: External diffusion from the external surface of the photocatalyst to the bulk fluid.

2.3.3.3   Parameters Affecting the Mass Transfer of CO_2 Photocatalytic Reaction

In addition to the adsorption rate of CO_2, desorption rate of the product and the boundary layer effect, there are some system parameters that can also have an impact on the mass transfer rate:

i.   Partial pressure of the system: The CO_2 partial pressure determines the gas ability to overcome the effect of mass transfer resistance especially in the liquid phase. High pressure helps in the improvement of the adsorption, absorption, and diffusion through the pores of the photocatalyst [63].

ii. Temperature: Increasing the temperature increases the rate of photocatalytic CO_2 reduction, this is mainly attributed to the boosting in the molecular kinetic energy

which influences the diffusion of reactants and the desorption of products over the photocatalyst [70].

iii. Concentration: Mass transfer is the transport of a substance (mass) from one location to another or the movement of individual chemical species from a high-concentration region to a lower concentration region. According to Fick's law, the difference in concentrations is the direct driving force of mass transfer by diffusion. So, higher concentrations of the reactants (CO_2 + H_2O) are more favorable for enhanced mass transfer of molecules.

iv. Particle size: The rate of a photocatalytic reaction is strongly affected by the photocatalyst particle size. For large size particles (with large diameter), the reactants (CO_2 + H_2O) take longer time to diffuse into the interior of the photocatalyst which limits the overall reaction rate, while very short time is needed for tiny particles to reach the center of the photocatalyst and thus better photocatalytic performance can be achieved [71].

v. Stirring: Stirring and turbulence (turbulence may occur as a result of stirring or bubbling of CO_2) have a strong impact on the improvement of liquid phase CO_2 reduction system, the main concept beyond that is limiting the mass transfer resistance of the boundary layers which are liquid layers formed over the photocatalyst surface. Stirring increases the molecules velocity over the photocatalyst surface which in turn minimizes the thickness of these boundary layers and enhances the CO_2 reduction efficiency [63].

vi. Surface area and porosity of photocatalyst: In terms of mass transfer, surface area and porosity of the catalyst are crucial factors in both liquid and gas phase systems. By increasing the surface area, more active sites for the adsorption of reactants will be available whereas increasing the porosity will attain more pathways for enhancing the internal diffusion [72].

vii. pH of the system: High pH (7-14) increases the solubility of CO_2 for liquid systems, while for the gas phase systems, basic functionalization over the surface of the photocatalyst enhances the adsorption of CO_2, resulting in enhancing the catalytic activity [73, 74].

2.3.4 Mechanism of Photocatalytic CO_2 Reduction

The knowledge about the reaction mechanism and what exactly happens in the CO_2 reduction is still not very clear, whereas, the product selectivity is also not well understood [75, 76]. Therefore, much attentions have been paid to clarify and explain the mechanism behind this reaction [75]. In addition to theoretical calculations [77, 78] and various microscopic and spectroscopic techniques [79, 80], many studies have been conducted to understand the main steps involved during CO_2 adsorption, activation, and dissociation. Investigations have shown that these steps are strongly affected by the crystal phases (e.g. anatase, rutile), the surface acidic and basic sites (e.g. hydroxyl group, amino group), defect disorders (e.g. oxygen vacancy VO), sacrificial agents or electron donors (e.g. H_2O, TEOA) and the electronic structure of the photocatalyst material [75]. In order to obtain valuable solar products like hydrocarbons, a reducing agent is needed for supplying hydrogen. The main reductants used to proceed CO_2 reduction are H_2O, H_2, CH_4 and CH_3OH [12]. Here in this study only H_2O is deeply discussed since water is considered to be the most inexpensive and nontoxic reductant.

2.3.4.1 Photocatalytic Reduction of CO_2 by H_2O

Among all the used reductants for photocatalytic CO_2 reduction, H_2O is the most economic and a naturally abundant source of hydrogen, as it is readily available. Water splitting is needed in the reduction reaction of CO_2 by H_2O to form hydrogen, which is necessary for the production of solar fuels [81, 82]. The reduction of H_2O to H_2 is more interesting in terms of kinetics and thermodynamics compared to the CO_2 reduction reaction as demonstrated in Equations (2.12)–(2.14) [76]. In terms of polarity, the H_2O molecule has a higher tendency to be adsorbed on photocatalyst surface (such as TiO_2) and thus, the formation of H_2 is more favourable than the formation of other products during CO_2 reduction [76, 83]. To overcome this limitation, several approaches have been suggested, like for example, the fabrication of photocatalysts (metal oxide photocatalysts) with oxygen vacancy sites for the enhancement of the CO_2 adsorption by locating one oxygen atom of CO_2 at bridging oxygen vacancy [84].

$$H_2O + h^+{}_{VB} \longrightarrow H^+ + OH^-$$ (2.12)

$$H^+ + e^-{}_{CB} \longrightarrow H^\bullet$$ (2.13)

$$H^\bullet + H^\bullet \longrightarrow H_2$$ (2.14)

The investigations have shown that the conversion of CO_2 by liquid or vapour water usually follows various pathways to form different products depending on the number of transferred electrons and protons, these products include formic acid (HCOOH), carbon monoxide (CO), formaldehyde (HCHO), methanol (CH_3OH), methane (CH_4) and ethanol (C_2H_5OH) as shown in Figure 2.7. It was also observed that during CO_2 reduction the thermodynamic potential decreases gradually as the number of electrons and protons transferred to CO_2 increases [85].
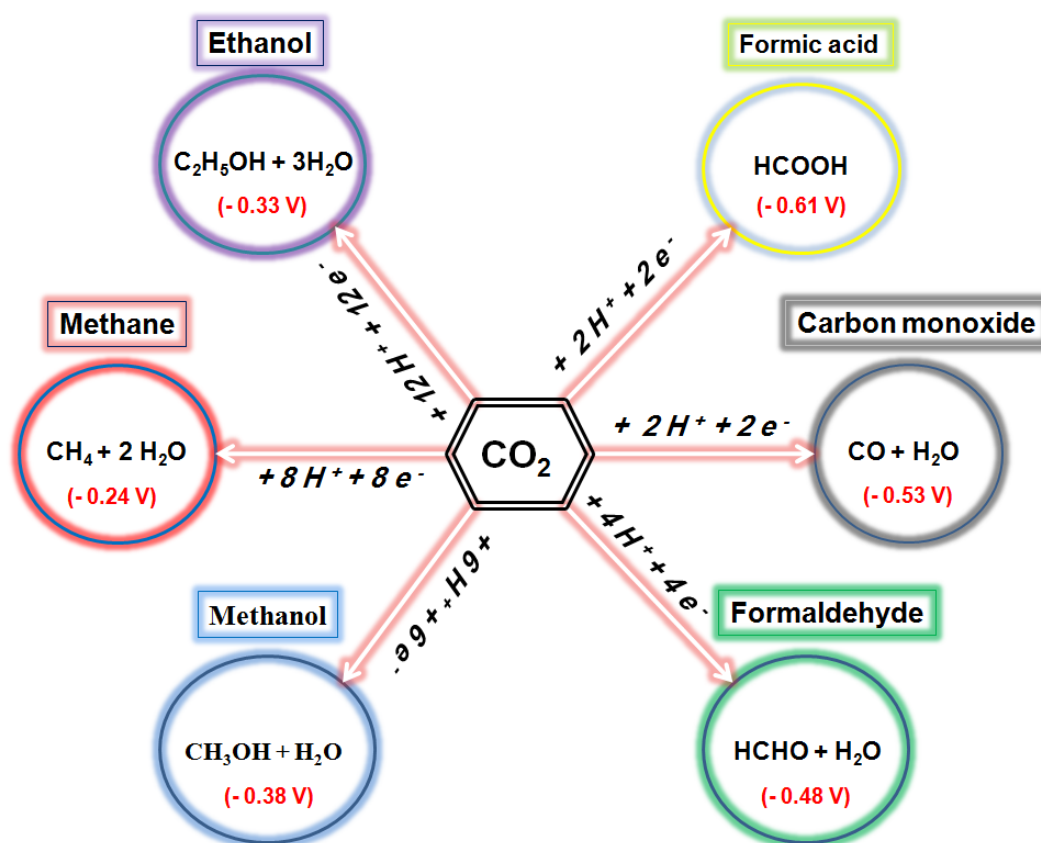
Figure 2.7   Various pathways for the photocatalytic CO_2 reduction into the main products with their thermodynamic potentials [76].

Generally, there are three famous proposed mechanisms for photocatalytic CO_2 reduction, the first mechanism (Mechanism-I) was proposed by Apno et al. [86], the

second (Mechanism-II) was developed by Subrahmanyam et al. [87] while Shkrob et al. reported the third mechanism (Mechanism-III) [79]. These three mechanisms are explained in more detailed equations as shown in Table 2.1.

Mechanism-I was developed as a result of using TiO_2 photocatalyst for the formation of carbon monoxide (CO), methane (CH_4) and methanol (CH_3OH). It was observed that only CO is generated by using pure TiO_2 while the selectivity is shifted to the production of CH_4 and CH_3OH by the addition of Cu. These solar fuel products were formed after a series of reactions between the C· and H· radicals.

In Mechanism-II, a different reaction pathway was developed by the formation of formic acid (HCOOH) as an initiator and then followed by the evolution of more products including formaldehyde (HCOH), methanol (CH_3OH), methane (CH_4) and ethane (C_2H_6) respectively. However, Koci et al. [88] studied the kinetics of CH_4 and CH_3OH formation by aldehyde pathway and found out that the kinetic data do not match with this mechanism.

A new reaction pathway known as glyoxal path way was reported in Mechanism-III, glyxol (HOCCOH) was firstly produced from the CO_2· radicals and then dissociated again into acetaldehyde (CH_3COH) followed by the formation of other products that depend on the dissociation of acetaldehyde. However, it is obvious that both Mechanism-II and Mechanism-III are conflicting since formaldehyde is missing in most of the CO_2 reduction products and hence, Mechanism-I is the most proven and leading reaction mechanism in which solar fuels are formed by the C · radicals dissociated from CO molecules. Firstly, the CO_2· intermediate is formed after the conversion of the raw CO_2 molecules, and then followed by reducing this intermediate into CO and C· radicals respectively to form solar fuels after finally reacting with H· radicals resulting from the dissociation of water. Electron Spin Response (ESR) spectroscopy was used to verify the formation of C· radicals and the other reaction intermediates. The dissociation of CO into C· was also confirmed and explained in details by Sasirekha and coworkers [89]. Furthermore, many studies investigated and proved the formation of reaction intermediates and C· radicals which provides clear evidences for the validity of Mechanism-I [90-93].

Table 2.1　　　Studies of reaction mechanisms in CO_2 photocatalytic reduction [63].

Mechanism I	Mechanism II	Mechanism III	Equation
$2\,CO_2 \longrightarrow 2\,CO + O_2$	$2\,CO_2 + 4\,H^\bullet \longrightarrow 2\,HCOOH + O_2$	$CO_2 \longrightarrow 2\,e^- + CO_2^\bullet$	(2.15)
$2\,CO \longrightarrow 2\,C^\bullet + O_2$	$HCOOH + 2\,H^\bullet \longrightarrow HCOH + H_2O$	$CO_2^\bullet + H^\bullet \longrightarrow OC^\bullet H + OH^-$	(2.16)
$C^\bullet + H^\bullet \longrightarrow CH_3OH$	$HCOH + 2\,H^\bullet \longrightarrow CH_3OH$	$OC^\bullet H + OC^\bullet H \longrightarrow HOCCOH$	(2.17)
$CH^\bullet + H^\bullet \longrightarrow CH_2^{\;\bullet}$	$CH_3OH + H^\bullet \longrightarrow CH_3^\bullet$	$HOCCOH + 4\,H^\bullet \longrightarrow CH_3COH$	(2.18)
$CH^\bullet_2 + H^\bullet \longrightarrow CH_3^{\;\bullet}$	$CH_3^\bullet + H^\bullet \longrightarrow CH_4$	$CH_3COH + H^\bullet \longrightarrow CH_3^\bullet + CO$	(2.19)
$CH^\bullet_3 + H^\bullet \longrightarrow CH_4$	$CH_3^\bullet + CH_3^\bullet \longrightarrow C_2H_6$	$CH_3^\bullet + H^\bullet \longrightarrow CH_4$	(2.20)
$CH_3^{\;\bullet} + OH \longrightarrow CH_3OH$			(2.21)

2.3.4.2 Photocatalytic Reduction of CO_2 by Other Reductants (H_2 and CH_4)

It is well known that CO_2 is a very stable and inert compound which cannot be easily reduced under mild conditions of room temperature and atmospheric pressure [94]. The choice of the reductant which provides the proton for the reduction reaction is considered to be as crucial as the selection of the photocatalyst material since the overall efficiency of the CO_2 reduction process is almost determined by the type of reductant [95]. Generally, H_2O has been the most commonly used reducing agent in many CO_2 photoreduction studies. However, water is a weak reductant and is hardly reducible and the photoreduction of H_2O to H_2 is more favorable in water splitting than in CO_2 reduction [96, 97]. Recently, H_2 and CH_4 have been reported as strong competitive reductants for CO_2 reduction compared to water [94, 95, 98]. The reaction formulas in the case of using H_2 or CH_4 as reductants are presented by Equations (2.22)–(2.23) as follows [94]:

$$CO_2 + H_2 \longrightarrow CO + H_2O \qquad \Delta H^{\circ} = 9.8\,\text{kcal/mole} \qquad (2.22)$$

$$CO_2 + CH_4 \longrightarrow 2CO + 2H_2 \qquad \Delta H^{\circ} = 59.1\,\text{kcal/mole} \qquad (2.23)$$

The first attempt to reduce CO_2 to methane by using H_2 gas as a reductant over Ru/TiO_2 photocatalyst was conducted by Thampi et al. [99] in 1987. By using hydrogen as a reductant, CO_2 was also photoreduced to CO by using Rh/TiO_2 [100], ZrO_2 [101] and MgO [94] under a total pressure of 25 kPa. Aliwi et al. [102] carried out the photoreduction of CO_2 in the presence of H_2S over Bi_2S_3 and CdS to produce HCHO and HCOOH. In addition, it has been found that CO can also be formed as a result of substituting H_2 with CH_4 over MgO [94] and ZrO_2 [103, 104]. Tahir et al. [98] investigated using CH_4 and H_2O together as reducing agents for CO_2 reduction over $Cu/g\text{-}C_3N_4$ nanocatalyst under visible light. The experiments indicated that the photoactivity of the catalysts and the selectivity of the different products are greatly dependent on the type of CO_2-reduction system ($CH_4/H_2O/CH_4+H_2O$).

Overall, the photoreactions using H_2 and CH_4 as reducing agents require high temperatures and pressures to be achieved and hence the development of CO_2 reduction systems which can proceed under mild condition is still essentially required.

2.3.5 Charge Transfer Mechanisms

When light irradiation strikes the photocatalyst surface, the electrons are excited by photons with sufficient energy from the valance band (VB) of the semiconductor to its conduction band (CB), leaving holes in the VB. For photocatalytic CO_2 reduction reactions, the energy level of the CB of a photocatalyst (either MOFs or other semiconductors) and the corresponding reduction potentials of the desired CO_2 reduced product determine the possibility of producing any specific product as illustrated in Figure 2.8 (a) and (b) [105, 106]. As the negativity of the CB potential increase, the driving force for the CO_2 reduction process will increase, consequently, the CB potential of a semiconductor needs to be considerably more negative than that of corresponding CO_2 reduction reaction in order to boost the photoactivity. However, the VB potential of a semiconductor is required to be more positive than that of the oxidation half-reaction for overall reaction to inhibit the photo-corrosion of the photocatalyst [107]. There are also different parameters that must be considered when designing photocatalysts such as light harvesting ability, charge carriers migration, corrosion resistance, surface area, chemical stability and photo-stability [108, 109].

In single component photocatalyst systems, it is challenging to fulfil all the above-mentioned properties for efficient photocatalysis. Moreover, these single semiconductors like the TiO_2 photocatalyst for instance, usually suffer from the rapid recombination of their photogenerated electron-hole pairs and have wide band gap, which obviously lowers the photoconversion efficiency and restricts their practical applications [110, 111]. Therefore, it is necessary to develop strategies to overcome these shortfalls for the enhancement of photocatalytic performance which can be achieved by using composites photocatalysts [112]. Coupling with semiconductors that have narrower band gaps and suitable band potentials can lead to construct heterostructures with different forms [113, 114], mainly known as Type I, II, III, Z-scheme and Step-scheme heterojunctions. Figure 2.9 summarizes the classifications of the most common heterojunction systems and their subdivisions. Detailed information about these heterojunction systems is discussed in the following sections.

(a)

Potentials (V vs. NHE), pH=7

Oxidation semiconductors

BiOBr WO₃ TiO₂ ZnO α-Fe₂O₃ BiVO₄

2.77 eV 2.80 eV 3.20 eV 3.20 eV 2.20 eV 2.40 eV 2.40 eV 2.37 eV 2.40 eV 2.03 eV 2.69 eV 3.52 eV

TaON ZnIn₂S₄ CdS Cu₂O g-C₃N₄ ZnS

Reduction semiconductors

CO_2/CO_2^- (-1.9 V)
CO_2/HCO_2H (-0.61 V)
CO_2/CO (-0.53 V)
$CO_2/HCHO$ (-0.48 V)
H_2O/H_2 (-0.42 V)
CO_2/CH_3OH (-0.38 V)
CO_2/CH_4 (-0.24 V)
H_2O/O_2 (+0.81 V)

(b)

Potential (V vs NHE), pH=7

MOF5 MIL-53(Fe) MIL-88A PCN-224 UiO-66 UiO-66-NH₂ NH₂-MIL-125 MIL-101-NH₂ MIL-101

3.4 eV 2.71 eV 2.46 eV 1.86 eV 3.5 eV 2.75 eV 2.64 eV 2.18 eV 2.06 eV

CO_2/CO_2^- (-0.91V)
CO_2/CO (-0.53V)
H_2O/H_2 (-0.42V)
CO_2/CH_3OH (-0.38V)
CO_2/CH_4 (-0.24V)
H_2O/O_2 (0.81V)

Figure 2.8   Band structures and positions on the basis of redox potentials at pH 7 for: (a) Traditional semiconductor materials [107] and (b) Metal organic framework photocatalysts.
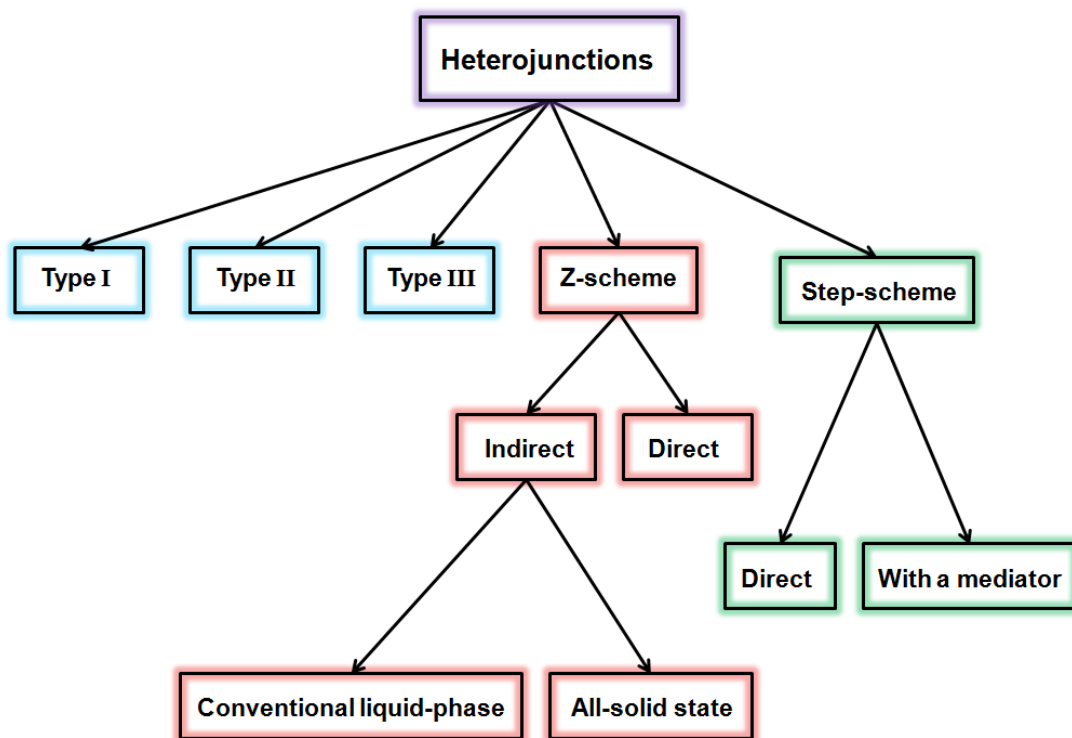
Figure 2.9   Categories of the main photocatalytic heterojunction systems.

2.3.5.1 Type I, II, III Heterojunctions

Generally, a heterojunction is an interface between two different semiconductors that have unequal band structures, which can result in band alignments [115, 116]. Based on these alignments, semiconductors can be classified into three types of conventional heterojunctions: straddling gap (Type I), staggered gap (Type II) and broken gap (Type III) as illustrated in Figure 2.10 [117].

In type-I heterojunction photocatalyst, the conduction band (CB) of semiconductor I (SC I) is lower than the corresponding band of semiconductor II (SC II), while it is the opposite case with the valence band (VB). These attitudes cause difficulty in the separation of electron–hole pairs due to their accumulation at the CB and the VB levels of semiconductor II [117, 118]. For the type-II heterojunction photocatalyst, the CB and the VB levels of SC I are higher than the corresponding levels in SC II and as a result, the photogenerated electrons will transfer to SC II, while the photogenerated holes will migrate to SC I under light irradiations with
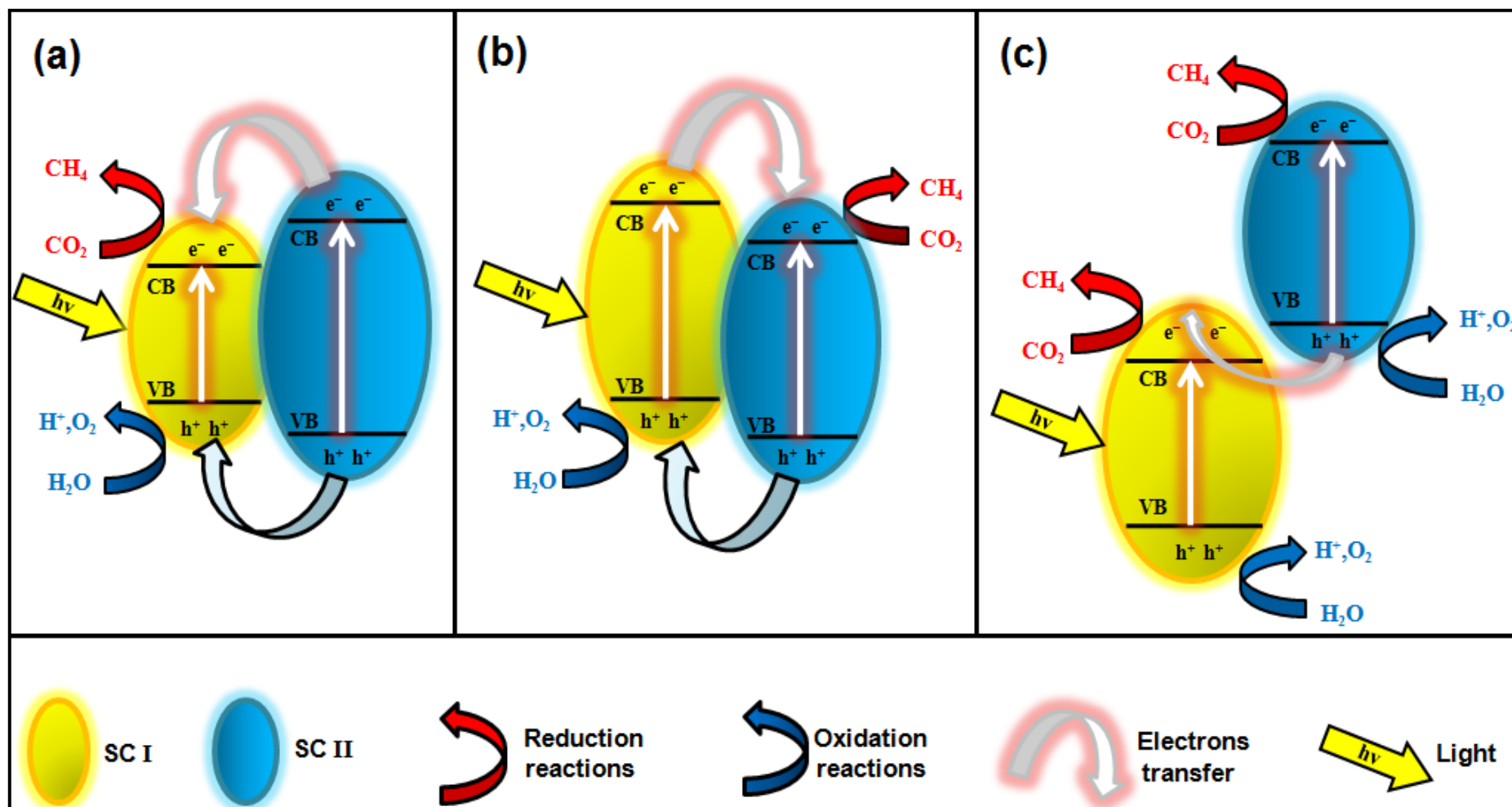
Figure 2.10   A Schematic presentation of three different heterojunctions structures for photocatalytic CO_2 reduction; (a) Type I heterojunction, (b) Type II heterojunction, (c) Type III heterojunction [117, 119]

limited charge recombination rate. Similar to the (Type-I) heterojunctions, (Type III) heterojunctions exhibit reduced photocatalytic activity where the electron–hole migration and separation between SC I and SC II cannot occur because their bandgaps do not intercept [120, 121].

It is worth mentioning that Type II heterojunction is the most typical heterostructures owing to its common occurrence in heterojunction structures and its significant role in suppressing the rapid recombination of photogenerated charges and promoting their separation [122, 123]. However, these heterojunctions including Type II are not favourable when the CB value of (SC I) is not suitable for reduction and VB of (SC II) is not suitable for oxidation reaction which makes the Z-scheme system the more promising structure [119].

2.3.5.2 Z-scheme Heterojunctions

Green plants convert CO_2 and H_2O to O_2 and carbohydrates through a process called natural photosynthesis [124, 125], in which the photogenerated electrons are transported through a Z-scheme structure. Inspired by this theory, Bard et al. [126] proposed the first concept of an artificial Z-scheme photocatalyst in 1979 for the conversion of CO_2 with H_2O into solar fuels with high redox ability and excellent spatial separation of charge carriers [127, 128]. A timeline comparing the historical background of the Z-scheme photocatalysts evolution with the discovery time of the next heterojunction system (S-scheme) is demonstrated in Figure 2.11 (a).

Generally, a Z-scheme system consists of one reduction semiconductor with high CB position (SC I) and another oxidation semiconductor with low VB position (SC II). There are two main types of Z-scheme photocatalytic systems, direct and indirect Z-schemes. The indirect Z-scheme systems include the conventional liquid-phase and the all-solid-state Z-scheme systems as illustrated in Figure 2.11 (c)-(d). In direct Z-scheme system (Figure 2.11 (b)), the two photocatalysts (SC I and SC II) are directly connected to each other and no redox mediators are involved between them.
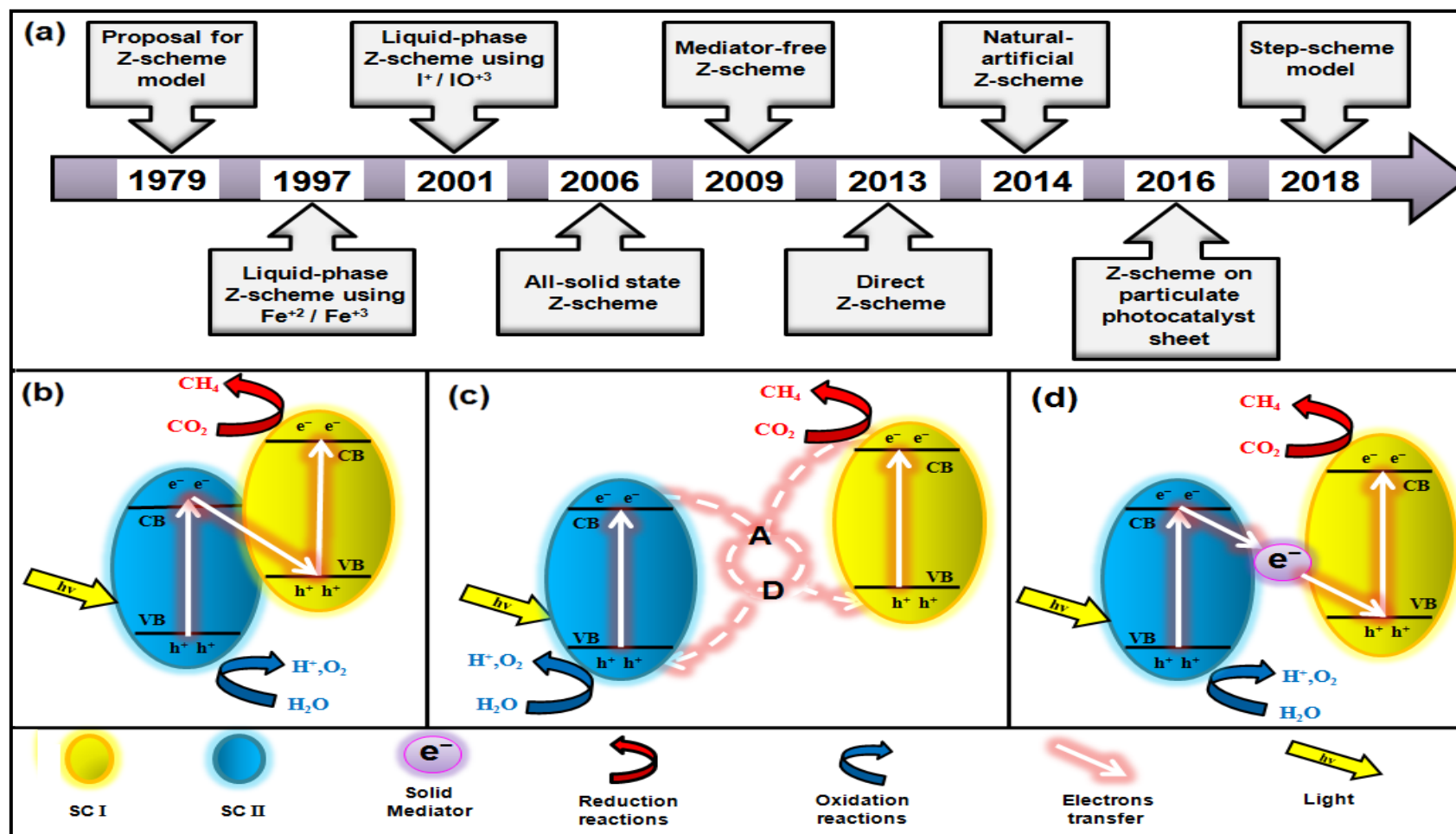
Figure 2.11 (a) Timeline of Z-scheme photocatalysts evolution compared to the time of first proposed S-scheme hetrojunction system, (b) Electron–hole separation in a direct Z-scheme system, (c) Electron–hole separation in a traditional liquid-phase Z-scheme photocatalytic system, (d) Electron–hole separation in an all solid-state Z-scheme heterojunction system [119, 129].

When the electrons in SC II are excited, they will recombine at the heterostructure interface with the holes in SC I. The efficiency of the photocatalytic process is enhanced due to retention of electrons and holes on various counterparts for reduction and oxidation reactions, respectively [130].

However, in the liquid-phase Z-scheme system as shown in Figure 2.11 (c), the two photocatalysts are connected through a proper shuttle redox mediator [131] which is an acceptor (A) and donor (D) pair that assists the two photocatalyst Z-scheme system in transferring the electron-hole charges without being physically contacted through the following redox reaction equations [117]:

$$A + e^- \rightarrow D \tag{2.24}$$

$$D + h^+ \rightarrow A \tag{2.25}$$

For the all solid-state Z-scheme systems (Figure 2.11 (d)), a solid electron mediator is introduced at the interface of SC I and SC II. These solid mediators can be noble metals like (Pt and Au) or carbon based materials like (rGO and CNNs) [132, 133].

2.3.5.3 Step-scheme Heterojunctions

Since the conventional type-II heterojunction has recently shown significant limitations of charge transfer mechanism in terms of kinetics, Fu et al. [134] proposed for the first time the new heterojunction system named as step-scheme (S-scheme) heterojunctions. In type-II heterojunctions, photogenerated electrons transfer from the semiconductor with a higher conduction band (CB) to that with a lower CB, while the photogenerated holes are transferred from the semiconductor of lower valence band (VB) value to the semiconductor with higher VB values. The interfacial charges transfer in this heterojunction system has a negative impact by reducing the redox abilities of photogenerated charges and this mechanism is considered to be thermodynamically unfavourable in photocatalytic oxidation and reduction reactions. In S-scheme heterojunction system as shown in Figure 2.12, two n-type semiconductor photocatalysts (SC I and SC II) are involved in the system in which they represent oxidation and reduction photocatalysts, respectively. The electron transfer mechanism is more like "step" (macroscopic viewpoint) or "N" (microscopic viewpoint) type. The electrons are separated in a space located in the CB of SC II while holes are separated in a space located in the VB of SC I. The internal electric field between SC I and SC II is the source of the driving force of charge carrier transfer. Normally, the oxidation photocatalyst SC I has greater work function and lower Fermi level, in contrast, the reduction photocatalyst SC II has smaller work function and higher Fermi level. When the system is activated, the electrons in SC II will transfer to SC I across their interface which results in building an electrical field with a pathway from SC II to SC I. Eventually, the materials are photooxidized at the VB of SC I and photoreduced at the CB of SC II. So, in a typical S-scheme heterojuction system, holes and electrons will always be available in the VB of SC I and in the CB of SC II respectively, thus enhancing the process kinetics of this process and increasing the overall photocatalytic performance. In comparison with the Z-scheme family, the S-scheme heterojunctions have fundamentally different charge transfer mechanisms. Their unique system provides better reaction dynamics which can be expressed as stronger redox ability and thus enhancing the photocatalytic performance [135].

37
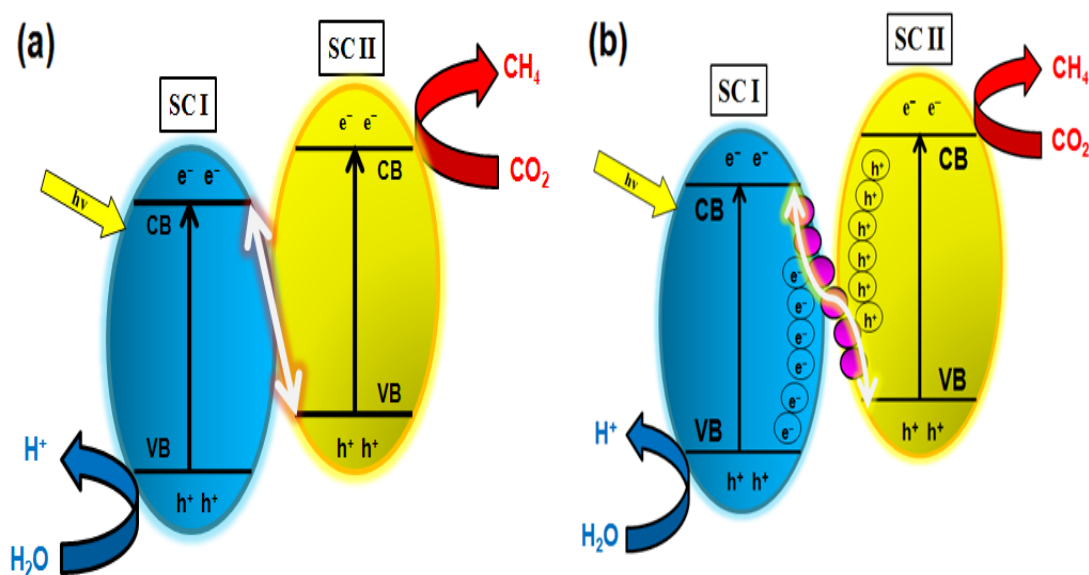
Figure 2.12　　Schematic illustrations of Step-type heterojunction systems: (a) Direct S-scheme heterojunction system, (b) S-scheme heterojunction system with a mediator.

The weakness of the Z-scheme heterojunctions can be explained in terms of the unfavourable charge transfer routes occurring in both traditional (liquid) Z-scheme and all-solid-state Z-scheme heterojunctions. Furthermore, the redox couples in the liquid Z-scheme system are not stable which can result in unwanted side reactions. In addition to the pH sensitivity and the light shielding effect which can also limit its applications [135].

Recently, it was discovered that not all the photogenerated electrons and holes are useful. Nevertheless, the S-scheme system owes a unique strategy of retaining the effective charges while eliminating those ineffective to achieve maximum redox ability and efficient charge separation. This phenomenon was further proved by experimental work [134, 136, 137]. However, the S-scheme heterojunction systems still have some limitations in which their applications are mainly limited to powder photocatalysts and cannot be applied in the photo-electrochemical fields.

2.3.5.4 Charge Transfer Mechanisms in MOFs

Generally, building an effective heterojunction can strongly enhance the photocatalysts performance by facilitating the transfer of charges between the two heterojunction phases. The formation of MOF composites with other semiconductors can significantly increase the photocatalytic activity much higher than both pure MOF and the other pure photocatalyst material, this is mainly attributed to the synergistic effect between these coupled materials [138]. Crake et al. [139] coupled the NH_2-UiO-66 MOF with one of the most widely researched semiconductors for CO_2 reduction (TiO_2) to form a Type II heterojunction (Figure 2.13 (a)) which increased the photocatalytic activity of reducing CO_2 to CO 1.9 times higher than that of pure TiO_2.

A novel MOF-based/metal sulfide composites was synthesized solvothermally for photocatalytic degradation of Rh B dye, named as $ZnIn_2S_4$/UiO-66-$(SH)_2$ [140]. The Type II heterojunction shown in Figure 2.13 (b) resulted in more efficient separation of the photogenerated charge carriers and hence, higher photocatalytic activity of composite was observed compared to that of both single materials. A type II heterojunction was also formed by coating UiO-66 MOF with g-C_3N_4 nanosheets for photocatalytic degradation of Rh B dye under visible light irradiation, the new g-C_3N_4/UiO-66 nanohybrids shown in Figure 2.13 (c) improved the photocatalytic reaction mechanism and exhibited about 3.3 and 6 times better and faster photocatalytic activity for the oxidation of Rh B than that of UiO-66 and g-C_3N_4, respectively [141].

A Z-scheme heterojunction based on metal−organic frameworks was prepared for photocatalytic CO_2 reduction by Meng and co-workers [142], the heterostructure as illustrated in Fig. 13 (d) consisted of oxygen-defective ZnO (O-ZnO), UiO-66-NH_2 MOF and reduced graphene oxide (rGO) which acted as a solid electron mediator for suppressing any charges recombination. The effective spatial separation of photogenerated charges via the Z-scheme resulted in superior activity of reducing CO_2 to CH_3OH and HCOOH.
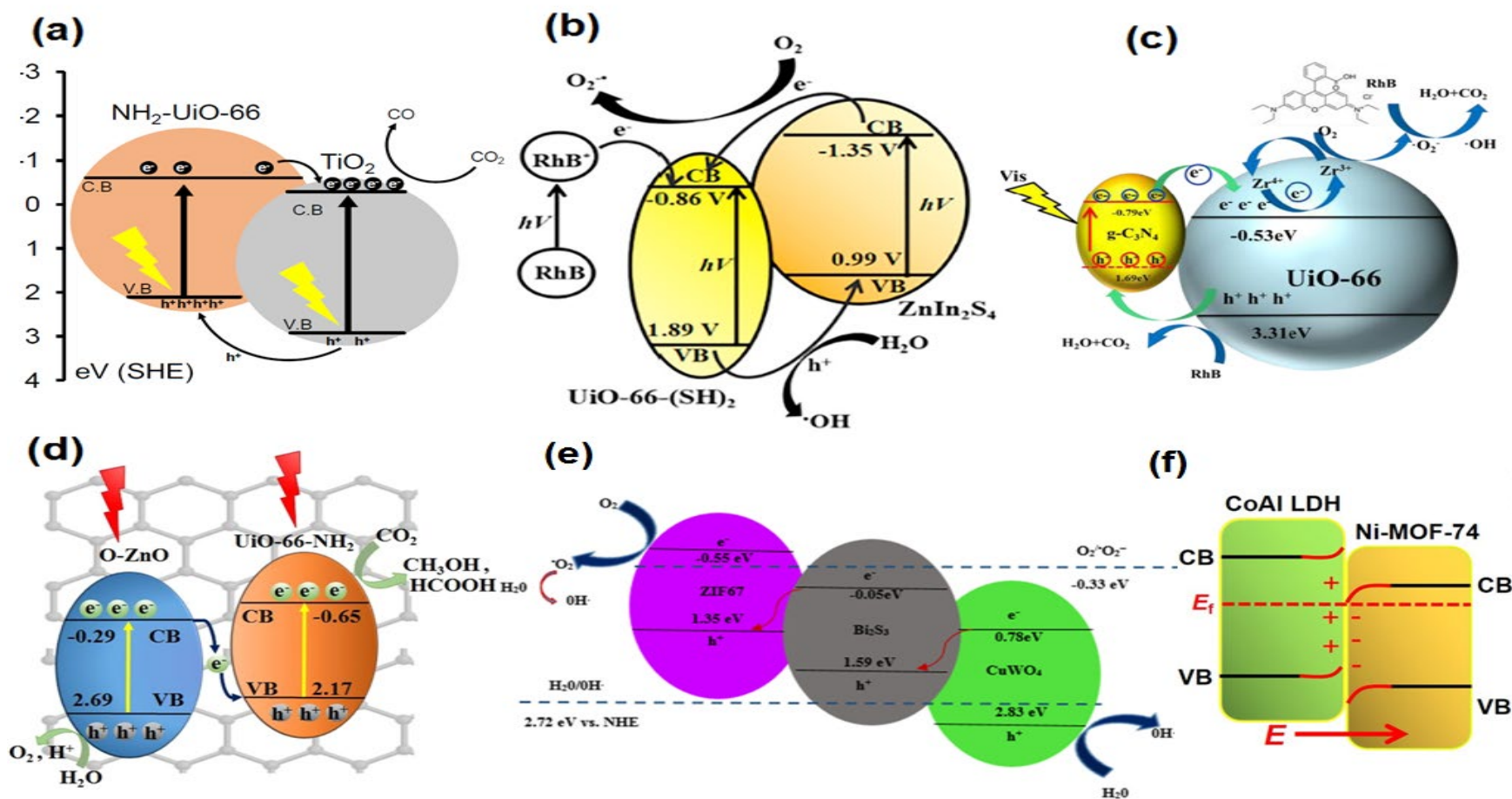
Figure 2.13 (a) Type II hetrojunction in TiO_2/NH_2-UiO-66 for photocatalytic CO_2 reduction [139], (b) Type II hetrojunction of $ZnIn_2S_4$/UiO-66-$(SH)_2$ for photocatalytic degradation [140], (c) Type II hetrojunction in g-C_3N_4/UiO-66 nanocomposite [141], (d) Z-scheme with solid mediator in O-ZnO/rGO/UiO-66-NH_2 catalyst [142], (e) Double Z-scheme heterojunction of $CuWO_4/Bi_2S_3$/ZIF-67 composite [143], (f) CoAl LDH@Ni-MOF-74 S-scheme heterojunction photocatalyst [144].

40

A double Z-scheme ternary heterojunction was also synthesized by Askari and co-workers [143]. The $CuWO_4/Bi_2S_3/ZIF-67$ named composite, as illustrated in Figure 2.13 (e), exhibited considerably enhanced photocatalytic performance for the degradation of antibiotics.

Metal–organic framework (Ni-MOF-74) was coupled with the layered double hydroxides (CoAl LDH) to fabricate an S-scheme heterojunction photocatalyst for efficient hydrogen evolution under visible light irradiation. Higher photocatalytic activity for hydrogen evolution was observed compared to both Ni-MOF-74 and CoAl LDH. The S-scheme heterojunction promoted the recombination of an electron population from the conduction band (CB) of Ni-MOF-74 and holes from the valence band (VB) of CoAl LDH as illustrated in Figure 2.13 (f), it also suppressed the recombination of other electrons from the CB of CoAl LDH and holes from the VB of Ni-MOF-74 [144].

2.3.6   Strategies for Improving MOFs Photocatalytic CO_2 Reduction Efficiency

Since MOF-based materials have similar photocatalytic properties of semiconductors, the general strategies that are used to improve the photocatalytic performance of semiconductor-based photocatalysts can also be applied to MOF-based photocatalysts to improve the CO_2 photoreduction efficiency. Owing to the structural tunability of MOFs, their performance can be enhanced using various strategies which involve improving either the light absorption or the efficiency of electron-hole separation. Strategies of maximizing light harvesting are mainly based on the modification of the organic ligands and the metal clusters of MOFs to reduce their HOMO and LUMO energy gaps for stronger visible light absorption, this can be achieved by introducing photosensitizers or functionalized linkers [145-147]. However, the efficiency of charge separation in MOFs can be improved by the fabrication of MOF composites and the using of metal doping or metal substitution techniques [148-151]. The effect of applying these different strategies on MOF photocatalytic performance is discussed and explained in more details in section 2.5.

2.4 Synthesis of Metal-Organic Frameworks (MOFs)

Up to date, huge efforts have been devoted to develop photocatalysts for CO_2 reduction and a number of excellent studies in this field have already been done. The examined photocatalysts include different materials with different properties such as semiconductors, homogeneous molecular complexes and metal-incorporated zeolites [152]. Recently, new materials known as metal-organic frameworks (MOFs) have been introduced as photocatalysts. These are a new class of hybrid porous crystalline materials, whose structures consist of metal oxide clusters linked by organic molecules to form a 3D micro-porous framework as shown in Figure 2.14 [145].
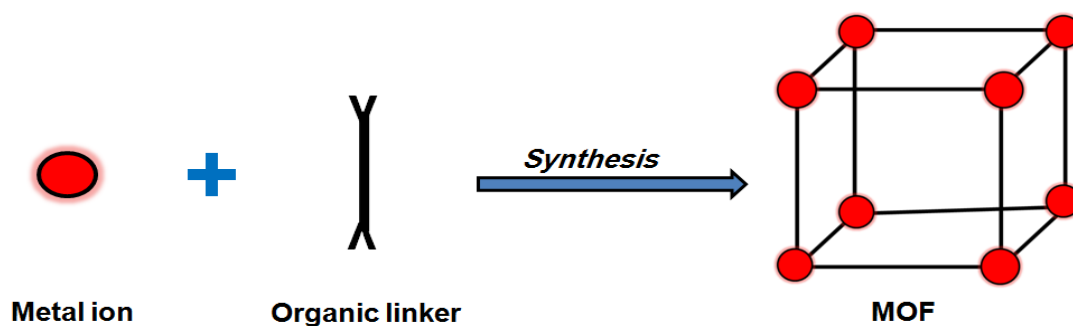
Figure 2.14   Combining metal ions or clusters with multipodal rigid organic linkers to form MOFs.

The first attempts to develop an MOF with photocatalytic properties were made by Chen [153] and by Natarajan [154]. MOFs are also used in many other fields as shown in Figure 2.3 (a). Moreover, MOFs are considered to be the promising photocatalysts compared to other materials like Zeolites in terms of structural analogy. Also, they are superior to other semiconductors due to their high ability of light harvesting and their unique tenability which offers a good opportunity to synthesize visible-light photocatalysts, making them worthy competitors with the most utilized and studied semiconductors like TiO_2 for example [145, 155]. They own many advantageous properties, including well-organized configuration, very large and porous specific surface area; which is favourable for gas adsorption, tunable pore structures and high flexibility of chemical composition, all these merits make these materials very attractive in applications involving gas adsorption and CO_2 reduction and hence achieving the maximum utilization of solar energy for solar fuels production [156].

Generally, the synthesis of MOFs can be made by combining the tree major components; metal salt, ligand and solvent [62] by using different methods for MOF synthesis such as the solvothermal method which represents about 70 % by usage in this field [157]. However, other synthesis approaches such as the slow evaporation synthesis, microwave assisted synthesis, electrochemical synthesis, sonochemical synthesis and mechanochemical synthesis have also been used as other options for MOF synthesis as shown in Figure 2.15.
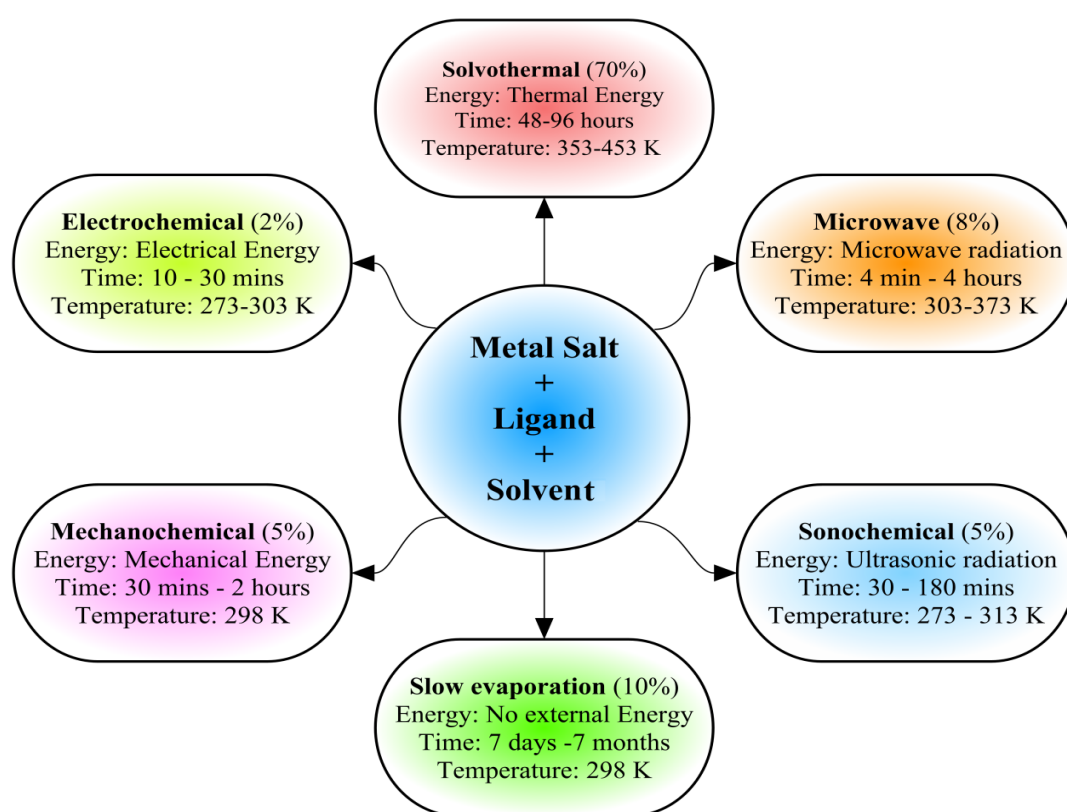
Figure 2.15   A scheme illustrating the different methods for MOF synthesis with their usage percentages and synthesis conditions [157].

The liquid phase reactions that involve heating a mixture of organic linkers with a metal salt in a solvent system are required for the synthesis of most MOFs. The used organic linkers can be carboxylates, phosphates or heterocyclic compounds [158]. The selection of the solvent is mainly based on the reactivity, solubility, redox potential and stability constant [157]. A summary of several MOFs prepared by different synthesis methods is illustrated in Table 2.2 which explains the different conditions such as temperature, time, electric current and composition of solvents required for each method. It is clear from the table that the solvothermal synthesis represents the majority of the synthesis methods used for MOFs fabrication.

Table 2.2   A summary for the most commonly used MOFs and their synthesis methods.

MOF	Synthesis Method	Conditions	Ref.
MIL-101(Fe)	Solvothermal	110 °C, 24 h	[145]
MIL-53(Fe)	Solvothermal	170 °C, 24 h	[145]
MIL-88(Fe)	Solvothermal	100 °C, 12 h	[145]
MIL-101(Cr)	Solvothermal	220 °C, 4 h	[159]
MIL-101-SO$_3$H	Solvothermal	180 °C, 72 h	[146]
NH$_2$-MIL-125(Ti)	Solvothermal	150 °C, 72 h	[149]
Al-MIL-53	Electrochemical	Electrolyte: KCl, 90 °C, 10 mA	[160]
Al-MIL-100	Electrochemical	Electrolyte: KCl, 60 °C, 50 mA	[160]
Al-MIL-53-NH$_2$	Solvothermal	130 °C, 120 h	[161]
Al-MIL-53-NH$_2$	Electrochemical	Electrolyte: KCl, 90 °C, 10 mA	[160]
Fe-MIL-100	Solvothermal	150 °C, 6 days	[162]
Fe-MIL-53	Microwave	300 W, 150 °C, 10 min	[163]
Fe-MIL-101-NH$_2$	Microwave	150 °C, 15 min	[164]
Cr-MIL-100	Microwave	220 °C, 4 h	[165]
Cr-MIL-101	Microwave	600 W, 210 °C, 40 min	[165]

Table 2.2, continued.

MOF	Synthesis Method	Conditions	Ref.
Cr-MIL-101	Microwave	600 W, 210 °C, 40 min	[165]
UiO-66	Solvothermal	120 °C, 24 h	[166]
UiO-67	Mechanochemical	3 h, 30 Hz	[167]
UiO-66/CNNs	Sonochemical	10 min	[168]
UiO-66-Cr CAT	Solvothermal	85 °C	[169]
UiO-66-Ga CAT	Solvothermal	85 °C	[169]
UIO-66-NH$_2$/GR	Sonochemical & Solvothermal	30 min 120 °C, 40 min	[170]
UiO-67 Mn (bpy) (CO)$_3$Br	Sonochemical	10 min,	[171]
HKUST-1	Solvothermal	180 °C, 12 h	[172]
HKUST-1	Microwave	300 W, 140 °C, 1 h	[173]
HKUST-1	Electrochemical	12-19 V, 1.3 A, 150 min	[174]
HKUST-1	Mechanochemical	25 Hz, 15 min	[175]
HKUST-1	Sonochemical	150 W, 1 h	[176]
ZIF-4	Mechanochemical	5-60 min, 30 Hz	[177]
ZIF-7	Sonochemical	110 W, 47 kHz 60 °C, 3 h	[178]

MOF	Synthesis Method	Conditions	Ref.
ZIF-8	Solvothermal	85 °C, 72 h	[179]
ZIF-8	Electrochemical	Electrolyte: MTBS 25 °C, 50 mA	[160]
ZIF-8	Sonochemical	300 W, 1 h	[180]
ZIF-8	Microwave	140 °C, 3 h	[181]
ZIF-8	Mechanochemical	5-60 min, 30 Hz	[177]
ZIF-8	Sonochemical	110 W, 47 kHz 45°C, 4-6-9 h	[178]
ZIF-8	Solvothermal	140°C, 24 h	[178]
ZIF-9	Solvothermal	110 °C, 4 h	[182]
ZIF-11	Sonochemical	110 W, 47 kHz 60 °C, 6-9-12 h	[178]
ZIF-11	Solvothermal	100 °C, 96 h	[178]
ZIF-20	Sonochemical	110 W, 47 kHz 45 °C, 3-6-9-12 h	[178]
ZIF-20	Solvothermal	65 °C, 72 h	[178]
ZIF-67	Microwave	900 W, 5 min	[183]
MOF-2	Solvothermal & Solvothermal	70 °C, 3 h 200 °C, 8 h	[174]
MOF-5	Solvothermal	120 °C, 24 h	[184]

MOF	Synthesis Method	Conditions	Ref.
MOF-5	Microwave	800 W, 105 °C, 30 min	[185]
MOF-5	Sonochemical	60 W, 30 min	[186]
MOF-74	Sonochemical & Solvothermal	20 min 120 °C, 24 h	[151]
Mg-MOF-74	Sonochemical & Solvothermal	500 W 125 °C for 24 h	[187]
Mg-MOF-74	Sonochemical	500 W, 1 h	[188]
Co-MOF-74	Microwave	180 W, 130 °C, 60 min	[189]
Au@Pd@MOF-74	Sonochemical & Solvothermal	15 min 120 °C, 24 h	[151]
MOF-177	Sonochemical & Microwave	500 W 40 min	[190]
MOF-525	Solvothermal	80 °C, 24 h	[191]
MOF-545	Solvothermal	135 °C, 80 h	[191]
MOF (CuCG1)	Solvothermal & Slow evaporation	110 °C, 48 h 25 °C, 30 days	[192]
IRMOF-3	Solvothermal	85 °C, 96 h	[193]
IRMOF-3	Microwave	150 W, 35 S	[194]
IRMOF-8	Solvothermal	120 °C, 24 h	[174]

Table 2.2, continued.

MOF	Synthesis Method	Conditions	Ref.
Cu–MOF	Microwave	300 W, 140-170 °C, 70 min	[173]
Cu-porphyrin MOF[e]	Solvothermal	100 °C, 48 h	[195]
Co-2,6-$C_7H_3NO_4^{-2}$ MOF	Slow evaporation	25 °C, 2 weeks	[196]
[(Co(tib)$_2$) SO$_4$]$_n$	Solvothermal	100 °C, 24 h	[197]
CPO-27-Mg/TiO$_2$	Solvothermal	110 °C, 72 h	[198]
CAU-1	Solvothermal	180 °C, 72 h	[199]
CAU-1	Solvothermal	180 °C, 72 h	[199]
Ni MOLs	Sonochemical	40 kHz, 8 h	[200]
Ni$_3$(HITP)$_2$ MOF	Solvothermal & Sonochemical	150 °C, 12 h 24 h	[201]
2D Ni$_3$HITP$_2$	Solvothermal & Sonochemical	165 °C, 3 h 24 h	[202]
NNU-28	Solvothermal	100 °C, 72 h	[203]
PCN-6	Sonochemical	300 W, 1 h	[204]
PCN-222	Solvothermal	130 °C, 80 h	[205]
PCN-233	Solvothermal	120 °C, 12 h	[206]
PCN-234	Solvothermal	120 °C, 12 h	[206]
PCN-235	Solvothermal	150 °C, 24 h	[206]

MOF	Synthesis Method	Conditions	Ref.
PCN-236	Solvothermal	150 °C, 12 h	[206]
PCN-237	Solvothermal	150 °C, 12 h	[206]
PCN-238	Solvothermal	150 °C, 12 h	[206]
PCN-240	Solvothermal	150 °C, 24 h	[206]
PCN-241	Solvothermal	150 °C, 12 h	[206]
PCN-242	Solvothermal	150 °C, 12 h	[206]
PCN-243	Solvothermal	150 °C, 48 h	[206]
PCN-245	Solvothermal	150 °C, 12 h	[206]
PCN-246	Solvothermal	120 °C, 12 h	[206]
PCN-247	Solvothermal	150 °C, 12 h	[206]
PCN-248	Solvothermal	150 °C, 24 h	[206]
PCN-250	Solvothermal	140 °C, 12 h	[206]
PCN-251	Solvothermal	140 °C, 12 h	[206]
PCN-252	Solvothermal	150 °C, 12 h	[206]
PCN-253	Solvothermal	150 °C, 12 h	[206]
PCN-254	Solvothermal	150 °C, 12 h	[206]
PCN-255	Solvothermal	150 °C, 12 h	[206]
PCN-256	Solvothermal	150 °C, 12 h	[206]
PCN-257	Solvothermal	150 °C, 12 h	[206]

Table 2.2, continued.

MOF	Synthesis Method	Conditions	Ref.
PCN-260	Solvothermal	150 °C, 24 h	[206]
PCN-261-NH$_2$	Solvothermal	150 °C, 12 h	[206]
PCN-261-CH$_3$	Solvothermal	150 °C, 12 h	[206]
PCN-261-Chiral	Solvothermal	150 °C, 12 h	[206]
PCN-262	Solvothermal	150 °C, 12 h	[206]
PCN-263	Solvothermal	150 °C, 73 h	[206]
PCN-264	Solvothermal	150 °C, 24 h	[206]
PCN-265	Solvothermal	150 °C, 12 h	[206]
PCN-266	Solvothermal	150 °C, 12 h	[206]
PCN-280	Solvothermal	150 °C, 12 h	[206]
PCN-285	Solvothermal	150 °C, 12 h	[206]
Re-UiO[f]	Solvothermal	100 °C, 72 h	[207]
Zn-MOF nanosheets	Sonochemical & Solvothermal	30 min 80 °C, 16 h	[208]
Zn/PMOF	Solvothermal	Hot plate, 3 h	[209]
DMOF-1–Zn	Electrochemical	Electrolyte: LiClO$_4$ 0.8 mA, 25 °C, 3 h	[210]
Zr-SDCA-NH$_2$	Solvothermal	100 °C, 72 h	[211]
ZrPP-1-Co	Solvothermal	140 °C, 24 h	[212]

2.4.1   Solvothermal Synthesis

This method is the most commonly used technique for MOFs preparations, the synthesis involves heating a mixture of organic linkers (bridging ligands) with a metal salt in high boiling solvent systems as shown in Figure 2.16 (a) [158]. The most commonly used solvents are organic solvents such as dimethyl formamide, diethyl formamide, acetonitrile, acetone, ethanol and methanol. A mixture of more than one solvent can be used to overcome the insolubility issues [157]. The solvothermal reactions are carried out by using a thermal energy source at different temperature ranges from 353 to 453 K depending on the materials and the reaction requirements. However, for reactions performed at temperatures higher than 400 K, Teflon-lined autoclaves are used [213]. The process could last from 48 to 96 hours to produce fine particle powders that cannot be achieved by most conventional procedures [158].

2.4.2   The Slow Evaporation Synthesis

This technique is one of the conventional methods for the preparation of MOFs in which no external energy supply is required. The evaporation of the solvent occurs gradually which increases the suspension concentration until the dry powder particles are obtained. This method is commonly favourable because it is a room-temperature process, however, the long periods of time needed remains one of its significant disadvantages compared to other conventional methods [214-216]. Figure 2.16 (b) illustrates the slow evaporation process.

2.4.3   Microwave-assisted Synthesis

The microwave-assisted synthesis techniques have been widely used for rapid synthesis of MOFs [217]. The process involves heating the solution in a sealed Teflon vessel with microwaves at a temperature from 303K to 373K for a period of time between 4 minutes to 4 hours to produce nanosized crystals [218]. This technique can produce high quality crystals exactly the same as those obtained with the regular solvothermal processes in addition to extra benefits like fast

crystallization, phase selectivity [219, 220], narrow particle size distribution [221] and facile morphology control [222, 223]. The microwave-assisted process is shown in Figure 2.16 (c).

2.4.4 Electrochemical Synthesis

The electrochemical synthesis method is used where fast preparation of large MOF crystals for certain applications is needed, the process is conducted under mild conditions through adjustment of solvent pH at room temperature and unlike other methods, no metal salts are required, only a mixture consisting of organic linkers and an electrolyte which will provide the metal ions by anodic dissolution [224]. The electrochemical method can also provide a continuous production process to obtain a higher solid content compared to other normal batch techniques [225]. Figure 2.17 (a) shows an electrochemical system set-up.

2.4.5 Sonochemical Synthesis

This method is based on sonochemistry in which the molecules undergo chemical change due to the application of intensive ultrasonic radiation ranging from 20 kHz to 10 MHz [157]. Reduced crystallization time and much smaller particles size can be achieved compared with the conventional solvothermal synthesis [226, 227]. As shown in Figure 2.17 (b), the required MOF is prepared by introducing its substrate solution mixture into a conical Pyrex reactor fitted to a sonicator bar with an adjustable power output. After the sonication process is conducted, bubbles known as acoustic cavitation will be formed and collapsed which creates local hot spots with very high temperature (~5000 K) and pressure (~1000 bar) [226, 228]. Finally, fine crystalline material will be produced as a result of this extremely fast heating process [225].

2.4.6 Mechanochemical Synthesis

Mechanochemical synthesis method as shown in Figure 2.17 (c) is a solvent-free technique where MOFs are produced via a process of performing chemical

reactions by applying mechanical force. Porous MOFs are formed as a result of the breakage of intramolecular bonds followed by a chemical transformation for a short period of time ranging from of 10-60 min [225]. Recently, the mechanochemical synthesis method has been efficiently employed for the rapid synthesis of MOFs by using Liquid Assisted Grinding (LAG) which involves the addition of small amounts of a solvent into the solid reaction mixture [177]. It was found that by varying the amount of added solvent in the LAG process, 1-dimensional, 2-dimensional and 3-dimensional coordination polymers could be obtained from the same reaction mixture [229-231].
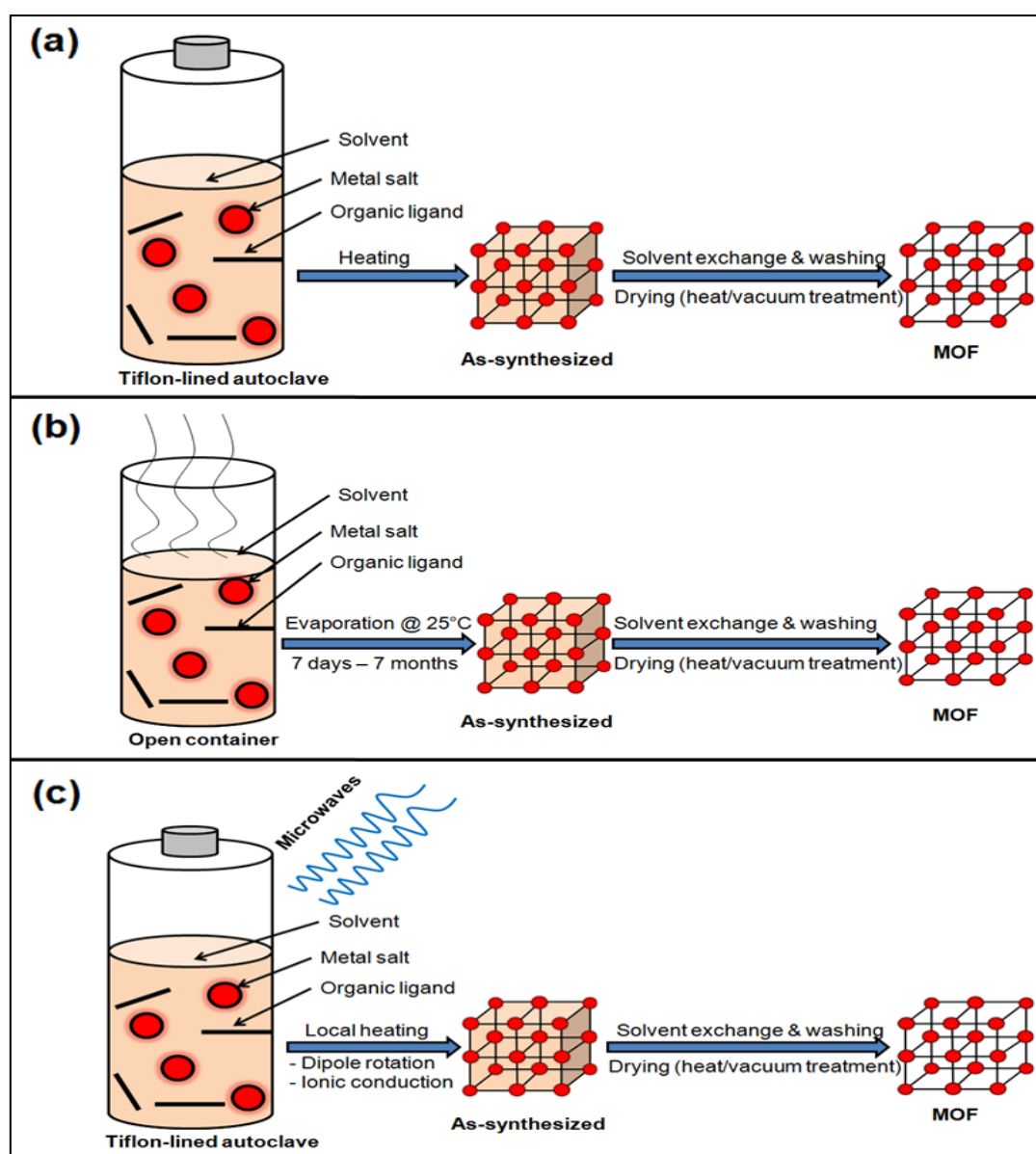
Figure 2.16   A scheme illustrating three different MOF synthesis methods; (a) Solvothermal [185], (b) Slow evaporation and (c) Microwave-assisted synthesis [232].
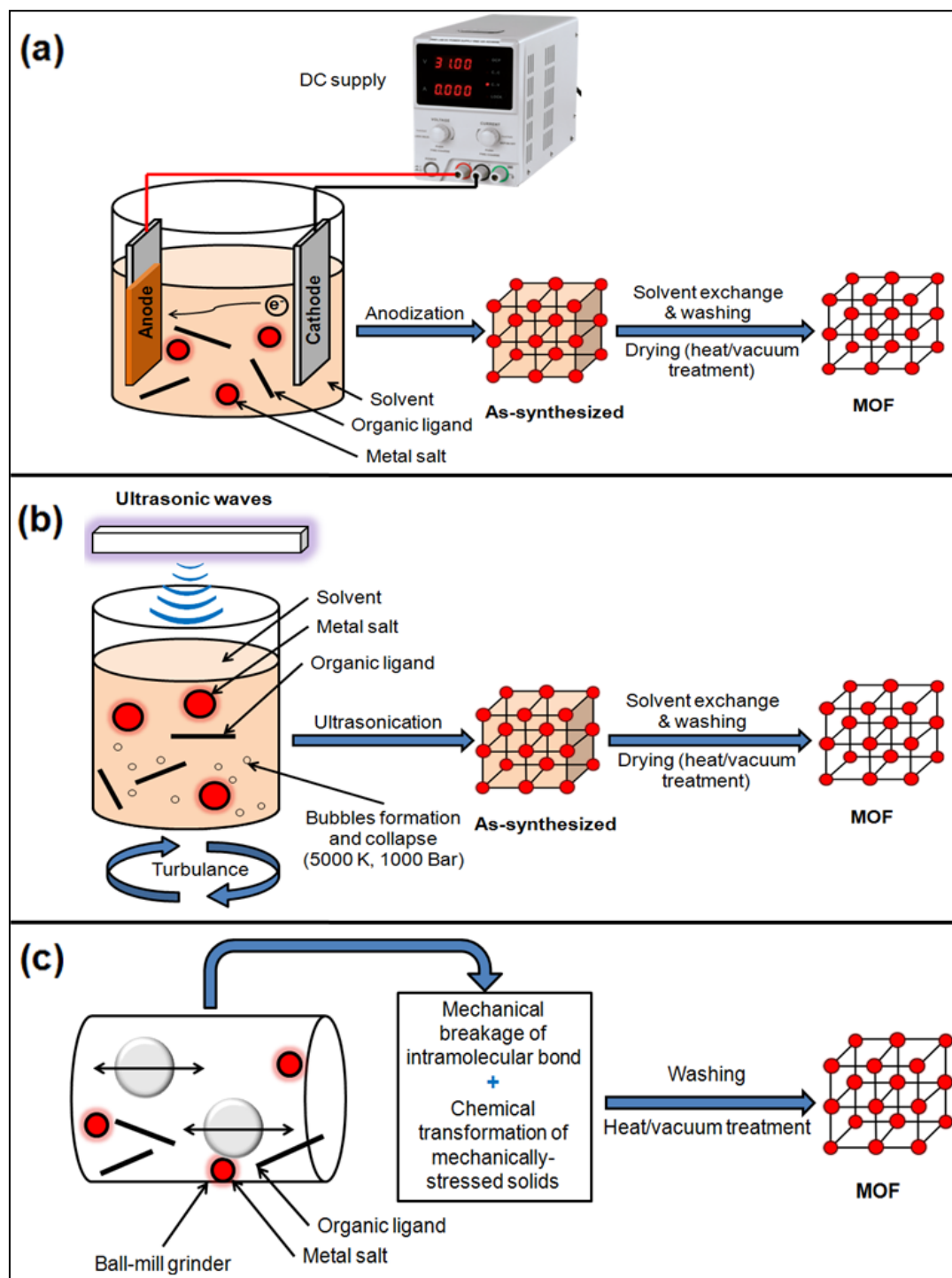
Figure 2.17 A scheme illustrating three MOF synthesis methods; (a) Electrochemical [233], (b) Sonochemical [204] and (c) Mechanochemical synthesis [185].

2.5 Classifications of MOF Photocatalysts

In terms of classification, MOFs can be classified into groups according to the ways the MOF photocatalyst was fabricated or engineered. A scheme representing the different types of MOFs photocatalysts is shown in Figure 2.18. MOFs are classified into main four types: (1) Pure MOFs, (2) Functionalized and Metal Added MOFs, (3) Metal Exchanged and Doped MOFs and (4) MOF-based composites. The following sections summarize the recent developments development in photocatalytic CO_2 reduction by using different classes of MOFs as photocatalysts based on the published papers for the latest ten years.

2.5.1 Unmodified (Pure) MOFs

These are a number of 'pure' MOFs that have been studied and investigated without any synthetic modifications. They have shown good photocatalytic activity for CO_2 reduction and successfully reduced CO_2 into other products. The characteristic properties of these MOFs photocatalysts which have a significant impact on their photocatalytic activities are determined by their constituents [74]. They basically consist of two main constituents which are metal clusters and organic linkers. These MOFs include various types such as Zr-based MOFs, Fe-based MOFs and Zn-based MOFs as shown in Figure 2.19. The recent developments in using unmodified pure MOFs as photocatalysts for photocatalytic CO_2 reduction are summarized in Table 2.3.
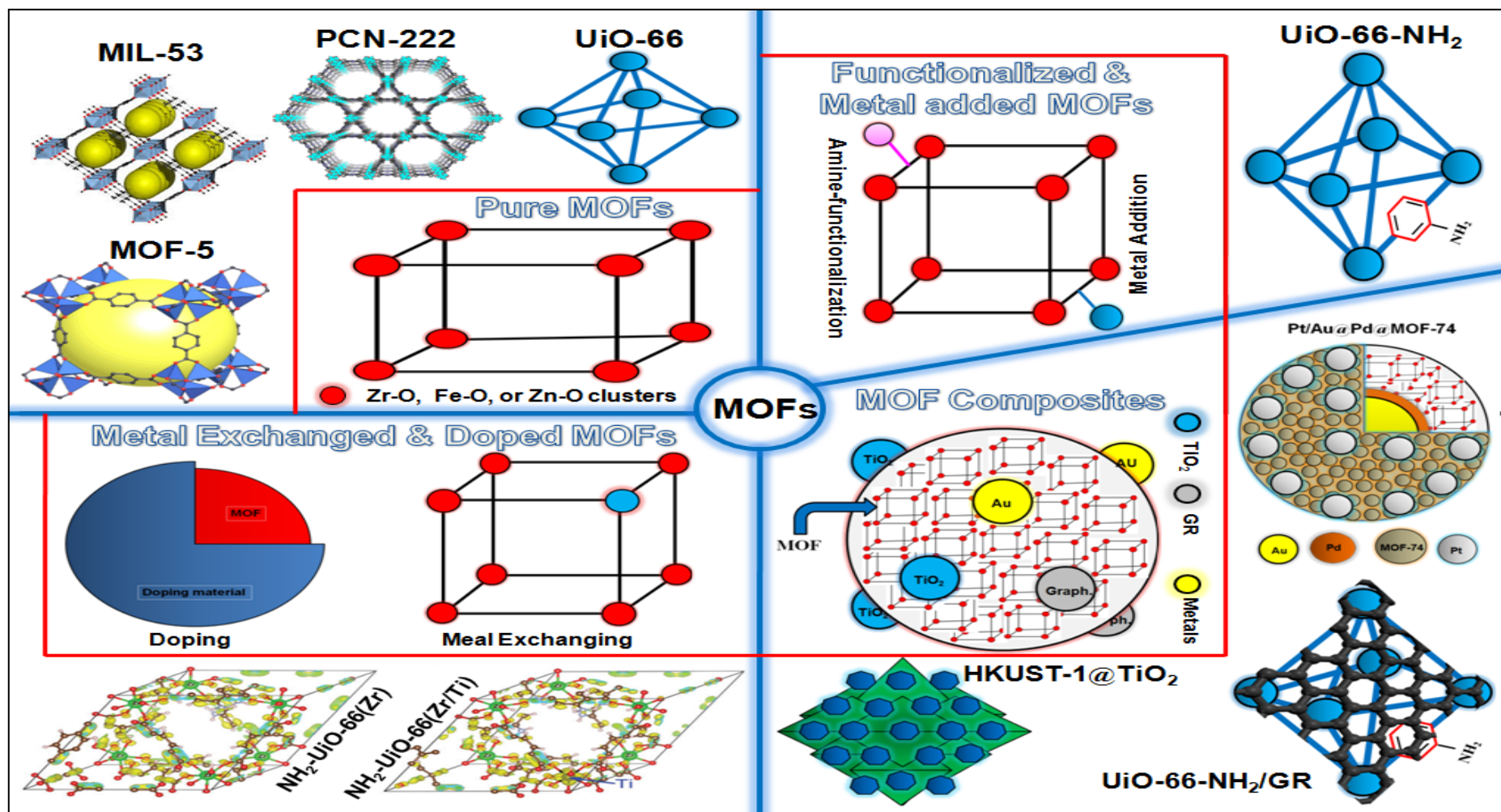
Figure 2.18   MOF photocatalysts classifications: Unmodified pure MOFs, Functionalized and Metal added MOFs, Metal ion exchanged and Doped MOFs, and MOF composites.
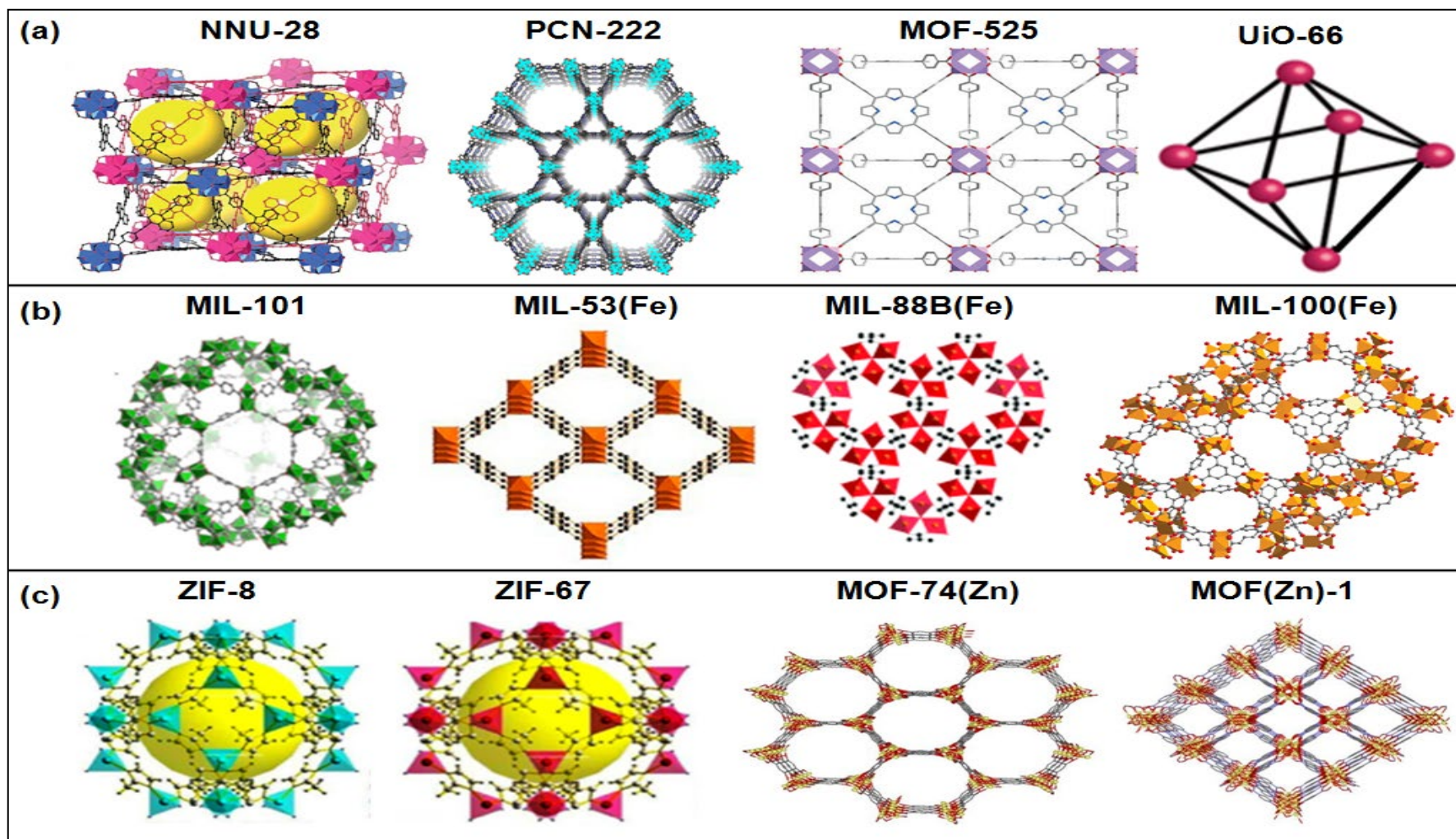
Figure 2.19   A scheme illustrating the most common types of pure MOFs: (a) Zr-based MOFs, (b) Fe-based MOFs, (c) Zn-based MOFs.

Table 2.3   Unmodified (Pure) MOFs photocatalysts for CO_2 reduction and their photocatalytic reactions.

Year	Photocatalyst(s)	Feed Composition	Light source *Power* *Wavelength* *Intensity*	Reactor *Parameters*	Product (μmol g^{-1} h^{-1})	Comments	Ref.
2019	MOF-74	H_2O vapor, 30 mg Catalyst	500W Xe lamp	Fixed-bed flow Reactor Vol. = 600 mL Time = 5 h.	CO = 1.484 CH_4 = 0	No CH_4 was detected with the pure MOF	[151]
2016	NNU-28	60 mL (v/v = 30:1) MeCN & TEOA 50 mg catalyst	300W Xe lamp 420–800 nm	Press. = 1 atm.	$HCOO^-$ = 52.8	The dual catalytic routes showed high efficiency.	[203]
2016	MOF-525	2mL (v/v=4:1) MeCN & TEOA 2 mg catalyst	300 W 400–800 nm	Time = 6 h	CO = 64.02 CH_4 = 6.2	Pure MOF	[234]
2016	Zn/PMOF	H_2O vapor 300 mg Catalyst	300W Hg lamp	Batch Reactor Vol. = 1 Liter Press. = 20 psia Temp. = 100 °C	CH_4 = 8.7 μ mol/g	After 4 hours, photocatalytic deactivation occurred.	[209]
2015	PCN-222	60 mL(v/v =10:1) MeCN, TEOA 50 mg Catalyst	300W Xe lamp 420–800 nm	Time = 10 h	$HCOO^-$ = 60	Good photocatalytic activity for CO_2 reduction to formate. Band gap = 1.75 eV	[235]

Table 2.3, continued.

Year	Photocatalyst(s)	Feed Composition	Light source *Power* *Wavelength* *Intensity*	Reactor *Parameters*	Product $(\mu mol\ g^{-1}\ h^{-1})$	Comments	Ref.
2015	UiO-66	5 mL (v/v = 4:1) MeCN, TEOA	300W Xe lamp 400–800 nm	Batch Reactor Vol. = 330 mL Press. = 80 Kpa	CO = 0	Pure MOF. Band gap 4.1 eV	[168]
2014	MIL-101(Fe)	60 mL (v/v=5:1) MeCN & TEOA 50 mg Catalyst	300W Xe lamp 420–800 nm	Reaction flask Time = 8 h	HCOO⁻ = 147.5	The highest efficiency.	[145]
2014	MIL-53(Fe)	60 mL (v/v=5:1) MeCN & TEOA 50 mg Catalyst	300W Xe lamp 420–800 nm	Reaction flask Time = 8 h	HCOO⁻ = 74.2	Contains a BDC linker similar to that in MIL-101(Fe) but with different structures. One-dimensional pores.	[145]
2014	MIL-88(Fe)	60 mL (v/v=5:1) MeCN & TEOA 50 mg Catalyst	300W Xe lamp 420–800 nm	Reaction flask Time = 8 h	HCOO⁻ = 22.5	Exhibited the lowest efficiency among other tested MOFs. Formed by 3-D porous network with microporous channels.	[145]

2.5.1.1 Zr-based MOFs

These classes are highly porous MOF photocatalysts; this is mainly attributed to the Zr ions in Zr–O clusters which show variable valence states from Zr^{4+} to Zr^{3+} [236]. They are also known for their remarkable structural suitability in photocatalytic reactions due to the Zr-carboxylate coordination bonds which enable the synthesis of MOFs with higher surface area and better electronic structures. Furthermore, they exhibit higher superiority compared to other MOFs in terms of functionalization with different functional groups by various synthesis methods [237, 238].

Chen et al. [203] investigated the use of zirconium MOF (NNU-28) as a photocatalyst for CO_2 reduction and found out that CO_2 was photocatalytically reduced into $HCOO^-$ with a formation rate of 52.8 $\mu mol\ g^{-1}\ h^{-1}$ under visible light and in the presence of TEOA as a sacrificial agent. The dual catalytic routes in NNU-28 showed high absorption ability of visible light which resulted in higher photocatalytic efficiency.

A Zirconium-based porphyrin (PCN-222) was tested to investigate how the CO_2 photocatalytic reduction is significantly affected by the rate of charges transfer and the ability of CO_2 gas adsorption [235]. CO_2 was successfully photoreduced into formate under visible light irradiation with the use of 1:10 TEOA in MeOH. PCN-222 exhibited both high adsorption selectivity of CO_2 over N_2 and high evolution rate of $HCOO^-$ compared to other pure MOF photocatalysts.

Zhang and coworkers [234] investigated the photocatalytic conversion of CO_2 by using MOF-525 and compared it to its other composites. CO_2 was successfully reduced into CO and CH_4 under visible light with presence of TEOA as an electron donor. The porphyrin MOF showed evolution rates of 64.02 and 6.2 $\mu mol\ g^{-1}\ h^{-1}$, respectively. However, the incorporation of MOF-525 with other composites exhibited much higher improved activity and CH_4 selectivity especially with the MOF-525-Co composite.

2.5.1.2 Fe-based MOFs

Iron (Fe)-based MOF photocatalysts and their developments have significantly attracted researcher's interests owing to their nontoxicity, earth abundance, alterable structures and their ability to harvest visible light [239, 240]. Compared to Ti- and Zr-containing MOFs, Fe-containing MOFs can be directly excited by visible light due to the existence of extensive oxo-iron (Fe–O) clusters [147, 241]. During the photocatalytic reactions, the Fe sites act as photocatalytic centers while the organic linkers work on the charge separation and limiting the charge recombination rate [74].

In 2014, Wang et al. [145] have tested three different Fe-containing MOFs which are MIL-101(Fe), MIL-53(Fe) and MIL-88B(Fe). $HCOO^-$ was detected with all tested MOFs photocatalysts under visible light. Although all the tested MOF photocatalysts had both similar band gap and absorption spectra, MIL-101(Fe) has shown the highest selectivity and production rate (147.5 $\mu mol\ g^{-1}\ h^{-1}$) because of its higher adsorption capacity which is equivalent to 26.4 $cm^3\ g^{-1}$ compared to 13.5 cm^3 g^{-1} and 10.4 $cm^3\ g^{-1}$ that of MIL-53(Fe) and MIL-88B(Fe) respectively. The impact of amino-functionalization for the aforementioned MOFs was also investigated and found to be greatly enhancing the activity for photocatalytic CO_2 reduction.

2.5.1.3 Zn-based MOFs

These porous materials are usually used as co-catalysts in photocatalytic CO_2 reduction systems in which they act as alternatives for the noble metals due to their abundance and good stability under light irradiation so that they are normally referred as noble-metal-free systems [242, 243]. They include a wide range of types such as the ZIF (Zeolitic Imidazolate Framework) MOFs series (ZIF-7, ZIF-8, ZIF-9, ZIF-11, ZIF-67 and ZIF-68).

In 2019, MOF(Zn)-1 was synthesized for the first time by Cabrero et al. [244] for CO_2 methanation. The novel MOF photocatalyst is structurally very similar to the known MOF-74(Zn). CO_2 was photocatalytically reduced into CH_4 at mild

conditions (215 °C) under UV-Vis light and without the addition of any sacrificial agents or the inclusion of any metallic nanoparticles. CH_4 was formed with an initial production rate of 4 μmol g^{-1} h^{-1} and 30 μmol g^{-1} after 24 hours and no CH_4 was observed by performing the photocatalytic reaction at room temperature.

Han et al. [151] also tested the ability of the Zn-based MOF-74 for photocatalytic CO_2 reduction and compared it to some Metal-MOF composites. CO_2 was reduced into CO (7.42 μmol g^{-1}) after 5 hours irradiation with the presence of H_2O. No CH_4 was observed with the pure MOF, however, by the inclusion of Pt, the CH_4 yield reached (9.04 μmol g^{-1} h^{-1}) with an approximate selectivity of 50%.

By using zinc-based porphyrin (Zn/PMOF), CO_2 was also photoreduced into CH_4 in a gaseous-system reactor under UV/Visible light in the presence of H_2O vapour as a sacrificial electron donor [209]. Zn/PMOF showed 80.6% higher CH_4 evolution (8.7 μmol g^{-1} h^{-1}) compared to ZnO. However, after 4 hours, a photocatalytic deactivation was observed, this might be attributed to the CH_3OH buildup which was adsorbed on the photocatalyst.

2.5.2 Functionalized and Metal-added MOFs

In order to provide additional reaction pathways or to increase the light absorption and the chemical stability of MOFs, ligands of these materials are modified by either organic functionalization or inorganic materials addition, in other words; by using the Amine functionalization or Metal addition as shown in Table 2.4.

Table 2.4 Functionalized and Metal-added MOFs photocatalysts for CO_2 reduction and their photocatalytic reactions.

Year	Photocatalyst(s)	Feed Composition	Light source Power Wavelength Intensity	Reactor Parameters	Product (μmol g^{-1} h^{-1})	Comments	Ref.
2019	MIL-101-EN	n/a	Xe lamp 330 nm	Vol. = 500 mL Press. = 71 kPa Time = 10 h	CO = 47.2 CH$_4$ = 1.8	Exhibited durable photocatalysis throughout 4 recycle runs (total of 40 hours)	[146]
2019	AD-MOF-1	Acetonitrile (aqueous solution) (TIPA) , Catalyst	Visible-light	Press. = 1 atm Temp. = 293 K Time = 4 h	HCOOH = 179	No photosensitizer or noble metal co-catalysts are used in both MOFs. Bang gap = 1.76 eV	[245]
2019	AD-MOF-2	Acetonitrile (aqueous solution) (TIPA) , Catalyst	Visible-light	Press. = 1 atm Temp. = 293 K Time = 4 h	HCOOH = 443	Band gap = 1.52 eV	[245]
2019	NH$_2$-MIL-125(Ti)	15 mL DI-water 15 mg Catalyst	Visible-light 300W Xe lamp 420 nm	Press. = 0.6 MPa Temp. = 60 Vol. = 200 mL	CH$_4$ = 0.69	Band gap = 2.75 eV	[246]
2018	Zr-SDCA-NH$_2$	29.1 mg H$_2$SDCA-NH$_2$ 50 mL (v\v = 30:1) CH$_3$CN & TEOA 40 mg Catalyst	300W Xe lamp 420-800 nm	Vol. = mL Press. = 1 atm	HCOO$^-$ = 37.8	Chemically stable and highly porous. Showed high CO_2 uptake, broad visible light adsorption and increased photocatalytic efficiency.	[211]

Table 2.4, continued.

Year	Photocatalyst(s)	Feed Composition	Light source *Power Wavelength Intensity*	Reactor *Parameters*	Product (μmol g^{-1} h^{-1})	Comments	Ref.
2018	MAF-X27-OH	4:1 CH_3CN/H_2O TEOA, [Ru(bpy)$_3$]Cl$_2$	420 nm	Press. = 1 atm Time = 10 h	CO = 21 H$_2$ = 0.6	TEOA is used as sacrificial agent. The [Ru(bpy)$_3$]Cl$_2$ was used as a photosensitizer. CO selectivity = 97.2 %	[247]
2018	ZrPP-1-Co	5 mL (*v/v* = 4/1) acetonitrile &TEOA 20 mg Catalyst	300W Xe lamp 420 nm	Vol. = 25 mL Press. = 1 atm Temp. = 20 ºC	CO = 14	TEOA is used as a sacrificial reagent	[212]
2016	MOF-525-Zn	2 mL (v/vb= 4:1) MeCN & TEOA 2mg Catalyst	300 W 400–800 nm	n/a	CO = 200.6 CH$_4$ = 36.76	Both activity performance and CH$_4$ improved after incorporation of active sites.	[234]
2016	Re-UiO^f	2 mL MeCN 0.1 mL TEOA 0.03 mL H$_2$O	LED lamp 410 nm	n/a	CO = 6.44 H$_2$ = 0.4	The partial hydrogenation of the bpy ligand caused the decomposition.	[207]
2015	MOF-253-Ru(CO)$_2$Cl$_2$	6 mL (v/v=10:1) MeCN & TEOA 5 mg Catalyst	420–800 nm	n/a	CO = 46.5 HCOO$^-$ = 16.8 H$_2$ = 2.2	n/a	[150]

Table 2.4, continued.

Year	Photocatalyst(s)	Feed Composition	Light source *Power Wavelength Intensity*	Reactor *Parameters*	Product (μmol g^{-1} h^{-1})	Comments	Ref.
2015	Photosensitized MOF-253-Ru(CO)$_2$Cl$_2$	6mL (v/v=10:1) MeCN & TEOA 5 mg Catalyst	420–800 nm	n/a	CO = 68.5 HCOO$^-$=205.8 H$_2$ = 47.8	The photocatalytic performance was much increased when the catalyst is sensitized.	[150]
2015	UiO-67 Mn (bpy) (CO)$_3$Br	20 mL (v/v 4:1) DMF & TEOA 0.5 mM Mn catalyst 0.5 mMm [Ru(dmb)$_3$] (PF$_6$)$_2$, 0.2M BNAH	LED 470 nm 2.51×10^{-7} einstein/s	Quartz Cell Vol. = 36 mL Time = 18 h	HCOO$^-$ = 110	It displayed a selectivity of 96% over 4 h.	[171]
2015	Cp*Rh@UiO-67	[Ru(bpy)$_3$]Cl$_2$. 6H$_2$O 1.0 mM, (v/v=5:1) MeCN & TEOA 1.4 mg Catalyst	300W Xe lamp >415 nm	Quartz Cuvette Vol. = 1cm^3 Temp. = 20 C^o	HCOO$^-$ = 464 H$_2$ = 285	Photocatalyst loadings higher than 10 mol % resulted in decomposition of formate into CO$_2$ and H$_2$. Band gap = 2.4 eV	[248]
2015	NH$_2$-UiO-66	3 mL C$_2$H$_3$N, 2 mL H$_2$O, 1 mL TEOA, 10 mg bby, 20 mg CdS, 1 mg catalyst	300W Xe lamp >420 nm	Vol. = 80 ml Press. = 1 atm Temp. = 30 ºC	CO = 0.1 H$_2$ = 0.1	The lowest efficiency	[249]

Table 2.4, continued.

Year	Photocatalyst(s)	Feed Composition	Light source *Power Wavelength Intensity*	Reactor *Parameters*	Product ($\mu mol\ g^{-1}\ h^{-1}$)	Comments	Ref.
2014	NH$_2$-MIL-101(Fe)	60 mL (v/v=5:1) MeCN & TEOA 50 mg Catalyst	300W Xe lamp 420–800 nm	Reaction flask Time = 8 h	HCOO$^-$ = 445	n/a	[145]
2014	NH$_2$-MIL-53(Fe)	60 mL (v/v=5:1) MeCN & TEOA 50 mg Catalyst	300W Xe lamp 420–800 nm	Reaction flask Time = 8 h	HCOO$^-$=116.2	n/a	[145]
2014	NH$_2$-MIL-88(Fe)	60 mL (v/v=5:1) MeCN & TEOA 50 mg Catalyst	300W Xe lamp 420–800 nm	Reaction flask Time = 8 h	HCOO$^-$ = 75	n/a	[145]
2013	Copper porphyrin MOF^e	100 mL (v/v=1:99) TEOA & H$_2$O 30 mg Catalyst	300W Xe lamp >420 nm	Quartz Vessel Temp. = 5 ºC Flow=0.2mL min^{-1}	CH$_3$OH=262.6 ppm/g. h	CO$_2$ adsorption and photocatalytic activity were promoted by the Cu presence in the porphyrin based MOF	[195]
2013	NH$_2$-UiO-66	1.0 µ mol [Ru(bpy)$_3$]Cl$_2$ .6H$_2$O 5 mL acetonitrile & H$_2$O, 1mL TEOA 0.8 µmol Catalyst	>420 nm	Press. = 1 atm Temp. = 20 ºC Time = 30 min	CO = 1.2 H$_2$ = 2.2	The -NH$_2$ functionalization clearly enhanced the photocatalytic activity.	[250]

Table 2.4, continued.

Year	Photocatalyst(s)	Feed Composition	Light source *Power Wavelength Intensity*	Reactor *Parameters*	Product ($\mu mol\ g^{-1}\ h^{-1}$)	Comments	Ref.
2013	NH_2-UiO-66(Zr)	60 mL (v/v=5:1) MeCN & TEOA 50 mg Catalyst	500W Xe lamp 420–800 nm	Reaction flask Press. = 1 atm Temp. = 273 K	$HCOO^- = 26.4$	The interactions between the ligands and the metal clusters enhanced the Photocatalytic performance	[147]
2013	$(NH_2)/(NH_2)_2$-UiO-66(Zr)	60 mL (v/v=5:1) MeCN & TEOA 50 mg Catalyst	500W Xe lamp 420–800 nm	Reaction flask Press. = 1 atm Temp. = 273 K	$HCOO^- = 41.4$	The second amino group increased the CO_2 adsorption and enhanced the photocatalytic performance.	[147]
2012	NH2-MIL-125(Ti)	60 mL (v/v=5:1) MeCN & TEOA 50 mg Catalyst	500W Xe lamp 420–800 nm	n/a	$HCOO^- = 16.3$	Uneconomical and environmentally unsafe since TEOA has to be used as a sacrificial electron donor.	[73]
2011	(Re^I(CO)$_3$ (dcbpy) Cl) / UiO-67	2 mL MeCN 0.1 mL TEA 1–2 μmol Catalyst	450W Xe lamp >300 nm	Time = 20 h	CO = 10.9 TON H_2 = 2.5 TON	Attaching MOF with Re-containing ligand eliminated its decomposition. TON is the number of evolved product molecules per catalytic site.	[251]
2011	(Re^I(CO)$_3$ (dcbpy) Cl)	2 mL MeCN 0.1 mL TEA 1–2 μmol Catalyst	450W Xe lamp >300 nm	Time = 20 h	CO = 3.5 TON H_2 = 0.6 TON	Triethylamine (TEA) is used as a sacrificial agent.	[251]

2.5.2.1 Amine functionalization

In general, the introduction of the organic functional groups (e.g. $-NH_2$, $-COOH$ and $-OH$) into metal-organic frameworks can promote the interactions of reactant molecules with the modified linkers. Among these groups; Amines which can significantly enhance these interactions by offering basic sites to attract the acidic CO_2 molecules and repelling water by inducing surface hydrophobicity and hence; increasing the CO_2 adsorption as illustrated in Figure 2.20 (a) [63, 74]. Many experimental studies and investigations have confirmed and approved the improvement of MOFs photocatalytic activity for CO_2 reduction, the CO_2 adsorption capacity and the optical absorption range by using NH_2 modifications which add additional energy levels to the band gap of the MOFs that effectively decreases the band gap as shown in Figure 2.20 (b) [23].

Amine functionalization of MIL-125(Ti) was investigated by Fu et al. [73]. CO_2 was successfully photoreduced into $HCOO^-$ under UV and visible light irradiations. The introduction of NH_2 linkers didn't only increase the interactions between the NH_2-modified MIL-125(Ti) and CO_2 molecules but it also enhanced the light harvesting by broadening of the optical absorption range in which the absorption edge of the functionalized MOF photocatalyst was shifted from 350 nm (that of pure MIL-125(Ti)) to 550 nm. The photocatalytic reaction was conducted under visible-light illumination in MeCN solvent with the presence of TEOA as a sacrificial agent by acting as an electron donor. As a result of these improvements, the new amine-functionalized MOF was brought to higher CO_2 adsorption and hence higher catalytic activity.
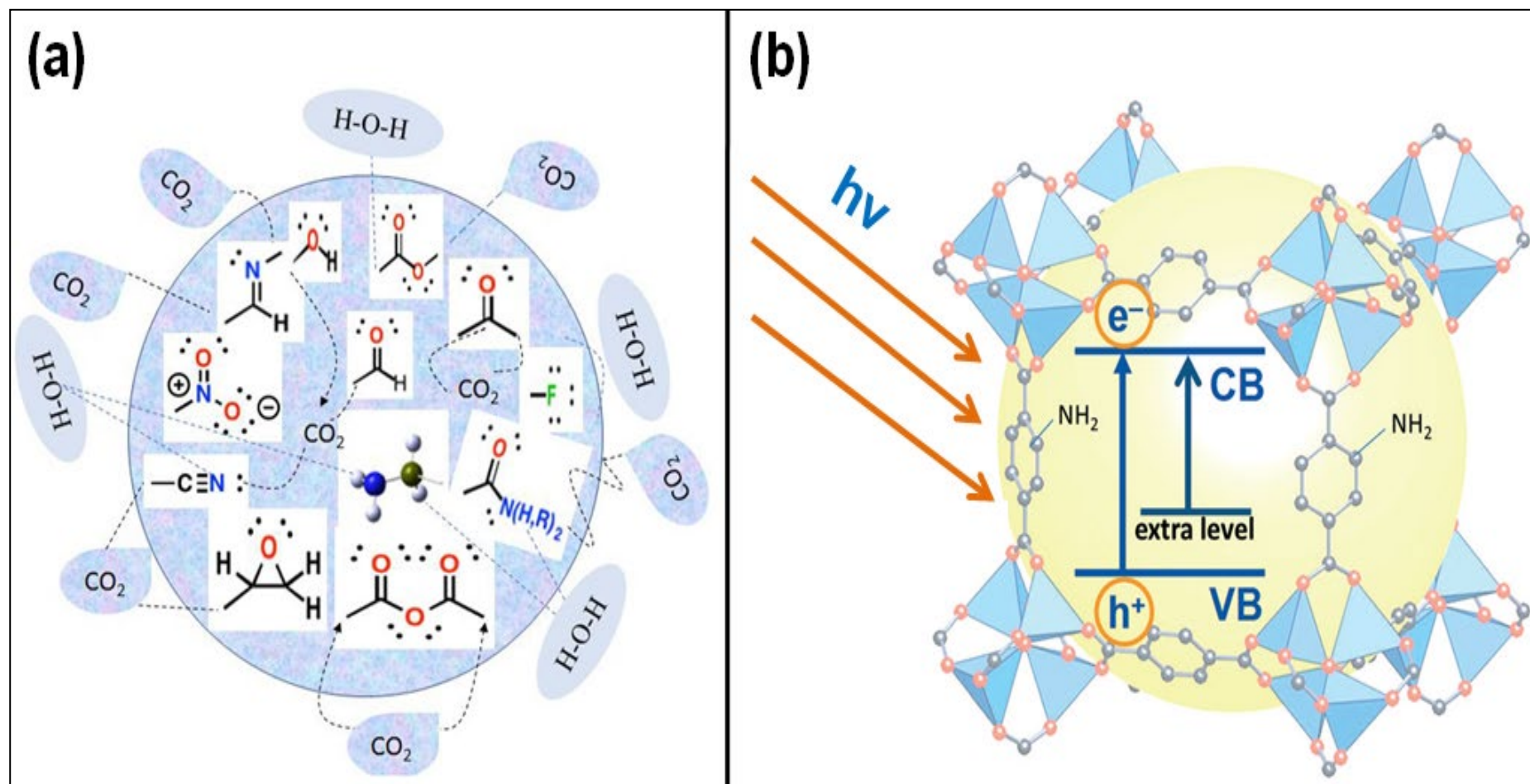
Figure 2.20   (a) Surface functional groups effect on CO_2 reduction using H_2O [63], (b) An illustration of the effect of $-NH_2$ on adding an additional energy level to the band gap of the MOFs which effectively decreases the band gap with respect to the unsubstituted MOF giving the MOF visible light photoresponse [23].

Sun et al. [147] observed an increase in CO_2 adsorption capacity by synthesizing a functionalized visible light-responsive photocatalyst. CO_2 was reduced into $HCOO^-$ which was the only product formed by using this new functionalized NH_2-UiO-66 photocatalyst, However the unmodified UiO-66 showed no photocatalytic activity. Different amounts of $-NH_2$ linkers as shown in Figure 2.21 (a) were also studied at the same conditions by synthesizing a photocatalyst in the form of $(NH_2)/(NH_2)_2$-UiO-66(Zr). It was found that increasing the number of the amino groups is favourable in the enhancement of photocatalytic activity. The same impact of amine functionalization on visible light harvesting and photocatalytic activity of UiO-66 was also reported by Lee et al. [252].
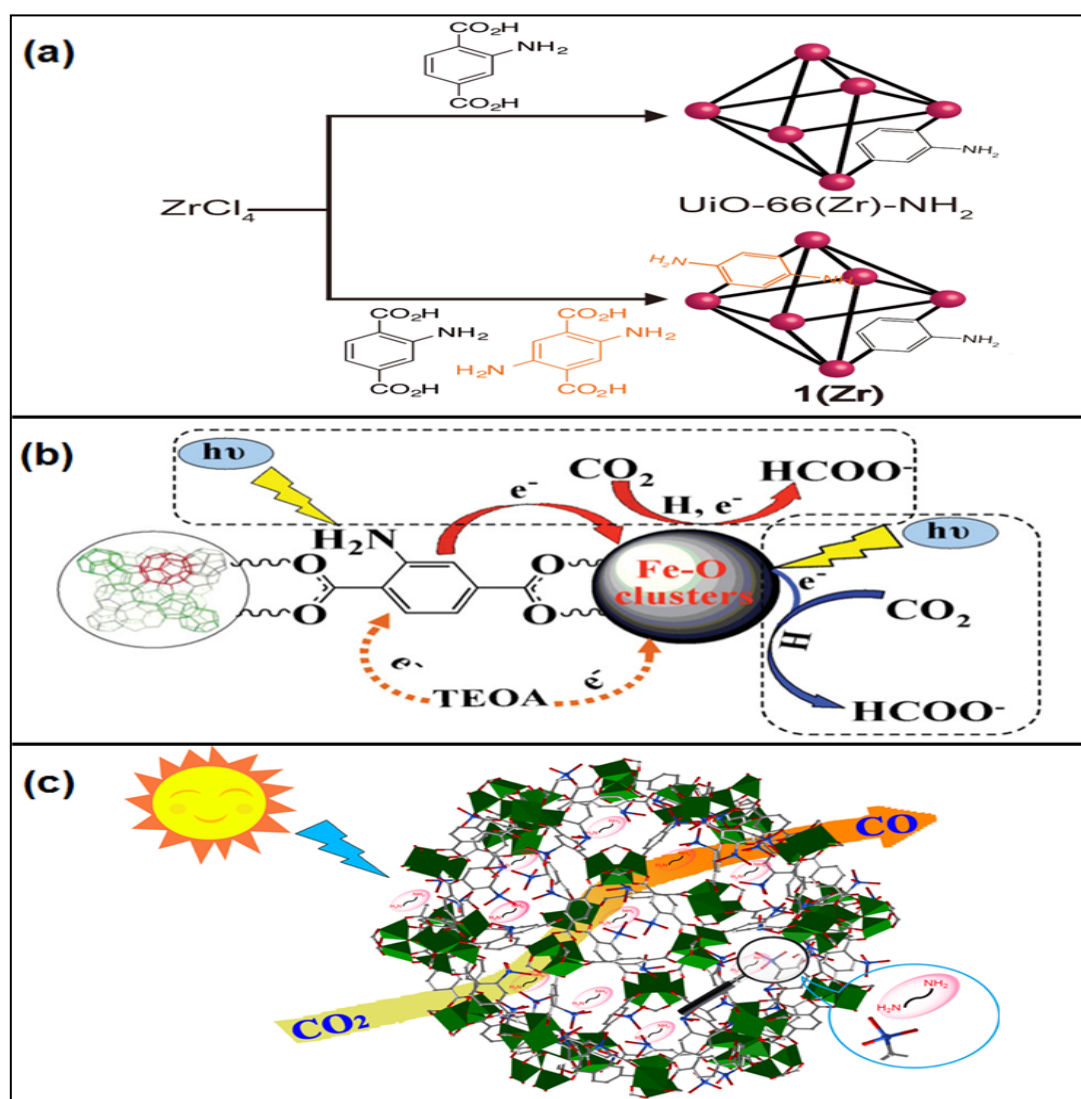
Figure 2.21   (a) Amine functionalization of UiO-66(Zr) [252], (b) Dual excitation pathways in amine-functionalized Fe-containing MOF [145], (c) A scheme of MIL-101-EN photocatalytic routes for CO_2 reduction [146].

Wang et al. [145] also tested the amine functionalization effect on Fe-based MOF materials [MIL-101(Fe), MIL53(Fe), and MIL-88B(Fe)] and observed higher CO_2 adsorption and catalytic activity with each different functionalized MOF photocatalyst. The amine linkers in the form of antenna provided an additional pathway for conversion by allowing the photogenerated electron to transfer from the excited organic linkers to the catalytically active Fe-O sites and thus, enhancing the photocatalytic activity for CO_2 reduction as shown in Figure 2.21 (b).

Xie et al. [146] introduced three different alkylamines [ethylenediamine (EN), diethylenetriamine (DETA) and triethylenetetramine (TETA)] into MIL-101-Cr using post-modification method. The alkylamine functionalization worked basically on promoting the charge separation and the rate of electron migration and thus enhancing the CO_2 reduction. Among these alkylamines, the EN-modified MOF shown in Figure 2.21 (c) exhibited the highest selectivity of 96.5% and the highest CO evolution rate of 47.2 $\mu mol\ g^{-1}\ h^{-1}$ compared to MIL-101-Cr, DETA and TETA-modified photocatalysts.

2.5.2.2 Metal Addition

Another useful strategy used for improving the photocatalytic activity is by adding metallic molecular catalysts to be bonded to the MOF linkers. The mechanism of these MOFs focuses mainly on promoting charge separation. These MOFs containing metal particles in their structure offer opportunities in terms of chemical and mechanical stability, multi-functionality and tenability [21, 253].

Wang and co-workers [251] did a brilliant work in this field by incorporating [$Re^I (CO)_3$ (dcbpy) Cl] (H_2L_4) ligand into UiO-67 which showed that CO_2 could be photocatalytically reduced into CO and H_2 under visible irradiation. None of these products were detected when using pure UiO-67, the reaction was therefore considered to be proceeded by the Re complex. By attaching the Re-containing ligand with the MOF, the decomposition was also observed to be greatly suppressed.

Another new modified MOF was also synthesized from UiO-67 by incorporation with Rhodium to form Cp*Rh@UiO-67 as shown in Figure 2.22 (a). CO_2 was reduced into $COOH^-$ and H_2. It has been observed that high loadings of the photocatalyst will result in decomposition of formate into CO_2 and H_2 and hence loss of formate selectivity and photocatalytic activity (Figure 2.22 (b)). However, maintaining a loading of less than 10 mol % retained the MOF catalytic activity and stability [248].
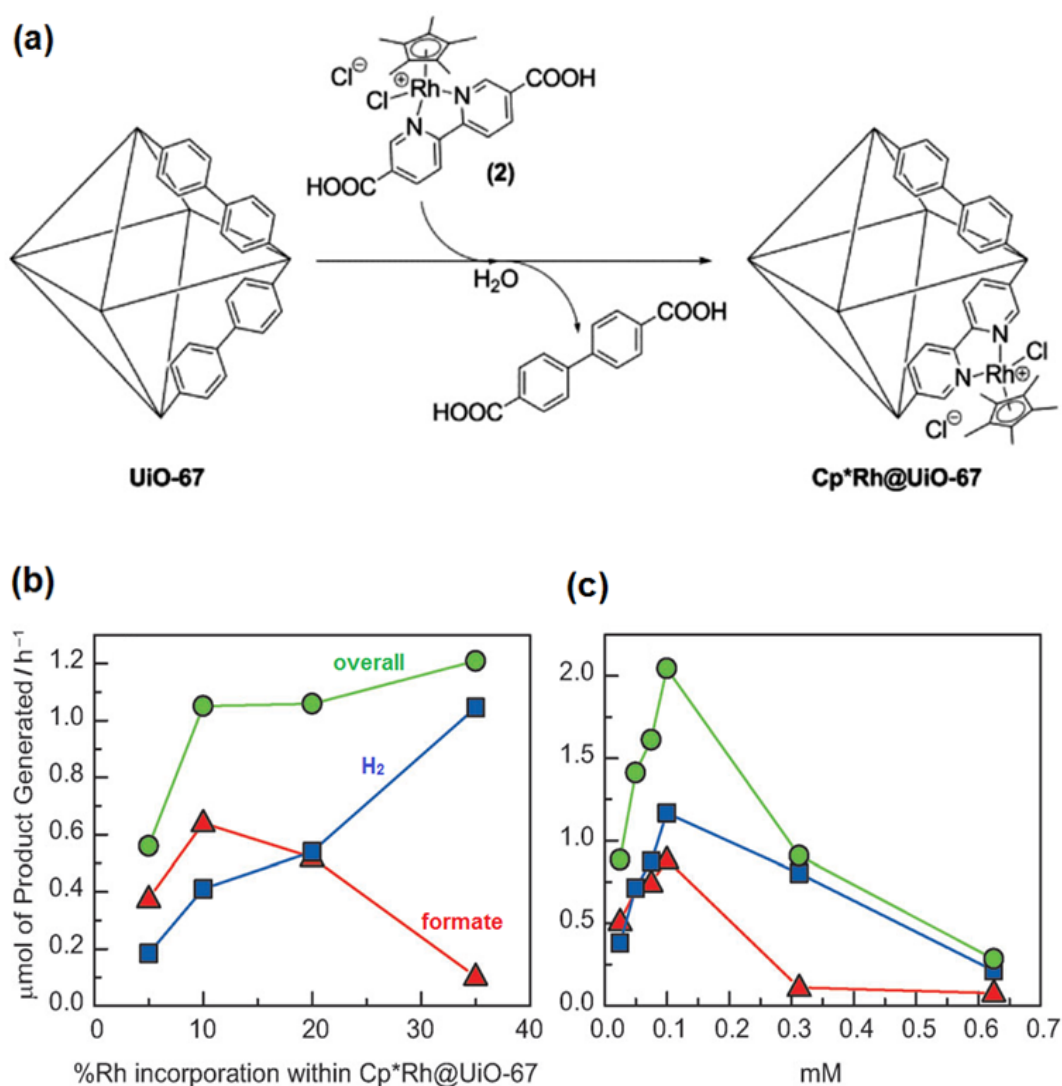
Figure 2.22   (a) Synthesis of Cp*Rh@UiO-67 through linker Post Synthetic Exchange (PSE) [248], (b) The effect of rhodium catalyst loading on the production rate of formate and hydrogen, (c) The effect of % rhodium molar incorporation within Cp*Rh@UiO-67.

Lee et al. [169] also investigated the Post-synthetic exchange of UiO-66 as shown in Figure 2.23 (a). No catalytic activity was observed with unmodified UiO-66 but when it has been incorporated with Cr and Ga monocatecholato groups onto the linkers to form UiO-66-Cr CAT and UiO-66-Ga CAT respectively, they showed good photocatalytic CO_2 reduction. Although both MOFs reduced CO_2 to HCOOH with the aid of TEOA and BNAH under visible light, the Cr-derivative showed better efficiency than Ga even after three cycles (6 hours each) due to its open shell electronic structure (Figure 2.23 (b)).
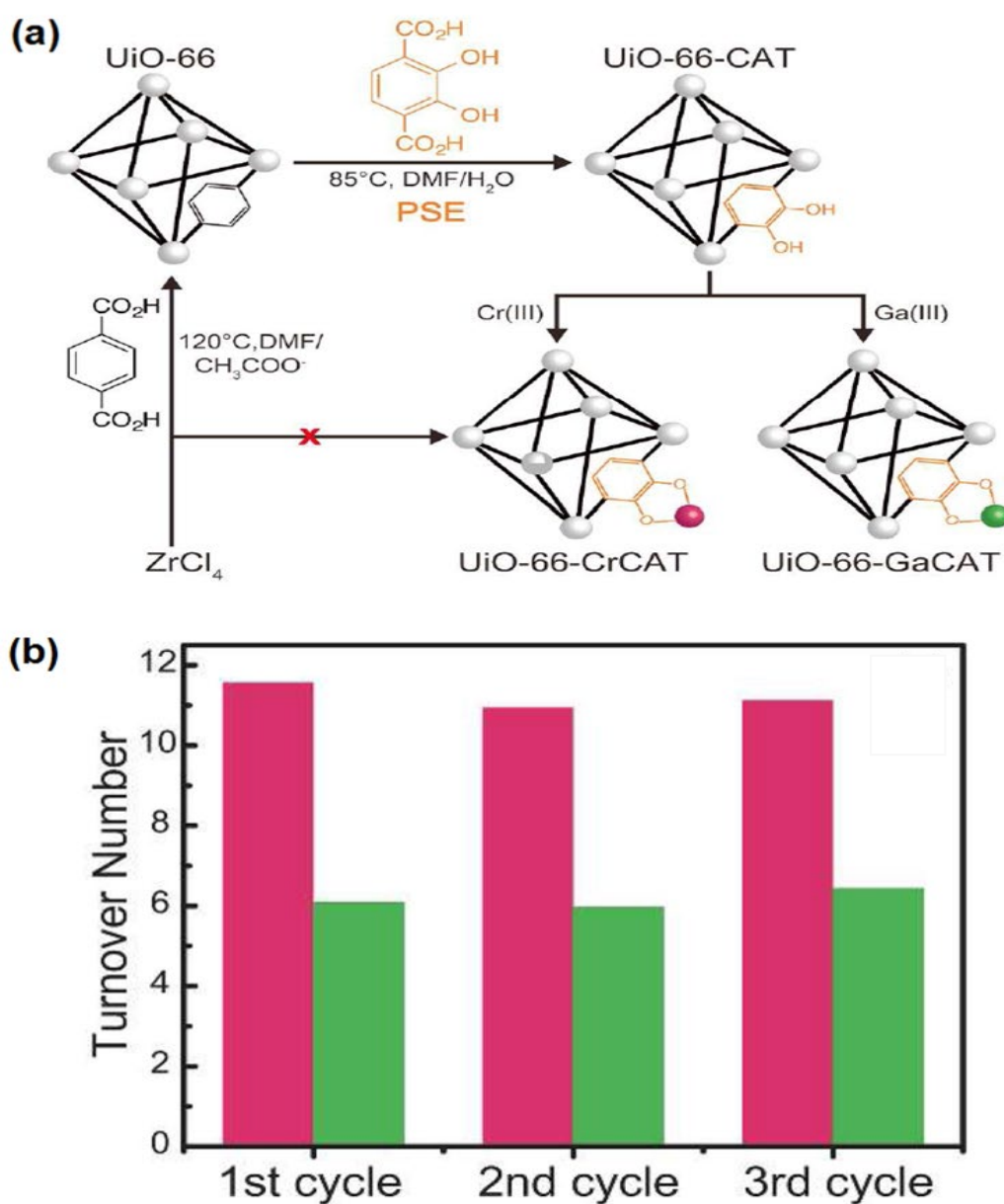
Figure 2.23   (a) Synthesizing of UiO66-CrCAT & UiO-66-GaCAT through post-synthetic exchange, (b) The photocatalytic activity of UiO-66-CrCAT (red bars) and UiO-66-GaCAT (green bars) over three cycles (each cycle is 6 hours) [169].

Sun et al. [150] successfully photo-reduced CO_2 into CO, H_2 and $HCOO^-$ under visible light irradiation by synthesizing a combination of MOF-253 and Ru-carbonyl complex [MOF-253-Ru-$(CO)_2$ Cl_2]. The main reason for selecting this Ru complex is the feature of being acting as both a photocatalyst and a photosensitiser. MOF-253- $Ru(CO)_2$ Cl_2 was then photosensitized using $Ru(bpy)_2$ Cl_2 because of its ability to form MOF-253 supported [Ru $(bpy)_2$ $(X_2bpy)^{+2}$] by reacting with the surface N,N-chelated sites. No photocatalytical activity was observed with MOF-253, by using MOF-253- Ru $(CO)_2$ Cl_2, the light absorption edge was broadened from 370 to 470 nm but with only moderate catalytic activity. The light absorption edge was more even extended further to 630 nm by photosensitisation which resulted in higher catalytic activity.

2.5.3   Metal Exchanged and Doped MOFs

2.5.3.1   Metal Ion Exchange in MOFs

The main concept in MOF Post-synthesis metal exchange is prompting the charge separation by altering the redox potential to enhance the photocatalytic performance of MOF-based photocatalysts and hence, increasing the photocatalytic reduction of CO_2. Many investigations have been conducted on this field as shown in Table 2.5.

Table 2.5   Metal Ion Exchanged and Doped MOFs photocatalysts for CO_2 reduction and their photocatalytic reactions.

Year	Photocatalyst(s)	Feed Composition	Light source *Power Wavelength Intensity*	Reactor *Parameters*	Product ($\mu mol\ g^{-1}\ h^{-1}$)	Comments	Ref.
2018	Ni MOLs	$[Ru(bpy)^3]Cl_2 \cdot 6H_2O$ TEOA	420 nm	Time = 2 h	CO = 12.5 H_2 = 0.28	For photoreduction of diluted CO_2. CO selectivity = 97.8% (in pure CO_2 feed).	[254]
2015	$(NH_2)_2$-UiO-66 (Zr/Ti)	5 mL (v/v=4:1) MeCN & TEOA 0.1M BNAH 5 mg Catalyst	300W Xe lamp 420–800 nm	n/a	$HCOO^-$ = 1052	The photoexcited electrons exhibited high charge transfer from the linkers to the metal clusters.	[252]
2015	NH_2-UiO-66 (Zr/Ti)	5 mL (v/v=4:1) MeCN & TEOA 0.1M BNAH 5 mg Catalyst	300W Xe lamp 420–800 nm	n/a	$HCOO^-$ = 741	n/a	[252]
2015	NH_2-UiO-66(Zr)	60 mL (v/v=5:1) MeCN & TEOA 50 mg Catalyst	300W 420–800 nm	Time = 10 h	$HCOO^{-h}$ = 3.4	n/a	[255]

Table 2.5, continued.

Year	Photocatalyst(s)	Feed Composition	Light source *Power Wavelength Intensity*	Reactor *Parameters*	Product (μmol g^{-1} h^{-1})	Comments	Ref.
2015	NH$_2$-UiO-66(Zr/Ti)	60 mL (v/v=5:1) MeCN & TEOA 50 mg Catalyst	300W 420–800 nm	Time = 10 h	HCOO^{-h} = 5.8	70% increase in CO$_2$ reduction. 22% increase in CO$_2$ adsorption capacity	[255]
2014	Pt-NH$_2$-MIL-125(Ti)	60 mL (v/v=5:1) MeCN & TEOA 50 mg Catalyst	300W Xe lamp 420–800 nm	n/a	HCOO$^-$ = 32.4	Showed high photocatalytic performance for the production of HCOO$^-$ compared to both NH$_2$-MIL-125(Ti) and Au-NH$_2$-MIL-125(Ti)	[149]
2014	Au-NH$_2$-MIL-125(Ti)	60 mL (v/v=5:1) MeCN & TEOA 50 mg Catalyst	300W Xe lamp 420–800 nm	n/a	HCOO$^-$ = 16.3	TEOA is used as a sacrificial agent.	[149]

. Sun et al. [150] synthesized Ti-substituted NH_2-UiO-66 (Zr/Ti) MOF from NH_2-UiO-66(Zr) by using a post-synthetic exchange (PSE) method as shown in Figure 2.24. It has shown an enhanced performance due to the Ti-substituent which acted as a mediator to facilitate the transfer of electrons. The CO_2 reduction to formate was found to be increasing up to 70%, in addition to an increase of 22% in CO_2 adsorption capacity. The transfer of excited electrons from the MOF linkers to the metal clusters (from Ti^{3+} to Zr^{4+}) was indicated by Molecular simulations and EPR.
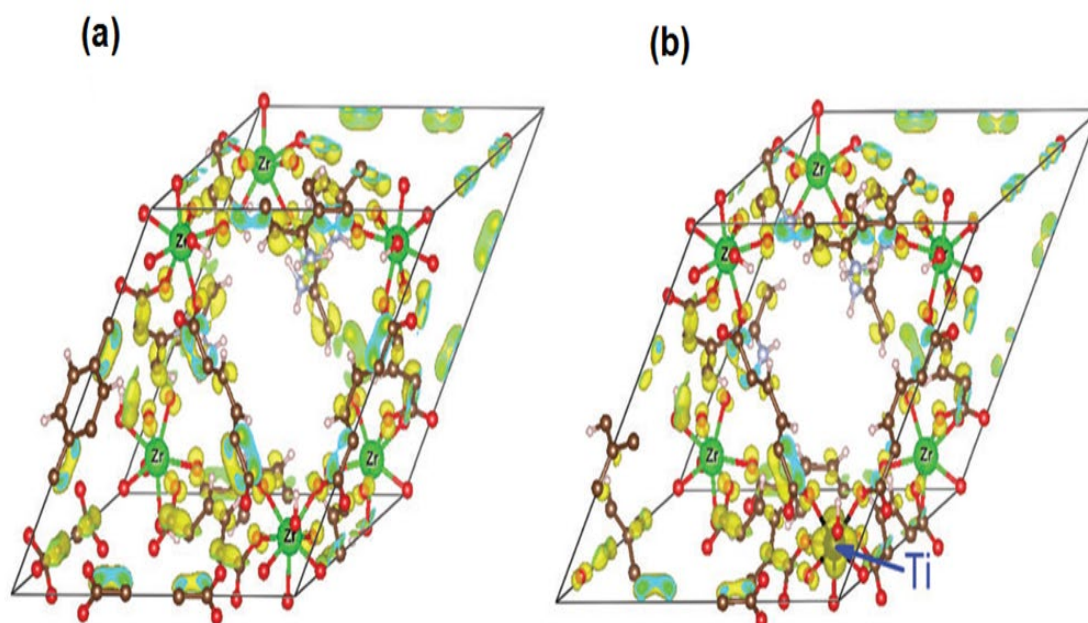
Figure 2.24   PSE method in which: (a) NH_2-UiO-66 (Zr) is used to synthesize, (b) NH_2-UiO-66 (Zr/Ti) MOF [150].

Lee et al. [252] similarly investigated the post-synthetic exchange of Ti into NH_2-UiO-66(Zr) by introducing the diamine-substituted ligands which greatly enhanced the photocatalytic ability by increasing the light absorption and charge transfer as a result of introducing new energy levels. Photoluminescence spectroscopy was used to indicate the increase in charge transfer of photo-excited electrons from the linkers to the metal clusters as observed by Sun et al. [255] with EPR.

2.5.3.2 Metal Doped MOFs

Metal doping is one of the different strategies which have been developed to lower the band gap and promote the charge separation, especially in semiconductor photocatalysts. This is done by coating or doping the catalytic particles with a porous layer of noble metals.

Sun et al. [149] investigated doping NH_2-MIL-125(Ti) with two noble metals to fabricate M-doped NH_2-MIL-125(Ti) (M = Pt or Au). The nanoparticle clusters of these two noble metals were bonded onto the amine group on the organic linker of these MOFs. CO_2 was reduced into $HCOO^-$ and H_2 in both doped MOFs under visible light irradiation in a saturated CO_2 system with the presence of TEOA. However, only $HCOO^-$ was detected when using pure NH_2-MIL-125(Ti), indicating that the electron-trapping effect of noble metals was formed and thus changed the catalytic selectivity. Pt-NH_2-MIL-125(Ti) showed higher photocatalytic performance for the production of formate compared to both NH_2-MIL-125(Ti) and Au-NH_2-MIL-125(Ti).

2.5.4 MOF-Based Composites as Photocatalysts

Most of pure MOFs exhibit low chemical stability and photocatalytic reaction drawbacks, to limit this; MOFs are incorporated with other materials to form the heterojunctions which enable the photogenerated electrons to transfer of from one material to another, resulting in efficient charge separation and improvement in selectivity [21, 74]. MOFs are mainly incorporated with either semiconductors (e.g. TiO_2, g-C_3N_4, CNNS, Graphene, CdS etc.) and/or metals (e.g. Ag, Re, Pt, Au etc.). Table 2.6 shows different MOF–based photocatalysts for photocatalytic CO_2 reduction.

Table 2.6   MOF-Based Composites as photocatalysts for CO_2 reduction and their photocatalytic reactions.

Year	Photocatalyst(s)	Feed Composition	Light source *Power Wavelength Intensity*	Reactor *Parameters*	Product (μmol g^{-1} h^{-1})	Comments	Ref.
2019	Au@Pd@MOF-74	H_2O vapor, 30 mg Catalyst	500W Xe lamp	Fixed-bed Reactor Vol. = 600 mL Time = 5 h.	$CH_4 = 0$ $CO = 2.46$	This confirms the ability of Au@Pd NPs to increase the production of CO compared to the pure MOF-74.	[151]
2019	Pt/MOF-74	H_2O vapor, 30 mg Catalyst	500W Xe lamp	Fixed-bed Reactor Vol. = 600 mL Time = 5 h.	$CH_4 = 1.81$ $CO = 1.77$	The CH_4 selectivity increased to more than 50% with Pt NPs.	[151]
2019	Pt/Au@Pd@MOF-74	H_2O vapor, 30 mg Catalyst	500W Xe lamp	Fixed-bed Reactor Vol. = 600 mL Time = 5 h.	$CH_4 = 2.47$ $CO = 0.484$	The CH_4 production is promoted by the presence of Pt NPs. The Au@Pd NPs and Pt NPs worked together to increase the CH_4 yield and selectivity while CO yield decreased.	[151]
2019	2D/2D MOF/rGO NHPG-2	16 mL (1:1:6) TEOA/H2O/MeCN 40 mg photosensitizer [Ru(bpy)$_3$] Cl$_2$·6H$_2$O	100 W LED lamp 100- 420 nm	Pyrex glass Reactor Vol. = 250 mL Press. = 80 kPa Temp. = 4 ºC	$CO = 10.58$ $H_2 = 0.95$	Produced the highest CO yield compared to all other photocatalysts including rGO, NHPG-0.5, NHPG-2 and NHPG-4	[202]

Table 2.6, continued.

Year	Photocatalyst(s)	Feed Composition	Light source *Power* *Wavelength* *Intensity*	Reactor *Parameters*	Product ($\mu mol\ g^{-1}\ h^{-1}$)	Comments	Ref.
2019	CsPbBr$_3$ QDs/UiO-66 (NH$_2$)	10 mg Catalyst in H$_2$O/ethyl acetate (1:300)	300W Xe lamp 420 nm	Glass Reaction Cell Press. = 80 kPa Temp. = 5 °C	CO = 8.21 CH$_4$ = 0.26	The 15% loading content of (CsPbBr$_3$ QDs) was observed to be the best.	[256]
2019	N-CNDs/NH$_2$-UiO-66	4 mL acetonitrile 1 mL ethanol 2mg Catalyst	300W Xe lamp 400-800 nm	Quartz glass Reactor Vol. = 10 mL Temp. = 20 °C Time = 2 h	HCOO$^-$ = 10.9	Photocatalytic activity increased with the amount of NCNDs added in synthesizing of NH$_2$-UiO-66.	[257]
2018	UiO-66-NH$_2$/GR	3 mL H$_2$O, 40 mL DMF, 5mL TEOA, 20 mg Catalyst	300W Xe lamp > 410 nm	Homeade Glass Reactor Temp. = 25 °C, 5 h	HCOOH =33.5 H$_2$ = 13.2	Exhibited 11 times higher photocatalytic efficiency than pure UiO-66-NH$_2$.	[170]
2018	CdS/NH$_2$-UiO-66	9 mL acetonitrile 6 mL H$_2$O 3 mL TEOA 10 mg bipyridine 16.5 mg Catalyst	300W Xe lamp 400− 760 nm	Custom-made Glass Reactor Press. = 1 atm Vol. = 200 mL Temp. = 20 °C	CO = 521.9	The CO selectivity with CdS/NH$_2$-UiO-66 is 99% and 97 % obtained with CdS membrane.	[258]

Table 2.6, continued.

Year	Photocatalyst(s)	Feed Composition	Light source Power Wavelength Intensity	Reactor Parameters	Product (μmol g^{-1} h^{-1})	Comments	Ref.
2018	Cobalt(II) Tripodal Complexes [Co(BQPA)Cl] ClO$_4$	0.4 mm [Ru(phen)$_3$] (PF$_6$)$_2$ 0.2m TEOA in (4:4) MeCN/H$_2$O	450 nm 75 mWcm^{-2}	Press. = 1 atm Time. = 12 h	CO = 13.3 H$_2$ = 0.26	Developing photosensitizers with higher durability and lower cost is the future challenge.	[259]
2018	CsPbBr$_3$@ZIF-67	H$_2$O vapor Catalyst	620 nm 150 mW cm^{-2}	Sealed Pyrex bottle Temp. = 20 ^{o}C Time. = 3 h	CH$_4$ = 10.2 CO = 1.67	The composite catalysts exhibit enhanced CO$_2$ reduction activity. Band gap = 1.99 eV	[260]
2018	Zn-MOF/ZIF-67 nanosheets	6 mL (4:1:1) MeCN/MeOH/TEOA 10 mg Catalyst	Xe lamp 420 nm 120mW/cm^2	Temp. = 20 ^{o}C Time = 6 h	CO = 687 H$_2$ = 156 n mol/6h	ZIF-67 is used as co-catalyst	[208]
2018	Ni$_3$(HITP)$_2$ MOF	2 mg Catalyst, 80 mg (Ru(bpy)^3) Cl$_2$·6H$_2$O TEOA/H$_2$O/MeCN	100 W LED lamp 420 nm	Pyrex glass Reactor Press. = 80 kPa Temp. = 4 ^{o}C	CO = 34500	No products were detected when no photosensitizer (Ru(bpy)^3) Cl$_2$·6H$_2$O was used in the system.	[201]
2018	TiO$_2$-NH$_2$-UiO66(Zr) (18.5%)	(1.5 : 1) CO$_2$:H$_2$ 3 mg Catalyst	150 W Xe lamp > 325	Gas/Solid Reactor Vol. = 132 mL Time = 6 h	CO = 4.24	Light absorption properties shifted to visible light compared to UV light in TiO$_2$.	[139]

Table 2.6, continued.

Year	Photocatalyst(s)	Feed Composition	Light source *Power* *Wavelength* *Intensity*	Reactor *Parameters*	Product (μmol g^{-1} h^{-1})	Comments	Ref.
2018	3D g-C$_3$N$_4$/C-NPs	H$_2$O vapor 0.1g Catalyst	500W Xe lamp 330 – 450 nm	Stainless Steel Reactor Press. = 110 kPa Temp. = 30 ºC Vol.= 2700 mL	CO = 229 CH$_4$ = 112	Exhibited both high surface area and large porosity. Band gap = 2.7 eV	[261]
2017	Cd$_{0.2}$ Zn$_{0.8}$ S@UiO-66-NH$_2$	100 mL aque. sol. (0.1 M Na OH) 0.1 g Catalyst	300W Xe lamp 420 nm	Closed gas circulation system Temp. = 20 ºC	H$_2$ = 5846.5 CH$_3$OH = 6.8	The system is covered with tin foil to eliminate the interfering with the surrounding light.	[262]
2016	PCP-Ru^{II}	H$_2$O TEOA Photocatalyst	380 nm	n/a	H$_2$ = n/a HCOOH = n/a CO = n/a	The presence of H$_2$O was crucial to the exchange reaction.	[263]
2016	CPO-27 Mg/TiO$_2$	H$_2$O vapor 10mg Catalyst	16 W laser 365 nm	quartz Schlenktube Vol. = 10 ml	CO = 4.09 CH$_4$ = 2.35	The best efficiency.	[198]
2016	CPO-27-Mg	H$_2$O vapor 10mg Catalyst	16 W laser 365 nm	quartz Schlenktube Vol. = 10 ml	CO = 0 CH$_4$ = 0	n/a	[198]

Table 2.6, continued.

Year	Photocatalyst(s)	Feed Composition	Light source *Power* *Wavelength* *Intensity*	Reactor *Parameters*	Product ($\mu mol\ g^{-1}\ h^{-1}$)	Comments	Ref.
2016	Ag ⊂ Re3-MOF	20 mL acetonitrile 1 mL triethylamine	300W Xe lamp 400-700 nm	Sealed Cell Reactor Press. = 1 atm Time = 6 h	CO = 0.0142 TON	The silver coated Re-MOF enhanced the photo-activity and stability. CO selectivity = 96%	[264]
2016	Co-ZIF-9	H_2O vapor 50mg Catalyst	300W Xe lamp 200–900 nm 494 mW cm^{-2}	Vol. = 390 mL Press. = 70 Kpa Base area = 8.1cm^2	CO = 0 CH_4 = 0 H_2 = 0	Did not show any activity.	[182]
2016	Co-ZIF-9/TiO_2	H_2O vapor 50mg Catalyst	300W Xe lamp 200–900 nm 494 mW cm^{-2}	Vol. = 390 mL Press. = 70 Kpa Base area = 8.1cm^2	CO = 17.58 CH_4 = 1.98 H_2 = 2.6	Exhibited highest photocatalytic activity with 3wt % Co-ZIF-9.	[182]
2015	UiO-66/CNN_S	5mL (v/v =4:1) MeCN, TEOA	300W Xe lamp 400–800	Batch Reactor Vol. = 330 Ml Press. = 80 Kpa	CO = 9.9	Exhibited higher CO_2 photocatalytic activity, larger surface area and stronger ability for CO_2 adsorption compared to CNNs	[168]
2015	CNNs	5mL (v/v =4:1) MeCN, TEOA	300W Xe lamp 400–800	Batch Reactor Vol. = 330 mL Press. = 80 Kpa	CO = 2.9	Band gap = 2.78 eV	[168]

Table 2.6, continued.

Year	Photocatalyst(s)	Feed Composition	Light source *Power Wavelength Intensity*	Reactor *Parameters*	Product (μmol g^{-1} h^{-1})	Comments	Ref.
2015	Ru-MOF [j] (non-interpenetrated)	63 mL (v/v=20:1) MeCN & TEOA 40 mg Catalyst	500W Xe lamp 420–800 nm	Schlenk Tube Vol. = 100ml	HCOO$^-$ = 67.1	n/a	[265]
2015	Ru-MOF [j] (interpenetrated)	63 mL (v/v=20:1) MeCN & TEOA 40 mg Catalyst	500W Xe lamp 420–800 nm	Schlenk Tube Vol. = 100ml	HCOO$^-$ = 71.7	Compared to non-interpenetrated MOF, it exhibited higher thermal and photo-stability for CO$_2$ reduction.	[265]
2015	Ru-MOF [i] (nanoflower)	60 mL (v/v=20:1) MeCN & TEOA 40 mg Catalyst	Xe lamp 420–800 nm	Schlenk Tube Vol. = 100ml	HCOO$^-$ = 77.2	The best efficiency	[266]
2015	Ru-MOF [i] (microcrystals)	60 mL (v/v=20:1) MeCN & TEOA 40 mg Catalyst	Xe lamp 420–800 nm	Schlenk Tube Vol. = 100ml	HCOO$^-$ = 52.7	n/a	[266]
2015	Co-ZIF-9	5 mL acetonitrile & H$_2$O, 1mL TEOA, 10 mg bpy, 20 mg CdS 1 mg catalyst	300W Xe lamp >420 nm	Vol. = 80 ml Press. = 1 atm Temp. = 30 ºC	CO = 12.6 H$_2$ = 2.8	The highest efficiency	[249]

Table 2.6, continued.

Year	Photocatalyst(s)	Feed Composition	Light source *Power* *Wavelength* *Intensity*	Reactor *Parameters*	Product ($\mu mol\ g^{-1}\ h^{-1}$)	Comments	Ref.
2015	Co-MOF-74	5 mL acetonitrile & H_2O, 1mL TEOA, 10 mg bpy, 20 mg CdS 1 mg catalyst	300W Xe lamp >420 nm	Vol. = 80 ml Press. = 1 atm Temp. = 30 ºC	CO = 9.9 H_2 = 1.9	Coupling the MOF-74 with the Co exhibited better results than those observed with Mn.	[249]
2015	Mn-MOF-74	5 mL acetonitrile & H_2O, 1mL TEOA, 10 mg bpy, 20 mg CdS 1 mg catalyst	300W Xe lamp >420 nm	Vol. = 80 ml Press. = 1 atm Temp. = 30 ºC	CO = 0.3 H_2 = 0.5	n/a	[249]
2015	Zn-ZIF-8	5 mL acetonitrile & H_2O, 1mL TEOA, 10 mg bpy, 20 mg CdS 1 mg catalyst	300W Xe lamp >420 nm	Vol. = 80 ml Press. = 1 atm Temp. = 30 ºC	CO = 0.2 H_2 = 0.2	n/a	[249]
2014	TiO_2 on HKUST-1	5mL H_2O vapor 300 mg Catalyst	300W Xe lamp < 400 nm	Vol. = 1 Liter Press. = 0.15 MPa Temp. = 313 K	CH_4 = 2.64	Under UV light. Ar is used as a Co-catalyst. Band gap = 1.6 - 3.1eV	[148]

Table 2.6, continued.

Year	Photocatalyst(s)	Feed Composition	Light source _Power Wavelength Intensity_	Reactor _Parameters_	Product (μmol g^{-1} h^{-1})	Comments	Ref.
2014	Co-ZIF-9/g-C$_3$N$_4$	5 mL MeCN & H$_2$O 1 mL TEOA, 10 mg bpy, 20 mg g-C$_3$N$_4$ 1 mg Catalyst	>420 nm	Press. = 1 bar Temp. = 30 ℃ Time = 2h	CO = 495 H$_2$ = 78.6	Co-ZIF-9 is used as a co-catalyst while the g-C$_3$N$_4$ is acting as a semiconductor photocatalyst	[267]
2013	Zn$_2$GeO$_4$/ZIF-8 nanorods	0.1L 0.1M Na$_2$SO$_3$ 200 mg Catalyst	500W Xe lamp	Reaction cell Time = 1.5 h	CH$_3$OH =0.22	Higher photocatalytic activity of CO$_2$ was observed compared to the bare Zn$_2$GeO$_4$	[229]
2013	CdS-UiO-66(NH$_2$)	0.1mmol Alcohol 1.5 mL BTF 8 mg Catalyst	300W Xe lamp < 420 nm	Vol. = 10 mL Press. = 0.1 MPa Temp. = 4 ℃	C$_7$H$_6$O (Benzaldehyd)	This photocatalysis is not for CO$_2$ reduction. It's for oxidation of alcohols to aldehydes.	[268]
2013	Co-ZIF-9	1.0 μ mol (Ru (bpy)$_3$)Cl$_2$. 6H$_2$O 5 mL acetonitrile & H$_2$O, 1 mL TEOA 0.8 μ mol Catalyst	>420 nm	Press. = 1 atm Temp. = 20 ℃ Time = 30 min	CO = 41.8 H$_2$ = 29.9	The CO$_2$ photoreactions were conducted by using (Ru (bpy)$_3$) Cl$_2$·6H$_2$O and Co-ZIF-9 as a photosensitizer.	[250]

2.5.4.1 TiO₂-MOF Composites

TiO$_2$ has been researched extensively as a photocatalyst since the development of photocatalysis, although using titanium-based semiconductors for photocatalytic reaction has some disadvantages attributed to its poor visible light absorption, spectrum range and significant charge recombination, TiO$_2$ grant some favourable features such as being non-toxic, abundant, naturally occurring and easy to be structurally adapted. Combining MOFs with TiO$_2$ can both limit the drawbacks of each component and increase the overall photocatalytic efficiency.

TiO$_2$ particles were graphted onto (Cu$_3$ (BTC)$_2$) microcrystals known as HKUST-1 by Li et al. [148] to form a TiO$_2$ @ HKUST-1 nanocomposite for photocatalytic CO$_2$ reduction under UV light as shown in Figure 2.25 (a). The composites contained about 33 wt. % of TiO$_2$. Although the CO$_2$ adsorption capacity was decreased by around a third, the production of CH$_4$ from TiO$_2$@HKUST-1 was found to be five times higher compared to pure TiO$_2$ as shown in Figure 2.25 (b), this high evolution of CH$_4$ was caused as a result of effective electron–hole separation.
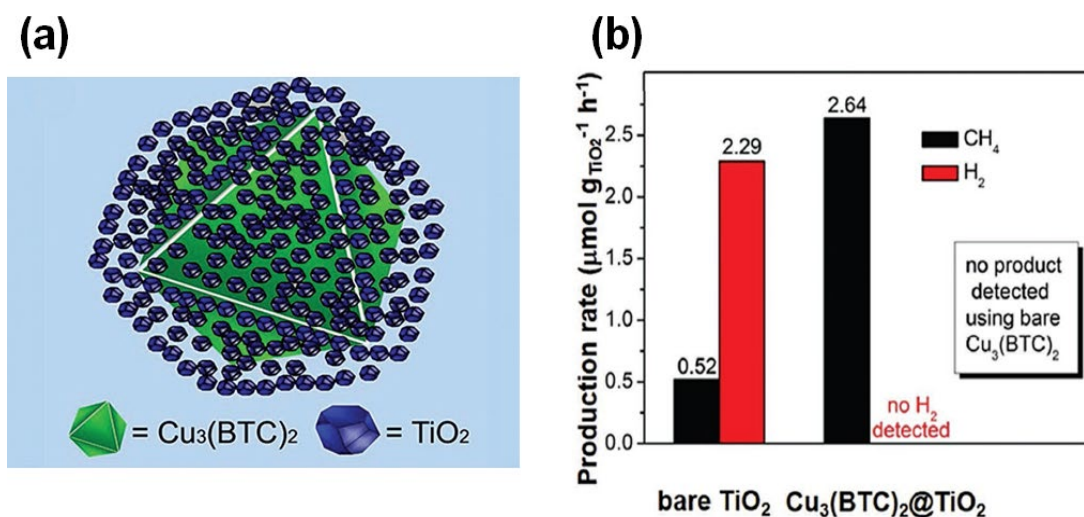
Figure 2.25   (a) Structural illustration of TiO$_2$ on HKUST-1 (b) A comparison in terms of photocatalytic CO$_2$ reduction between TiO$_2$, Cu$_3$(BTC)$_2$, and TiO$_2$@Cu$_3$(BTC)$_2$ [148].

A TiO$_2$-NH$_2$-UiO-66 composite was synthesized by Crake et al. [139] using an *in situ* growth strategy as shown in Figure 2.26 (a-b), the CO$_2$ photoreduction

activity was significantly enhanced compared to pure TiO_2. The reaction was carried out for 6 hours under UV-Vis irradiation, both of functionalized MOF and bare TiO_2 exhibited the lowest activity respectively as illustrated in Figure 2.26 (c) while by combining both components with different weight ratios, the photoactivity and the CO evolution rate was found to be much increasing as the NH_2-UiO-66 content increases. However, after exceeding 20 wt. % of the MOF content, the CO evolution rate was declined. The high CO_2 adsorption capacity gained from NH_2-UiO-66 and the effective interfacial charge transfer caused by the formation of heterojunctions between NH_2-UiO-66 and TiO_2 highly improved the photocatalytic performance. Su et al. [262] also fabricated a series of $Cd_{0.2}Zn_{0.8}S$/NH_2-UiO-66 nanocomposites and successfully reduced CO_2 at the same conditions and with different NH_2-UiO-66 contents by using a solvothermal method.
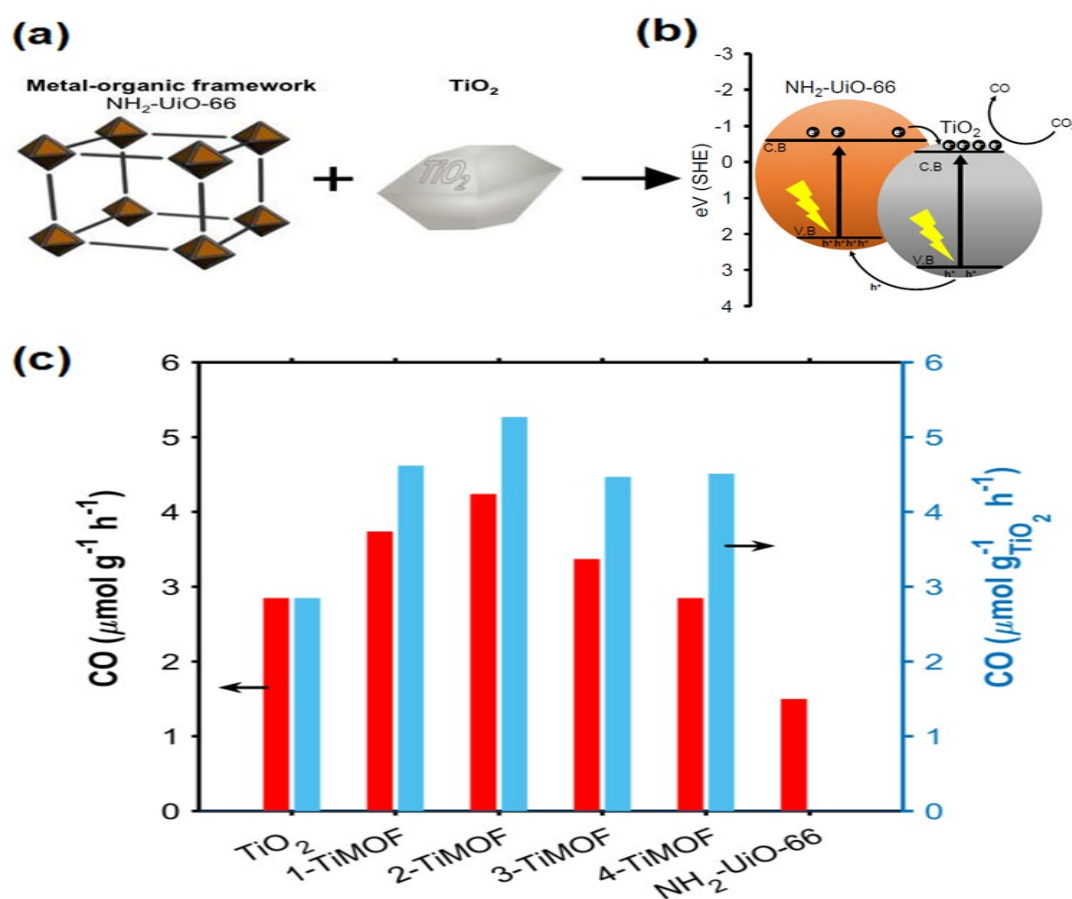
Figure 2.26   (a) A schematic illustration of NH_2-UiO-66 and TiO_2, (b) The proposed mechanism of photocatalytic CO_2 reduction over TiO_2-NH_2-UiO-66, (c) The CO evolution rates by using TiO_2, NH_2-UiO-66 and TiO_2-NH_2-UiO-66 nanocomposites with different MOF wt. %, the red bars represents the CO evolution rate based on the grams of the overall catalyst and the blue bars represents the CO evolution rate based on the grams of the TiO_2 catalyst [139].

TiO$_2$ has also been assembled onto a Mg-based MOF; CPO-27-Mg (also known as Mg$_2$((NH$_2$)$_2$-BDC)) by Wang et al. [198] to form TiO$_2$/CPO-27-Mg composite using solvothermal synthesis as illustrated in Figure 2.27 (a). This MOF composite exhibited enhanced CO$_2$ adsorption capacity and photocatalytic activity for CO$_2$ conversion. CO$_2$ was photoreduced into CO, CH$_4$ and H$_2$ under UV illumination for 10 hours in the presence of H$_2$O vapour. The evolution of these products was much higher than that of TiO$_2$ and CPO-27-Mg (which showed no photocatalytic activity). The nanocomposite with CPO-27-Mg amount of (39.3 wt. %) exhibited the highest evolution of CO (4.09 µmol g^{-1} h^{-1}) and CH$_4$ (2.35 µmol g^{-1} h^{-1}) as shown in Figure 2.27 (b).
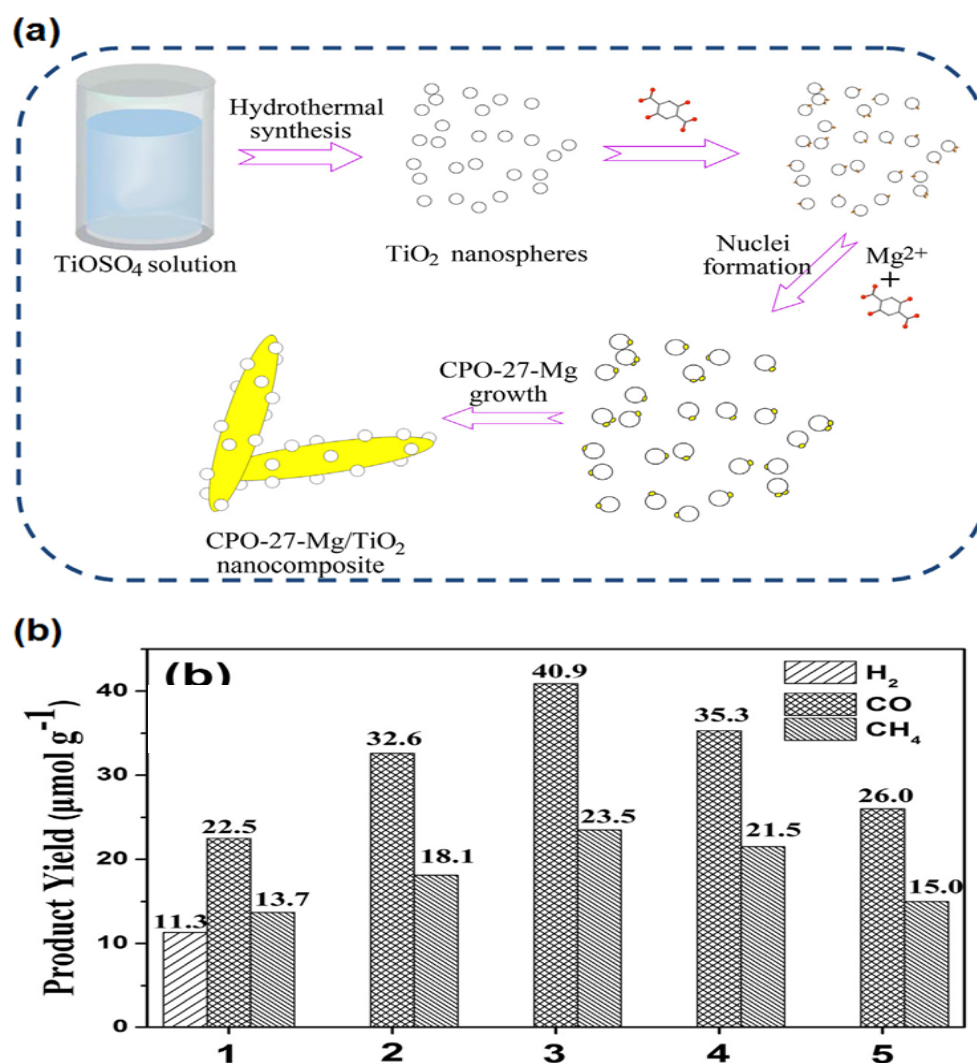
Figure 2.27   (a) the synthesis procedure of CPO-27-Mg/TiO$_2$ nanocomposite using solvothermal method, (b) The evolution of CO, CH$_4$ and H$_2$ over CPO-27-Mg/TiO$_2$ nanocomposites with different amounts of CPO-27-Mg [(1=0%) (2=26.1%) (3=39.3%) (4=57.2%) (5=68.7%)] after 10 hours irradiation [198].

Yan et al. [182] fabricated TiO$_2$ with Co-ZIF-9 to form Co-ZIF-9-TiO$_2$ composites by using an *in situ* synthetic procedure (Figure 2.28 (a)). A series of Co-ZIF-9-TiO$_2$ nanocomposites of various TiO$_2$ loadings were tested as illustrated in Figure 2.28 (b). The light absorption spectra of the newly synthesized composites shifted from UV (TiO$_2$ absorption) towards visible, CO$_2$ was successfully photoreduced into CO, H$_2$ and CH$_4$. The highest photocatalytic activity (8.79 μmol CO, 1.3 μmol H$_2$ and 0.99 μmol CH$_4$) was exhibited by Co-ZIF-9-TiO$_2$ (with 3 wt. % Co-ZIF-9) under visible light irradiations for 10 hours. However, no activity was observed with the use of Co-ZIF-9 alone.
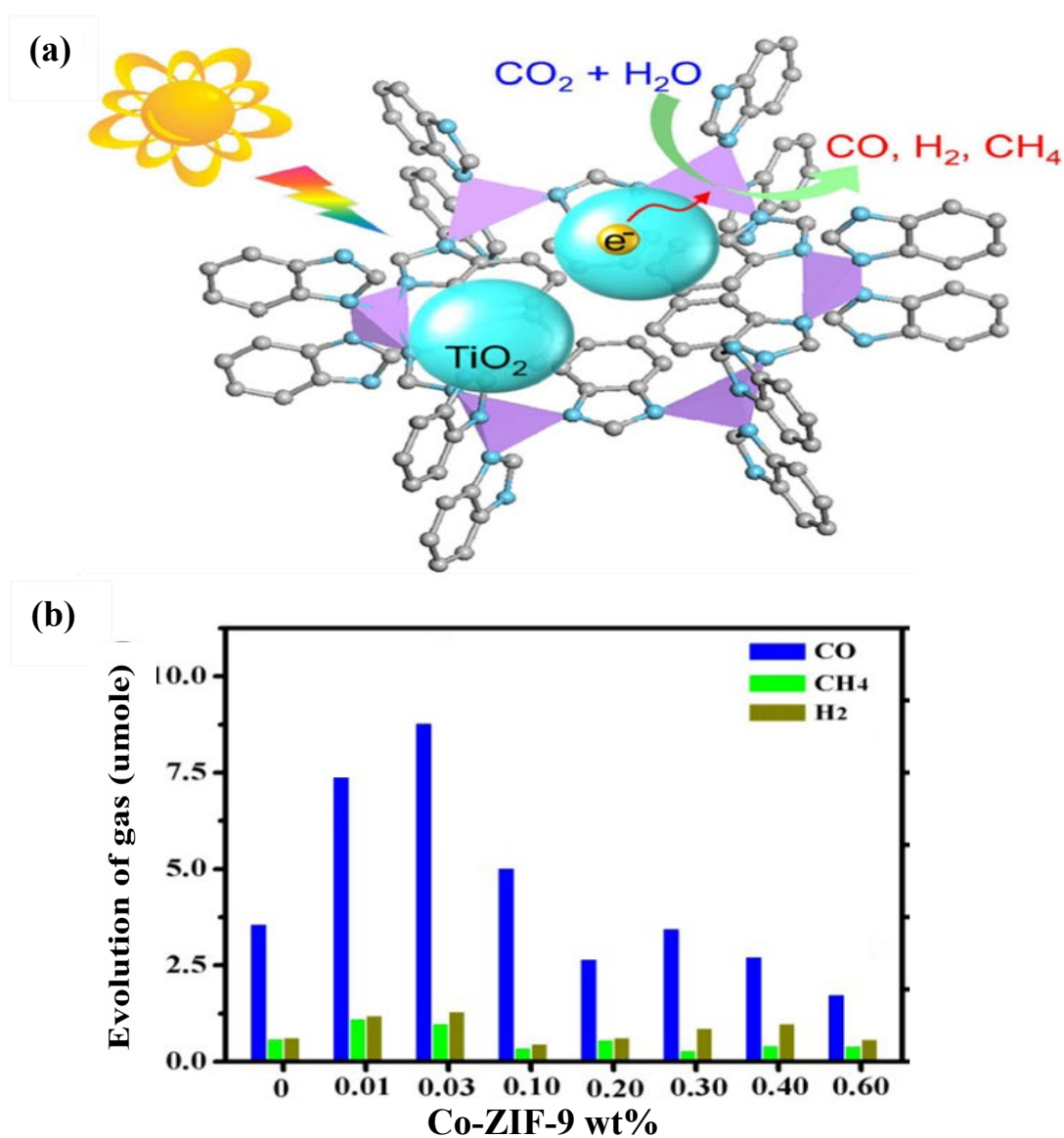
Figure 2.28   (a) The structure design of Co-ZIF-9/TiO$_2$ nanocomposite, (b) The evolution of CO, CH$_4$ and H$_2$ over the different Co-ZIF-9-TiO$_2$ composites [182].

2.5.4.2 Graphene–MOF Composites

In recent years, MOFs have become the focus of attention for solar energy conversion applications due to their superiority over the inorganic catalysts in terms of specific surface area, design flexibility and porous structure [269]. However, MOFs suffer from poor electrical conductivity which restricts their photoactivity. Combining graphene with MOFs to form different structures of heterojunctions is a possible option to overcome this problem [270]. Moreover it will also adjust the photothermal stability of MOFs and increase visible light harvesting [241, 271]. This is what inspired researchers to design graphene-MOF photocatalysts for achieving better performance in photocatalytic CO_2 reduction.

Generally, the UiO-66-NH_2 MOF is the most widely studied MOF in the field of CO_2 reduction due to its strong capacity of CO_2 absorption. However, it has some limitations related to its week conductivity and poor visible light response. To overcome these limitations Wang et al. [170] synthesized a novel UiO-66-NH_2/GR composite (Figure 2.29 (a)) via a microwave-assisted method by incorporation of UiO-66-NH_2 with different amounts of graphene (0.5 to 3.0 wt. %). HCOOH and H_2 with low concentration of CH_4 were produced from the CO_2 photocatalytic reduction under visible light irradiation as illustrated in Figure 2.29 (b-d). The new hybrid MOF composite exhibited both high activity and selectivity. The CO_2 photocatalytic efficiency of UiO-66-NH_2/2.0GR, expressed as the HCOOH generation performance was the highest (35.5 μmol) among all the tested samples; around 11 times as of that for pure UiO-66-NH_2 and doubled in comparison with that of UiO-66-NH_2/GR sample that was obtained by using the traditional hydrothermal synthesis. Zhao et al. [258] also used UiO-66-NH_2 but with different semiconductor other than graphene to synthesize a hybrid membrane of CdS/NH_2-UiO-66 with high efficiency for photocatalytic CO_2 reduction. CO was the main product detected from the membrane system after 6 hours irradiation under visible light. Besides, traces of HCOOH and H_2 appeared within the system. The CO product evolution was 521.9 μmol g^{-1} compared to only 188.29 and 127.52 μmol g^{-1} for CdS and NH_2-UiO-66 membranes respectively. CdS/NH_2-UiO-66 membrane system also exhibited 99% CO selectivity compared to 97% that of CdS membrane.
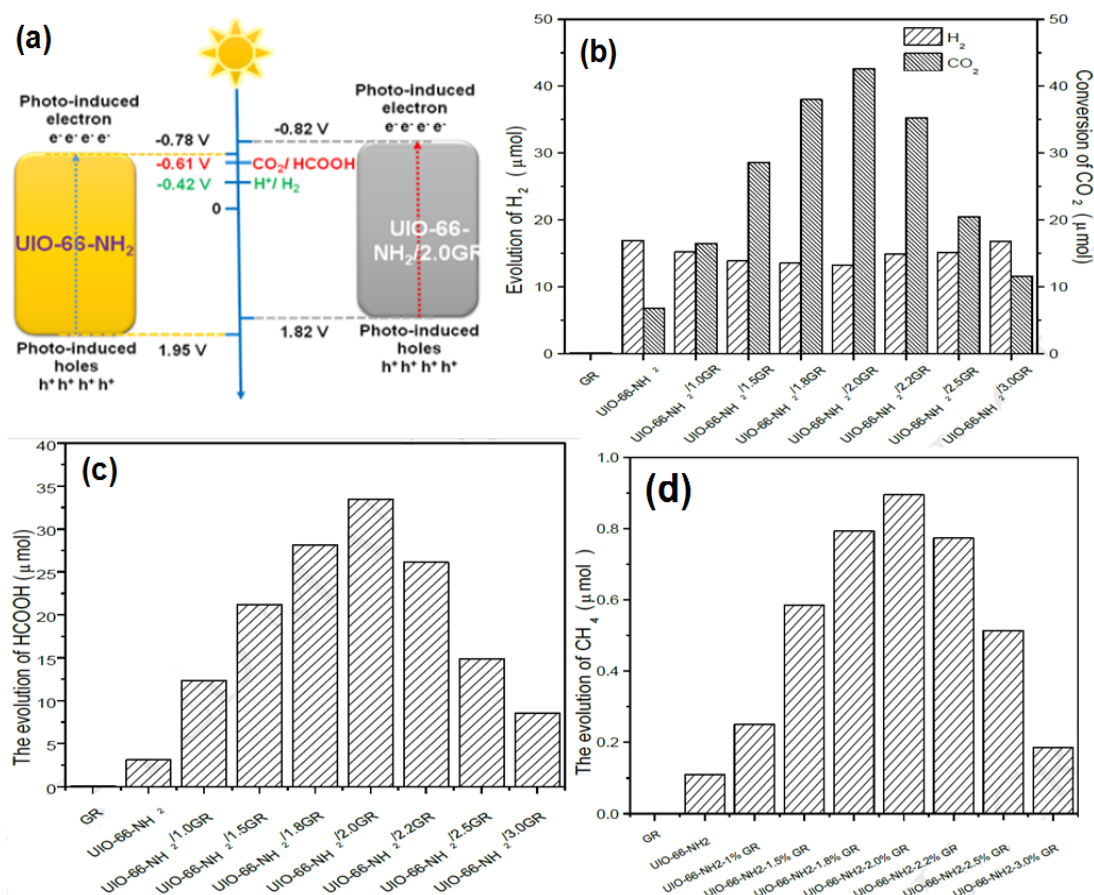
Figure 2.29   (a) The potentials of valence and conduction bands of UiO-66-NH$_2$ and UiO-66-NH$_2$/2.0GR, (b) The evolution of H$_2$ and the conversion of CO$_2$, (c-d) the evolution of formic acid and CH$_4$ over various catalysts [170].

Shi et al. [168] coupled Carbon Nitride Nanosheets (CNNs) with UiO-66 to prepare UiO-66/CNNs composite using self-assembly synthesis method through the electrostatic reaction between negative charges represented by carbon nitride nanosheets (CNNs) and positive charges represented by UiO-66 as shown in Figure 2.30 (a). The photoreaction was carried out under visible light for 6 hours in the presence of (v/v= 4:1) MeCN and TEOA. The CO$_2$ was photoreduced into CO for both CNNs and CNNs/UiO-66 whereas no activation was observed for UiO-66. However, UiO-66/CNNs composite exhibited higher CO$_2$ adsorption capacity and CO formation rate (9.9 μmol g^{-1} h^{-1}) compared to both CNNs (2.9 μmol g^{-1} h^{-1}) and UiO-66/ bulk CN (3.2 μmol g^{-1} h^{-1}) as shown in Figure 2.30 (b). The high efficiency of the UiO-66/CNNs composite is attributed to the formation of heterojunctions between CNNs and UiO-66 (Figure 2.30 (c)) which enhanced the electron supplies leading to high performance in photocatalytic CO$_2$ conversion.
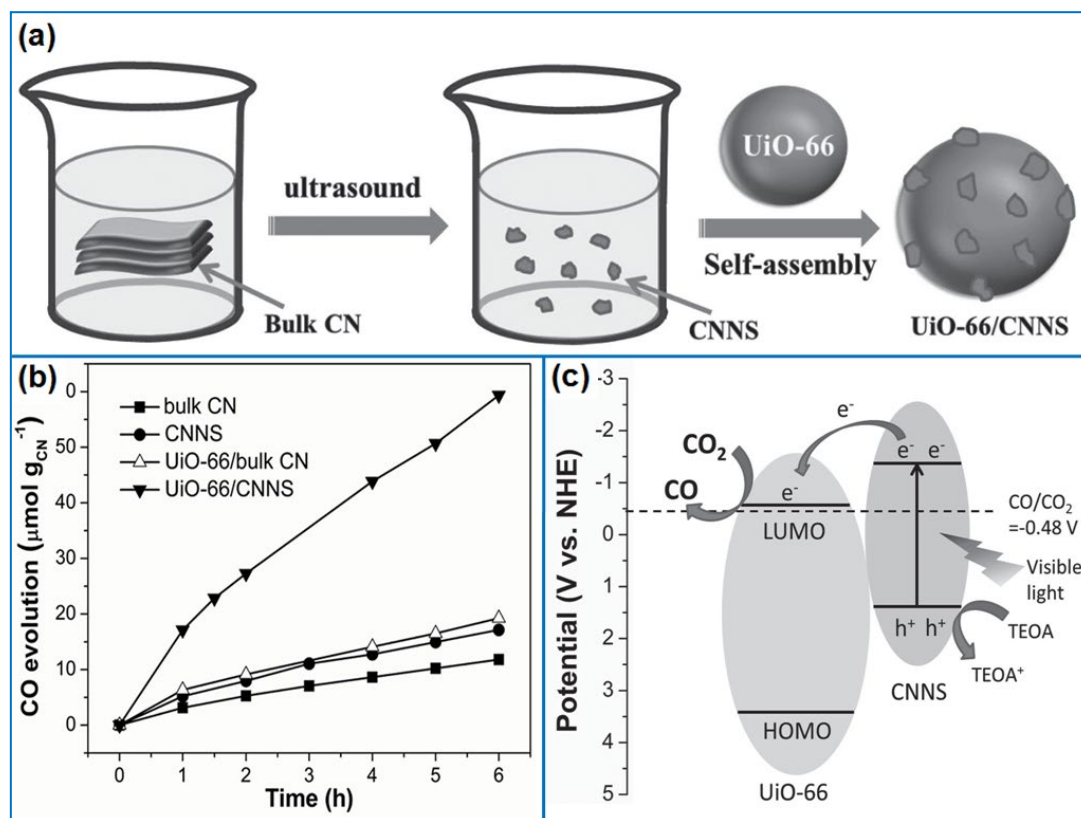
Figure 2.30 (a) A scheme illustrating the preparation of UiO-66/CNNs photocatalyst, (b) The CO evolution over bulk CN, CNNs, UiO-66/bulk CN, and UiO-66/CNNs photocatalysts for different periods of time (1-6 hours), (c) The proposed mechanism of photocatalytic CO_2 reduction over the UiO-66/CNNs photocatalyst under visible light irradiation [168].

Wang et al. [249, 267] investigated the coupling of graphitic Carbon Nitrides (g-C_3N_4) with Co-ZIF-9 and then studied the effect of using bpy (2,2'-Bipyridine) as an assistant agent for electron transfer and TEOA as a sacrificial agent by donating electrons to carry out the CO_2 photocatalytic reduction. The semiconductor played the role of being as a photocatalytic host while the MOF acted as a cocatalyst. CO_2 was reduced into CO and H_2 under visible light irradiation. Both mixtures displayed higher photocatalytic activities than their pure states. Wang et al. [261] also incorporated carbon with g-C_3N_4 to form graphene-like g-C_3N_4/C nanosheets named as 3D g-C_3N_4/C-Ns composite as illustrated in Figure 2.31 (a-b). CO_2 was successfully photoreduced into CO and CH_4 under visible light illumination and in the presence of H_2O vapor, high reduction performance was observed for the new MOF-composite photocatalyst which was attributed to its high ability for adsorbing gas reactants, high surface area accompanied with enormous porous catalytic sites as

shown in Figure 2.31 (c-d), efficient light harvesting and high transmission of photogenerated excited electrons with impeded charge recombination.
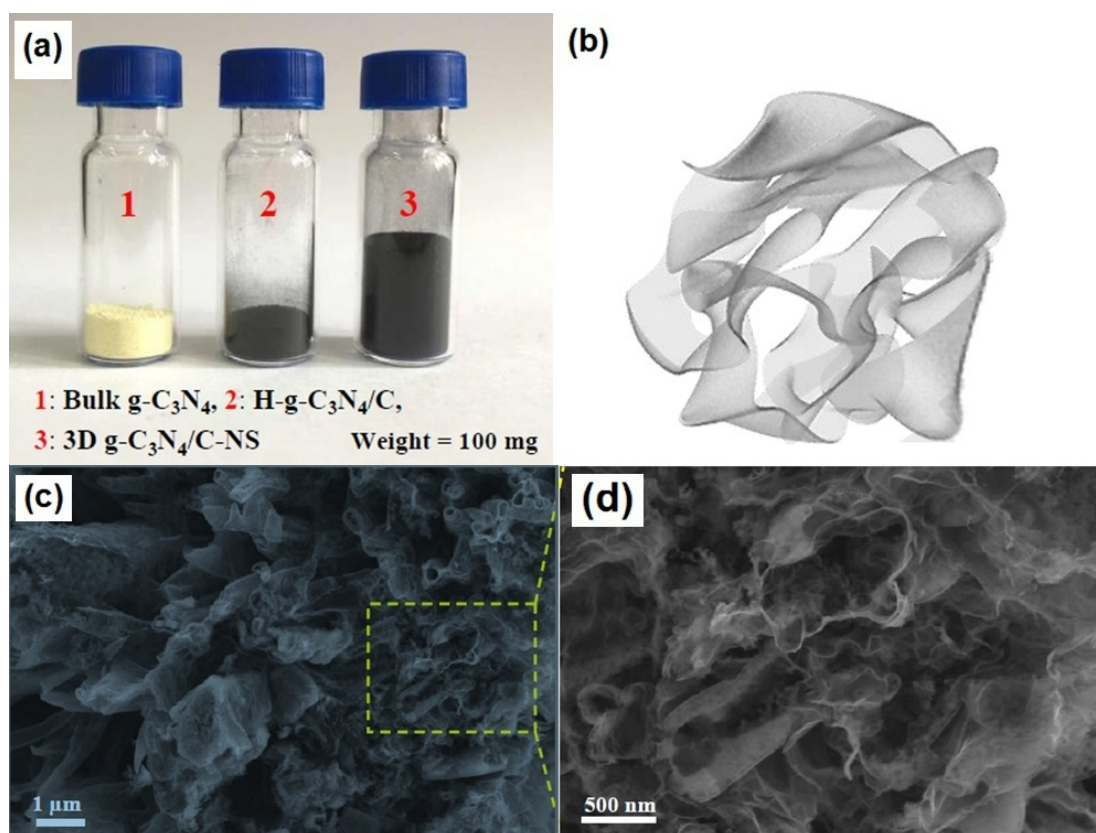
Figure 2.31   (a-b) A photograph and a schematic illustration of 3D g-C$_3$N$_4$/C-Ns, (c-d) SEM images showing the 3D porous nanosheets in 3D g-C$_3$N$_4$/C-Ns [261].

2.5.4.3 Metal-MOF Composites

Most of metals especially the noble metals possess the effect of Localized Surface Plasmon Resonance (LSPR), For example, Ag nanoparticles have the ability to absorb visible light and undergo an excitation state and thus act as a type of sensitizers to enhance the visible light harvesting and increase the photocatalytic performance [74]. The strong electromagnetic field exhibited when Ag nanoparticles were combined with TiO$_2$ [272, 273] proves the impact of (LSPR) in the enhancement of photocatalytic activities for the composites. This impact can also be applied to increase the photocatalytic activity of MOFs. Choi et al. [264] investigated a series of Ag nanocubes–MOF composites to synthesize Ag⊂Re$_n$-MOF, in which n represents the number of Re^I(5, 5′-dcbpy)(CO)$_3$Cl in a unit cell and the MOF used

here is a zirconium MOF (UiO-67), this photocatalyst had two distinct functional units (Ag nanocubes and Re-complex photosensitizers) at the same time as shown in Figure 2.32. CO_2 was reduced into CO (96% selectivity) under visible light (400-700 nm) in the presence of TEA. The Ag-nanocubes coated with Re-MOF did not only exhibit improved photocatalytic activity but long-term stability as well.
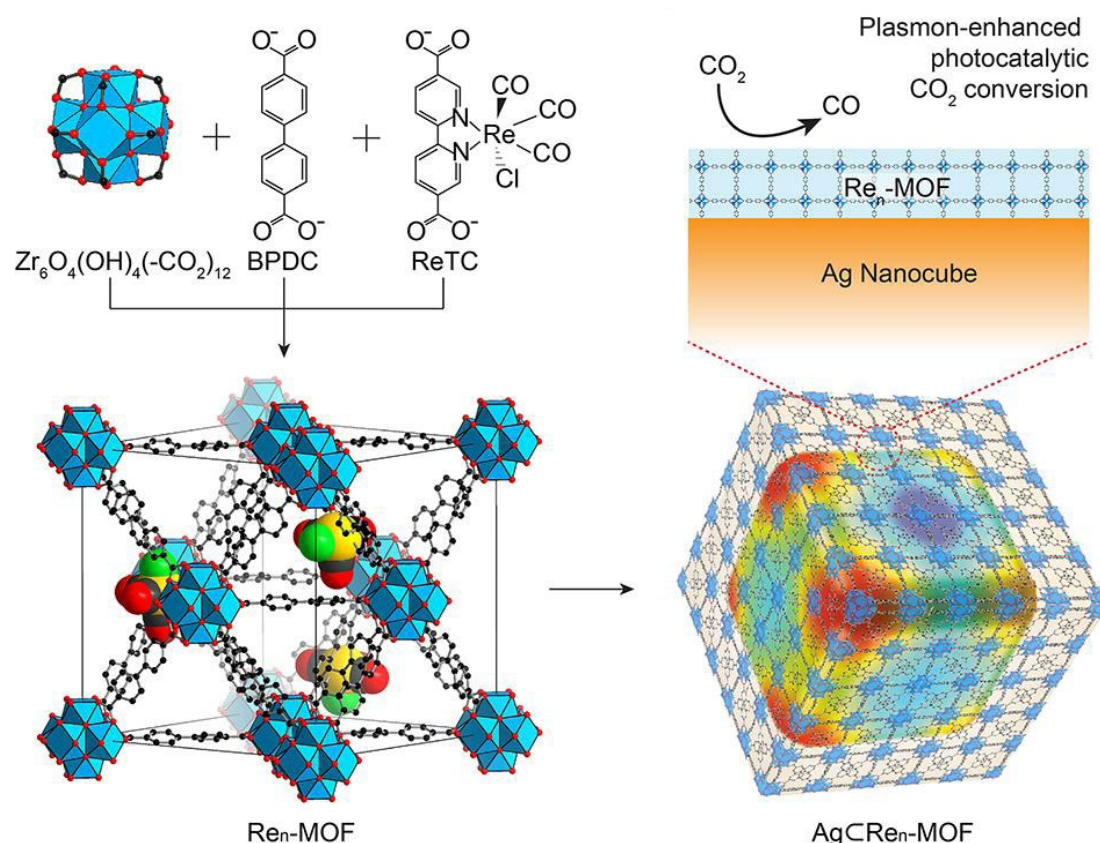
Figure 2.32   Structures of Ren-MOF and Ag⊂Ren-MOF for Plasmon-enhanced photocatalytic CO_2 reduction [264].

Han et al. [151] incorporated MOF-74 with various metals (Au, Pd and Pt) to form different Zn-based MOF composites; Au@Pd@MOF-74, Pt/MOF-74, and Pt/Au@Pd@MOF-7 as shown in Figure 2.33. Only CO was produced for both MOF-74 (7.42 μmol g^{-1}) and Au@Pd@MOF-74 (12.31 μmol g^{-1}) after 5 hours of light irradiations with the presence of H_2O. However, with the inclusion of Pt NPs with the MOF, CH_4 (9.04 μmol g^{-1}) was observed in addition to CO (8.85 μmol g^{-1}) with a CH_4 selectivity of more than 50%. Finally, for Pt/Au@Pd@MOF-74, the CH_4 selectivity increased up to 84% with a yield of 12.35 μmol g^{-1}. To conclude, Pt NPs promoted the production of CH_4 and when Au@Pd NPs and Pt NPs are incorporated

together, the CH4 yield and selectivity will increase, while the CO yield gets repressed.
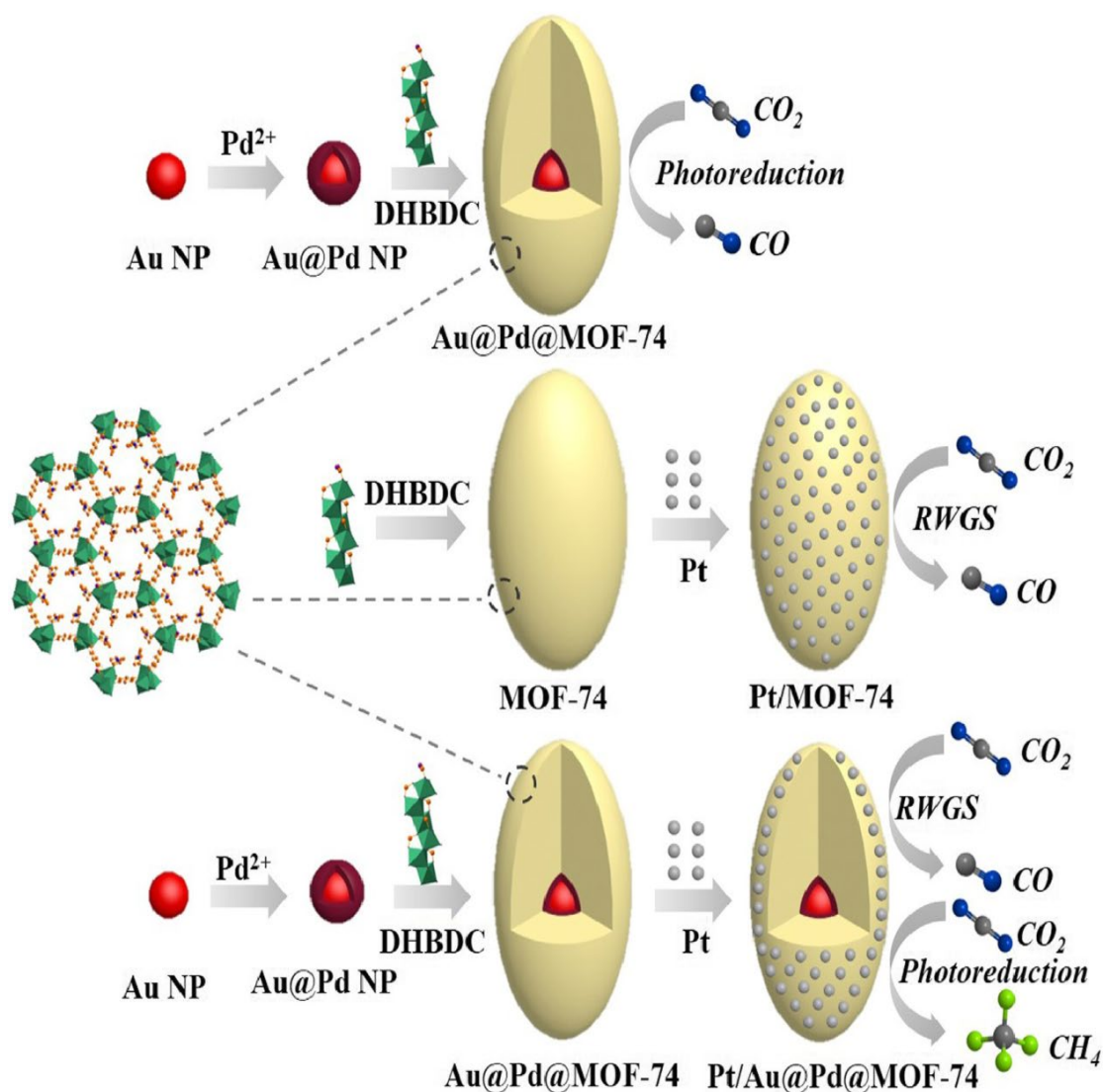
Figure 2.33 A scheme showing the synthesis of Au@Pd@MOF-74, Pt/MOF-74 and Pt/Au@Pd@MOF-74 [151].

2.6   Other Semiconductors for Photocatalytic CO₂ Reduction

2.6.1   Titanium Dioxide (TiO₂) Nanotube Arrays

TiO₂ belongs to the family of transition metal oxides and it is one of the most studied compounds in materials science. Owing to some outstanding properties, it is widely used in the field of photocatalysis. TiO₂ is known to be a non-toxic, low cost,

environmentally friendly and corrosion-resistant material. Various investigations have established that TiO_2 is much more effective as a photocatalyst in the form of nanoparticles than in bulk powder [274, 275]. However, the 1D nanostructures are known for their unique chemical and physical properties, these 1D nanostructures own higher specific area and better charge transfer compared to other TiO_2 nanoparticles. Moreover, all the semiconductors with 1D nanostructures offer more light scattering and trapping which can facilitate the light absorption more efficiently in the photocatalytic reactions [276]. At the end of the twentieth century, Zwilling et al. [277] reported for the first time the feasibility to grow highly ordered arrays of TiO_2 nanotubes by simple electrochemical anodization of pure titanium metal sheets [274]. The hierarchical, vertically oriented TiO_2 nanotube arrays (TNTs) as shown in Figure 2.34 offer large internal surface area, more light harvesting compared to TiO_2 nanoparticals [278]. Generally, the TNTs system facilitates the electron flow through the walls by providing shortcuts, whereas, in nanoparticle systems, the electron pathways are lengthened due to the random connections between the particles [279], which makes TNTs a good photocatalyst for photocatalytic CO_2 reduction.
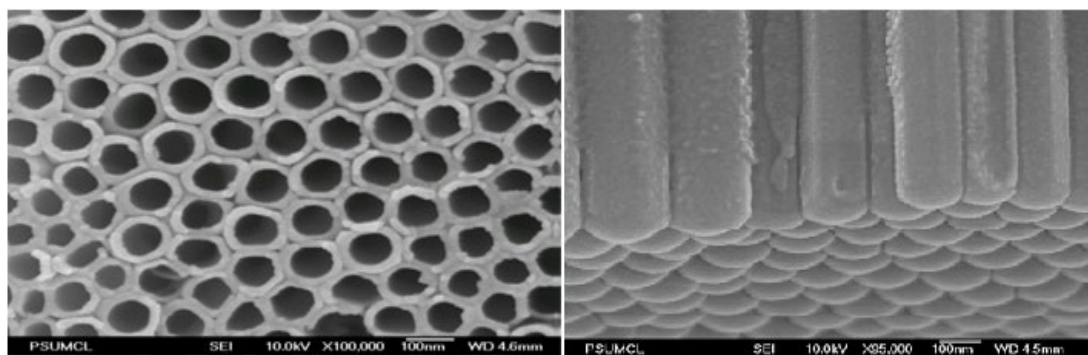
Figure 2.34   Illustrative FESEM surface top and bottom images of a nanotube-array sample grown at 60 V in an ethylene glycol electrolyte containing 0.25 wt% NH_4F [280].

2.6.1.1 Synthesis of TiO₂ Nanotube Arrays

The most common method to synthesize TiO_2 NTs is by the electrochemical anodization in which a titanium foil is exposed to a sufficient anodic voltage in a two-electrode configuration, the Ti foil is used as the working electrode (anode) and a Pt foil is used as the counter electrode (cathode). These electrodes are submerged in

an NH_4F/ethylene glycol electrolyte solution. After the anodic oxidation, the samples are rinsed with deionized water and annealed at 500 °C for 2 hours to obtain the final shape of TiO_2-NTs.

2.6.1.2 Limitations and Improvements of TiO_2 Nanotubes

Although TiO_2 NTs have unique properties as a photocatalyst in terms of surface area and structural properties, it suffers from having a high recombination rate of photo-generated charge carries which results in low yield rates. Also being UV-active only limits their applications in the solar photocatalysis field.

Besides the optimization of NTs characteristics in terms of length and thickness, the improvement of photocatalytic activity can also be done by synthesizing of TiO_2 NTs composites [278]. Sim et al. [281] used RGO and Pt with TNTs through a simple method and successfully synthesized a visible light-responsive ternary composite photocatalyst named as RGO/Pt–TiO_2-NTs. A significant impact on the improvement of CH_4 production rate was observed after the depositions of Pt and RGO into the surface of TiO_2 NTs. The RGO functioned as an electron reservoir by capturing the photogenerated electrons to suppress electron–hole pairs recombination while the LSPR effect of Pt NPs enabled the visible light harvesting properties of the composite.

In order to improve the light harvesting efficiency and thus the photocatalytic efficiency of TiO_2 NTs in visible region, many studies were conducted to incorporate these NTs with other semiconductors, especially those having high ability to absorb visible light radiations like graphene oxide and MOFs.

2.6.2 Graphitic Carbon Nitrides (g-C_3N_4)

The graphitic carbon nitride (g-C_3N_4) is one of the famous metal-free organic semiconductors which have attracted much attention in the field of photocatalytic CO_2 reduction. The g-C_3N_4 is not only cheap, nontoxic and easy to prepare, but also

exhibits good stability in various pH solutions under light irradiation and also has a narrower band gap (~2.7 eV) which makes this semiconductor very active under visible light [282]. Furthermore, the C-N and C=N functional groups in g-C_3N_4 are favorable for its construction with other semiconductor composites [283]. Due to all these exceptional properties, the composites of g-C_3N_4 were widely investigated and studied through different synthesis methods [284-289]. The GO addition to g-C_3N_4 for example, have shown significant enhancement in visible light absorption and in limiting the charges recombination rate of pure g-C_3N_4. Recently, MOF-g-C_3N_4 composites have also been introduced to photocatalysis fields, however, it is worth mentioning that coupling g-C_3N_4 with MOFs for photocatalytic CO_2 reduction is still very limited and needs to be more researched and investigated. Figure 2.35 shows clear FESEM images of pure g-C_3N_4 nanosheets.
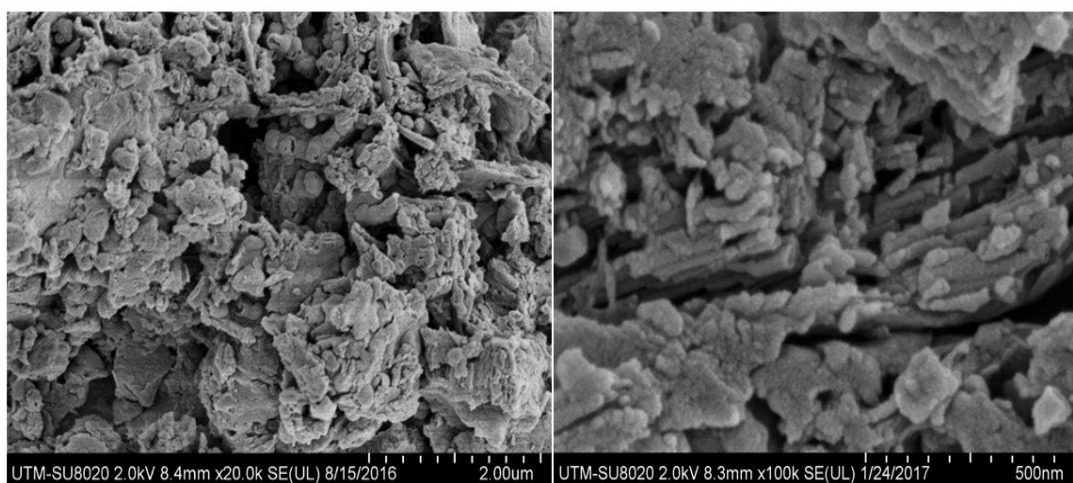
Figure 2.35   FESEM images of pure g-C_3N_4 nanosheets.

2.6.3   Graphene Oxide (GO)

Graphene oxide is a two-dimensional (2D) crystalline material which is made of oxy-functionalized carbon atoms packed in hexagonal forms as illustrated in Figure 2.36 [290]. RGO can be obtained after reducing GO by using different reduction methods such as thermal, solvothermal, chemical and electrochemical techniques [291]. GO has shown excellent mechanical, electrical and thermal properties in various applications. In photocatalysis, GO is incorporated to other

semiconductors to improve the overall photocatalytic properties since graphene does not only accurately modify the surface of the photocatalysts but can also facilitate electron transport efficiently and suppress the recombination of electron–hole pairs [292, 293].
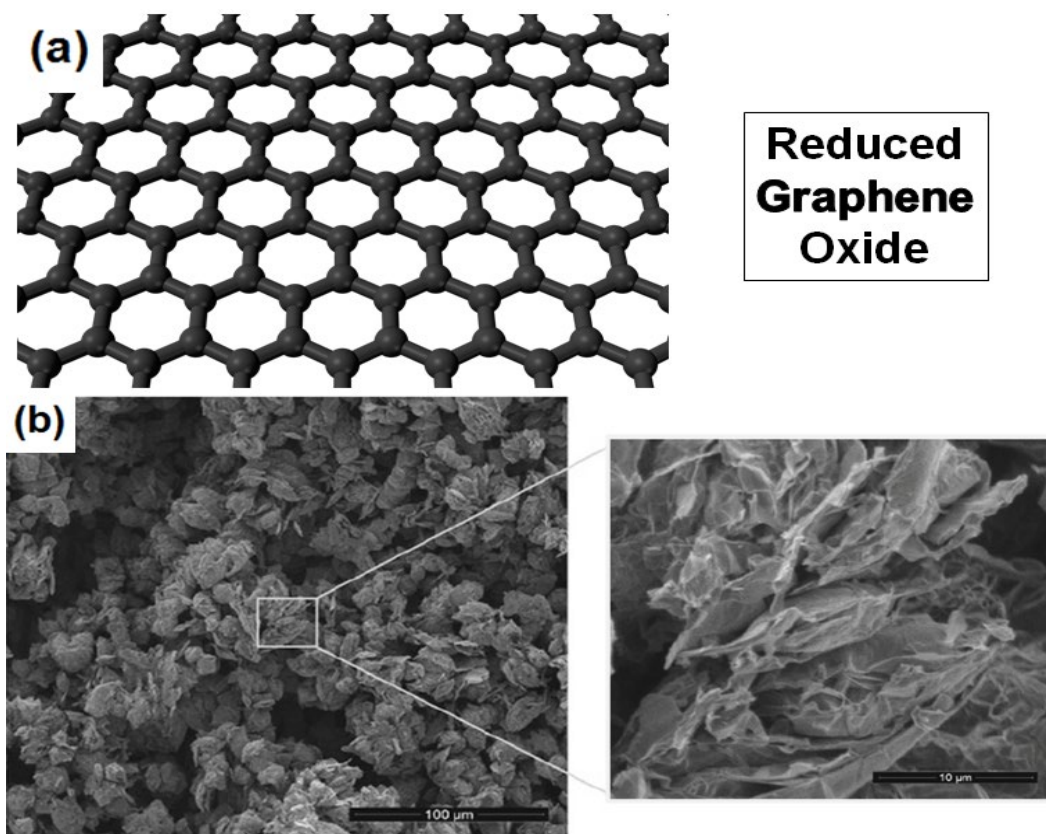
Figure 2.36   (a) Structure of reduced graphene oxide (RGO), (b) SEM image of thermally synthesized reduced graphene oxide [294].

Recently, many studies have introduced the incorporation of graphene oxide with metal-organic frameworks (MOFs) for improving the photocatalytic performance. During the synthesis of MOF-composites at high temperatures, both the surface area and the amount of effective active sites of MOFs are reduced, to overcome this issue, graphene oxide (GO) is introduced as a mechanical support for the nanoparticles to prevent their agglomeration. Incorporation with GO will also limit the MOFs poor performance in terms of electrical conductivity and will combine the advantages of MOFs and graphene resulting in better stability, improved conductivity and higher surface area [270, 295].

MOFs/graphene composites can be prepared by using physical mixing or hydrothermal treatment, however, the hydrothermal synthesis is considered to be a more common and more effective way for combining these composites [296]. The UiO-66-NH$_2$-RGO MOF/graphene composite for photocatalytic CO_2 reduction was successfully synthesized using microwave-assisted solvothermal synthesis. The MOF/graphene composite exhibited much higher results than both pure composites and the UiO-66-NH$_2$/GR sample which was obtained via traditional hydrothermal synthesis [170]. Figure 2.37 shows a schematic illustration of the UiO-66-NH$_2$/GR composite and its characterizations.
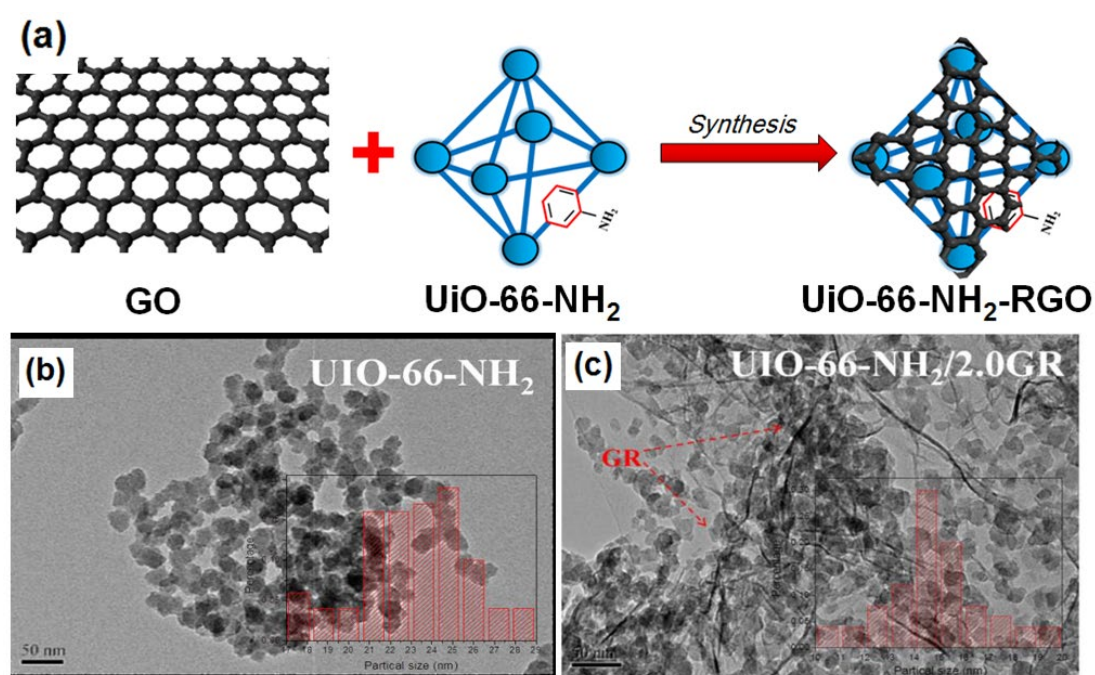
Figure 2.37   (a) A schematic illustration for the UiO-66-NH$_2$/GR synthesis, (b) TEM image of UiO-66-NH$_2$ [170], (c) TEM image of UiO-66-NH$_2$/2.0RGO [170].

2.7   Research Gap

A wide range of photocatalysts including MOFs have been used in the field of photocatalytic CO_2 reduction. However, no studies have been reported yet for using the NH_2-MIL125(Ti) MOF for enhancing the photocatalytic performance of the graphitic carbon nitrides (g-C_3N_4) and titanium dioxide nanotubes (TiO_2) photocatalysts with the use of graphene oxide mediator. Furthermore, this study aimed for using the visible light only as a light source for maximum utilization of solar light energy. Compared to the previous studies, only water was used as a reducing agent in this research without any use of sacrificial agents or other toxic chemicals that could have a negative impact on the environment. Here in, the amino functionalized MIL-125(Ti) MOF was used with two of the most common and inexpensive semiconductors (g-C_3N_4 and TiO_2). The graphene oxide was used as a solid electron mediator between the MOF and each of these semiconductors. This research is intensively focusing on using new combinations of novel noble metal-free nanocomposites named as g-C_3N_4-RGO-NH_2-MIL125(Ti) and NH_2-MIL125(Ti)-GO-TNTs fabricated through a new synthesis approach of electrochemical, thermal, hydrothermal and sonochemical methods for efficient photocatalytic CO_2 reduction to solar fuels. Table 2.7 summarizes the main characteristics and limitations related to the photocatalyst materials used in this research.

Table 2.7   Summary of characteristics and limitations of the used photocatalysts.

Catalyst	TiO₂ NTs	g-C₃N₄	GO/RGO	NH₂-MIL-125(Ti)
Characteristics	* Large surface area. * Corrosion- resistant. * Good chemical stability. * Environmentally friendly. * Easy to synthesize. * Most extensively studied material. * Higher photocatalytic performance than other TiO₂ nanoparticles.	* Visible light active. * Good morphology. * Widely used. * Cheap and easy to prepare.	* High specific surface area. * UV/Vis active. * Tunable bandgap and low toxicity. * Excellent electrical, thermal and mechanical properties. * Promotes the electrons transfer. * Limits charges recombination. * Can be introduced as mechanical support for MOF.	* Extremely large specific surface area beneficial for CO₂ adsorption. * Adjustable and well-ordered pore size. * Excellent chemical composition. * Excellent textural and structural properties. * Various means available for synthesis. * Can be used for CO₂ reduction with no sacrificial agents.
Limitations	* Wide-bandgap. * UV-active only. * Suffers from high charge recombination rate.	* High charges recombination. * Considerably low absorption of solar light.	* Needs cautious design of the composites to attain high quality. * Properties depend largely on its microstructures. * Production of graphene-based nanomaterials is still confronted with many challenges.	* Performs poorly alone in terms of electrical conductivity. * Lack of thermal stability at high temperatures. * The amount of effective sites are reduced with high temperatures. * Challenges of structural instability.

2.8   Summary

MOFs are currently attracting researcher's attention in the field of photocatalytic CO_2 reduction due to their exceptional textural properties, adaptability for specific applications, diverse and easy synthesis methods. In this review, the fundamentals of MOF-based photocatalysis for CO_2 reduction such as the principles, thermodynamics, mass transfer concepts, mechanisms and their strategies for improving charge transfer are well explained. This chapter critically summarizes the classifications of MOF photocatalysts for CO_2 reduction with the recent studies for the latest ten years. A lot of calculations were done based on the experimental results to construct illustrative and informative tables since the yields were not clearly provided in some of original works.

To conclude, MOFs are considered to be the new promising photocatalysts in the field of CO_2 reduction, however, they still have some limitations. Firstly, they are not enough explored yet and the reported studies for using MOFs in the field of CO_2 reduction are considerably limited with very low production yields which might be attributed to their poor electrical conductivity. Secondly, most of MOF synthesis methods are limited with low-throughput productions which might restrict their applications due to the high product cost. The MOF mechanism and dynamics for photocatalytic CO_2 reduction are not very clear and need to be more investigated. Last but not least, the usage of the sacrificial reagents such as TEOA and TEA in most of CO_2 photocatalytic processes is not economic and has a negative impact on the environment. To address all these issues and challenges, the following future recommendations should be considered:

- For practical application of MOF photocatalysis toward large-scale processes, more focus is needed in studying the physicochemical properties of these materials such as visible light absorption, electronic structure, crystallographic properties, porosity and the surface area.

- MOF-composites are far more efficient in photocatalytic CO_2 reduction than pure MOFs. So, the incorporation of MOFs with high conductive and visible-active

semiconductor materials like graphene will increase visible light harvesting, the CO_2 adsorption and the photocatalytic activity.

- The challenge of forming MOF composites remains struggling due to the complex MOF chemistry, the material selection also remains crucial. Thus, huge efforts should be exerted by carrying out more intensive research works to fulfil the requirements for more practical and sustainable MOF applications in the field of photocatalysis.

- Better understanding of the photocatalytic mechanisms of MOFs such as the Z-schemes and S-schemes is highly needed since it is considered to be the key for developing and engineering of photocatalysts with efficient charge separation and transport.

- Increasing the products selectivity is one of the most challengeable goals during the photoreduction of CO_2 since most photocatalytic systems result in a mixture of products and the separation of these products dramatically increases the overall cost of the CO_2 reduction process using MOFs. So, professional selection of metal nodes, organic linkers, and/or other integrated components aiming highly selective photocatalysis is highly desired during the synthesis.

- In most of MOF photocatalytic reactions, sacrificial agents are necessary; these agents act as electron donors for enhancing the overall photocatalytic performance. However, they are expensive and environmentally toxic, so more economical and clean solar fuel productions without these sacrificial agents are urgently needed in future.

CHAPTER 3

RESEARCH METHODOLOGY

3.1   Introduction

This chapter describes the experimental work and discusses deeply the research methodology for photocatalytic CO_2 reduction to produce solar fuels over the modified MOF-composite photocatalysts. This section covers in details the materials with their specifications that are used in this research and the methodology for synthesizing both single and composite catalysts. Moreover, the characterization aimed at increasing surface area and obtaining mesoporous particles are also thoroughly deliberated. The design of the photoreactor and the photocatalytic CO_2 reduction over the novel g-C_3N_4-RGO-NH_2-MIL-125(Ti) and NH_2-MIL-125(Ti)-GO-TiO_2 NTs ternary nanocatalysts are explained. Analysis of the operating parameters to get the highest solar fuel yield rates are also part of this chapter. Finally the equations that are used for calculating the yield rates, selectivity and quantum yields are discussed at the end of this chapter. Figure 3.1 illustrates the main steps of the experimental work.
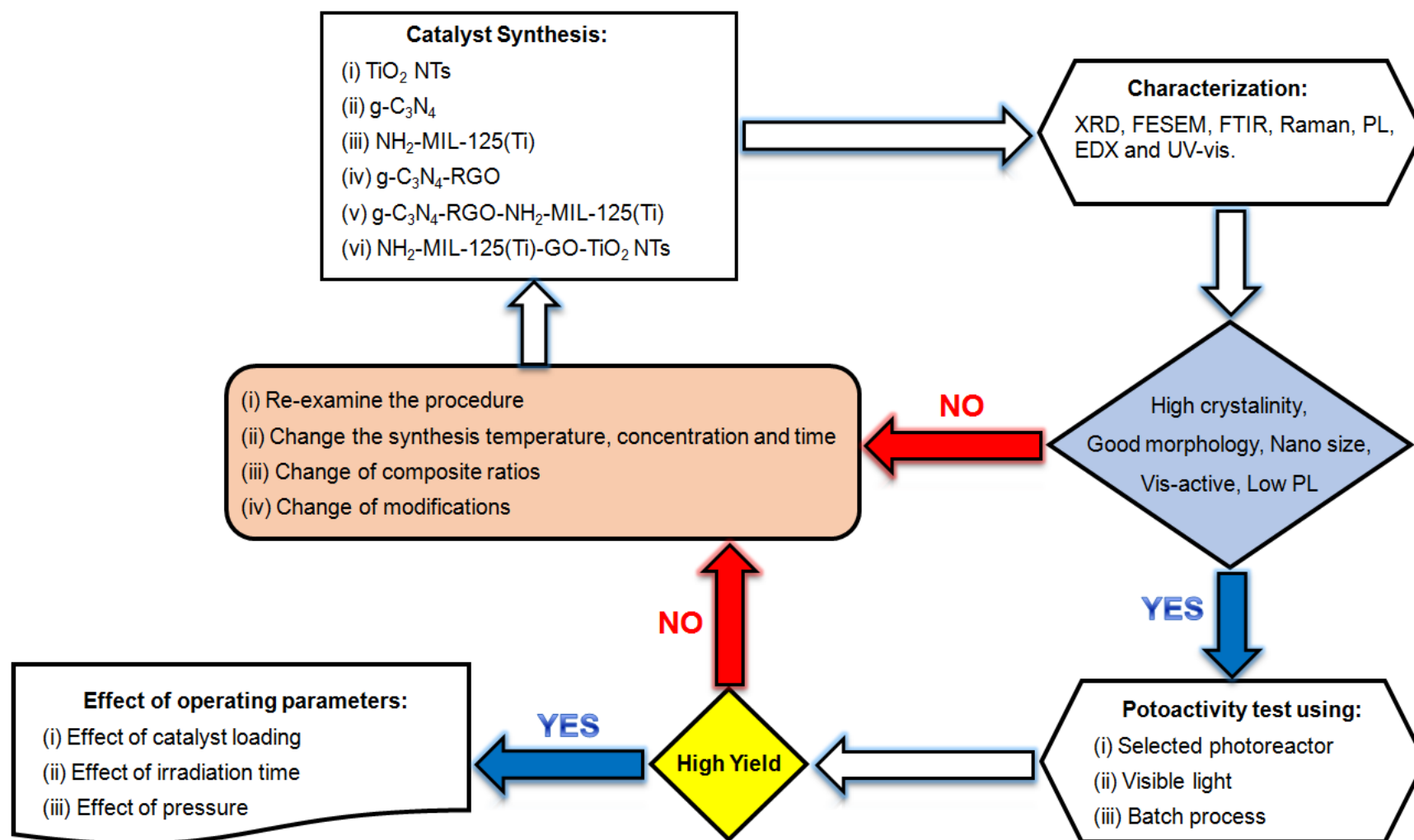
Figure 3.1　　Flow chart of general research methodology.

3.2   Materials of Research

All materials and chemicals for the preparation of catalysts were of analytical grade and were used as received without any further purification. Table 3.1 summarizes all these materials along with their specifications and supplying sources.

Table 3.1   Type, characteristics and source of materials used for photocatalysts synthesis.

Material Type	Characteristics	Source	Photocatalyst
Titanium metal sheet Ti	MW: 47.87 g/mol purity: 99.7%	Sigma-Aldrich	TNTs
Platinum metal foil Pt	MW: 195.08 g/mol purity: 99.9%	Sigma-Aldrich	TNTs
Ethylene Glycol $C_2H_6O_2$	MW: 62.07 g/mol purity: 99.0%	Sigma-Aldrich	TNTs
Ammonium Fluoride NH_4F	MW: 37.04 g/mol purity: 98.0%	Sigma-Aldrich	TNTs
Water H_2O	MW: 18.02 g/mol Deionized (DI)	Lab DI Plant	TNTs RGO
2-propanol C_3H_8O	MW: 60.1 g/mol purity: 99.9%	Sigma-Aldrich	TNTs
Methanol CH_3OH	MW: 32.04 g/mol purity: 99.8%	Sigma-Aldrich	MOF RGO
Melamine $C_3H_6N_6$	MW: 126.12 g/mol purity: 99 %	Sigma-Aldrich	g-C_3N_4
Titanium Isopropoxide $C_{12}H_{28}O_4Ti$	MW: 284.22 g/mol purity: 99.9%	Sigma-Aldrich	MOF
2-AminoTerephthalic Acid (H_2ATA)	MW: 181.15 g/mol purity: 99%	Sigma-Aldrich	MOF
DMF C_3H_7NO	MW: 73.09 g/mol purity: 99.8%	Sigma-Aldrich	MOF
Graphene Oxide $C_xO_yH_z$	MW: —— purity: 99%	CREG Lab	RGO

3.3 Catalyst Synthesis

Two separate ternary nanocomposite photocatalysts were investigated and studied. The first composite consists of TiO_2 nanotube arrays, graphene oxide and the amine-functionalized MIL-125(Ti) MOF while the second composite contains graphic carbon nitrides (g-C_3N_4), reduced graphene oxide and NH_2-MIL-125(Ti). Both TiO_2 NTs and g-C_3N_4 are used as the main incorporation platforms to increase the production of solar fuels. Graphene oxide can efficiently facilitate electrons transport and limit the charge recombination rate in both semiconductors (TiO_2 and g-C_3N_4). GO can also increase the ability of these semiconductors to boost visible light absorption. The NH_2-MIL-125(Ti) MOF is used to increase both surface area and the CO_2 gas adsorption. The functionalization of MOF can also increase visible light harvesting. The g-C_3N_4 was prepared by the calcination of melamine while the TiO_2 nanotube arrays were synthesized using electrochemical anodization process. GO was not prepared; it was used as a previously synthesized powder through a modified Tour's method. However, the pure GO powder was reduced to RGO through a solvothermal heating processes. NH_2-MIL-125(Ti) was synthesized using a solvothermal method. The whole synthesis steps of the different catalysts are summarized in Figure 3.2. The followings are the set of pure and composite photocatalysts that were prepared in this study.

(i) TiO_2 NTs

(ii) g-C_3N_4

(iii) NH_2-MIL-125(Ti)

(iv) g-C_3N_4-RGO

(v) g-C_3N_4-RGO-NH_2-MIL-125(Ti)

(vi) NH_2-MIL-125(Ti)-GO-TiO_2 NTs
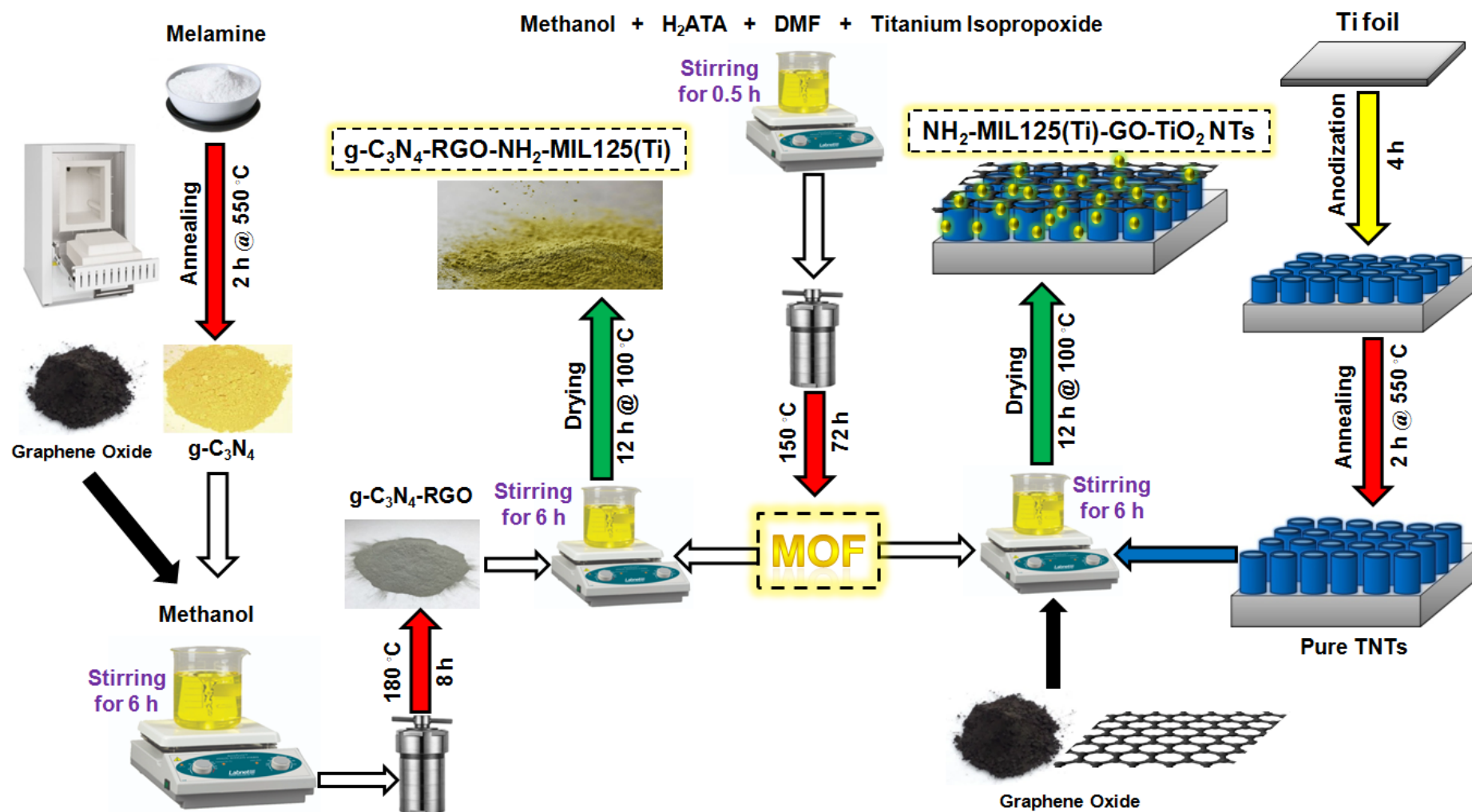
Figure 3.2   Schematic illustration for photocatalysts preparation procedure.

3.3.1 Preparation of TiO$_2$ Nanotube Arrays

Highly ordered TNTs were prepared using electrochemical anodization method. Firstly, the Ti metal foils (4 cm * 2.5 cm, 0.25 mm thickness) were polished, cleaned and sonicated in ethanol, methanol and deionized water respectively for 5 minutes each time to remove any residuals and then followed by drying at 100 °C. Secondly, the Ti foils were anodized in an electrolyte solution (100 mL of ethylene glycol (EG), 2 mL of DI water and 1.12 g of NH$_4$F) at room temperature for 4 hours by using a two-electrode system with a platinum sheet as a counter electrode (cathode) and a Ti foil as the working electrode (anode). The anodization process was conducted at a constant voltage of 30 volt supplied by a DC power source (HY3006D: 0-30V/0-5A). Finally, after rinsing with DI water and drying, the anodized Ti foils were annealed at 550 °C for 2 hours in a muffle furnace to obtain the TiO$_2$ nanotube arrays with high growth.

3.3.2 Preparation of g-C$_3$N$_4$

The graphitic carbon nitride photocatalyst (g-C$_3$N$_4$) was synthesized by directly heating of melamine. A certain amount (10 g) of the low-cost melamine powder was placed in a covered alumina crucible and then calcinated in a muffle furnace for 2 hours at 550 °C with a heating rate of 20 °C min^{-1} , then the sample was collected and crushed into fine powder after being left to cool down to room temperature.

3.3.3 Preparation of NH$_2$-MIL-125(Ti)

The NH$_2$-MIL-125(Ti) metal-organic framework was synthesized by a solvothermal method. In a typical synthesis, 6.6 mmole (1.0869 g) of 2-Amino terephthalic acid (H$_2$ATA) and 1.5 mmole (0.4263 g) of titanium isopropoxide wre dissolved in a solution of 18 mL DMF and 2 mL methanol. Then the mixture was transferred to a 50 mL Teflon-lined stainless-steel autoclave to be sealed and heated

in a muffle furnace at 150 °C for 72 hours. After the hydrothermal treatment, a yellow suspension was obtained to be cooled at room temperature, precipitated and washed several times with DMF and methanol, respectively to remove any residual molecules that can block the catalyst pores. Finally, the purified sample was dried at 80 °C for 12 hours to be activated and ready for the future use.

3.3.4   Preparation of g-C_3N_4-GO and g-C_3N_4-RGO Composites

After the successful synthesis of the g-C_3N_4 catalyst, different composites of g-C_3N_4-GO with different GO contents (0%, 0.25%, 0.5%, 1% and 2%) were prepared by mixing them in a methanol solution for 6 hours using a magnetic stirrer and then dried overnight at 100 °C. The g-C_3N_4-RGO composite was prepared by reducing the GO in the g-C_3N_4-GO into RGO through a hydrothermal treatment process, this was done by dissolving a certain amount of the g-C_3N_4-GO composite in 40 mL of methanol under vigorous magnetic stirring for 6 hours and then transferring the solution into a 50 mL Teflon-lined autoclave to be heated in a muffle furnace at 180 °C for 8 hours. Finally the g-C_3N_4-RGO composite was collected after being dried overnight at 100 °C.

3.3.5   Preparation of g-C_3N_4-RGO-NH_2-MIL-125(Ti)

After determining the best GO and RGO ratios in the g-C_3N_4 composites for photocatalytic CO_2 reduction, certain amounts of the optimized g-C_3N_4-RGO composite are mixed in methanol with different ratios (0%, 10%, 20% and 30%) of the functionalized MOF for more photocatalytic enhancements. After 6 hours of stirring, the solutions were dried at 100 °C for 12 hours.

3.3.6   Preparation of NH$_2$-MIL-125(Ti)-GO-TiO$_2$ NTs

The TiO$_2$ NTs composite was prepared by immersing the pure TNTs plates in 250 mL beaker containing separately prepared methanol solution of NH$_2$-MIL-125(Ti) and GO (1%) so that a total of 0.1 g of NH$_2$-MIL-125(Ti)-GO is dissolved in 50 mL methanol and then sonicated for 15 min and finally left to dry on the surface of the TNTs plates at 100 °C for 12 hours.

3.4   Characterization of Catalysts

Nanocatalyst characterizations are significantly helpful to understand the role of catalysts for particular applications and to enhance the rate of reaction in terms of yield rates and selectivity. The first-hand information about newly developed material such as particle structure pore morphology, mesoporosity, optical properties and structural characters are usually collected employing various analytical techniques. In the field of nanotechnology and hybrid materials developments, they have vital importance. In this perspective, the characterizations of newly synthesized photocatalysts were measured using different methods. Here in, the X-ray diffraction (XRD) was used to analyze the crystallinity and structure of the synthesized photocatalysts; this was conducted by the high-resolution Bruker Advance D8 diffractometer operated at voltage 40 kV, current of 40 mA, and under Cu Kα radiation source. Raman Spectrometer (Lab RAM HR Evolution, HORIBA) was employed to determine the Photo-luminance (PL) and Raman spectra of the samples with emitted lasers of 325 and 532, respectively. The surface morphology and microstructures were examined by using Field Emission Scanning Electron Microscope (FE-SEM, Hitachi SU8020). The elemental state of the composites was analyzed by Energy Dispersive X-ray (EDX) measurements. FTIR technology was also used for identifying the molecular structure, chemical bonds and functional groups that can exist in the different types of samples and this analysis was performed using a PerkinElmer spectrometer (model Shimadzu IRTracer 100). Finally, the Ultraviolet–visible (UV–Vis) diffuse reflectance spectra of the samples were obtained using a Perkin Elmer, LAMDA 365 spectrophotometer. All the

characterization methods are summarized in Table 3.2 with their relevant applications.

Table 3.2   Summary of catalyst characterization methods and their applications.

Method	Application
X-ray Diffraction Spectroscopy (XRD)	To characterize the general crystallinity, shape and structure of nanomaterials
Raman Spectroscopy	To identify the different molecules by providing the structural fingerprints after determining their vibrational modes
Photoluminescence Spectroscopy (PL)	To study the optoelectronic properties by determining the separation and transfer efficiency of the photogenerated charges
Field Emission Scanning Electron Microscopy (FESEM)	To characterize the surface morphology of nanomaterials
Energy Dispersive X-ray (EDX)	To identify the elemental and quantitative composition of the samples
Fourier Transform Infrared Spectroscopy (FTIR)	To identify the molecular structure, chemical bonds and functional groups
UV-Vis Diffuse Reflectance Spectroscopy (DRS)	To characterize photo response of the nanomaterials

3.5   Photocatalytic CO$_2$ Reduction over the MOF-composites

The photocatalytic CO$_2$ reduction was performed in a gas-phase fixed-bed photoreactor under visible light irradiation as shown in Figure 3.3. The stainless-steel chamber photoreactor with a total volume of 88 mL was equipped with a quartz window at the top surface for allowing the passing of light irradiations. A 35 W HID Xe lamp fixed with a reflector for concentrating light, was used as a source of visible light with a light intensity of (20 mW cm^{-2}). 100 mg of the g-C$_3$N$_4$-RGO-NH$_2$-MIL-125(Ti) powder catalyst was thoroughly dispersed at the bottom surface of the photoreactor chamber while the prepared TNTAs composite, coated with ~25 mg of RGO-NH$_2$-MIL-125(Ti) powder was placed on a metal support centered at the bottom of the reactor chamber and directly facing the lamp with a distance of about 6 cm. Pure compressed carbon dioxide gas (99.99%) with a constant flow rate of 20 mL min^{-1} was bubbled through water (at a temperature of 25 °C) so that the H$_2$O vapour is carried with the CO$_2$ gas into the photoreactor chamber, then it was purged in the whole photocatalytic system for 1 h before starting the experiment to remove any other trace gases. After that, the inlet and outlet valves were closed and the light source was switched on so that the CO$_2$ gas starts to be photocatalytically reduced, after a series of redox reactions, into CO and CH$_4$ gases. Finally, gas products were collected after each 1 h intervals using a special gas syringe and then analyzed by HP 6890, Gas Chromatograph equipped with two detectors; flame ionization detector (FID) and thermal conductivity detector (TCD) and also with a Carboxen 1010 PLOT capillary column.
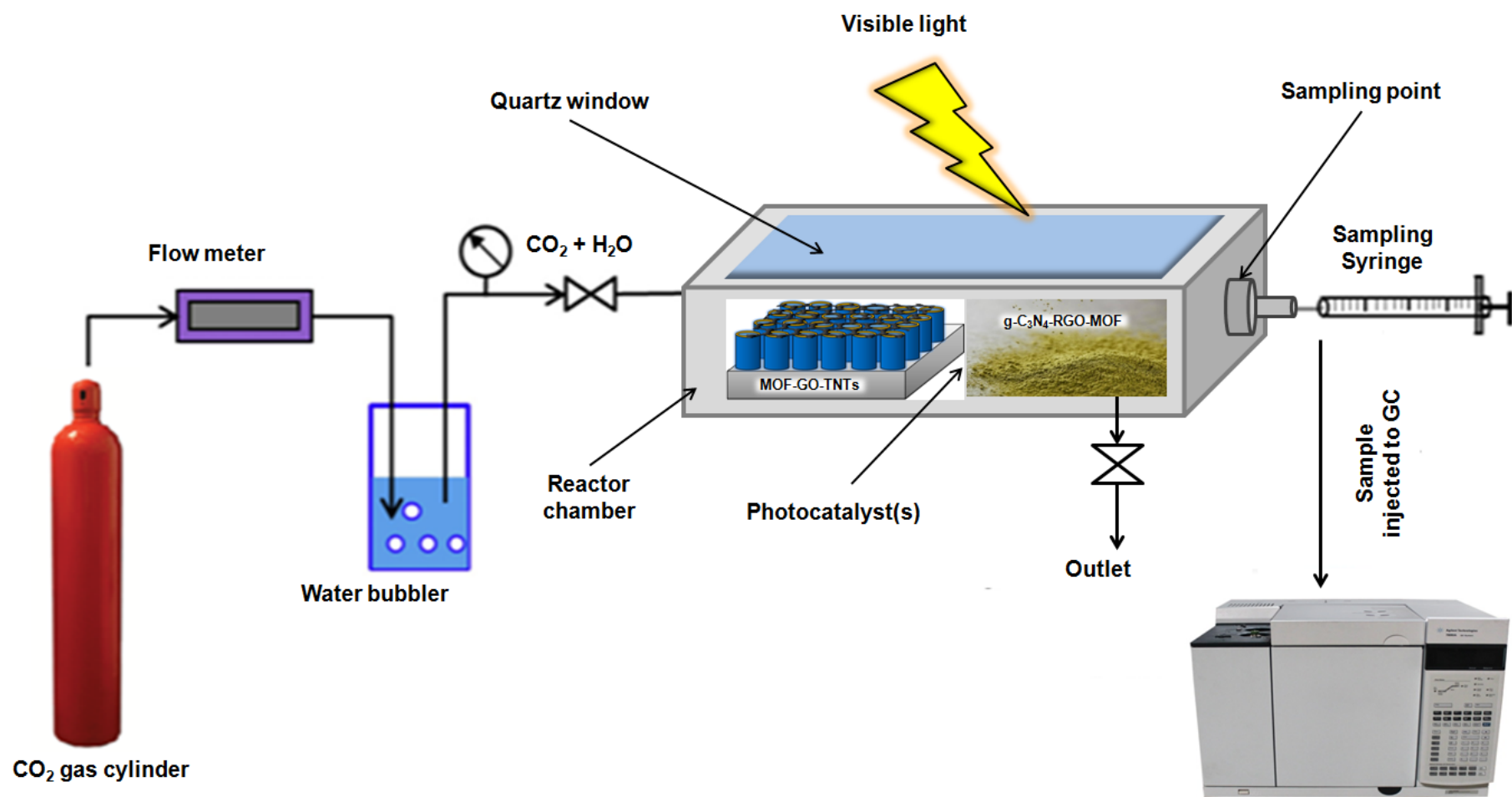
Figure 3.3   Photoreactor setup for photocatalytic CO_2 reduction over the MOF-composite photocatalysts

3.6   Study of Operating Parameters

Based on the initial evaluation of the system performance and results, the following stage was to optimize the photocatalytic system of both MOF-composite photocatalysts by manipulating the operating parameters. The different operating parameters that were tested in this research are listed below as follows:

(i)   The effect of g-C_3N_4-RGO-NH_2-MIL-125(Ti) powder catalyst loading on the photocatalytic production was investigated using different weights of 25, 50, 100 and 200 mg, this weight range of loadings was chosen since it represents the most suitable values according to the bottom area of the photoreactor chamber.

(ii)   The effect of pressure on the photocatalytic CO_2 reduction over the two ternary MOF-composites was also investigated in a batch system by applying different CO_2 gauge pressures (0.2, 0.4 and 0.8 bar) that are suitable with the photoreactor design to avoid any possible leakage during the photoreduction process.

(iii)   The effect of irradiation time (1, 2, 3 and 4 hours) on the production of CO and CH_4 was tested throughout all the conducted experiments.

(iv)   The long-term stability of both MOF-composites was investigated for three cycles in terms its continuous performance and photoactivity for producing the same products (CO and CH_4) with approximate values.

The main criteria for evaluating the performance of the MOF-composite photocatalysts and the effect of parameters changes are based on the efficiency of the photocatalytic CO_2 reduction and the solar gas yields (CO and CH_4). The data collected data were helpful to determine the suitable modified catalysts for visible light photocatalytic activity.

3.7   Products Sampling and Analysis

The gas samples of the solar products were collected from the sampling point in the stainless-steel photoreactor using a special gas syringe after different irradiation time intervals. Then the gas samples were injected and analyzed by the HP 6890 Gas Chromatograph to calculate the CO and CH_4 gas yield rates, quantum yields and products selectivity using calculations explained in the next section.

3.8   Calculations of Yield Rates, Selectivity and Quantum Yield Rates

The yield rates of the solar gas products (CO and CH_4) for the g-C_3N_4-RGO-NH_2-MIL-125(Ti) photocatalyst were calculated by using the Equation (3.1) while Equation (3.2) was used for the NH_2-MIL-125(Ti)-GO-TNTs photocatalyst.

$$\text{Product yield rate} \, (\mu mole \, \text{g}^{-1} \, \text{h}^{-1}) = \frac{\text{No. of moles produced} \, (\mu mole)}{\text{wt. of catalyst (g)} \times \text{time (h)}} \qquad (3.1)$$

$$\text{Product yield rate} \, (\mu mole \, \text{m}^{-2} \, \text{h}^{-1}) = \frac{\text{No. of moles produced} \, (\mu mole)}{\text{catalyst area (m}^{-2}) \times \text{time (h)}} \qquad (3.2)$$

The selectivity of the products (CO and CH_4) was also calculated using Equation (3.3) as following:-

$$\text{Product selectivity (\%)} = \frac{\text{No. of the product moles} \, (\mu mole)}{\text{No. of all products moles} \, (\mu mole)} \times 100 \qquad (3.3)$$

The performance analysis measured in terms of energy consumption was also adopted by calculating the quantum yields (QY). Generally, the quantum yield in heterogeneous photocatalysis can be defined as the ratio of reacted number of electrons to the number of incident photons at that time period as presented in Equation (3.4). However, when one electron-hole pair is produced by each photon,

the quantum yields can be expressed as the ratio of the production rate of products (μmol/s) to the photonic flux (μmol/s) as demonstrated in Equation (3.5). Therefore, the quantum yields for the CO and CH_4 production during the photocatalytic CO_2 reduction were calculated using Equations (3.6) and (3.7).

$$QY\ (\%) = \frac{\text{Number of reacted electrons}}{\text{Number of incedent photons}} \times 100 \tag{3.4}$$

$$QY\ (\%) = \frac{n \ \times \ \text{production rate} \ (\mu\text{mole/s})}{\text{Flux rate} \ (\mu\text{mole/s})} \times 100 \tag{3.5}$$

$$CH_4 \ QY\ (\%) = \frac{8 \times [CH_4]}{\dfrac{I \ \times \ \lambda}{h \ \times \ c} \ \times \ \dfrac{1}{N_A} \ \times \ A} \times 100 \tag{3.6}$$

$$CO\ QY\ (\%) = \frac{2 \times [CO]}{\dfrac{I \ \times \ \lambda}{h \ \times \ c} \ \times \ \dfrac{1}{N_A} \ \times \ A} \times 100 \tag{3.7}$$

where 8 and 2 are the numbers of consumed electrons for the formation of CH_4 and CO respectively, $[CH_4]$ and $[CO]$ represent the production rates (μmol s^{-1}) during the photoreaction, I is the light intensity of the lamp (W m^{-2}), λ is the wavelength of light (m), h is the Planck's constant (J.s), c is the speed of light (m s^{-1}), N_A is the number of Avogadro's (μmole^{-1}) and A is the irradiated area (m^2).

CHAPTER 4

RESULTS AND DISSCUSSION

4.1   Introduction

In this chapter, all the synthesized photocatalysts were characterized to study their chemical, physical, electronic and optical properties before conducting the experiments. The two MOF-composites were characterized using several physicochemical methods including XRD, Raman spectroscopy, FESEM, EDX mapping, FTIR, PL spectroscopy and UV-Vis DRS. Then the photocatalytic efficiency and the solar fuels production rates over the g-C_3N_4-RGO-NH_2-MIL-125(Ti) and NH_2-MIL-125(Ti)-GO-TNTs composites were evaluated. The products selectivity and the apparent quantum yields (AQY) were also calculated. Moreover, the effect of the operating parameters such as irradiation time, catalyst loading and CO_2 pressure were analyzed. The catalyst life-time and its photocatalytic performance after 3 cycles were investigated. Finally, the reaction mechanisms for both MOF-composites were proposed and explained in details.

4.2   Characterizations of g-C₃N₄-RGO-NH₂-MIL-125(Ti) Composite

4.2.1   X-ray Diffraction Analysis

The X-ray diffraction analysis was used to confirm the existence of all catalyst materials in the ternary g-C$_3$N$_4$-RGO-NH$_2$-MIL-125(Ti) nanocomposite. As depicted in Figure 4.1 (a), the prominent MOF diffraction peaks at 2θ: 6.8°, 9.5°, 11.5°, 16.5° and 17.9° corresponding to the (101), (200), (211), (222) and (312) planes [297-300], respectively, were shown in both patterns of pure MOF and MOF-composite samples indicating that the NH$_2$-MIL-125(Ti) MOF has been successfully synthesized. These results were also in a good agreement with previous reported studies [301-303]. For the g-C$_3$N$_4$, one of its characteristic peaks appeared at 2θ: 13° which corresponds to the (100) diffraction plane that reveals the inter-layer structural packing of the graphitic carbon nitride aromatic system, while the strong peak centered at 2θ: 27.5° matches the plane (002) (JCPDS card No. 87-1526) [304], known as the characteristic interplanar stacking peak with a distance of 0.326 nm between layers [305, 306]. The diffractogram of pure GO displayed a characteristic peak of interlayer spacing at 2θ: 9.9°, which is indexed to (001) plane of GO [307, 308]. However, in reduced GO, this peak disappeared, suggesting the successful conversion of GO to reduced GO in which a new broad peak at 2θ: 23.5° in addition to another small peak at 2θ: 42.8° corresponding to (002) and (111) RGO diffraction planes, respectively, were appeared [309-311]. None of these peaks appeared clearly in g-C$_3$N$_4$-GO and g-C$_3$N$_4$-RGO composites, possibly due to the low content (1%) of GO and RGO. Similarly, the characteristic RGO peaks did not appear in the XRD pattern of the ternary g-C$_3$N$_4$-RGO-NH$_2$-MIL-125(Ti) composite, which is also due to the same reasons of very low content of RGO compared to other catalysts. However, the presence of RGO in the ternary composite was determined by other powerful techniques as discussed in the next sections.
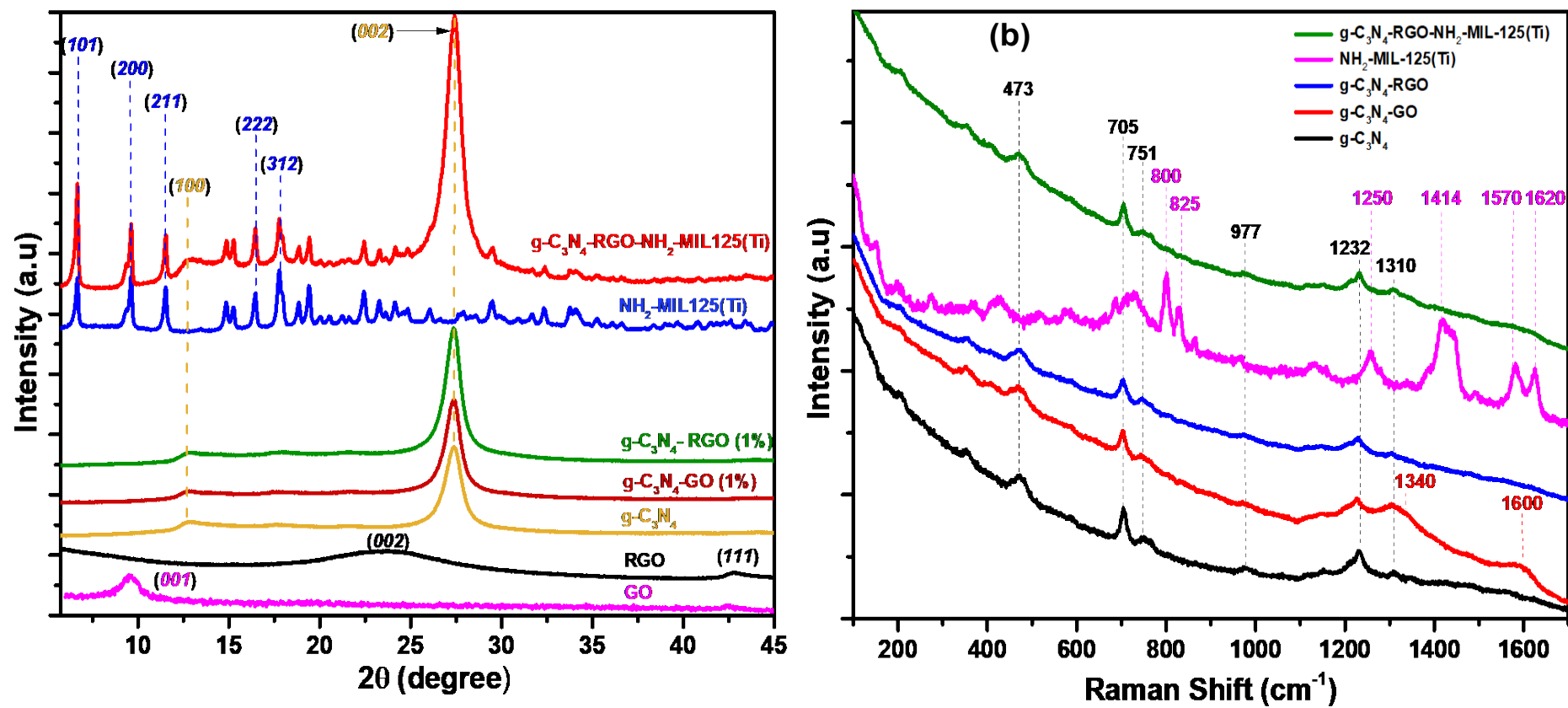
Figure 4.1   (a) XRD patterns of GO, RGO, g-C$_3$N$_4$, g-C$_3$N$_4$-GO, g-C$_3$N$_4$-RGO, NH$_2$-MIL-125(Ti) and g-C$_3$N$_4$-RGO-NH$_2$-MIL-125(Ti) and (b) Raman spectra of g-C$_3$N$_4$, g-C$_3$N$_4$-RGO, NH$_2$-MIL-125(Ti) and g-C$_3$N$_4$-RGO-NH$_2$-MIL-125(Ti).

4.2.2 Raman Analysis

The prepared samples were further analyzed by Raman spectroscopy. As shown in Figure 4.1 (b), several peaks were detected on the NH_2-MIL-125(Ti) MOF spectrum, it displayed two intense close peaks at 800 and 825 cm^{-1} followed by two other peaks at 1250 and 1414 cm^{-1}, which are related to the bending and symmetric stretching of the Ti-O framework [312]. It also exhibited peaks at 1570 and 1620 cm^{-1} corresponding to the C−C and N−H bond bending vibrations of the organic linker [313]. These results were similar to the previous reports [314, 315], which confirms the successful fabrication of NH_2-MIL-125(Ti) MOF. However, these peaks did not show clearly on the spectrum of g-C_3N_4-RGO-NH_2-MIL-125(Ti) composite.

The pure g-C_3N_4 displayed several characteristic peaks of the C-N extended network at 473, 705, 751,977, 1232 and 1310 cm^{-1}, which are in consistency with those obtained from the pristine g-C_3N_4 in literature [316, 317]. GO is known for its two prominent peaks of carbon networking structures, the first one is at around 1340 cm^{-1}, known as G-band, while the second corresponds to the typical G-band at around 1600 cm^{-1} [318, 319]. However, the broad peak ranging from 1270 to 1350 cm^{-1} in the g-C_3N_4-GO spectrum indicates the successful combination of both materials in the composite by overlapping their two peaks (1310 and 1340 cm^{-1}). The Raman spectrum g-C_3N_4-GO also shows clearly the second characteristic peak of GO at 1600 cm^{-1}. On the other hand, the GO peaks did not show in both g-C_3N_4-RGO and g-C_3N_4-RGO-NH_2-MIL-125(Ti) composites confirming the reduction of GO to RGO. However, the first peak shifted to the position of the g-C_3N_4 peak (1310 cm^{-1}), while the second shifted to 1560 cm^{-1} in the ternary composite.

4.2.3 Field Emission Scanning Electron Microscopy (FESEM)

The morphologies of g-C_3N_4, NH_2-MIL-125(Ti), GO and g-C_3N_4-RGO-NH_2-MIL-125(Ti) catalysts were characterized by Field Emission Scanning Electron Microscopy (FESEM) as shown in Figure 4.2. The FESEM image of pure graphitic carbon nitrides in Figure 4.2 (a) shows clearly the typical layered stacking structure of g-C_3N_4 folded nanosheets. As shown in Figure 4.2 (b), the NH_2-MIL-125(Ti) MOF displayed uniform disk-like particles with a diameter ranging from of 50 to 100 nm which is considered as a good particle size compared to previous observations of 200 and 600 nm [320, 321]. The small particle size has a great impact on increasing the surface area and hence, the reaction rate. However, a large corrugated GO sheet can be clearly seen in Figure 4.2 (c). The g-C_3N_4-RGO-NH_2-MIL-125(Ti) composite displayed a good catalyst-mixing morphology, although the NH_2-MIL-125(Ti) content was only 20% wt. %, Figure 4.2 (d-e) shows a large amount of MOF compared to g-C_3N_4-RGO, confirming the characteristic feature of MOFs represented by the huge surface area of the NH_2-MIL-125(Ti) MOF.

4.2.4 Energy Dispersive X-ray (EDX) Analysis

The elemental identification and quantitative analysis of the prepared g-C_3N_4-RGO-NH_2-MIL-125(Ti) was conducted using Energy Dispersive X-ray technique. The EDX spectrum was performed over different spots of the ternary composite to ensure that even and equal dispersion of g-C_3N_4, RGO and NH_2-MIL-125(Ti) is obtained. However, the EDX mapping analysis confirmed the presence of Ti, O, C, and N, which are considered as the main elements of the ternary nanocomposite. The elemental atomic ratios were found to be 26.2 %, 30.8 %, 38.3 % and 4.7 %, respectively as illustrated in Figure 4.3 (a)-(f). The EDX also revealed the good mixing and dispersion between the three composites. Furthermore, the absence of any other elements in the g-C_3N_4-RGO-NH_2-MIL-125(Ti) indicated the high purity of the synthesized nanocomposite.
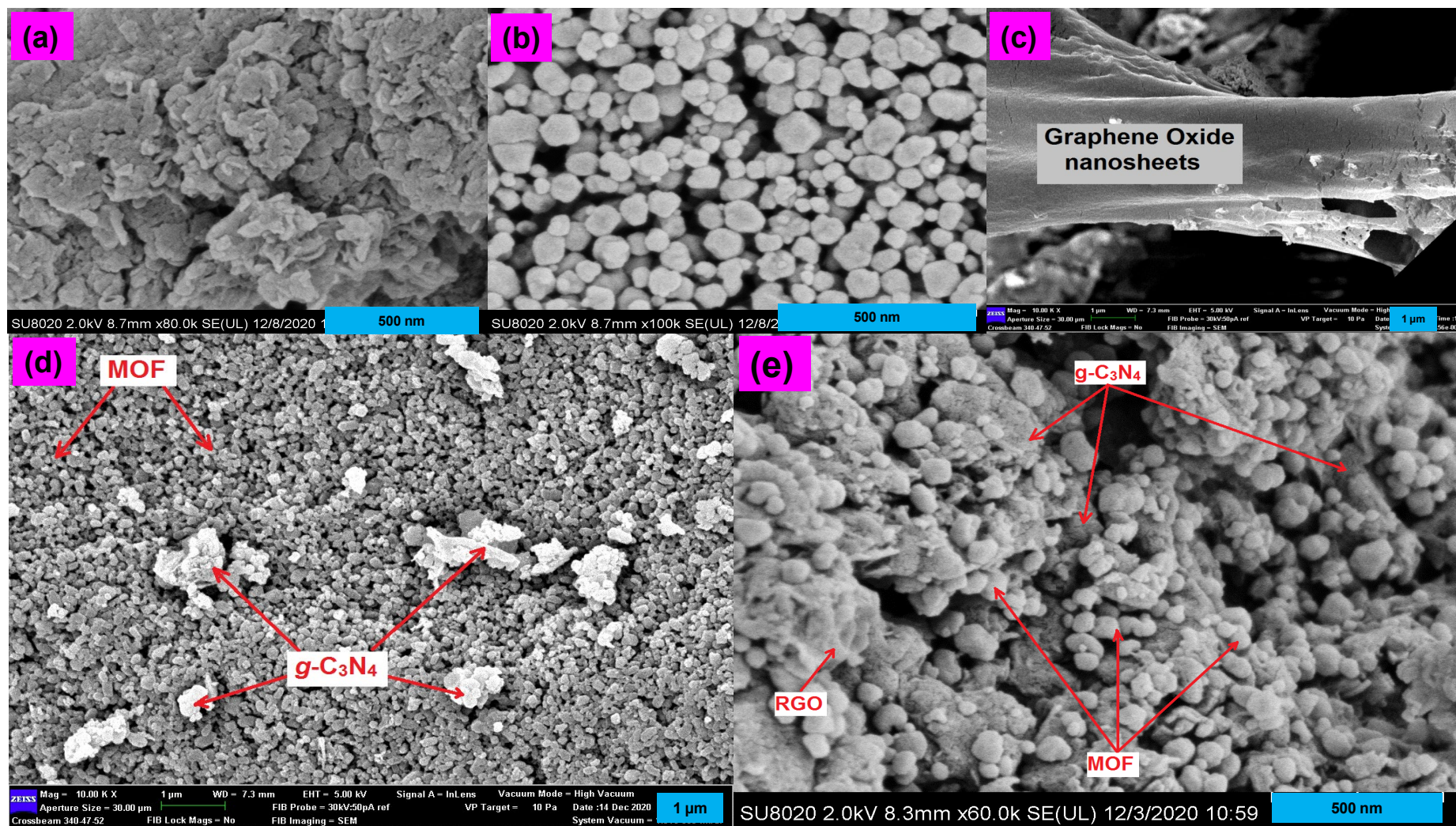
Figure 4.2   FESEM images of (a) Pure g-C$_3$N$_4$, (b) Pure NH$_2$-MIL-125(Ti), (c) Pure GO, (d-e) g-C$_3$N$_4$-RGO-NH$_2$-MIL-125(Ti).
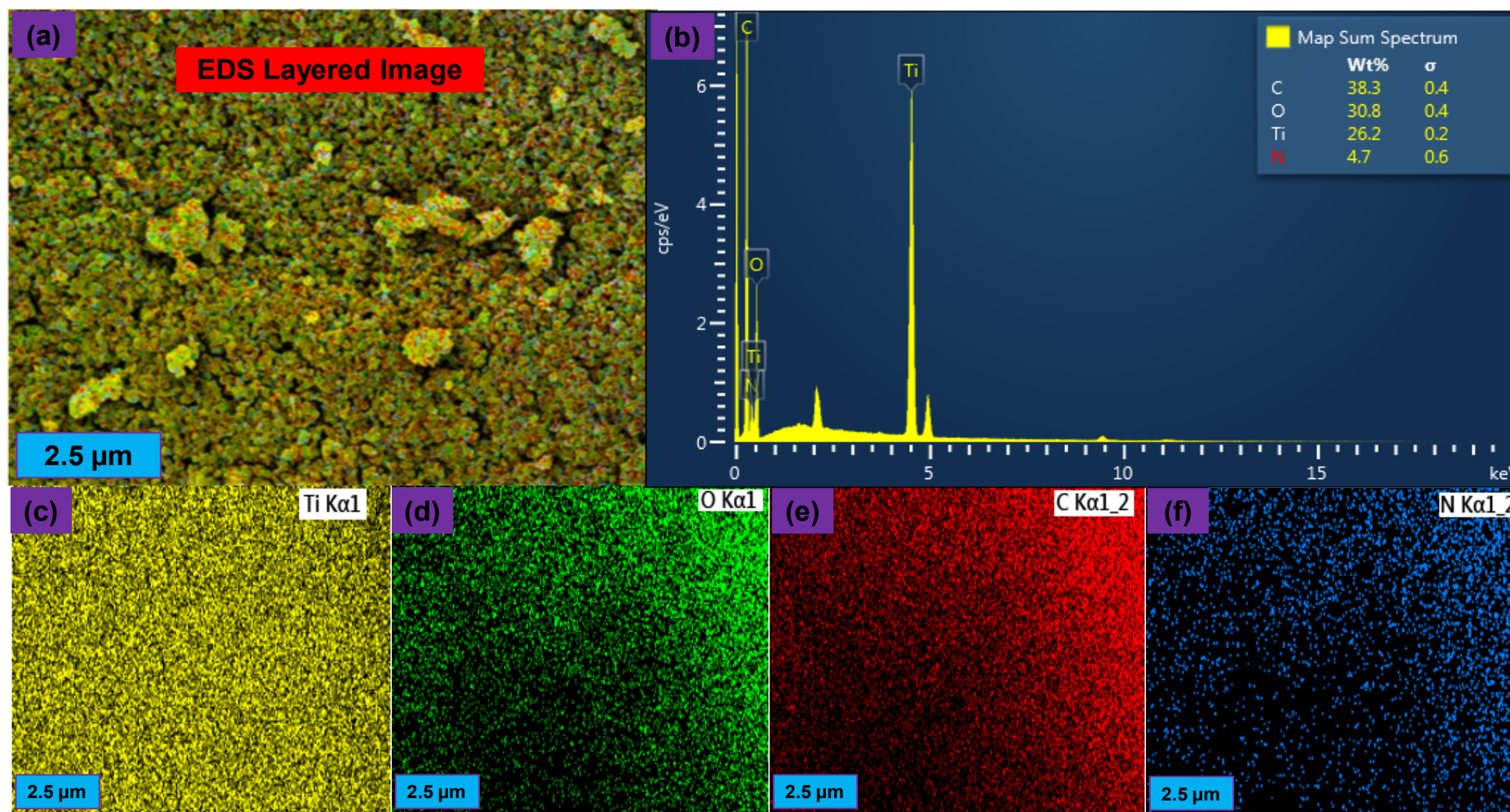
Figure 4.3   EDX analysis of g-C₃N₄-RGO-NH₂-MIL-125(Ti): (a) Layered image, (b) EDX Plot with elemental composition, (c-f) mapping distribution of Ti, O₂, C and N₂ respectively.

4.2.5   Fourier Transform Infrared (FTIR) Analysis

Fourier Transform Infrared Spectroscopy (FT-IR) is a widely used technique which provides valuable information about the molecular structure, chemical bonds and functional groups that can exist in different types of specimens. The analysis was performed using a PerkinElmer spectrometer (model Shimadzu IRTracer 100). As illustrated in Figure 4.4, a spectroscopy range of mid infrared (MIR) (3500 to 400 cm-1) was used since most of the expected compounds lies in this molecular vibration range.

The g-C_3N_4 spectrum shows strong peaks at 1240, 1320, 1409, 1554, and 1639 cm^{-1} considering that this region (1200−1650 cm^{-1}) is related to the typical stretching modes of C–N heterocycles [322]. However, the peak at 808 cm^{-1} is ascribed to the triazine; one of the nitrogen-containing heterocycles in g-C_3N_4, while the broadened peak centered in the region of 3000−3400 cm^{-1} is the result of the typical stretching vibrations of =NH and –NH_2 functional groups [323, 324]. Similar to XRD analysis, both g-C_3N_4-GO and g-C_3N_4-RGO composites displayed almost similar FTIR spectra to pure g-C_3N_4 due to low contents of GO and RGO (1%). This also reveals that GO and RGO had little effect on the network of g-C_3N_4 that was well-retained.

The FTIR spectra of the NH_2-MIL-125(Ti) MOF exhibited two small peaks at 3442 and 3355 cm^{-1} which are attributed to the stretching vibration of -NH brought by the organic linker [246, 325] while the bands at 1380-1661 cm^{-1} and 1434 cm^{-1} are ascribed to the symmetrical stretching vibration of -C=O and -OH groups. The bands in the range between 425 and 770 cm^{-1} belong to the O-Ti-O vibrations [303]. The ternary composite showed similar peaks to single catalysts with only one new shifted peak of the (O-Ti-O) vibrations at 454 cm^{-1}.
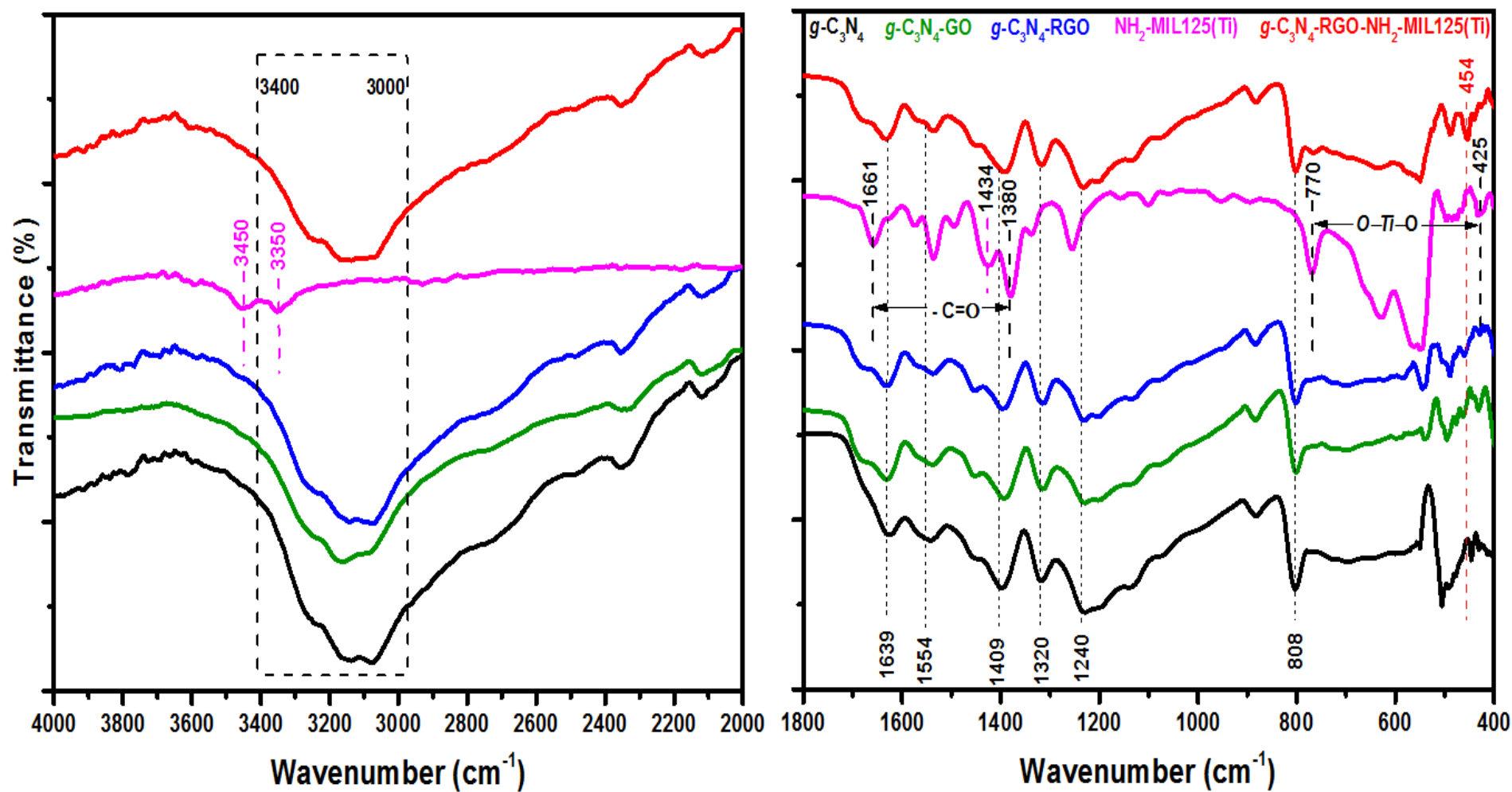
Figure 4.4 FTIR analysis of g-C₃N₄, g-C₃N₄-GO (1%), g-C₃N₄-RGO (1%), NH₂-MIL-125(Ti) and g-C₃N₄-RGO-NH₂-MIL-125(Ti) samples.

4.2.6 UV-Vis Diffuse Reflectance Spectroscopy (UV-Vis DRS)

The optical characteristics of pristine g-C$_3$N$_4$, g-C$_3$N$_4$-GO, g-C$_3$N$_4$-RGO, pure NH$_2$-MIL-125(Ti) and g-C$_3$N$_4$-RGO-NH$_2$-MIL-125(Ti) were investigated by UV-vis DRS as shown in Figure 4.5 (a). The bare MOF showed an intense absorption peak in the visible light range confirming its role in improving the utilization of solar energy. This high absorption ability is mainly attributed to the amino functionalization in which the H$_2$ATA linker influences the O to Ti charge transfer in the Ti-O clusters [73]. The g-C$_3$N$_4$, g-C$_3$N$_4$-GO and g-C$_3$N$_4$-RGO catalysts exhibited different absorptions peaks in which the reducing of GO to RGO in the g-C$_3$N$_4$-GO composite slightly increased the absorption of light. Moreover, the addition of MOF to the g-C$_3$N$_4$-RGO composite clearly enhanced the light absorbance under visible light irradiations as shown in the g-C$_3$N$_4$-RGO-NH$_2$-MIL-125(Ti) spectrum.

The band gap energies for the g-C$_3$N$_4$, g-C$_3$N$_4$-GO, g-C$_3$N$_4$-RGO, pure NH$_2$-MIL-125(Ti) and g-C$_3$N$_4$-RGO-NH$_2$-MIL-125(Ti) composites were also calculated using Tauc plot according to the Kubelka−Munk (K−M) function by plotting of the $(\alpha\ hv)^2$ values versus the photon energy (hv) values and then extrapolating the maximum slope to the x axis as shown in Figure 4.5 (b). Band-gap energies of 2.86, 2.78, 2.76, 2.5 and 2.7 eV were obtained for the tested composite samples, respectively. The slight shift in the band-gap energy towards higher wavelength was obviously due to the presence of MOF in the composite sample. Furthermore, the bandgap energy of g-C$_3$N$_4$ was used to calculate the valance and conduction band positions by using the well-known empirical equations demonstrated in Equations (4.1) and (4.2) to understand the direction of charge transfer in the ternary composite.

$$E_{CB} = \chi - E^{e} - \frac{1}{2} E_{bg} \tag{4.1}$$

$$E_{VB} = E_{CB} + E_{bg} \tag{4.2}$$

where E_{CB} is the conduction band edge, χ is the geometric mean of Mullikan electronegativity of a semiconductor (for g-C$_3$N$_4$ = 4.73 eV), E^e is the energy of free

electron on the hydrogen scale (= 4.5 eV), E_{bg} is the band gap energy (=2.86 eV) and E_{VB} is the valance band edge. By using Equation (4.1), the CB value for g-C$_3$N$_4$ was calculated to be -1.2 eV while the VB value of 1.66 eV was obtained by using Equation (4.2). Similar VB/CB results of -1.22 and 1.67 for g-C$_3$N$_4$ were reported by B. Tahir and co-workers [326] which are in a good agreement with the current results. However, according to literature, the NH$_2$-MIL-125(Ti) MOF has a narrow band gap of 2.5 eV, it is also known to have conduction and valance band positions of -0.4 and 2.1 eV, respectively. In this study, the same MOF band gap energies of was obtained and hence, the conduction and valance band positions are used according to the values reported in literature.
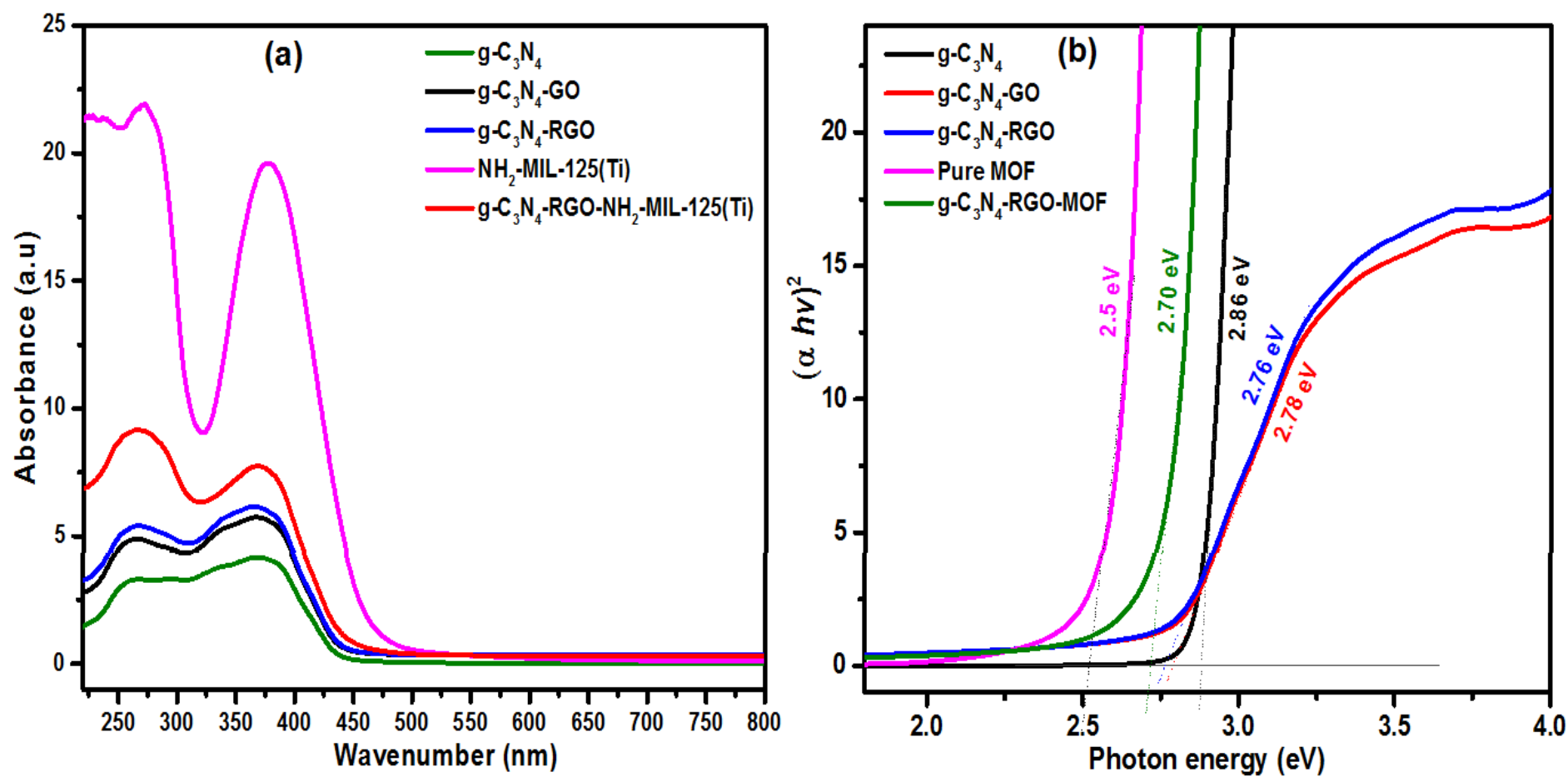
Figure 4.5 (a) The UV-Vis DRS spectra and (b) The Tauc plot calculations of g-C$_3$N$_4$, g-C$_3$N$_4$-GO, g-C$_3$N$_4$-RGO, pure NH$_2$-MIL-125(Ti) and g-C$_3$N$_4$-RGO-NH$_2$-MIL-125(Ti) samples.

4.2.7 Photoluminescence (PL) Spectroscopy Analysis

Photoluminescence (PL) analysis is generally used to determine the separation and transfer efficiency of the photogenerated charge carriers in which the recombination of photogenerated electron-hole pairs can release energy to form PL emission, and thus higher peaks are not favorable in terms of suppressing charge recombination rates, on the other hand, lower peak intensity is considered as an indication of higher charge separation efficiency and hence, higher photocatalytic activity. As shown in Figure 4.6, the PL spectrum of pure g-C$_3$N$_4$ exhibited the highest intensity peak due to its fast recombination rate of photogenerated charges. Clearly, the PL intensity of g-C$_3$N$_4$ was significantly decreased with the loading of GO and furthermore with the RGO which proves its great role as a mediator in limiting the charges recombination rate. However, the lowest excitation intensity of composites was observed after the addition of MOF in the g-C$_3$N$_4$-RGO-NH$_2$-MIL-125(Ti) composite. It is also worth mentioning that the pure MOF exhibited a very small PL spectrum; almost similar to conductors, confirming its role in reducing the high recombination rates.
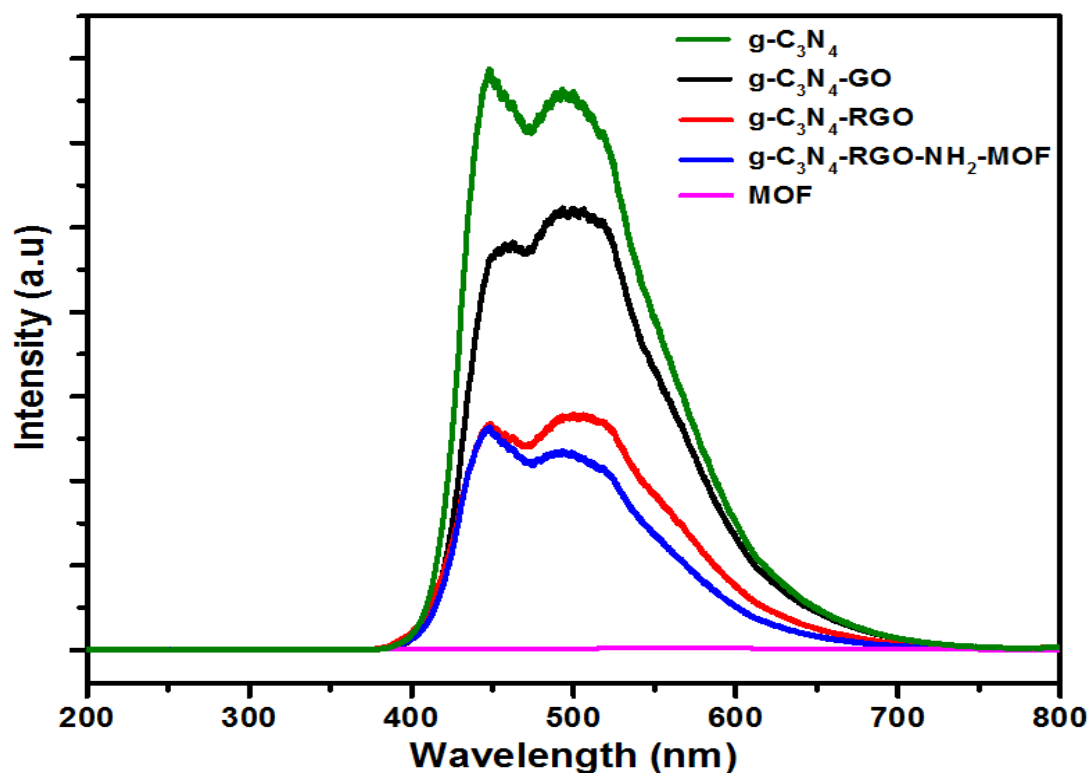
Figure 4.6   The PL spectra of the prepared samples.

4.3 Photocatalytic CO$_2$ Reduction over g-C$_3$N$_4$-RGO-NH$_2$-MIL-125(Ti)

Initially, a series of preliminary experiments were conducted for quality assurance to ensure that all of the products were generated only as a result of the photocatalysis process. Neither CO nor CH$_4$ were detected without using the light source. Furthermore, several experiments were performed using water vapour with N$_2$ gas instead of CO$_2$ and none of the products were detected even in the presence of the photocatalysts under light irradiations. This confirms that both CO and CH$_4$ were not obtained from the catalysts themselves or from any other sources, but they were formed as a result of reducing CO$_2$ during a photocatalysis process which utilized the solar light with the aid of photocatalysts. All experiments were repeated many times and the average results have been reported.

4.3.1 Effect of GO Loading on the Activity of Pure g-C$_3$N$_4$ Catalyst

Different GO amounts (0 wt. %, 0.25 wt. %, 0.5 wt. %, 1 wt. % and 2 wt. %) were mixed with the g-C$_3$N$_4$ catalyst and tested under visible light for determining the maximum composite efficiency that can be achieved for reducing CO$_2$. Clearly, the production of both CO and CH$_4$ gases was observed to be continuously increasing with the irradiation time by using all types of photocatalyst composites as shown in Figure 4.7 (a) and (b). However, the best efficiency was performed with the use of 1 wt. % GO, which produced CH$_4$ and CO gases with values of 25.6 μmol g^{-1} and 132.3 μmol g^{-1}, respectively, after 4 hours irradiation. These values are considered as the optimum values with a production enhancement of about 28% and 76% for CH$_4$ and CO, respectively, compared to pure g-C$_3$N$_4$. This photocatalytic enhancement in the g-C$_3$N$_4$-GO composites is attributed to many reasons; in fact, adding GO improved both the electrical and optical properties of the pure g-C$_3$N$_4$. Many other studies confirmed the role of adding GO in improving the catalytic activity of g-C$_3$N$_4$ [327-330]. However, by increasing the GO content more than 1 wt. %, the evolution of the products started to decline, this could be explained as a result of the shielding effect that significantly reduces the light irradiations striking the photocatalyst surface. The same photocatalytic trends were observed by Xiang and co-workers [331], but in photocatalytic hydrogen production. Li et al. [332] also

reported that adding GO exhibits an obvious influence on the photocatalytic activity of g-C$_3$N$_4$-GO composites for hydrogen production, however, the maximum production rate was achieved with the use of 0.5 wt. % GO.

Furthermore, the CO evolution rate was found to be always higher than that of CH$_4$ (4 to 5 times), this can be explained on the basis of energy band theory. Generally, in the CO$_2$ reduction process, the photo-excited electrons are consumed more efficiently only when the CB potential of a semiconductor is more negative than the reduction reaction potential of the desired CO$_2$ reduced product [107, 333]. Therefore, the modified catalyst has more feasibility in driving the CO$_2$ reduction process towards CO product, since the CO$_2$ to CO reduction reaction has lower reduction potential difference (CO$_2$ / CO = -0.53V) compared to CO$_2$ to CH$_4$ reduction reaction (CH$_4$ / CO = -0.24V) resulting in significant difference in the produced amounts of CO and CH$_4$ in the batch photoreactor system.

4.3.2 Effect of Reducing GO to RGO on the Activity of g-C$_3$N$_4$-GO Composite

Graphene oxide was further reduced to RGO after determining the best GO ratio (1 wt. %) with g-C$_3$N$_4$ and then compared to that of g-C$_3$N$_4$-GO. Compared to the normal GO composite, reduced GO composite exhibited better results with an enhancement of 17% and 7% for CO (from 132.3 to 154.7 μmole g^{-1}) and CH$_4$ (from 25.6 to 27.4 μmole g^{-1}), respectively after 4 hours irradiation as shown in Figure 4.7 (c) and (d). GO is known for its oxidized state which can be expressed as a huge number of oxygen functional groups, this high oxygen content in fact has a negative impact on the optical and conductive properties [334, 335], therefore, the removal of oxygen is essential for the recovery of the aromatic double bonds of carbon, however, the reduction processes do not repair GO to pure graphene in which at least some of these oxygen groups will still remain to form RGO. These reduction processes can be conducted by chemical, thermal or hydrothermal methods. GO in a g-C$_3$N$_4$-RGO composite was reduced by Ong and co-workers [336] through a chemical treatment method in which a certain amount of NaBH$_4$ was added to a water-based g-C$_3$N$_4$-GO suspension to reduce the GO to RGO, the composite (with

15 wt% RGO) was then tested in a continuous gas-phase system in which the CO_2 gas was photoreduced into CH_4 gas only (13.93 µmole g^{-1}) after 10 h irradiation.

In this study, the reduction process was conducted by a hydrothermal treatment process and the improvement of the photocatalytic efficiency in terms of optoelectronic properties by reducing GO to RGO was further proved in the characterization section in which the g-C_3N_4-RGO composite exhibited both higher absorbance of visible light and higher separation efficiency of electron-hole pairs compared to the g-C_3N_4-GO. The superiority of RGO-composites over GO-composites in terms of photocatalytic performance was observed and reported in many other studies [281, 337-340].
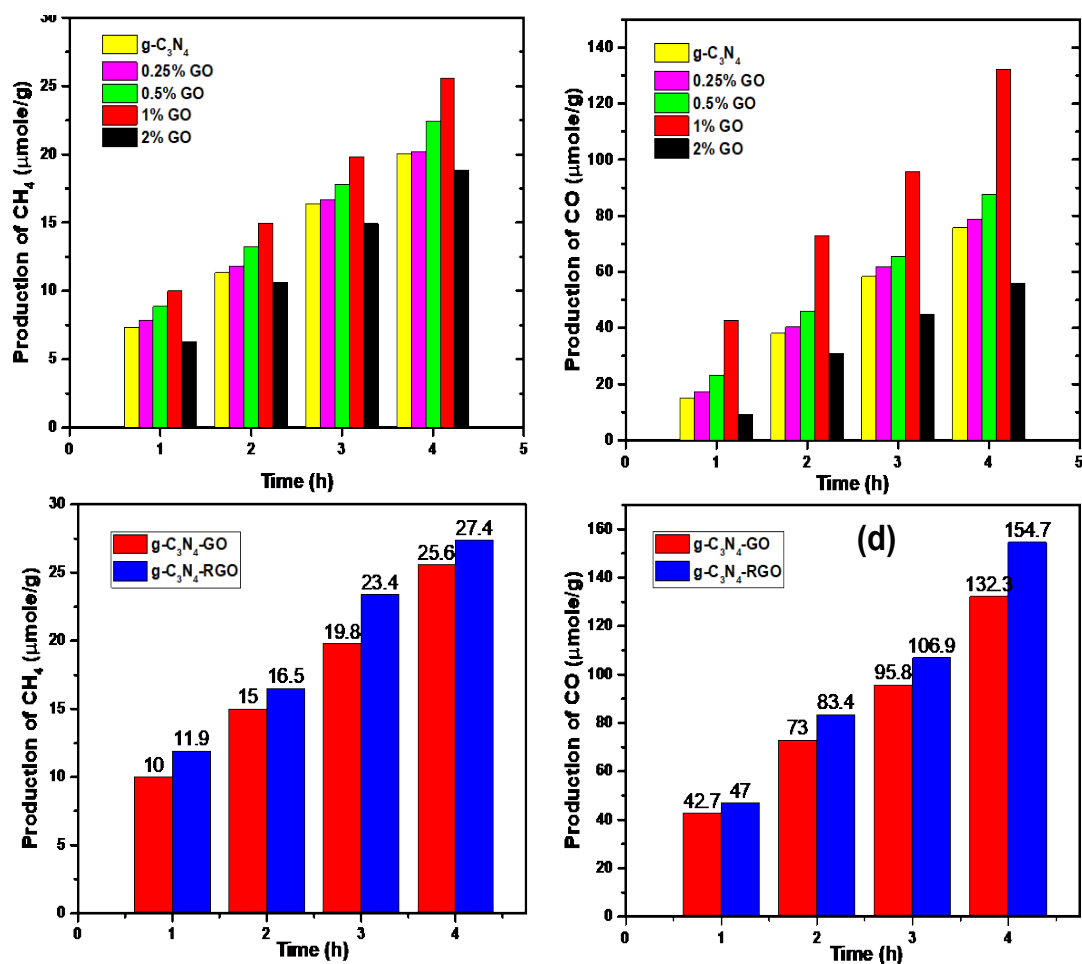
Figure 4.7 (a) and (b) The effect of GO addition on the photocatalytic CO_2 reduction performance of g-C_3N_4 (100 mg catalyst) for CH_4 and CO production, (c) and (d) The effect of reducing GO to RGO in the g-C_3N_4 composite of 1 wt.% GO for photocatalytic reduction of CO_2 to CH_4 and CO.

4.3.3 Effect of MOF Loading on the Activity of the g-C$_3$N$_4$-RGO

Pure NH$_2$-MIL-125(Ti) photocatalyst was tested under visible light for the photocatalytic reduction of CO$_2$ and eventually exhibited results of 144.9 and 8.91 μmol g^{-1} of CO and CH$_4$, respectively, after 4 hours irradiation. Then, the photocatalytic enhancement of g-C$_3$N$_4$-RGO was investigated by the addition of MOF. The maximum photocatalytic efficiency was obtained with the addition of 20 wt. % MOF as shown in Figure 4.8. The g-C$_3$N$_4$-RGO-MOF (20%) exhibited a CO production of 383.79 μmol g^{-1} compared to 154.73 μmol g^{-1} that of zero-MOF g-C$_3$N$_4$-RGO. However, the CH$_4$ production was found to be reducing from 27.4 to 13.8 μmol g^{-1}, this is mainly attributed to the high CO production selectivity of NH$_2$-MIL-125(Ti) compared to its selectivity towards CH$_4$. These results also confirm the successful fabrication of a Z-scheme heterojunction photocatalyst with enhanced photocatalytic activity of CO$_2$ reduction.

4.3.4 Effect of Photocatalyst Loading

The effect of g-C$_3$N$_4$-RGO-MOF (20%) loading for the photocatalytic CO$_2$ reduction using a fixed-bed gas reactor is presented in Figure 4.9. Different amounts of the photocatalyst (0.025, 0.05, 0.1 and 0.2 g) were loaded into the photoreactor chamber, the production rates of both products were found to be gradually increasing with catalyst loading, up to 0.1 g. The best production values of 13.8 and 383.79 μmol g^{-1} were observed for CH$_4$ and CO, respectively, after 4 h with 0.1 g catalyst loading. This can be explained on the basis of the active sites availability, in which increasing the catalyst loading provides more of these active sites for the reaction. However, further catalyst loading increase of 0.2 g shows decreasing in the results with lowest values of 6.02 μmol g^{-1} CH$_4$ and 98.47 μmol g^{-1} CO. This is attributed to limited light penetration caused by the accumulation of catalyst particles and the decreasing of the catalyst surface area which results in lower photocatalytic CO$_2$ reduction. This also reveals that the best ratio between the catalyst weight and the reactor surface area is 35.7 g for every square meter by considering the reactor area used in this study which was 0.0028 m^{-2}.
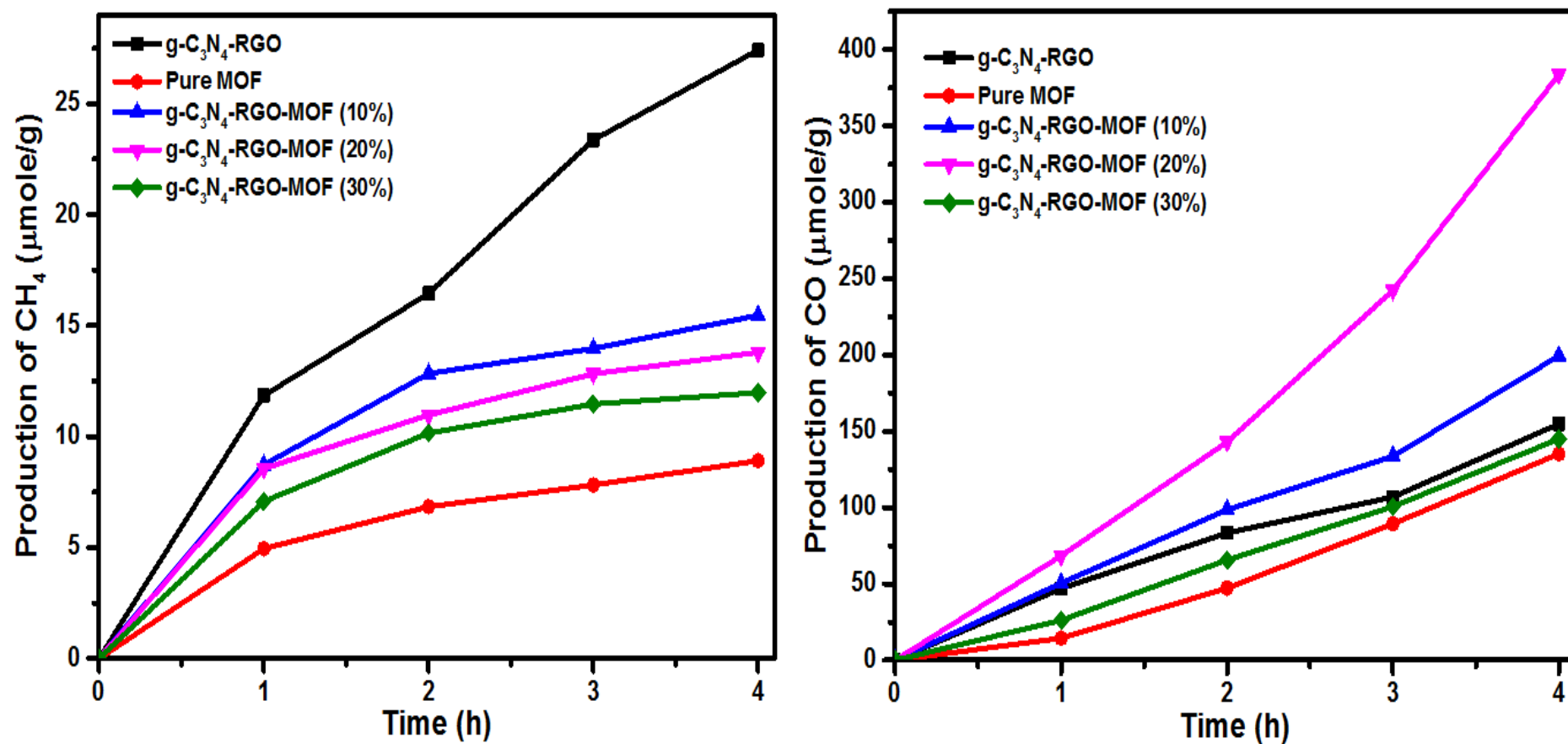
Figure 4.8   The amount of CO and CH$_4$ evolutions over g-C$_3$N$_4$-RGO, Pure MOF, g-C$_3$N$_4$-RGO-MOF (10%), g-C$_3$N$_4$-RGO-MOF (20%) and g-C$_3$N$_4$-RGO-MOF (30%).
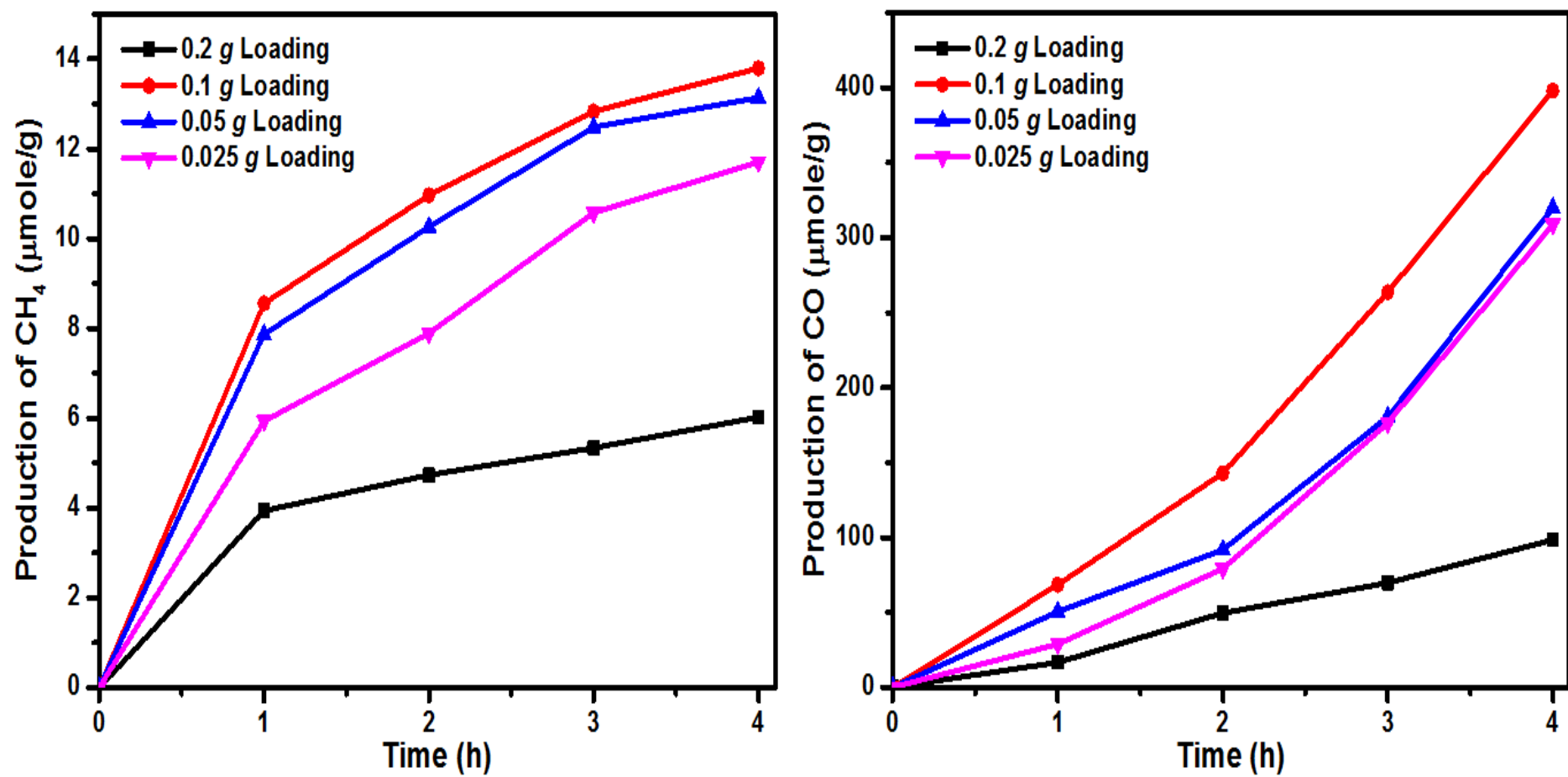
Figure 4.9   The effect of catalyst loading on the production of CH4 and CO.

4.3.5 Effect of Pressure

The effect of pressure on the photocatalytic CO_2 reduction over the g-C_3N_4-RGO-NH$_2$-MIL-125(Ti) ternary composite was also investigated by applying different pressures of CO_2 gas (0.2, 0.4 and 0.8 bar) in a batch system. As illustrated in Figure 4.10, it was observed that the production rates of both CO and CH_4 increased with the increase of pressure and reached up to 25.08 and 597.63 $\mu mol\ g^{-1}$, respectively at 0.8 bar. This is attributed to many reasons such as: (i) increasing the pressure increases the concentration and the availability of CO_2 gas on the surface of the photocatalyst, (ii) increasing the pressure reduces the boundary layer thickness around the catalyst particles and hence increases the rate of mass transfer, (iii) both of adsorption and diffusion rates of the CO_2 gas through the pores of the photocatalyst are improved with high pressures. However, at excessively high pressures of CO_2, the overall evolution rates of products may start to decrease as reported in other experiments conducted by other research groups [91, 341, 342], this can occur as a result of the competitive adsorption between CO_2 molecules on the active sites of the ternary composite during the photocatalytic reduction process. High pressures can also affect on the viscosity of the CO_2 gas.
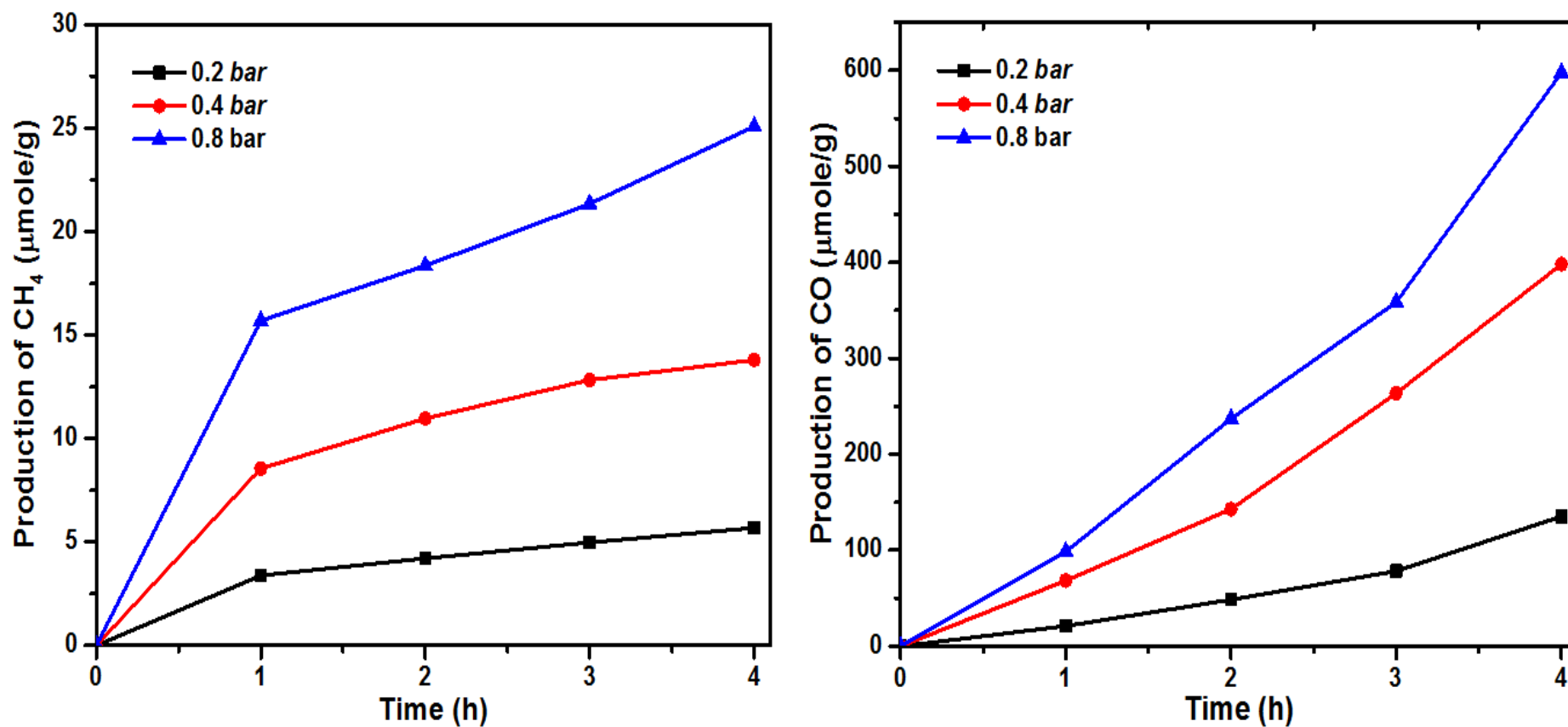
Figure 4.10   The amount CH4 and CO evolution rates over g-C3N4-RGO-NH2-MIL-125(Ti) by applying different pressure values (0.2, 0.4 and 0.8 bar).

4.3.6   Stability of the Photocatalyst

The catalyst life time is crucial during any continuous chemical reaction operation. Therefore, the stability of the g-C_3N_4-RGO-NH_2-MIL-125(Ti) composite for photocatalytic CO_2 reduction was investigated in terms its continuous performance and photoactivity for producing the same products (CH_4 and CO) with approximate values. This stability test for the photocatalyst was performed by irradiating the same sample for three cycles. In every cycle the photoreactor was illuminated for 4 hours after being cleaned with N_2 followed by purging and saturating with pure CO_2 gas for 1 hour. After saturating the reactor chamber with the water-humidified CO_2 gas, a sample was tested after 1 hour in dark conditions and considered as a blank sample to confirm that the evolution of products is occurring only under the light irradiations and also to ensure that no traces are left from the previous run. The production of CH_4 and CO in the three cycles is shown in Figure 4.11 (a)-(b). It is clear that the ternary g-C_3N_4-RGO-NH_2-MIL-125(Ti) composite maintained a good stability for the production of both CO and CH_4. However, there was a little decrease in the production of CO in the second cycle which might be attributed to the instability of RGO, while no significant changes were observed during the third cycle in which after three cycles (12 h of irradiation for all cycles), the sample exhibited production rates that represent approximately (78% of CO) and (90% of CH_4) that were produced after the first cycle.
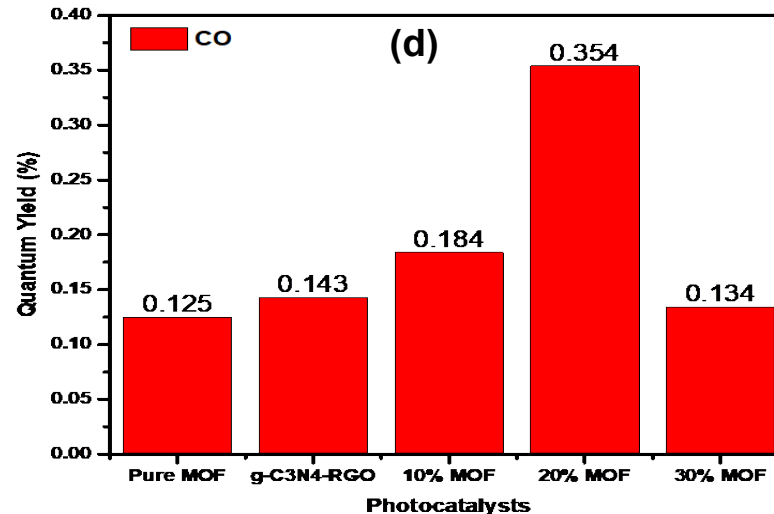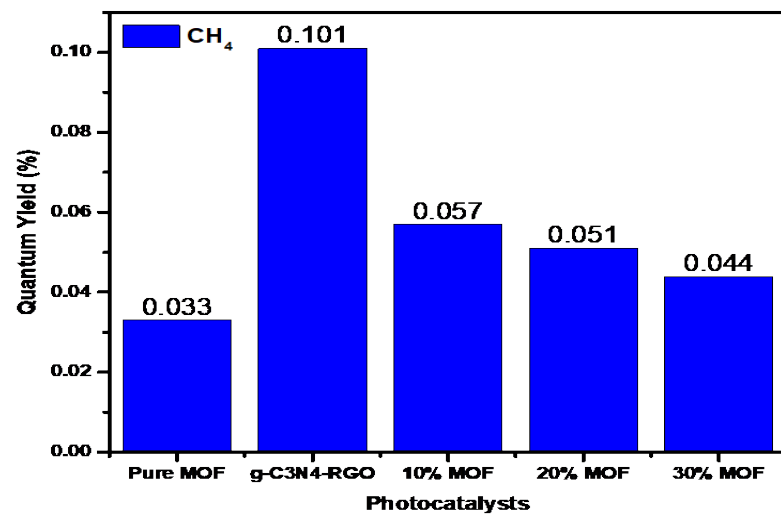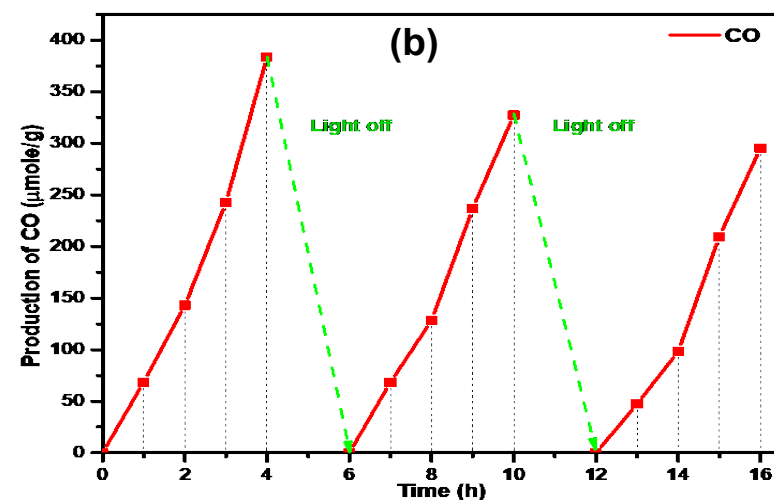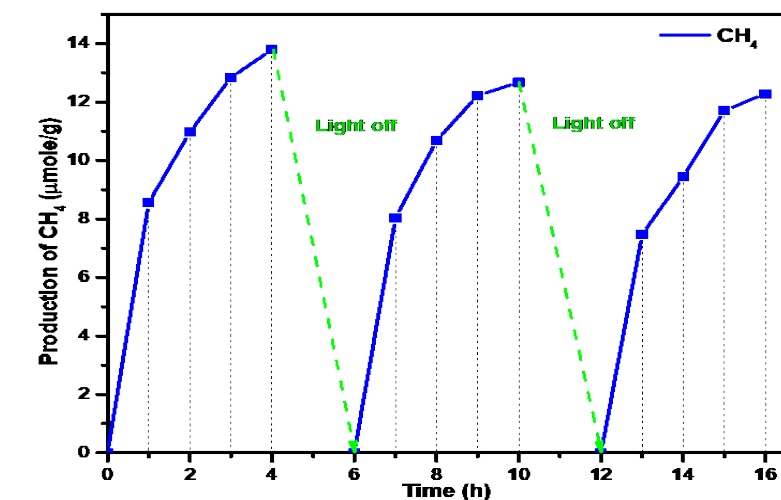
Figure 4.11　(a) and (b) The stability analysis of g-C_3N_4-RGO-NH_2-MIL-125(Ti) for photocatalytic CO_2 reduction to CO and CH_4 under visible light for three cycles, (c) and (d) The quantum yields for CH_4 and CO obtained over different photocatalysts after 4 hours irradiation.

4.3.7 Quantum Yield Calculations

Although the photocatalytic performance of a photocatalyst is typically evaluated by the products yields obtained in terms of μmol or μmol g^{-1}, it is still necessary to consider other factors that can have an impact on the photocatalytic activity such as the light intensity and wavelength. Therefore, performance analysis measured in terms of energy consumption is adopted by calculating the quantum yield (QY). The quantum yields of CH$_4$ and CO productions over the pure MOF, g-C$_3$N$_4$-RGO, g-C$_3$N$_4$-RGO-MOF (10%), g-C$_3$N$_4$-RGO-MOF (20%) and g-C$_3$N$_4$-RGO-MOF (30%) are summarized in Table 4.1.

Table 4.1   Summary of the Yield Rates, Products selectivity, Quantum Yields of CO and CH$_4$ and Apparent Quantum efficiencies over various photocatalysts.

Photocatalyst(s)	Yield Rate [a] (μmol g^{-1}) [a]		Selectivity (%)		Quantum Yield [b] (%)		Apparent Quantum Yield (%)
	CH$_4$	CO	CH$_4$	CO	CH$_4$	CO	
Pure MOF	8.9	135.1	6.18	93.82	0.033	0.125	0.158
g-C$_3$N$_4$-RGO	27.4	154.7	15.05	84.95	0.101	0.143	0.244
g-C$_3$N$_4$-RGO-MOF (10%)	15.5	199.4	7.20	92.80	0.057	0.184	0.241
g-C$_3$N$_4$-RGO-MOF (20%)	13.8	383.8	3.47	96.53	0.051	0.354	0.405
g-C$_3$N$_4$-RGO-MOF (30%)	12.0	144.9	7.64	92.36	0.044	0.134	0.178

(*a*) Yield rates calculated based on 4 h irradiation time and 100 mg of catalyst weight.

(*b*) Quantum yield calculated using a light intensity of 20 mW cm^{-2}, a wavelength of 450 nm and incident area of 20 cm^2.

As shown in Figure 4.11 (d), it is obvious that the g-C$_3$N$_4$-RGO-MOF (20%) composite exhibited the best QY of 0.354 % for CO compared to all other photocatalysts with a CO selectivity of 96.5 %. However, the best QY of 0.101 % for

CH$_4$ was obtained with g-C$_3$N$_4$-RGO as illustrated Figure 4.11 (c) it also exhibited a selectivity of 15 %. The total Apparent Quantum Yields (AQY %) have been also calculated for all photocatalysts which represent the total QYs of all products as illustrated in Table 4.1.

4.3.8   Proposed Reaction Mechanism

The separation efficiency of the photogenerated charges (e$^-$/h$^+$) and the band alignments of the valance and conduction bands can determine the performance of a photocatalyst in photocatalytic reactions. They also play significant role in the products selectivity by driving the reaction towards the desired product potentials.

In the current work, the highest occupied molecular orbital (HOMO) of the NH$_2$-MIL-125(Ti) MOF is more positive than the valance band VB of g-C$_3$N$_4$, while the conduction band (CB) of the g-C$_3$N$_4$ is more negative than the lowest unoccupied molecular orbital (LUMO) of NH$_2$-MIL-125(Ti). According to this band structure, a Z-scheme heterojunction with RGO as a solid electron mediator is very likely to develop under visible light irradiation. When the light strikes the surface of the ternary g-C$_3$N$_4$-RGO-NH$_2$-MIL-125(Ti) composite, it undergoes an excitation state which generates a huge number of electron-hole pairs followed by a series of oxidation and reduction (redox) reactions. The photocatalytic process can be summarized in 4 main steps (A-D) as illustrated in Equations (4.3) - (4.9).

A: The photocatalyst activation

$$MOF + h\nu \rightarrow MOF(e^-) + MOF(h^+) \tag{4.3}$$

$$RGO + MOF(e^-) \rightarrow RGO(e^-) + MOF \tag{4.4}$$

$$g\text{-}C_3N_4 + RGO(e^-) \rightarrow g\text{-}C_3N_4(e^-) + RGO \tag{4.5}$$
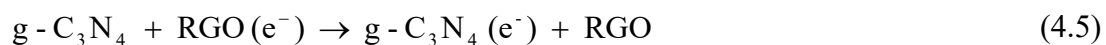
B: The oxidation process

$$2\,H_2O + 4\,h^+ \rightarrow O_2 + 4\,H^+ \tag{4.6}$$

C: The reduction process

$$CO_2 + e^- \rightarrow CO\cdot^- \tag{4.7}$$

D: The formation of products

$$CO_2 + 2\,H^+ + 2\,e^- \rightarrow CO + H_2O \tag{4.8}$$

$$CO_2 + 8\,H^+ + 8\,e^- \rightarrow CH_4 + 2\,H_2O \tag{4.9}$$

Figure 4.12 shows a schematic illustration of the proposed mechanism for photocatalytic CO_2 reduction over the g-C_3N_4-RGO-NH_2-MIL-125(Ti) composite in the presence of water under visible light. Upon light irradiation, the photo-excited electrons transfers from the VB to CB of the NH_2-MIL-125(Ti) MOF, leaving the holes in the VB as illustrated in Equation (4.3). These photo-induced electrons over the surface of NH_2-MIL-125(Ti) are passed across the RGO (Equation (4.4)) which acts as a solid electron mediator suppressing any possible charge recombination and forming a Z-scheme heterojunction bridge for electrons to reach the CB of g-C_3N_4 as shown in Equation (4.5). The holes remained at the VB of the MOF are consumed for the oxidation of water, enabling the formation of oxygen molecules and protons as demonstrated in Equation (4.6). However, the electrons are further consumed for the reduction of CO_2 to its radicals as shown in Equation (4.7). Finally, the production of CO and CH_4 is obtained through the involvement of 2 and 8 electrons as illustrated in Equations (4.8) and (4.9).

The enhanced photocatalytic efficiency for the production of CO and CH_4 in the current work can be linked with the successful fabrication of indirect Z-scheme heterojunction with efficient charges separation in addition to the synergistic effect of the visible-active MOF with large surface area and the solid RGO electron mediator with the hindered recombination rate, enabling higher productivity and quantum yields.
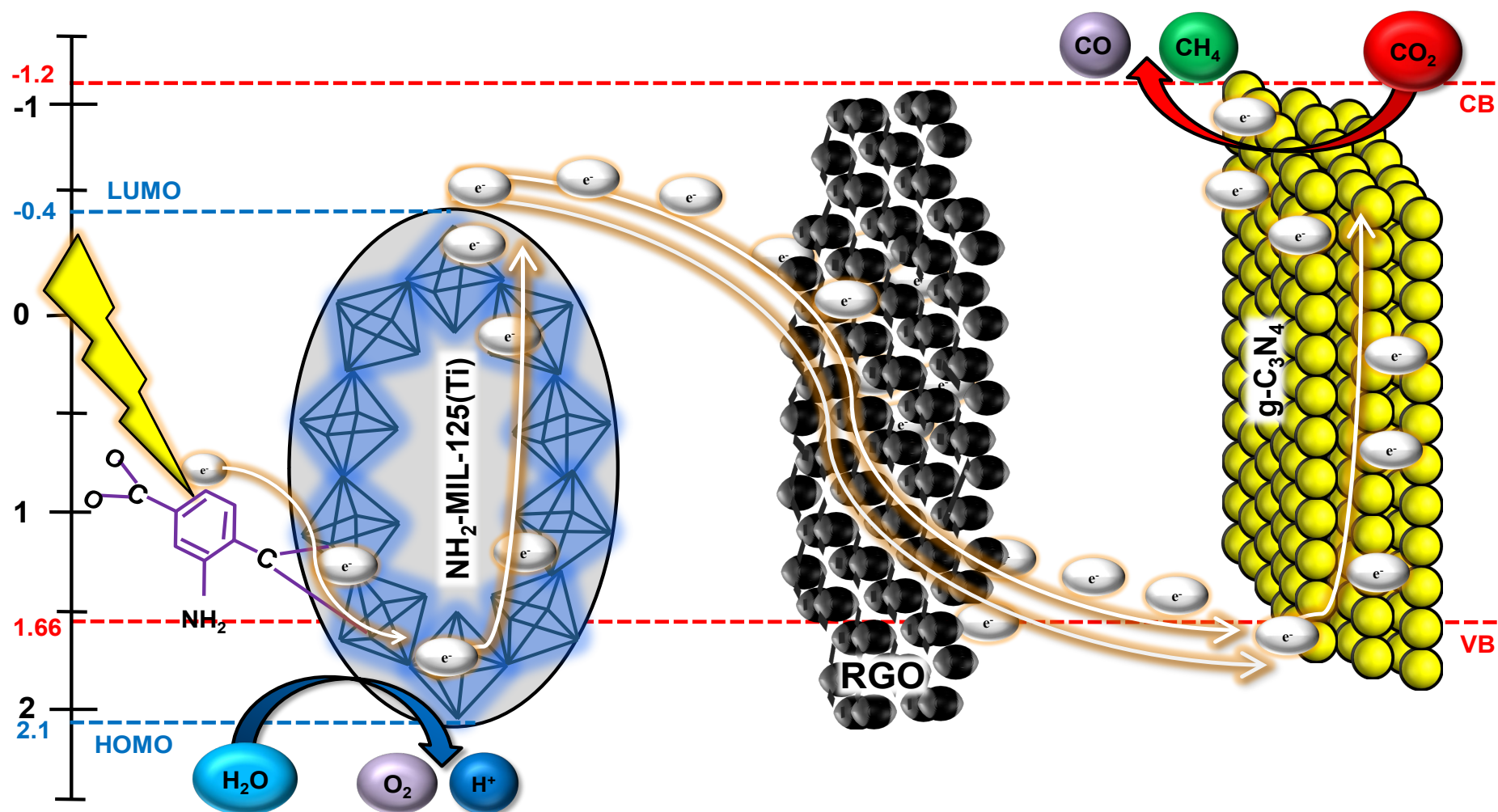
Figure 4.12   Schematic illustration for the separation and transfer of photogenerated charges and the formation of a Z-scheme heterojunction over the g-C₃N₄-RGO-NH₂-MIL-125(Ti) nanocomposite under visible light irradiation.

4.4   Characterizations of NH₂-MIL-125(Ti)-GO-TNTs Composite

4.4.1   X-ray Diffraction Analysis

Similar to the first MOF-composite, all the MOF diffraction peaks at 2θ: 6.8°, 9.5°, 11.5°, 16.5° and 17.9° indexed to the (101), (200), (211), (222) and (312) planes [297-300] were displayed in the XRD pattern of the NH₂-MIL-125(Ti)-GO-TNTs composite as shown in Figure 4.14. The GO characteristic peak at 2θ: 9.9° corresponding to the (001) plane did not appear in the ternary composite, this might be attributed to one of the reasons; because it was concealed in the sharp peak of MOF (2θ: 9.5°) as a result of its close location or due to the low content of GO (1%) in the NH₂-MIL-125(Ti)-GO powder composite. For TNTs, the same TiO₂ diffraction peaks of both anatase and rutile phases were detected in the pure TNTs foil and MOF-TNTs composite. Anatase and rutile are the most existent crystalline nanostructures in titanium dioxide, they are constructed by the Ti─O octahedrons connections through a different number of shared corners and/or faces that determines their type, in which the anatase tetragonal structure is formed as a result of corner (vertices) sharing octahedron that construct the (100) plane, while the rutile tetragonal structure is given by sharing edges of octahedrons at (001) planes [343]. This variety in structure gives more crystal stability to rutile amongst all other phases of TiO₂, while makes the anatase phase the best in terms of photocatalytic performance in several applications including CO₂ reduction.

As illustrated in Figure 4.13, the samples exhibited diffraction peaks at 2θ: 25.3°, 37.8°, 48.09°, 55.11°, 62.7° which are indexed to (101), (004), (200), (211) and (204) crystallographic planes of anatase phase, respectively (JCPDS card No. 21–1272) [285, 344, 345]. While the rutile phase peaks were displayed at 2θ: 27.4°, 36.1°, 54.3°, 69° corresponding to the crystal planes of (110), (101), (105) and (301) (JCPDS card No. 21–1276), respectively [344, 346]. When the pure sample of TNTAs contains only the anatase and rutile phases, the rutile phase percentage can be calculated, therefore, by measuring intensities of the most prominent peaks and using Equation (4.10) [328, 346], the rutile percent was found to be about 23% which is considered to be in the range of the optimum rutile percentage (20-40%) for the

best photocatalytic performance, confirming the successful formation of an efficient TiO_2 NTs composite for photocatalytic CO_2 reduction.

$$R = \frac{I_R}{I_R + 0.884\,I_A} \qquad\qquad (4.10)$$

where R is the rutile percentage, I_R and I_A are the rutile and anatase integrated diffraction peak intensities, respectively.
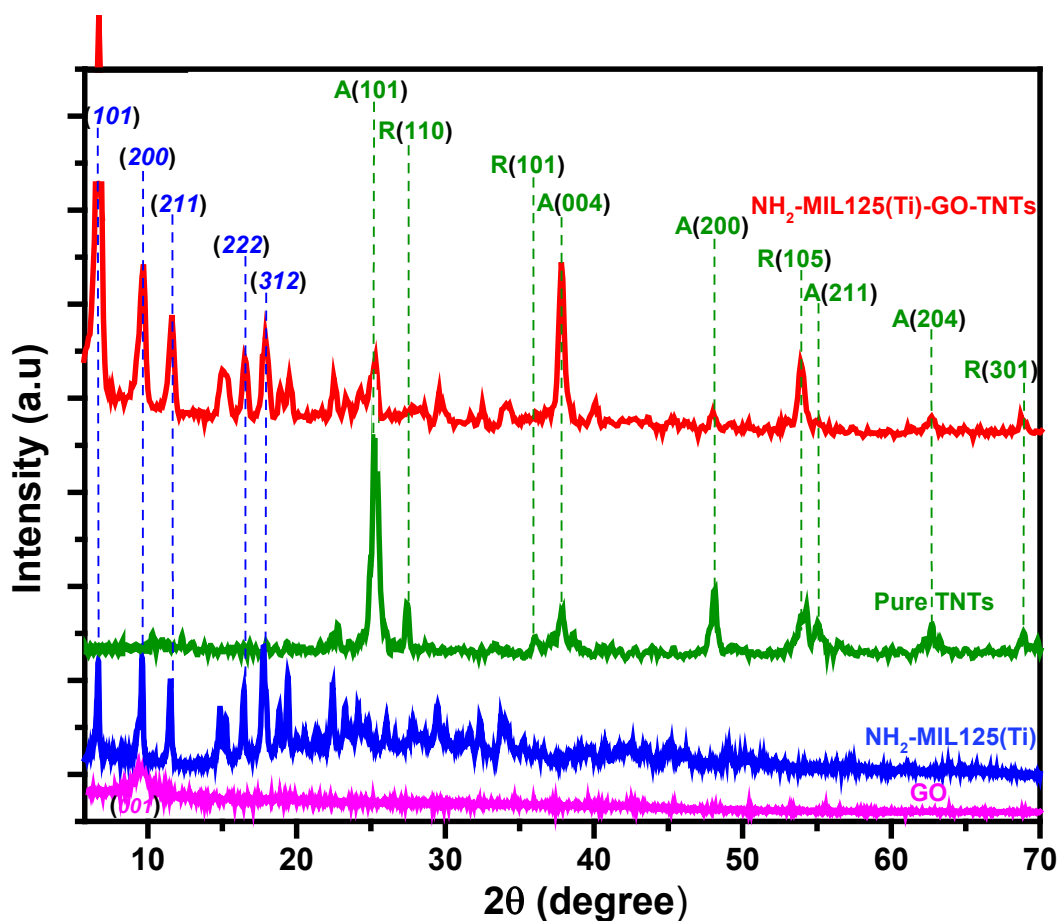
Figure 4.13   XRD patterns of GO, NH_2-MIL-125(Ti), TNTs and NH_2-MIL-125(Ti)-GO-TNTs samples.

4.4.2   Raman Analysis

As shown in Figure 4.14, the Raman spectrum of NH_2-MIL-125(Ti) MOF showed characteristic peaks at 800, 825, 1250, 1414, 1570 and 1620 cm^{-1} which are attributed to the vibration modes of the organic H_2BDC constituent of this titanium

149

based MOF [313]. Similar peaks were displayed in the NH$_2$-MIL-125(Ti)-GO-TNTs composite while no GO peaks were shown due to low content of GO. However, two small anatase peaks of TNTs at 144 and 511 cm^{-1} were shown which are ascribed to the E$_g$, and A$_{1g}$ modes, respectively [347].
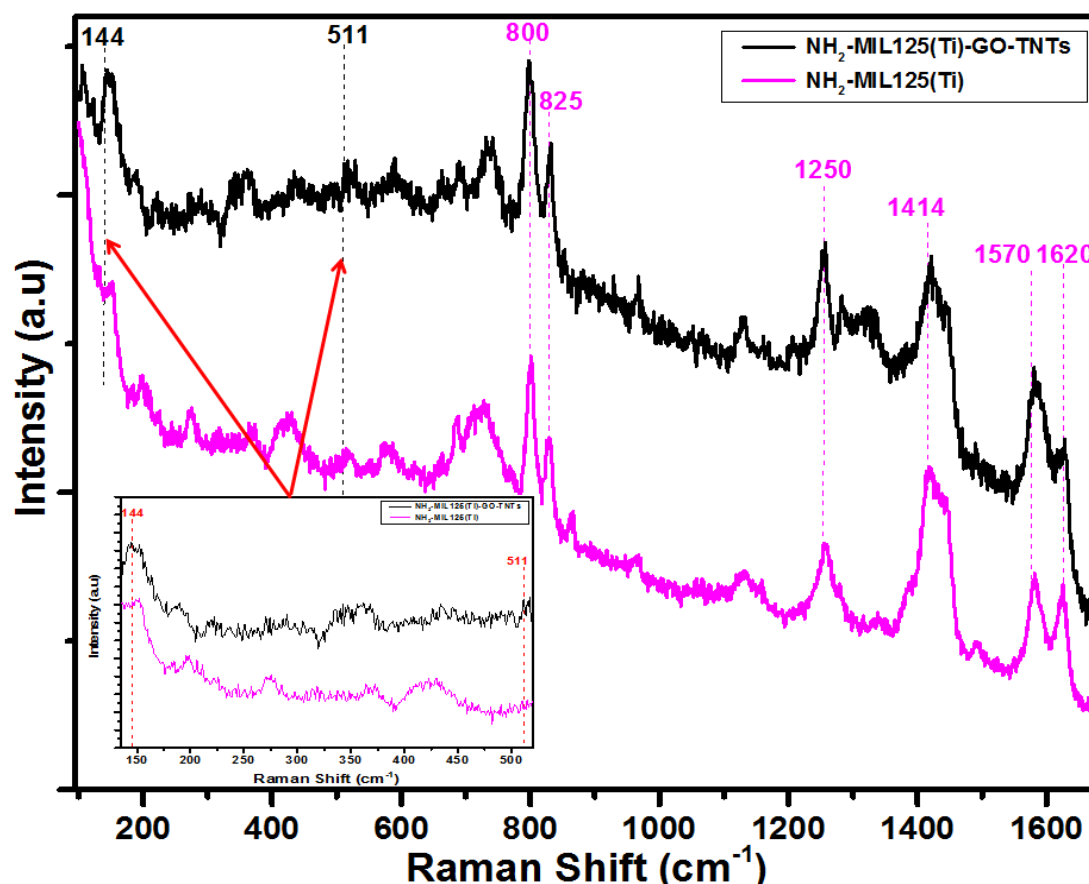
Figure 4.14   Raman spectra of NH$_2$-MIL-125(Ti) and NH$_2$-MIL-125(Ti)-GO-TNTs samples.

4.4.3   Field Emission Scanning Electron Microscopy (FESEM)

The FESEM images of NH$_2$-MIL-125(Ti), TiO$_2$ nanotube arrays and GO are shown in Figures 4.15 (a), (b) and (c) respectively. The MOF has shown uniform shapes and smooth surface with a particle size ranging from 60 to 100 nm. The morphology of TNTs was first investigated in the pure form to ensure the growth of well-aligned TiO$_2$ nanotubes over the Ti foil substrate prior to the MOF-GO coating. Figure 4.15 (b) displays a top view FESEM image of clean, hierarchical, and open-

pores TiO$_2$ nanotubes which represent the most important characteristics of TNTs. These vertically-orientated nanotubes; obtained after the electrochemical anodization followed by annealing at 550 °C, exhibited an average tube-mouth inner diameter of ~80 nm with an approximate thickness of ~23 nm. The drying deposition method has shown uniform distribution of NH$_2$-MIL-125(Ti) particles over and in the nanotube channels as shown in Figure 4.15 (d), (e) and (f). However, the GO nanosheets did not display very clearly in the ternary composite, this is mainly attributed to the low content of GO (1%) in the MOF-GO composite. Figure 4.15 (f) shows the cross-sectional views of the TNT nanocomposite, which illustrates that the nanotubes have grown efficiently on the Ti metallic substrate with an outstanding length reaching up to 10 μm, which gives more opportunity for the contact between the TiO$_2$ nanotubes and the other composites with the CO$_2$ and H$_2$O molecules. This length was much higher compared to previous reported results with size of (1, 2, 2.2, 5, 2, and 4.15 μm) [346, 348-352].

4.4.4 Energy Dispersive X-ray (EDX) Analysis

The elemental identification and quantitative analysis of the prepared NH$_2$-MIL-125(Ti)-GO-TNTs was conducted using Energy Dispersive X-ray technique. The EDX spectrum was performed over different spots over the TiO$_2$ nanotubes surface to ensure that equal dispersion of MOF-GO composite is obtained. However, the EDX mapping analysis confirmed the presence of Ti, O, C, and N, which are considered as the main elements of the ternary nanocomposite. The elemental atomic ratios are shown in Figure 4.16 (b-f), the composite exhibited Ti, O, C and N ratios of 28.9%, 31.3%, 37.9% and 1.8 %, respectively. The EDX mapping analysis has revealed good mixing and dispersion between the composites over the nanotubes. No other elements were detected indicating the high purity of the synthesized nanocomposite.
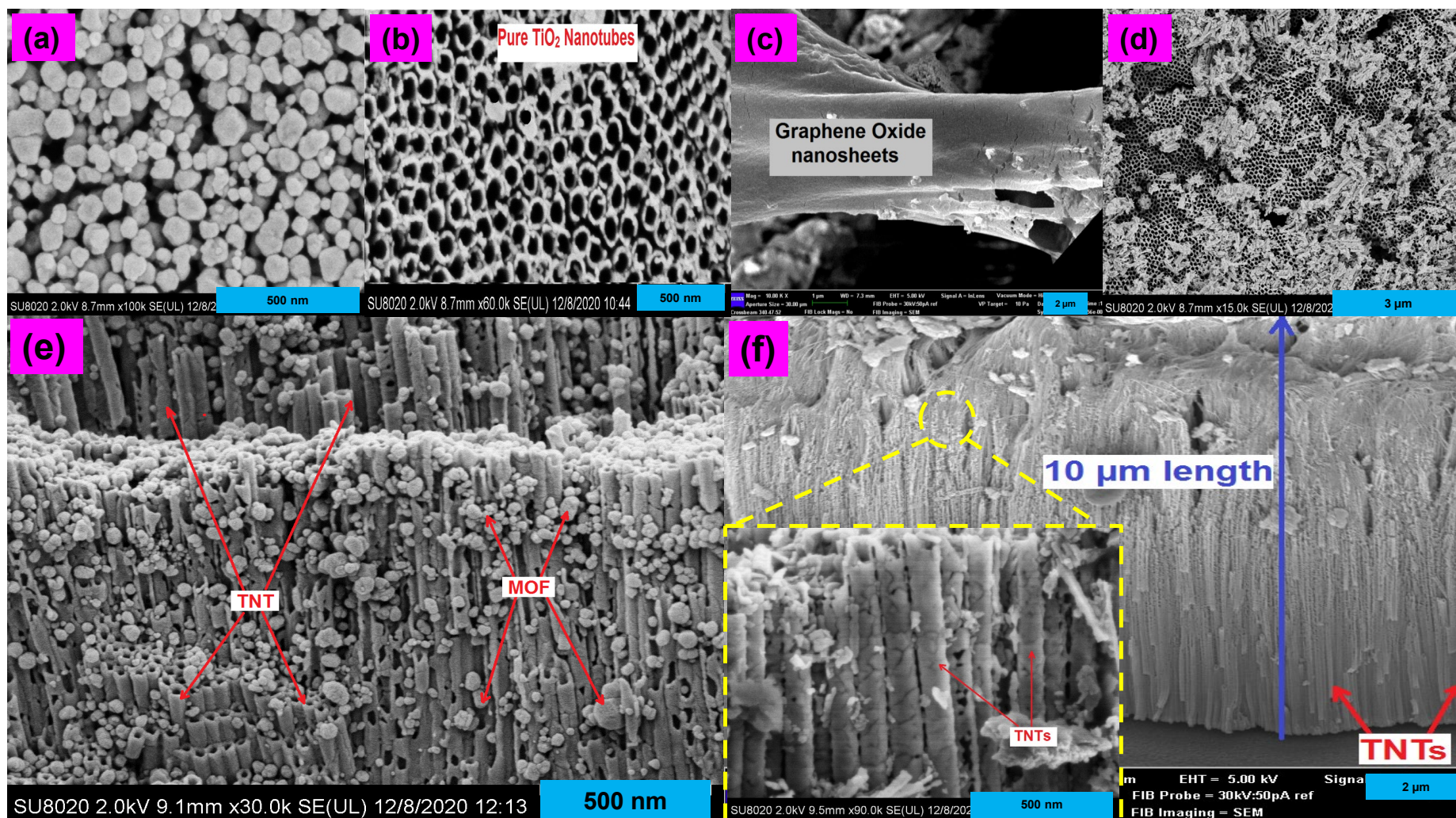
Figure 4.15   FESEM images of (a) Pure NH$_2$-MIL-125(Ti), (b) Pure TNTs, (c) Pure GO, (d-f) NH$_2$-MIL-125(Ti)-GO-TNTs composite.
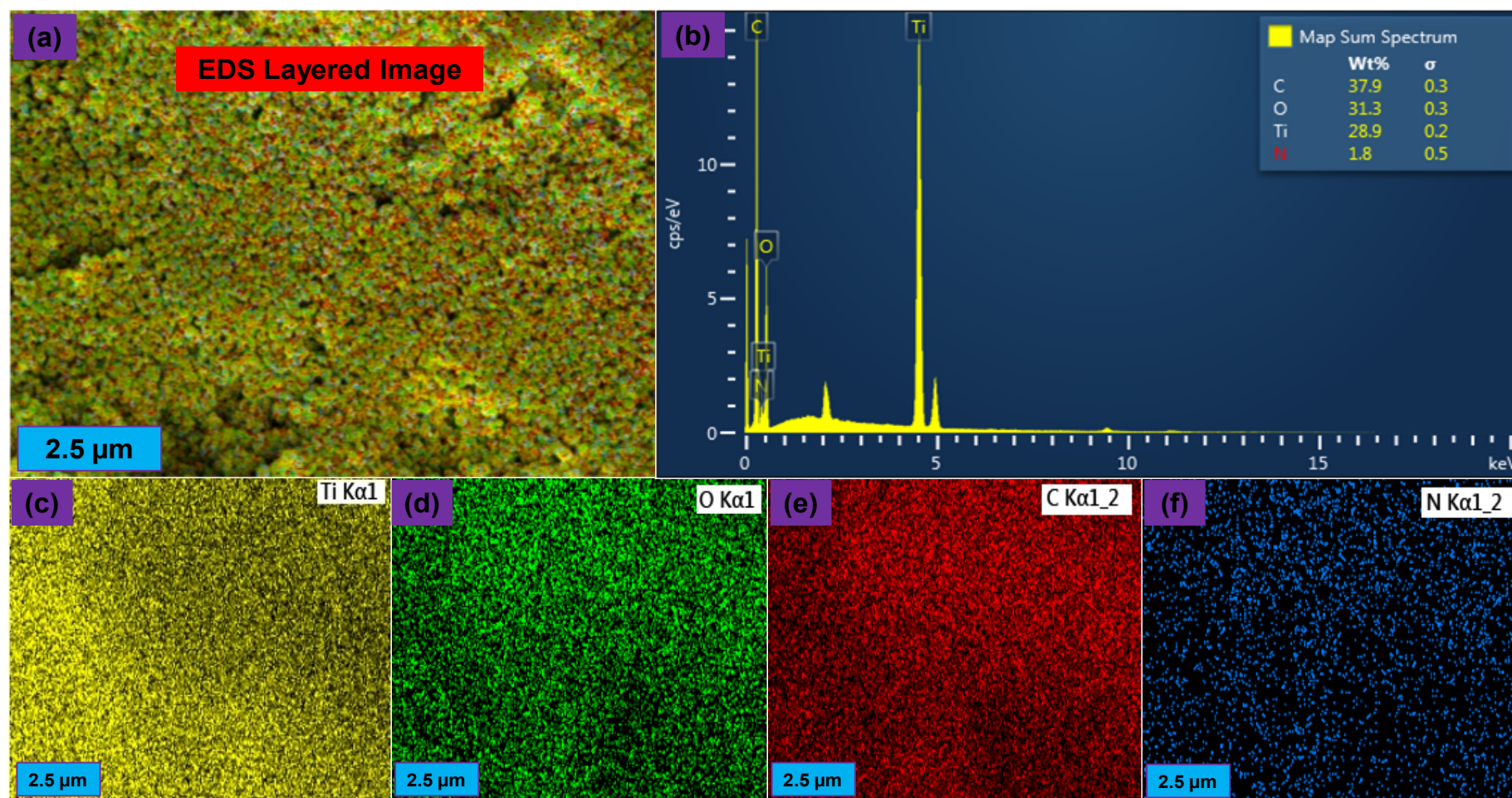
Figure 4.16 EDX analysis of NH$_2$-MIL-125(Ti)-GO-TNTs: (a) Layered image, (b) EDX Plot with elemental composition, (c-f) mapping distribution of Ti, O$_2$, C and N$_2$ respectively.

153

4.4.5 Fourier Transform Infrared (FTIR) Analysis

As shown in Figure 4.17, the NH$_2$-MIL-125(Ti) spectrum shows characteristic small peaks at 3442 and 3355 cm^{-1} which are attributed to the stretching vibration of -NH brought by the organic linker [325]. The symmetrical stretching vibration of -C=O is represented by bands from 1380 to 1661 cm^{-1}. However, the vibration band at 1434 cm^{-1} is attributed to the -OH groups. The existence of TiO$_2$ in the ternary composite was also confirmed by the typical vibration of Ti–O–Ti bands in the TNTs, this was represented by several peaks ranging from 426 cm^{-1} to 770 cm^{-1}, which are related to the anatase morphology. Two additional peaks were also shown in the MOF-composite at 2356 and 3750 cm^{-1}. However, the hydroxyl (–OH) group peaks in the TNTs composite was mainly overlapped by other peaks of other functional groups due to their close positions. No clear peaks of GO were shown, which might be attributed to its low content.
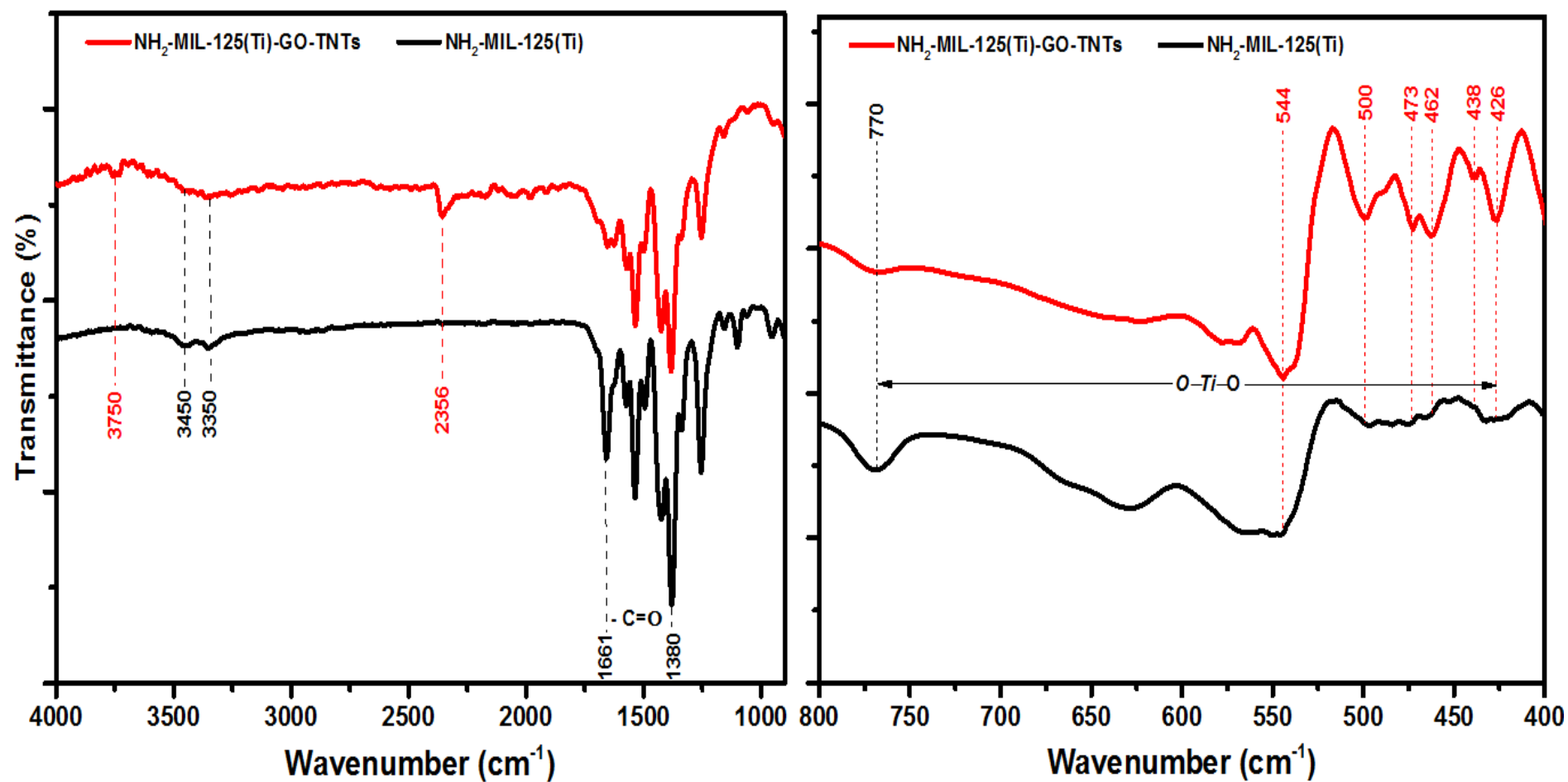
Figure 4.17   FTIR analysis of pure NH2-MIL-125(Ti) and NH2-MIL-125(Ti)-GO-TNTs samples.

4.5 Photocatalytic CO$_2$ Reduction over NH$_2$-MIL-125(Ti)-GO-TNTs

4.5.1 Effect of MOF-GO Coating on the Activity of TNT Arrays Photocatalyst

Pure TiO$_2$-NTs photocatalyst with an area of 10 cm^2 was tested under visible light for the photocatalytic reduction of CO$_2$ into CH$_4$ and CO and eventually exhibited results of 1713.61 and 23871.27 μmol m^{-2}, respectively, after 4 hours irradiation. The photocatalytic efficiency of the TiO$_2$-NTs foil with the same area was improved by coating it with NH$_2$-MIL-125(TI) and NH$_2$-MIL-125(TI)-GO composites as illustrated in Figure 4.18. The NH$_2$-MIL-125(TI)-GO-TNTs composite exhibited the best CO production yield of 29782.25 μmol m^{-2}. However, the production of CH$_4$ reduced compared to pure TNTs to 1054.74 μmol m^{-2}. Both MOF composites showed similar CH$_4$ selectivity of about 4% compared to 7% for pure TNTs. These observations are in agreement with the g-C$_3$N$_4$-RGO-NH$_2$-MIL-125(TI) results and confirm the high NH$_2$-MIL-125(Ti) MOF selectivity towards CO production and not to the CH$_4$ gas. The addition of GO has also shown clear enhancement which confirms the successful fabrication of a multi-heterojunction photocatalyst for more efficient photocatalytic CO$_2$ reduction.

Overall, the efficient and enhanced photocatalytic reduction of CO$_2$ to solar fuels could be achieved by using a wide range of critical strategies, including improving the CO$_2$ gas adsorption, promoting the separation efficiency of electron−hole pairs, limiting the photogenerated charge recombination and increasing visible light harvesting. Many reviews summarized the different TiO$_2$-based nanostructures [63, 353-355] . However, no reviews were specified for TNTs-MOF composites, in fact, TNTs composites in photocatalytic CO$_2$ reduction are still not enough researched yet. Therefore, the recent related developments of TNTs-based composites are summarized in Table 4.2, which demonstrates the reactants, light source information, reactor and reaction parameters, production rates and the preparation conditions so that clear comparisons can be seen among the previous and the current studies.
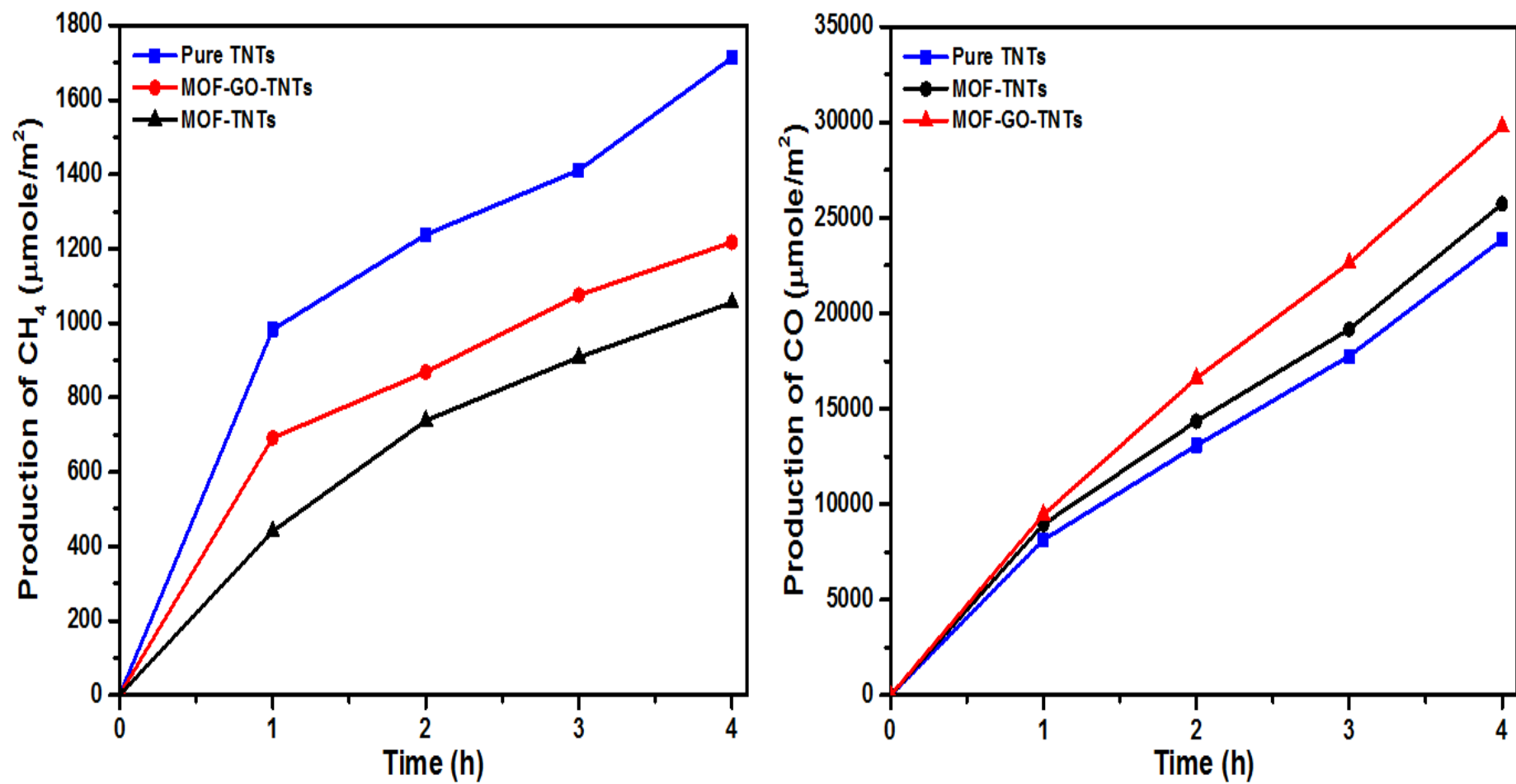
Figure 4.18 The CO and CH$_4$ production rates of photocatalytic CO$_2$ reduction over Pure TNTs, MOF-TNTs and MOF-GO-TNTs.

Table 4.2   A summary of the recent developments of photocatalytic CO_2 reduction performance over various TNTs-composites.

Photocatalyst(s)	Feed Composition	Light source Wavelength Intensity	Reactor Parameters	Product(s) (rate)	TNTs preparation parameters	Ref.
RGO/Pt–TiO$_2$ NTs	CO_2, H_2O vapor, catalyst	Visible light 500 W tungsten-halogen lamp	Continuous gas–reactor Vol. = 9.8 mL Flow = 100 mL min^{-1}	CH$_4$ = 2.88 µmol m^{-2} h^{-1}	**Anodization @ 50 V for 3 h** **Annealing @ 450 °C for 1h**	[281]
Ag-TiO$_2$ NTs	CO_2, H_2O vapor, catalyst	300 W Xe arc lamp	Pyrex reactor Time = 4 h	CH$_4$ = 12 mmol m^{-2} h^{-1}	**Anodization @ 30 V for 6 h.** **Annealing @ 550 °C for 2h**	[350]
Pt-MgO/TiO$_2$ NT films	CO_2, H_2O vapor, catalyst, 20 mL 0.1 mol/L KHCO$_3$	Hg lamp 300W	Gas-phase reactor Vol. = 358 mL Temp. = 25 °C Time = 6 h	CO = 10.4 CH$_4$ = 100.22 ppm cm^{-2} h^{-1}	**Hydrothermal treatment** @ 120 °C for 24 h **Annealing @ 500 °C for 4 h**	[352]
Pt-Au/R-TiO$_2$ NTs	CO_2, aqueous solution, catalyst	LED lamp 365 nm 208 mW cm^{-2}	Quartz cell reactor Vol. = 15 mL	CH$_4$ = 360 C$_2$H$_6$ = 28.8 µmol g^{-1} h^{-1}	**Anodization @ 60 V for 8 h.** **Annealing @ 450 °C for 2 h**	[356]
TiO$_2$-NTs (Flame annealed)	CO_2, H_2O vapor, catalyst	Visible light 50 W LED lamp 510 nm	Cylindrical reactor Press. = 50 psi Temp. = 80 °C	CH$_4$ = 67.9 µmol g^{-1} h^{-1}	**Anodization @ 15 V** **Annealing @ 750°C for 2 min**	[346]
RGO–TiO$_2$ NTs	CO_2 (1000 ppm in He), H_2O vapor, catalyst	100 W Xe lamp	Continuous gas–reactor Vol. = 15.4 mL Time = 1 h	CH$_4$ = 5.67 ppm cm^{-2} h^{-1}	**Anodization @ 55 V for 0.5 h** **Annealing @ 400 °C for 1 h**	[357]

Table 4.2, continued.

Photocatalyst(s)	Feed Composition	Light source *Wavelength* *Intensity*	Reactor *Parameters*	Product(s) (rate)	TNTs preparation parameters	Ref.
Cu_2O-TiO_2 NTs	CO_2, H_2O vapor, catalyst	Visible light 350 W Xe lamp	Stainless steel chamber Press. = 103 kPa Time = 4 h	CH_4 = 100 ppm h^{-1}	**Anodization @ 50 V for 4 h** **Annealing @ 450 °C for 3 h**	[351]
Graphene QDs- TiO_2 NTs	CO_2, H_2O vapor, catalyst	Visible light λ = > 430 nm	Stainless steel reactor Vol. = 15.4 cm^3	CH_4 = 0.16 ppm cm^{-2} h^{-1}	**Anodization @ 50 V for 45 min.** **Annealing @ 400 °C for 1 h**	[349]
Pd-RGO-TiO_2 NTs (wires)	CO_2, H_2O vapor, catalyst	UV–Vis light 100 mW cm^{-2}	Continuous liquid-gas phase reactor Temp. = 4 °C Time = 4 h	CH_3OH = 313 C_2H_4OH= 207 nM cm^{-2} h^{-1}	**Anodization @ 30 V for 8 h.** **Annealing @ 500 °C for 4 h**	[358]
g-C_3N_4-P-TiO_2 NTs	CO_2, Na_2SO_4 aqueous solution, catalyst	500 W Xe lamp	Gas-liquid phase glass reactor Time = 1 h	$C_2H_4O_2$ = 46.9 CH_3OH = 28.8 mg L^{-1} h^{-1}	**Anodization @ 20 V for 2 h** **Annealing @ 500 °C for 2 h**	[348]
RGO–TiO_2 NTs	CO_2 (1000 ppm in He), H_2O vapor, catalyst	100 W Xe lamp	Continuous gas–reactor Vol. = 15.4 mL Time = 1 h	CH_4 = 5.67 ppm cm^{-2} h^{-1}	**Anodization @ 55 V for 0.5 h** **Annealing @ 400 °C for 1 h**	[357]
Ti/TiO_2 NTs @PDA-Ag NP	CO_2, 150 mL of 0.1 M Na_2SO_4 solution, catalyst	UV–Vis light 125 W Hg lamp	Continuous gas–liquid stainless steel reactor Press. = 1.5 atm	CH_3OH = 16.3 µmol cm^{-2} h^{-1}	**Anodization @ 30 V for 50 h** **Annealing @ 450 °C for 2 h**	[359]

4.5.2 Effect of Pressure

The effect of pressure on the photocatalytic process over the NH_2-MIL-125(Ti)-GO-TNTs ternary composite was also investigated by using different CO_2 gauge pressures (0.2, 0.4 and 0.8 bar). Similar to the observations with g-C_3N_4-RGO-NH_2-MIL-125(Ti) composite, the production rates of both CH_4 and CO increased with the increase of pressure as shown in Figure 4.19. The maximum yield rates of 1995.8 μmol m^{-2} CH_4 and 45753.3 μmol m^{-2} CO were obtained with the pressure of 0.8 bar. It is also worth mentioning that the products ratios remained almost fixed with the variation of pressure, revealing that the pressure had no significant influence on the catalyst selectivity.

4.5.3 Stability of the Photocatalyst

The stability of the NH_2-MIL-125(Ti)-GO-TNTs ternary composite for photocatalytic CO_2 reduction was further studied and the results are shown in Figure 4.20. It is obvious that the composite maintained an excellent and long-term stability for both products after 12 h of the photoreaction. After the third cycle, the composite showed a production of 29285 μmol m^{-2} for CO, which represents more than 98 % of the first cycle production. However, the CH_4 production exhibited a slight increase of about 10 %, this might be attributed to the little change in the MOF activity which shifted the composite selectivity to the CH_4 gas. In comparison with other studies, Razzak et al. [357] tested the stability of RGO-TiO_2 NTs composite for 4 cycles (each cycle is 1 h only) and noticed a significant drop in the CH_4 production rate during the second cycle. After the fourth run, the production rate represented only 71% that of the first.

Overall, the comparison with similar studies [198, 356] suggests that the novel NH_2-MIL-125(Ti)-GO-TNTs composite is a promising photocatalyst for continuous photocatalytic CO_2 reduction with a good stability and performance.
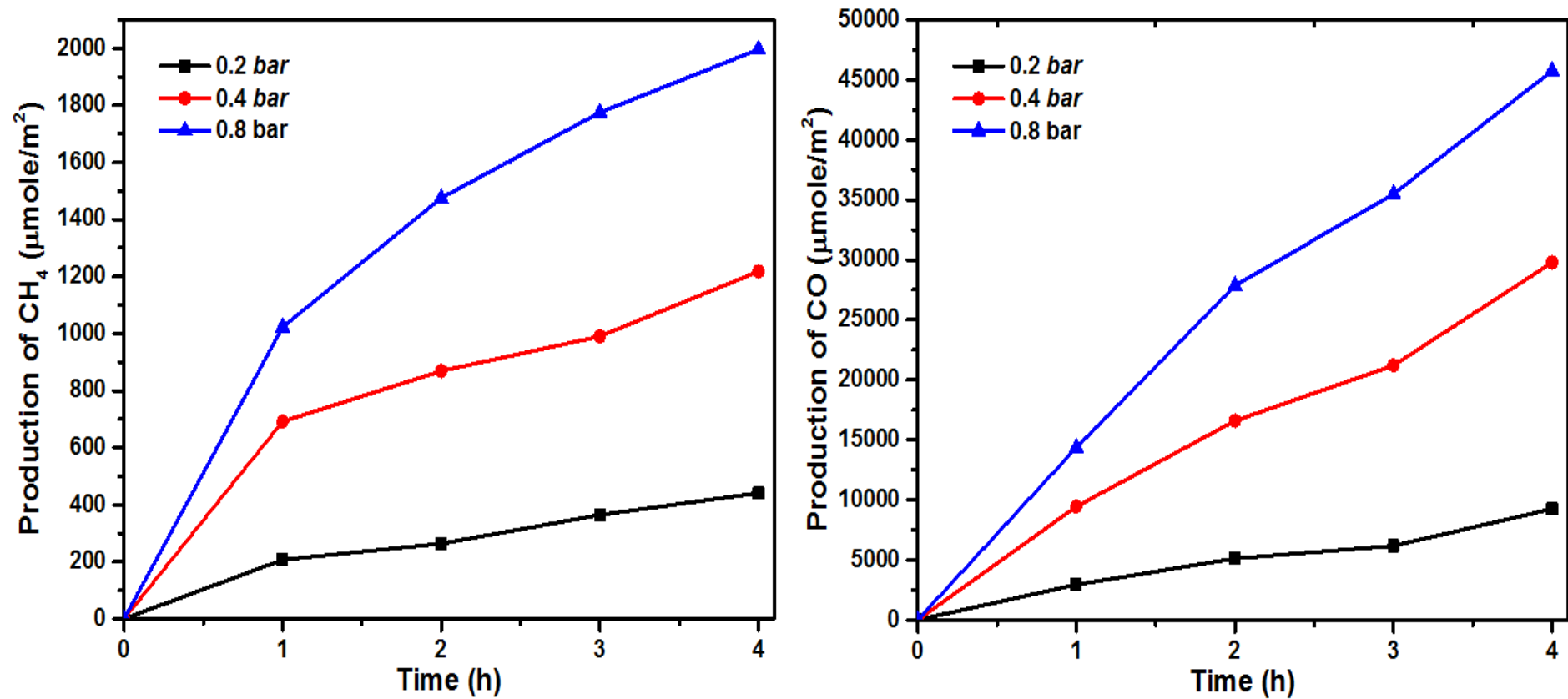
Figure 4.19   The amount CH$_4$ and CO evolution rates over NH$_2$-MIL-125(Ti)-GO-TNTs by applying different pressure values of 0.2, 0.4 and 0.8 bar.
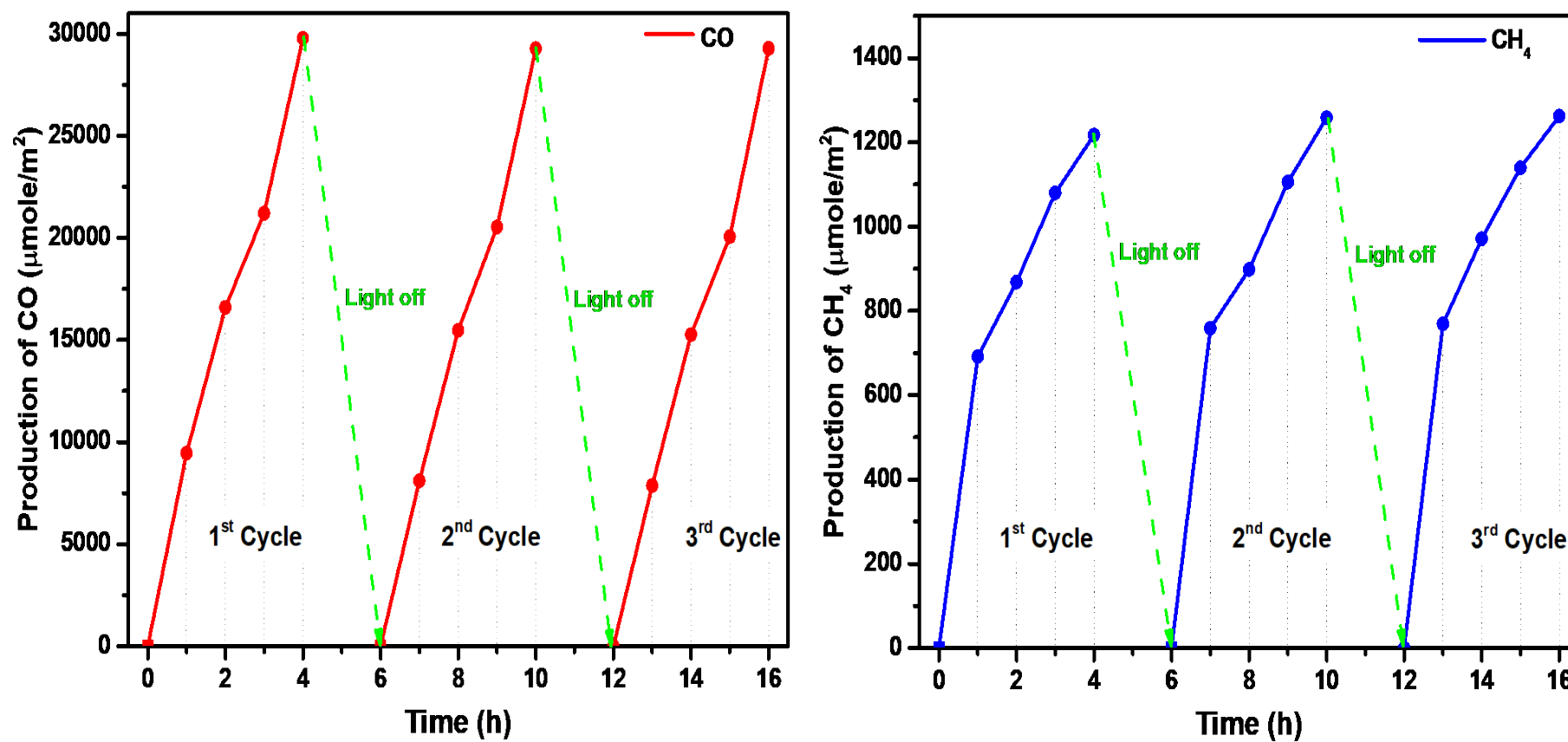
Figure 4.20 The stability analysis of NH_2-MIL-125(Ti)-GO-TNTs composite for photocatalytic CO_2 reduction to CO and CH_4 under visible light for three cycles.

4.5.4 Quantum Yield Calculations

The maximum quantum yield for CO production of 0.275 % was obtained with the use of MOF-GO-TNTs composite compared to 0.22 % with pure TNTs as shown in Table 4.3. Similar to the g-C$_3$N$_4$-MOF composite, the CH$_4$ QY was found to be decreasing with the addition of MOF which confirms again the high MOF selectivity towards CO compared to CH$_4$ production. However by considering the total AQY, the maximum result of 0.3198 % was achieved with the MOF-GO-TNTs composite. The novel ternary NH$_2$-MIL-125(Ti)-GO-TNTs composite exhibited a CO selectivity of 96 % and 3.94 % for the CH$_4$ gas.

Table 4.3   Summary of the Yield Rates, Products selectivity, Quantum Yields of CO and CH$_4$ and Apparent Quantum efficiencies over various photocatalysts.

Photocatalyst(s)	Yield Rate [a] (μmol m^{-2}) [a]		Selectivity (%)		Quantum Yield [b] (%)		Apparent Quantum Yield (%)
	CH$_4$	CO	CH$_4$	CO	CH$_4$	CO	
Pure TNTs	1713.6	23871.3	6.70	93.30	0.063	0.220	0.2836
MOF-TNTs	1054.7	25718.5	3.94	96.06	0.038	0.237	0.2763
MOF-GO-TNTs	1217.3	29782.3	3.93	96.07	0.045	0.275	0.3198

(*a*) Yield rates calculated based on 4 h irradiation time and over 0.001 m^{-2} catalyst area.
(*b*) Quantum yield calculated using a light intensity of 20 mW cm^{-2}, a wavelength of 450 nm and incident area of 20 cm^2.

4.5.5 Proposed Reaction Mechanism

The performance of any photocatalyst is entirely dependent on the efficiency of charges production and separation for carrying oxidation and reduction (redox) reactions. Generally, the conversion of CO_2 into $CO^{\bullet-}$ is considered to be as a rate-limiting step for the photo-reduction process. The CO_2 in gaseous form is known to be a thermodynamically stable molecule and difficult to break down. Thus, a suitable amount of energy (light) is needed to reduce the CO_2 into free radicals and then to valuable chemical products like CO and CH_4. Moreover, the presence of a reducing agent such as H_2O makes the CO_2 reduction more feasible by providing protons and electrons to react with the CO_2 gas and to form products, this lowers the required input energy [354]. Here in, when the light strikes the surface of the NH_2-MIL-125(Ti)-GO-TNT composite, it undergoes an excitation state which generates a population of photogenerated charges (electron-hole pairs) followed by a series of redox reactions. The photogenerated holes oxidize the water, while the photo-excited electrons reduce CO_2 to CO and CH_4. Figure 4.21 shows the proposed reaction mechanism and the detailed reaction steps are illustrated in Equations (4.11) - (4.19).

$$MOF + h\nu \rightarrow MOF(e^-) + MOF(h^+) \tag{4.11}$$

$$MOF(e^-) + TiO_2 \text{ Anatase} \rightarrow MOF + TiO_2 \text{ Anatase}(e^-) \tag{4.12}$$

$$TiO_2 \text{ Anatase}(e^-) + TiO_2 \text{ Rutile} \rightarrow TiO_2 \text{ Anatase} + TiO_2 \text{ Rutile}(e^-) \tag{4.13}$$

$$TiO_2 \text{ Rutile}(e^-) + GO \rightarrow TiO_2 \text{ Rutile} + GO(e^-) \tag{4.14}$$

$$MOF + TiO_2 \text{ Anatase}(h^+) \rightarrow MOF(h^+) + TiO_2 \text{ Anatase} \tag{4.15}$$

$$CO_2 + e^- \rightarrow CO\bullet^- \tag{4.16}$$

$$CO_2 + 2H^+ + 2e^- \rightarrow CO + H_2O \tag{4.17}$$

$$CO_2 + 8H^+ + 8e^- \rightarrow CH_4 + 2H_2O \tag{4.18}$$

$$2\,H_2O + 4\,h^+ \rightarrow O_2 + 4\,H^+ \tag{4.19}$$
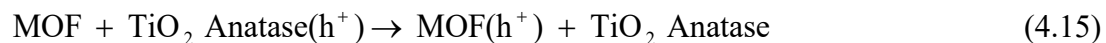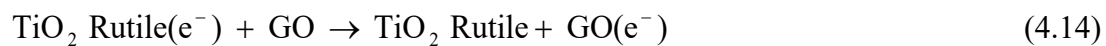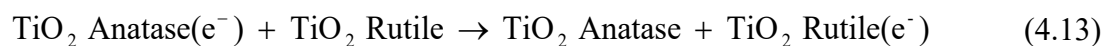
Upon light irradiation, the photo-excited electrons are transferred from the VB to CB of the NH2-MIL-125(Ti) MOF, leaving the holes in the VB as illustrated in Equation (4.11). The majority of these photo-induced electrons over the surface of MOF are transferred across the first heterojunction to the conduction band of the TiO2 Anatase phase as illustrated in Equation (4.12). Then, the photogenerated electrons are further passed through the second heterojunction to the CB of TiO2 Rutile phase as shown in Equation (4.13). Finally, the electrons are trapped by GO (Equation (4.14)) which facilitates the electron-hole separation in the TiO2, owing to its high conductive properties. The GO can also improve the weak light absorption of Rutile TiO2 under visible light, and thus enhancing the photocatalytic activity. Simultaneously, the holes on the valance bands of both Anatase and Rutile TiO2 phases are transferred across the heterojunction to the VB of NH2-MIL-125(Ti) as shown in Equation (4.15). The produced electrons and holes generate a series of reactions which can be divided into three stages: (ii) the oxidation reaction of water by holes, (ii) the reduction reactions of CO2 gas by electrons (iii) the formation of CO and CH4 products. In the oxidation reaction, the water is oxidized enabling the formation of oxygen and protons over the surface of NH2-MIL-125(Ti) as shown in Equation (4.19), this is carried out by consuming those holes generated in the MOF valance band in addition to those holes transferred from the VBs of Anatase and Rutile TiO2 phases. However, in the reduction step, the CO2 gas is reduced into free radicals by consuming the population of electrons trapped on the surface of GO as illustrated in Equation (4.16). In the last stage, the final CO and CH4 products were obtained through the involvement of 2 and 8 electrons, respectively, after the combination of the produced radicals as demonstrated in Equations (4.17) and (4.18).

The exhibited photocatalytic activity of NH2-MIL-125(Ti)-GO-TNT composite was improved as a result of the high production of electrons and protons attributed to the positive synergistic effect of visible-active NH2-MIL-125(Ti) MOF, hierarchical TiO2-NTs and the solid GO electron mediator. Therefore, an enhanced photocatalytic activity for CO and CH4 production was obtained by the construction

of multi-heterojunction system with efficient charge carrier production and separation under visible light irradiation.
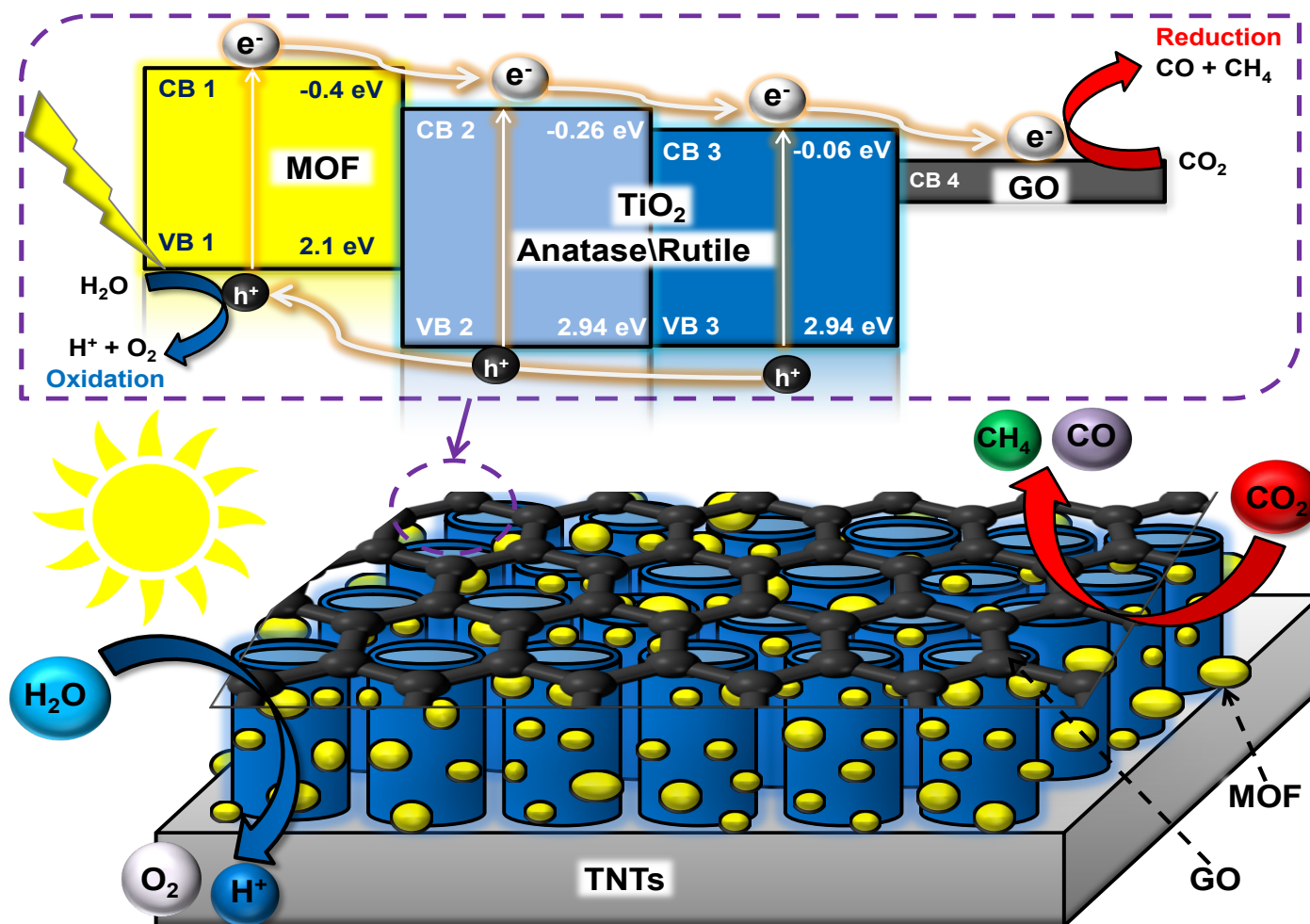
Figure 4.21   A schematic illustration for the separation and transfer of photogenerated charges and the formation of multi-heterojunctions over the NH₂ MIL-125(Ti)-GO-TNTs composite under visible light irradiation.

4.6   Summary

Based on the characterization results, it can be summarized that both g-C$_3$N$_4$-RGO-NH$_2$-MIL-125(Ti) and NH$_2$-MIL-125(Ti)-GO-TNTs composites exhibited good crystalline structures with well-ordered morphologies according to XRD and FESEM analyses. The existence of all composite elements, molecular structure, chemical bonds and functional groups was also proven by using other technologies such as Raman, FTIR and EDX. Finally, the UV-vis DRS and PL spectroscopy characterizations have confirmed the enhancement in the optoelectronic properties of composites by constructing efficient heterojunction systems.

The experimental results showed the best photocatalytic CO$_2$ reduction efficiency into CH$_4$ and CO over the two MOF-composites (g-C$_3$N$_4$-RGO-NH$_2$-MIL-125(Ti) and NH$_2$-MIL-125(Ti)-GO-TNTs) compared to their single catalyst components. Obviously, the NH$_2$-MIL-125(Ti) MOF showed higher product selectivity towards CO compared to CH$_4$. By testing the operating parameters it was found that higher pressures give more production yields with no significant changes in the selectivity for both MOF-composites. The best catalyst loading for the g-C$_3$N$_4$-RGO-NH$_2$-MIL-125(Ti) composite was found to be 100 mg.

CHAPTER 5

CONCLUSIONS AND RECOMMENDATIONS

5.1   Introduction

This chapter provides an insight into the conclusions of this research which was carried out for enhancing the photocatalytic CO_2 reduction into solar fuels over MOF-composites under visible light for sustainable and clean energy applications.

5.2   Conclusions

This study has been conducted according to the methodology procedure in Chapter 3. All the objectives of this research have been successfully achieved by fabricating two ternary MOF-composites. The most conclusive findings drawn from this research are listed below:

➢ Two MOF nanocomposites named as g-C_3N_4-RGO-NH_2-MIL-125(Ti) and NH_2-MIL-125(Ti)-GO-TNTs were successfully synthesized and characterized using different synthesis methods and technologies. Well-designed titania nanotubes arrays (TNTs) with controlled ratio of Anatase/Rutile phase were fabricated through a single step anodization process which exhibited hierarchal well-ordered nanotubes with an outstanding tube length of 10 μm.

➢ Both MOF-composites exhibited efficient photocatalytic CO_2 reduction under visible light in the presence of water vapour only; without any other sacrificial agents. The significant role of MOF in improving the optoelectronic properties of both g-C_3N_4 and TiO_2 NTs was clearly approved by both characterizations and the experimental work.

➤ The effects of various parameters on the photocatalytic performance of both MOF composites were investigated. The production of CO and CH_4 was found to be increasing continuously with both pressure and irradiation time. The highest photocatalytic performance was observed with 100 mg photocatalyst loading for the g-C_3N_4-RGO-NH_2-MIL-125(Ti) composite. The variation in MOF content in the g-C_3N_4-RGO-NH_2-MIL-125(Ti) composite also showed appreciable changes in its photocatalytic performance in which the best results were achieved with 20 wt. % MOF. Two reaction mechanisms with clear illustrations were proposed according to the band alignments and characterization results in which the g-C_3N_4-RGO-NH_2-MIL-125(Ti) composite displayed a Z-scheme heterojunction while a multi Type-II heterojunction system was proposed for the C_3N_4-RGO-NH_2-MIL-125(Ti)-GO-TNTs composite.

5.3   Future Recommendations

➤ More research is required for studying other operating parameters such as the reaction temperature and the light intensity.

➤ Further research of synthesis parameters of TNTs such as anodization time and voltage, electrolyte composition and the annealing temperature and time should be conducted.

➤ New techniques for controlling of the catalyst loading on the TNTs foil is required for future research to study its effect on the photocatalytic performance.

➤ Better understanding of the photocatalytic mechanisms of MOFs such as the Z-schemes and S-schemes is highly needed since it is considered to be the key for developing and engineering of photocatalysts with efficient charge separation and transport.

➤ For the current time implications and industrially feasibility, a scale-up study is necessary to design an appropriate photoreactor with thermodynamic analysis.

REFERENCES

1. Liu, Y., et al., Heterogeneous Fenton-like catalyst for treatment of rhamnolipid-solubilized hexadecane wastewater. Chemosphere, 2019. **236**: p. 124387.

2. Nakata, K. and A. Fujishima, TiO_2 photocatalysis: Design and applications. J. Photochem. Photobiol. C, 2012. **13**(3): p. 169-189.

3. Huskinson, B., et al., A metal-free organic–inorganic aqueous flow battery. Nature, 2014. **505**(7482): p. 195-198.

4. Alkhatib, I.I., et al., Metal-organic frameworks for photocatalytic CO_2 reduction under visible radiation: A review of strategies and applications. Catal. Today, 2020. **340**: p. 209-224.

5. Bekun, F.V., A.A. Alola, and S.A. Sarkodie, Toward a sustainable environment: Nexus between CO_2 emissions, resource rent, renewable and nonrenewable energy in 16-EU countries. Sci. Total Environ.   ,   2019. **657**: p. 1023-1029.

6. Goeppert, A., et al., Recycling of carbon dioxide to methanol and derived products–closing the loop. Chem. Soc. Rev., 2014. **43**(23): p. 7995-8048.

7. Mohammed, M., et al., Hydrogen rich gas from oil palm biomass as a potential source of renewable energy in Malaysia. Renew. Sust. Energ. Rev., 2011. **15**(2): p. 1258-1270.

8. Demirbas, A.H. and I. Demirbas, Importance of rural bioenergy for developing countries. Energy Convers. Manage., 2007. **48**(8): p. 2386-2398.

9. Gao, J., C. Jia, and B. Liu, Direct and selective hydrogenation of CO_2 to ethylene and propene by bifunctional catalysts. Catal. Sci. Technol., 2017. **7**(23): p. 5602-5607.

10. Tu, W., Y. Zhou, and Z. Zou, Photocatalytic conversion of CO_2 into renewable hydrocarbon fuels: state-of-the-art accomplishment, challenges, and prospects. Adv. Mater., 2014. **26**(27): p. 4607-4626.

11. Leung, D.Y., G. Caramanna, and M.M. Maroto-Valer, An overview of current status of carbon dioxide capture and storage technologies. Renew. Sust. Energ. Rev., 2014. **39**: p. 426-443.

12. Tahir, M. and N.S. Amin, Advances in visible light responsive titanium oxide-based photocatalysts for CO_2 conversion to hydrocarbon fuels. Energy Convers. Manage., 2013. **76**: p. 194-214.

13. Kabra, K., R. Chaudhary, and R.L. Sawhney, Treatment of hazardous organic and inorganic compounds through aqueous-phase photocatalysis: a review. Ind. Eng. Chem. Res., 2004. **43**(24): p. 7683-7696.

14. Fujishima, A. and K. Honda, Electrochemical photolysis of water at a semiconductor electrode. Nature, 1972. **238**(5358): p. 37-38.

15. Han, Q., et al., Atomically thin mesoporous nanomesh of graphitic C_3N_4 for high-efficiency photocatalytic hydrogen evolution. ACS Nano, 2016. **10**(2): p. 2745-2751.

16. Kamegawa, T., et al., Design of composite photocatalyst of TiO_2 and Y-zeolite for degradation of 2-propanol in the gas phase under UV and visible light irradiation. Molecules, 2014. **19**(10): p. 16477-16488.

17. Koodali, R.T. and D. Zhao, Photocatalytic degradation of aqueous organic pollutants using titania supported periodic mesoporous silica. Energy Environ. Sci., 2010. **3**(5): p. 608-614.

18. Dai, K., et al., Efficient visible-light-driven splitting of water into hydrogen over surface-fluorinated anatase TiO_2 nanosheets with exposed {001} facets/layered CdS–diethylenetriamine nanobelts. ACS Sustain. Chem. Eng., 2018. **6**(10): p. 12817-12826.

19. Ke, X., et al., Construction of flourinated-TiO_2 nanosheets with exposed {001} facets/CdSe-DETA nanojunction for enhancing visible-light-driven photocatalytic H_2 evolution. Ceram. Int, 2020. **46**(1): p. 866-876.

20. Tahir, B., M. Tahir, and N.S. Amin, Gold–indium modified TiO_2 nanocatalysts for photocatalytic CO_2 reduction with H_2 as reductant in a monolith photoreactor. Appl. Surf. Sci., 2015. **338**: p. 1-14.

21. Crake, A., Metal-organic frameworks based materials for photocatalytic CO_2 reduction. Mater. Sci. Technol., 2017. **33**(15): p. 1737-1749.

22. Kim, J., et al., CO_2 cycloaddition of styrene oxide over MOF catalysts. Appl. Catal. A, 2013. **453**: p. 175-180.

23. Dhakshinamoorthy, A., A.M. Asiri, and H. Garcia, Metal–organic framework (MOF) compounds: photocatalysts for redox reactions and solar fuel production. Angew. Chem. Int. Ed., 2016. **55**(18): p. 5414-5445.

24. Dan-Hardi, M., et al., A new photoactive crystalline highly porous titanium (IV) dicarboxylate. J. Am. Chem. Soc., 2009. **131**(31): p. 10857-10859.

25. Wang, H., et al., Synthesis and applications of novel graphitic carbon nitride/metal-organic frameworks mesoporous photocatalyst for dyes removal. Appl. Catal. B, 2015. **174**: p. 445-454.

26. Ritchie, H. and M. Roser, CO_2 and Greenhouse Gas Emissions. Our world in data, 2017.

27. Mikkelsen, M., M. Jørgensen, and F.C. Krebs, Synthesis and characterization of zwitterionic carbon dioxide fixing reagents. Int. J. Greenh. Gas Control., 2010. **4**(3): p. 452-458.

28. Alper, E. and O.Y. Orhan, CO_2 utilization: Developments in conversion processes. Petroleum, 2017. **3**(1): p. 109-126.

29. Haszeldine, R.S., Carbon capture and storage: how green can black be? Science, 2009. **325**(5948): p. 1647-1652.

30. Cebrucean, D., V. Cebrucean, and I. Ionel, CO_2 capture and storage from fossil fuel power plants. Energy Procedia, 2014. **63**: p. 18-26.

31. Onyebuchi, V.E., et al., A systematic review of key challenges of CO_2 transport via pipelines. Renew. Sust. Energ. Rev., 2018. **81**: p. 2563-2583.

32. Kelektsoglou, K., Carbon capture and storage: A review of mineral storage of CO_2 in Greece. Sustainability, 2018. **10**(12): p. 4400.

33. Gibbins, J. and H. Chalmers, Carbon capture and storage. Energy policy, 2008. **36**(12): p. 4317-4322.

34. ESRL, N., National Oceanic & Atmospheric Administration, Earth System Research Laboratory: Mauna Loa CO_2 Annual Mean Data by Dr. Pieter Tans, NOAA/ESRL (www. esrl. noaa. gov/gmd/ccgg/trends/) and Dr. Ralph KEELING, Scripps Institution of Oceanography (scrippsco2. ucsd. edu/). Book National Oceanic & Atmospheric Administration, Earth System Research Laboratory: Mauna Loa CO_2 Annual Mean Data by Dr. Pieter Tans, NOAA/ESRL (http://www. esrl. noaa. gov/gmd/ccgg/trends/) and Dr. Ralph KEELING, Scripps Institution of Oceanography (scrippsco2. ucsd. edu/), 2015.

35. Das, S. and W.W. Daud, RETRACTED: Photocatalytic CO_2 transformation into fuel: A review on advances in photocatalyst and photoreactor. 2014, Elsevier.

36. Abe, T., et al., CO$_2$ methanation property of Ru nanoparticle-loaded TiO$_2$ prepared by a polygonal barrel-sputtering method. Energy Environ. Sci., 2009. **2**(3): p. 315-321.

37. Wu, X.-Y. and A.F. Ghoniem, Mixed ionic-electronic conducting (MIEC) membranes for thermochemical reduction of CO$_2$: A review. Prog. Energy Combust. Sci., 2019. **74**: p. 1-30.

38. Smestad, G.P. and A. Steinfeld, photochemical and thermochemical production of solar fuels from H$_2$O and CO$_2$ using metal oxide catalysts. Ind. Eng. Chem. Res., 2012. **51**(37): p. 11828-11840.

39. Zhao, G., et al., Progress in catalyst exploration for heterogeneous CO$_2$ reduction and utilization: a critical review. J. Mater. Chem. A, 2017. **5**(41): p. 21625-21649.

40. Wee, J.-H., Carbon dioxide emission reduction using molten carbonate fuel cell systems. Renew. Sust. Energ. Rev., 2014. **32**: p. 178-191.

41. Jones, J.P., G.S. Prakash, and G.A. Olah, Electrochemical CO$_2$ reduction: recent advances and current trends. Isr. J. Chem., 2014. **54**(10): p. 1451-1466.

42. Chen, L.D., et al., Electric field effects in electrochemical CO$_2$ reduction. ACS Catal., 2016. **6**(10): p. 7133-7139.

43. Nitopi, S., et al., Progress and perspectives of electrochemical CO$_2$ reduction on copper in aqueous electrolyte. Chem. Rev., 2019. **119**(12): p. 7610-7672.

44. Usubharatana, P., et al., Photocatalytic process for CO$_2$ emission reduction from industrial flue gas streams. Ind. Eng. Chem. Res., 2006. **45**(8): p. 2558-2568.

45. Płaczek, M., A. Patyna, and S. Witczak. Technical evaluation of photobioreactors for microalgae cultivation. in E3S web of conferences. 2017. EDP Sciences.

46. Barua, S. and U.K. Deb, Hydrodynamics of Microalgae and CO$_2$ flow in a Tubular Photobioreactor and consequent effects on Microalgae growth. Rajshahi Univ. J. Sci. Eng., 2016. **44**: p. 75-83.

47. Gong, F., Z. Cai, and Y. Li, Synthetic biology for CO$_2$ fixation. Sci China Life Sci, 2016. **59**(11): p. 1106-1114.

48. Mangan, N.M., et al., pH determines the energetic efficiency of the cyanobacterial CO$_2$ concentrating mechanism. PNAS, 2016. **113**(36): p. E5354-E5362.

49.   Moraes, L., et al., Microalgal biotechnology for greenhouse gas control: carbon dioxide fixation by Spirulina sp. at different diffusers. Ecol. Eng., 2016. **91**: p. 426-431.

50.   Das, S. and W.W. Daud, A review on advances in photocatalysts towards CO_2 conversion. RSC Adv., 2014. **4**(40): p. 20856-20893.

51.   Long, J.R. and O.M. Yaghi, The pervasive chemistry of metal–organic frameworks. Chem. Soc. Rev., 2009. **38**(5): p. 1213-1214.

52.   Jiao, L., et al., Metal–organic frameworks: Structures and functional applications. Mater. Today, 2019. **27**: p. 43-68.

53.   Cheng, M., et al., Metal-organic frameworks for highly efficient heterogeneous Fenton-like catalysis. Coord. Chem. Rev., 2018. **368**: p. 80-92.

54.   Jiang, D., et al., The application of different typological and structural MOFs-based materials for the dyes adsorption. Coord. Chem. Rev., 2019. **380**: p. 471-483.

55.   Li, H., et al., Recent advances in gas storage and separation using metal–organic frameworks. Mater. Today, 2018. **21**(2): p. 108-121.

56.   Zhang, M., et al., Novel MOF-derived Co@ N-C bifunctional catalysts for highly efficient Zn–air batteries and water splitting. Adv. Mater., 2018. **30**(10): p. 1705431.

57.   Wu, M.X. and Y.W. Yang, Metal–organic framework (MOF)-based drug/cargo delivery and cancer therapy. Adv. Mater., 2017. **29**(23): p. 1606134.

58.   Wang, T., et al., Rational approach to guest confinement inside MOF cavities for low-temperature catalysis. Nat. Commun., 2019. **10**(1): p. 1-9.

59.   Klein, N., et al., A mesoporous metal–organic framework. Angew. Chem. Int. Ed., 2009. **48**(52): p. 9954-9957.

60.   Sahoo, P.C., S. Martha, and K. Parida. Solar fuels from CO_2 photoreduction over nano-structured catalysts. in Mater. Sci. Forum. 2016. Trans Tech Publ.

61.   Kočí, K., L. Obalová, and Z. Lacný, Photocatalytic reduction of CO_2 over TiO_2 based catalysts. Chem. Pap. - Chem. Zvesti, 2008. **62**(1): p. 1-9.

62.   Dhakshinamoorthy, A., Z. Li, and H. Garcia, Catalysis and photocatalysis by metal organic frameworks. Chem. Soc. Rev., 2018. **47**(22): p. 8134-8172.

63.   Shehzad, N., et al., A critical review on TiO_2 based photocatalytic CO_2 reduction system: Strategies to improve efficiency. J. CO2 Util., 2018. **26**: p. 98-122.

64.   Koch, S.W., et al., Semiconductor excitons in new light. Nat. Mater., 2006. **5**(7): p. 523-531.

65.   Liu, B., et al., Thermodynamic and kinetic analysis of heterogeneous photocatalysis for semiconductor systems. Phys. Chem. Chem. Phys., 2014. **16**(19): p. 8751-8760.

66.   González, C.A., et al., Pd/TiO_2 washcoated cordierite minimonoliths for hydrodechlorination of light organochlorinated compounds. Ind. Eng. Chem. Res., 2007. **46**(24): p. 7961-7969.

67.   Truong, Q.D., et al., Synthesis of TiO_2 nanoparticles using novel titanium oxalate complex towards visible light-driven photocatalytic reduction of CO_2 to CH_3OH. Appl. Catal. A, 2012. **437**: p. 28-35.

68.   Takanabe, K., Solar water splitting using semiconductor photocatalyst powders, in Sol. Energy for Fuels. 2015, Springer. p. 73-103.

69.   Mills, A. and S. Le Hunte, An overview of semiconductor photocatalysis. J. Photochem. Photobiol. A, 1997. **108**(1): p. 1-35.

70.   Albero, J., H. Garcia, and A. Corma, Temperature dependence of solar light assisted CO_2 reduction on Ni based photocatalyst. Top. Catal., 2016. **59**(8-9): p. 787-791.

71.   Jang, H.D., S.-K. Kim, and S.-J. Kim, Effect of particle size and phase composition of titanium dioxide nanoparticles on the photocatalytic properties. J. Nanopart. Res., 2001. **3**(2-3): p. 141-147.

72.   Chang, X., T. Wang, and J. Gong, CO_2 photo-reduction: insights into CO_2 activation and reaction on surfaces of photocatalysts. Energy Environ. Sci., 2016. **9**(7): p. 2177-2196.

73.   Fu, Y., et al., An amine-functionalized titanium metal–organic framework photocatalyst with visible-light-induced activity for CO_2 reduction. Angew. Chem. Int. Ed., 2012. **51**(14): p. 3364-3367.

74.   Li, R., W. Zhang, and K. Zhou, Metal–Organic-Framework-Based Catalysts for Photoreduction of CO_2. Adv. Mater., 2018. **30**(35): p. 1705512.

75.   Liu, L. and Y. Li, Understanding the reaction mechanism of photocatalytic reduction of CO_2 with H_2O on TiO_2-based photocatalysts: a review. Aerosol Air Qual. Res., 2013. **14**(2): p. 453-469.

76.   Karamian, E. and S. Sharifnia, On the general mechanism of photocatalytic reduction of CO_2. J. CO2 Util., 2016. **16**: p. 194-203.

77.   Indrakanti, V.P., J.D. Kubicki, and H.H. Schobert, Photoinduced activation of CO_2 on TiO_2 surfaces: Quantum chemical modeling of CO_2 adsorption on oxygen vacancies. Fuel Process. Technol., 2011. **92**(4): p. 805-811.

78.   Rodriguez, M.M., et al., A density functional theory and experimental study of CO_2 interaction with brookite TiO_2. J. Phys. Chem. C, 2012. **116**(37): p. 19755-19764.

79.   Shkrob, I.A., et al., Photoredox reactions and the catalytic cycle for carbon dioxide fixation and methanogenesis on metal oxides. J. Phys. Chem. C, 2012. **116**(17): p. 9450-9460.

80.   Lee, J., D.C. Sorescu, and X. Deng, Electron-induced dissociation of CO_2 on TiO_2 (110). J. Am. Chem. Soc., 2011. **133**(26): p. 10066-10069.

81.   Abe, R., Recent progress on photocatalytic and photoelectrochemical water splitting under visible light irradiation. J. Photochem. Photobiol. C, 2010. **11**(4): p. 179-209.

82.   Maeda, K., Photocatalytic water splitting using semiconductor particles: history and recent developments. J. Photochem. Photobiol. C, 2011. **12**(4): p. 237-268.

83.   Akhter, P., et al., Novel nanostructured-TiO_2 materials for the photocatalytic reduction of CO_2 greenhouse gas to hydrocarbons and syngas. Fuel, 2015. **149**: p. 55-65.

84.   Yuan, L. and Y.-J. Xu, Photocatalytic conversion of CO_2 into value-added and renewable fuels. Appl. Surf. Sci., 2015. **342**: p. 154-167.

85.   Habisreutinger, S.N., L. Schmidt-Mende, and J.K. Stolarczyk, Photocatalytic reduction of CO_2 on TiO_2 and other semiconductors. Angew. Chem. Int. Ed., 2013. **52**(29): p. 7372-7408.

86.   Anpo, M., et al., Photocatalytic reduction of CO_2 with H_2O on various titanium oxide catalysts. J. Electroanal. Chem., 1995. **396**(1-2): p. 21-26.

87. Subrahmanyam, M., S. Kaneco, and N. Alonso-Vante, A screening for the photo reduction of carbon dioxide supported on metal oxide catalysts for C_1–C_3 selectivity. Appl. Catal. B, 1999. **23**(2-3): p. 169-174.

88. Koci, K., L. Obalova, and O. Solcova, Kinetic study of photocatalytic reduction of CO_2 over TiO_2. CHEM PROCESS ENG-INZ, 2010. **31**: p. 395-407.

89. Sasirekha, N., S.J.S. Basha, and K. Shanthi, Photocatalytic performance of Ru doped anatase mounted on silica for reduction of carbon dioxide. Appl. Catal. B, 2006. **62**(1-2): p. 169-180.

90. Camarillo, R., et al., Preparation of TiO_2-based catalysts with supercritical fluid technology: characterization and photocatalytic activity in CO_2 reduction. J. Chem. Technol. Biotechnol., 2017. **92**(7): p. 1710-1720.

91. Tan, L.-L., et al., Photocatalytic reduction of CO_2 with H_2O over graphene oxide-supported oxygen-rich TiO_2 hybrid photocatalyst under visible light irradiation: process and kinetic studies. Chem. Eng. J., 2017. **308**: p. 248-255.

92. Xiong, Z., et al., Selective photocatalytic reduction of CO_2 into CH_4 over Pt-Cu_2O TiO_2 nanocrystals: The interaction between Pt and Cu_2O cocatalysts. Appl. Catal. B, 2017. **202**: p. 695-703.

93. Camarillo, R., et al., Enhancing the photocatalytic reduction of CO_2 through engineering of catalysts with high pressure technology: Pd/TiO_2 photocatalysts. J Supercrit Fluids, 2017. **123**: p. 18-27.

94. Teramura, K., et al., Photocatalytic reduction of CO_2 to CO in the presence of H_2 or CH_4 as a reductant over MgO. J. Phys. Chem Bs, 2004. **108**(1): p. 346-354.

95. Tahir, B., M. Tahir, and N.S. Amin, Performance analysis of monolith photoreactor for CO_2 reduction with H_2. Energy Convers. Manage., 2015. **90**: p. 272-281.

96. Pan, T.-C., et al., Study of the silver modified TiO_2 nanotube array applied to hydrogen evolution. Appl. Surf. Sci., 2014. **296**: p. 189-194.

97. Cao, S.-W., et al., Noble-metal-free g-C_3N_4/Ni(dmgH)$_2$ composite for efficient photocatalytic hydrogen evolution under visible light irradiation. Appl. Surf. Sci., 2014. **319**: p. 344-349.

98. Tahir, B., M. Tahir, and N.A.S. Amin, Photo-induced CO_2 reduction by CH_4/H_2O to fuels over Cu-modified g-C_3N_4 nanorods under simulated solar energy. Appl. Surf. Sci., 2017. **419**: p. 875-885.

99. Thampi, K.R., J. Kiwi, and M. Graetzel, Methanation and photo-methanation of carbon dioxide at room temperature and atmospheric pressure. Nature, 1987. **327**(6122): p. 506-508.

100. Kohno, Y., et al., Photo-enhanced reduction of carbon dioxide with hydrogen over Rh/TiO_2. J. Photochem. Photobiol., A, 1999. **126**(1-3): p. 117-123.

101. Kohno, Y., et al., Photoreduction of carbon dioxide with hydrogen over ZrO_2. Chem. Commun., 1997(9): p. 841-842.

102. Aliwi, S. and K. Al-Jubori, Photoreduction of CO_2 by metal sulphide semiconductors in presence of H_2S. Sol. Energy Mater., 1989. **18**(3-4): p. 223-229.

103. Kohno, Y., et al., Reaction mechanism in the photoreduction of CO_2 with CH_4 over ZrO_2. Phys. Chem. Chem. Phys., 2000. **2**(22): p. 5302-5307.

104. Kohno, Y., et al., Photoreduction of carbon dioxide with methane over ZrO_2. Chem. Lett., 1997. **26**(10): p. 993-994.

105. Jiang, Z., et al., Photocatalytic reduction of CO_2 to methanol by three-dimensional hollow structures of Bi_2WO_6 quantum dots. Appl. Catal. B, 2017. **219**: p. 209-215.

106. Sun, Z., et al., Catalysis of carbon dioxide photoreduction on nanosheets: fundamentals and challenges. Angew. Chem. Int. Ed., 2018. **57**(26): p. 7610-7627.

107. Zhang, W., A.R. Mohamed, and W.-J. Ong, Z-Scheme Photocatalytic Systems for Carbon Dioxide Reduction: Where Are We Now? Angew. Chem., 2020.

108. Liang, Z., et al., In-situ growth of 0D/2D Ni_2P quantum dots/red phosphorus nanosheets with pn heterojunction for efficient photocatalytic H_2 evolution under visible light. Appl. Surf. Sci., 2019. **484**: p. 293-299.

109. Li, Z., et al., Enhanced photocatalytic H_2 production over dual-cocatalyst-modified g-C_3N_4 heterojunctions. Chin. J. Catal., 2019. **40**(3): p. 434-445.

110. Zeng, D., et al., Sub-5 nm ultra-fine FeP nanodots as efficient co-catalysts modified porous g-C_3N_4 for precious-metal-free photocatalytic hydrogen

evolution under visible light. ACS Appl. Mater. Interfaces, 2019. **11**(6): p. 5651-5660.

111. Li, Y., et al., 2D/2D/2D heterojunction of Ti_3C_2 MXene/MoS_2 nanosheets/TiO_2 nanosheets with exposed (001) facets toward enhanced photocatalytic hydrogen production activity. Appl. Catal. B, 2019. **246**: p. 12-20.

112. Zeng, D., et al., Toward noble-metal-free visible-light-driven photocatalytic hydrogen evolution: monodisperse sub–15 nm Ni_2P nanoparticles anchored on porous g-C_3N_4 nanosheets to engineer 0D-2D heterojunction interfaces. Appl. Catal. B, 2018. **221**: p. 47-55.

113. Ke, J., et al., Nanostructured ternary metal tungstate-based photocatalysts for environmental purification and solar water splitting: a review. Nanomicro Lett, 2018. **10**(4): p. 69.

114. Wang, J., et al., gC_3N_4 photocatalysts with enhanced photoreduction CO_2 activity under visible light irradiation, ACS Appl. Mater. Interfaces, 2016. **8**(6): p. 3765-3775.

115. Ranjit, K.T. and B. Viswanathan, Synthesis, characterization and photocatalytic properties of iron-doped TiO_2 catalysts. J. Photochem. Photobiol. A, 1997. **108**(1): p. 79-84.

116. Vinodgopal, K. and P.V. Kamat, Enhanced rates of photocatalytic degradation of an azo dye using SnO_2/TiO_2 coupled semiconductor thin films. Environ. Sci. Technol., 1995. **29**(3): p. 841-845.

117. Low, J., et al., Heterojunction photocatalysts. Adv. Mater., 2017. **29**(20): p. 1601694.

118. Zhou, H., et al., Towards highly efficient photocatalysts using semiconductor nanoarchitectures. Energy Environ. Sci., 2012. **5**(5): p. 6732-6743.

119. Tahir, M., S. Tasleem, and B. Tahir, Recent development in band engineering of binary semiconductor materials for solar driven photocatalytic hydrogen production. Int. J. Hydrogen Energy, 2020.

120. Hyun, J.K., S. Zhang, and L.J. Lauhon, Nanowire heterostructures. Annu. Rev. Mater. Res., 2013. **43**: p. 451-479.

121. Shi, W. and N. Chopra, Nanoscale heterostructures for photoelectrochemical water splitting and photodegradation of pollutants. Nanomater. Energy, 2013. **2**(3): p. 158-178.

122. Ong, W.-J., et al., Highly reactive {001} facets of TiO_2-based composites: synthesis, formation mechanism and characterization. Nanoscale, 2014. **6**(4): p. 1946-2008.

123. Ong, W.J., et al., Facet-dependent photocatalytic properties of TiO_2-based composites for energy conversion and environmental remediation. ChemSusChem, 2014. **7**(3): p. 690-719.

124. Tachibana, Y., L. Vayssieres, and J.R. Durrant, Artificial photosynthesis for solar water-splitting. Nat. Photonics, 2012. **6**(8): p. 511.

125. Zhou, P., J. Yu, and M. Jaroniec, All-solid-state Z-scheme photocatalytic systems. Adv. Mater., 2014. **26**(29): p. 4920-4935.

126. Bard, A.J., Photoelectrochemistry and heterogeneous photo-catalysis at semiconductors. J. Photochem., 1979. **10**(1): p. 59-75.

127. Sepahvand, H. and S. Sharifnia, Photocatalytic overall water splitting by Z-scheme g-C_3N_4/$BiFeO_3$ heterojunction. Int. J. Hydrog. Energy, 2019. **44**(42): p. 23658-23668.

128. Wang, Z., et al., Direct Z-scheme $ZnIn_2S_4$/$LaNiO_3$ nanohybrid with enhanced photocatalytic performance for H_2 evolution. Int. J. Hydrogen Energy, 2020. **45**(7): p. 4113-4121.

129. Xu, Q., et al., Direct Z-scheme photocatalysts: Principles, synthesis, and applications. Mater. Today, 2018. **21**(10): p. 1042-1063.

130. Li, H., et al., Z-Scheme photocatalytic systems for promoting photocatalytic performance: recent progress and future challenges. Adv. Sci., 2016. **3**(11): p. 1500389.

131. Maeda, K., Z-scheme water splitting using two different semiconductor photocatalysts. ACS Catal., 2013. **3**(7): p. 1486-1503.

132. Biesinger, M.C., et al., Resolving surface chemical states in XPS analysis of first row transition metals, oxides and hydroxides: Cr, Mn, Fe, Co and Ni. Appl. Surf. Sci., 2011. **257**(7): p. 2717-2730.

133. Li, P., et al., All-solid-state Z-scheme system arrays of $Fe_2V_4O_{13}$/RGO/CdS for visible light-driving photocatalytic CO_2 reduction into renewable hydrocarbon fuel. Chem. Commun., 2014. **51**(4): p. 800-803.

134. Fu, J., et al., Ultrathin 2D/2D WO_3/g-C_3N_4 step-scheme H_2-production photocatalyst. Appl. Catal. B, 2019. **243**: p. 556-565.

135. Xu, Q., et al., S-scheme heterojunction photocatalyst. Chem, 2020.

136. Ge, H., et al., S-scheme heterojunction TiO_2/CdS nanocomposite nanofiber as H_2-production photocatalyst. ChemCatChem, 2019. **11**(24): p. 6301-6309.

137. He, F., et al., 2D/2D/0D $TiO_2/C_3N_4/Ti_3C_2$ MXene composite S-scheme photocatalyst with enhanced CO_2 reduction activity. Appl. Catal. B, 2020: p. 119006.

138. Crake, A., et al., The effect of materials architecture in TiO_2/MOF composites on CO_2 photoreduction and charge transfer. Small, 2019. **15**(11): p. 1805473.

139. Crake, A., et al., CO_2 capture and photocatalytic reduction using bifunctional TiO_2/MOF nanocomposites under UV–vis irradiation. Appl. Catal. B, 2017. **210**: p. 131-140.

140. Chen, J., et al., $ZnIn_2S_4/UiO-66-(SH)_2$ composites as efficient visible-light photocatalyst for Rh B degradation. Inorg. Chem. Commun., 2019. **102**: p. 25-29.

141. Zhang, X., et al., g-C_3N_4/UiO-66 nanohybrids with enhanced photocatalytic activities for the oxidation of dye under visible light irradiation. Mater. Res. Bull., 2018. **99**: p. 349-358.

142. Meng, J., et al., Z-scheme photocatalytic CO_2 reduction on a heterostructure of oxygen-defective ZnO/reduced graphene oxide/UiO-66-NH_2 under visible light. ACS Appl. Mater. Interfaces, 2018. **11**(1): p. 550-562.

143. Askari, N., et al., Fabrication of $CuWO_4/Bi_2S_3$/ZIF67 MOF: A novel double Z-scheme ternary heterostructure for boosting visible-light photodegradation of antibiotics. Chemosphere, 2020: p. 126453.

144. Jin, Z., Y. Li, and Q. Ma, CoAl LDH@Ni-MOF-74 S-Scheme Heterojunction for Efficient Hydrogen Evolution. Trans. Tianjin Univ., 2020: p. 1-12.

145. Wang, D., et al., Fe-based MOFs for photocatalytic CO_2 reduction: role of coordination unsaturated sites and dual excitation pathways. ACS Catal., 2014. **4**(12): p. 4254-4260.

146. Xie, Y., et al., Creating Chemisorption Sites for Enhanced CO_2 Photoreduction Activity through Alkylamine Modification of MIL-101-Cr. ACS Appl. Mater. Interfaces, 2019. **11**(30): p. 27017-27023.

147. Sun, D., et al., Studies on Photocatalytic CO_2 Reduction over NH_2-UiO-66 (Zr) and Its Derivatives: Towards a Better Understanding of Photocatalysis

on Metal–Organic Frameworks. Chem. Eur. J., 2013. **19**(42): p. 14279-14285.

148. Li, R., et al., Integration of an inorganic semiconductor with a metal–organic framework: a platform for enhanced gaseous photocatalytic reactions. Adv. Mater., 2014. **26**(28): p. 4783-4788.

149. Sun, D., et al., Noble metals can have different effects on photocatalysis over metal–organic frameworks (MOFs): a case study on M/NH₂-MIL-125 (Ti)(M= Pt and Au). Chem. Eur. J., 2014. **20**(16): p. 4780-4788.

150. Sun, D., et al., Construction of a supported Ru complex on bifunctional MOF-253 for photocatalytic CO_2 reduction under visible light. Chem. Commun., 2015. **51**(13): p. 2645-2648.

151. Han, Y., et al., Noble metal (Pt, Au@ Pd) nanoparticles supported on metal organic framework (MOF-74) nanoshuttles as high-selectivity CO_2 conversion catalysts. J. Catal., 2019. **370**: p. 70-78.

152. Chen, Y., et al., Metal–organic frameworks (MOFs) for photocatalytic CO_2 reduction. Catal. Sci. Technol., 2017. **7**(21): p. 4893-4904.

153. Yu, Z.-T., et al., Construction of a microporous inorganic–organic hybrid compound with uranyl units. Chem. Commun., 2004(16): p. 1814-1815.

154. Mahata, P., G. Madras, and S. Natarajan, Novel photocatalysts for the decomposition of organic dyes based on metal-organic framework compounds. J. Phys. Chem. B, 2006. **110**(28): p. 13759-13768.

155. Wang, C.-C., et al., Photocatalytic CO_2 reduction in metal–organic frameworks: a mini review. J. Mol. Struct., 2015. **1083**: p. 127-136.

156. Torrisi, A., R.G. Bell, and C. Mellot-Draznieks, Functionalized MOFs for enhanced CO_2 capture. Cryst. Growth Des., 2010. **10**(7): p. 2839-2841.

157. Dey, C., et al., Crystalline metal-organic frameworks (MOFs): synthesis, structure and function. Acta. Crystallogr. B. Struct. Sci. Cryst. Eng. Mater., 2014. **70**(1): p. 3-10.

158. Augustus, E.N., et al., Metal-organic Frameworks as Novel Adsorbents: A Preview. Am. J. Environ. Prot., 2017. **5**(2): p. 61-67.

159. Leng, K., et al., Rapid synthesis of metal–organic frameworks MIL-101 (Cr) without the addition of solvent and hydrofluoric acid. Cryst. Growth Des., 2016. **16**(3): p. 1168-1171.

160. Joaristi, A.M., J. Juan-Alca niz, P. Serra-Crespo, F. Kapteijn, J. Gascon. Cryst. Growth Des., 2012. **12**: p. 3489-3498.

161. Kim, J., W.Y. Kim, and W.-S. Ahn, Amine-functionalized MIL-53(Al) for CO_2/N_2 separation: Effect of textural properties. Fuel, 2012. **102**: p. 574-579.

162. Horcajada, P., et al., Synthesis and catalytic properties of MIL-100(Fe), an iron(III) carboxylate with large pores. Chem. Commun., 2007(27): p. 2820-2822.

163. Horcajada, P., et al., Metal–organic frameworks as efficient materials for drug delivery. Angew. Chem. Int. Ed., 2006. **118**(36): p. 6120-6124.

164. Taylor-Pashow, K.M., et al., Postsynthetic modifications of iron-carboxylate nanoscale metal− organic frameworks for imaging and drug delivery. J. Am. Chem. Soc., 2009. **131**(40): p. 14261-14263.

165. Jhung, S.H., et al., Microwave synthesis of chromium terephthalate MIL-101 and its benzene sorption ability. Adv. Mater., 2007. **19**(1): p. 121-124.

166. Abid, H.R., et al., Nanosize Zr-metal organic framework (UiO-66) for hydrogen and carbon dioxide storage. Chem. Eng. J., 2012. **187**: p. 415-420.

167. Ali-Moussa, H., et al., Synthesis and post-synthetic modification of UiO-67 type metal-organic frameworks by mechanochemistry. Mater. Lett., 2017. **197**: p. 171-174.

168. Shi, L., et al., Electrostatic Self-Assembly of Nanosized Carbon Nitride Nanosheet onto a Zirconium Metal–Organic Framework for Enhanced Photocatalytic CO_2 Reduction. Adv. Funct. Mater., 2015. **25**(33): p. 5360-5367.

169. Lee, Y., et al., Photocatalytic CO_2 reduction using visible light by metal-monocatecholato species in a metal–organic framework. Chem. Commun., 2015. **51**(92): p. 16549-16552.

170. Wang, X., et al., Microwave irradiation induced $UIO-66-NH_2$ anchored on graphene with high activity for photocatalytic reduction of CO_2. Appl. Catal. B, 2018. **228**: p. 47-53.

171. Fei, H., et al., Photocatalytic CO_2 reduction to formate using a Mn(I) molecular catalyst in a robust metal–organic framework. Inorg. Chem., 2015. **54**(14): p. 6821-6828.

172. Chui, S.S.-Y., et al., A chemically functionalizable nanoporous material [Cu_3 $(TMA)_2(H_2O)_3$]n. Science, 1999. **283**(5405): p. 1148-1150.

173. Seo, Y.-K., et al., Microwave synthesis of hybrid inorganic–organic materials including porous $Cu_3(BTC)_2$ from Cu (II)-trimesate mixture. Microporous Mesoporous Mater., 2009. **119**(1-3): p. 331-337.

174. Mueller, U., et al., Metal–organic frameworks—prospective industrial applications. J. Mater. Chem., 2006. **16**(7): p. 626-636.

175. Pichon, A. and S.L. James, An array-based study of reactivity under solvent-free mechanochemical conditions—insights and trends. CrystEngComm, 2008. **10**(12): p. 1839-1847.

176. Li, Z.-Q., et al., Ultrasonic synthesis of the microporous metal–organic framework $Cu_3(BTC)_2$ at ambient temperature and pressure: an efficient and environmentally friendly method. Mater. Lett., 2009. **63**(1): p. 78-80.

177. Beldon, P.J., et al., Rapid room-temperature synthesis of zeolitic imidazolate frameworks by using mechanochemistry. Angew. Chem. Int. Ed., 2010. **122**(50): p. 9834-9837.

178. Seoane, B., et al., Sonocrystallization of zeolitic imidazolate frameworks (ZIF-7, ZIF-8, ZIF-11 and ZIF-20). CrystEngComm, 2012. **14**(9): p. 3103-3107.

179. Banerjee, R., et al., High-throughput synthesis of zeolitic imidazolate frameworks and application to CO_2 capture. Science, 2008. **319**(5865): p. 939-943.

180. Cho, H.-Y., et al., High yield 1-L scale synthesis of ZIF-8 via a sonochemical route. Microporous Mesoporous Mater., 2013. **169**: p. 180-184.

181. Park, J.-H., S.-H. Park, and S.-H. Jhung, Microwave-syntheses of zeolitic imidazolate framework material, ZIF-8. J. Korean Chem. Soc., 2009. **53**(5): p. 553-559.

182. Yan, S., et al., Co-ZIF-9/TiO_2 nanostructure for superior CO_2 photoreduction activity. J. Mater. Chem. A, 2016. **4**(39): p. 15126-15133.

183. Zhang, H., et al., Microwave-Assisted solvent-free synthesis of zeolitic imidazolate framework-67. J. Nanomater., 2016. **2016**.

184. Eddaoudi, M., et al., Systematic design of pore size and functionality in isoreticular MOFs and their application in methane storage. Science, 2002. **295**(5554): p. 469-472.

185. Lee, Y.-R., J. Kim, and W.-S. Ahn, Synthesis of metal-organic frameworks: A mini review. Korean J. Chem. Eng., 2013. **30**(9): p. 1667-1680.

186.   Son, W.-J., et al., Sonochemical synthesis of MOF-5. Chem. Commun., 2008(47): p. 6336-6338.

187.   Yang, D.-A., et al., CO_2 capture and conversion using Mg-MOF-74 prepared by a sonochemical method. Energy Environ. Sci., 2012. **5**(4): p. 6465-6473.

188.   Kitaura, R., et al., Porous coordination-polymer crystals with gated channels specific for supercritical gases. Angew. Chem. Int. Ed., 2003. **115**(4): p. 444-447.

189.   Cho, H.-Y., et al., CO_2 adsorption and catalytic application of Co-MOF-74 synthesized by microwave heating. Catal. Today, 2012. **185**(1): p. 35-40.

190.   Jung, D.-W., et al., Facile synthesis of MOF-177 by a sonochemical method using 1-methyl-2-pyrrolidinone as a solvent. Dalton Trans., 2010. **39**(11): p. 2883-2887.

191.   Yu, K., et al., Highly efficient adsorptive removal of sulfamethoxazole from aqueous solutions by porphyrinic MOF-525 and MOF-545. Chemosphere, 2020. **250**: p. 126133.

192.   Howlader, P. and P.S. Mukherjee, Solvent directed synthesis of molecular cage and metal organic framework of copper(II) paddlewheel cluster. Isr. J. Chem., 2019. **59**(3-4): p. 292-298.

193.   Millward, A.R. and O.M. Yaghi, Metal− organic frameworks with exceptionally high capacity for storage of carbon dioxide at room temperature. J. Am. Chem. Soc., 2005. **127**(51): p. 17998-17999.

194.   Ni, Z. and R.I. Masel, Rapid production of metal−organic frameworks via microwave-assisted solvothermal synthesis. J. Am. Chem. Soc., 2006. **128**(38): p. 12394-12395.

195.   Liu, Y., et al., Chemical adsorption enhanced CO_2 capture and photoreduction over a copper porphyrin based metal organic framework. ACS Appl. Mater. Interfaces, 2013. **5**(15): p. 7654-7658.

196.   Murinzi, T., E. Hosten, and G. Watkins, Synthesis and characterization of a cobalt-2, 6-pyridinedicarboxylate MOF with potential application in electrochemical sensing. Polyhedron, 2017. **137**: p. 188-196.

197.   Shang, Q., et al., A novel nitrogen heterocyclic ligand-based MOF: synthesis, characterization and photocatalytic properties. New J. Chem., 2019. **43**(42): p. 16595-16603.

198. Wang, M., D. Wang, and Z. Li, Self-assembly of CPO-27-Mg/TiO_2 nanocomposite with enhanced performance for photocatalytic CO_2 reduction. Appl. Catal. B, 2016. **183**: p. 47-52.

199. Kim, M.K., et al., CAU-1 and CAU-2: New tubular alkali metal–organic framework materials, $A_3[C_6H_3 (CO_2)(CO_2H_{0.5})(CO_2H)]_2$ (A= K or Rb). CrystEngComm, 2010. **12**(5): p. 1481-1484.

200. Zhao, S., et al., Ultrathin metal–organic framework nanosheets for electrocatalytic oxygen evolution. Nat. Energy, 2016. **1**(12): p. 1-10.

201. Zhu, W., et al., Selective reduction of CO_2 by conductive MOF nanosheets as an efficient co-catalyst under visible light illumination. Appl. Catal. B, 2018. **238**: p. 339-345.

202. Mu, Q., et al., Electrostatic charge transfer for boosting the photocatalytic CO_2 reduction on metal centers of 2D MOF/rGO heterostructure. Appl. Catal. B, 2020. **262**: p. 118144.

203. Chen, D., et al., Highly efficient visible-light-driven CO_2 reduction to formate by a new anthracene-based zirconium MOF via dual catalytic routes. J. Mater. Chem. A, 2016. **4**(7): p. 2657-2662.

204. Kim, J., et al., Control of catenation in CuTATB-n metal–organic frameworks by sonochemical synthesis and its effect on CO_2 adsorption. J. Mater. Chem., 2011. **21**(9): p. 3070-3076.

205. Li, H., et al., Enhanced adsorptive removal of anionic and cationic dyes from single or mixed dye solutions using MOF PCN-222. RSC Adv., 2017. **7**(27): p. 16273-16281.

206. Feng, D., et al., Kinetically tuned dimensional augmentation as a versatile synthetic route towards robust metal–organic frameworks. Nat. Commun., 2014. **5**(1): p. 1-9.

207. Huang, R., et al., A Rhenium-Functionalized Metal–Organic Framework as a Single-Site Catalyst for Photochemical Reduction of Carbon Dioxide. Eur. J. Inorg. Chem., 2016. **2016**(27): p. 4358-4362.

208. Ye, L., et al., Assembly of highly efficient photocatalytic CO_2 conversion systems with ultrathin two-dimensional metal–organic framework nanosheets. Appl. Catal. B, 2018. **227**: p. 54-60.

209. Sadeghi, N., S. Sharifnia, and M.S. Arabi, A porphyrin-based metal organic framework for high rate photoreduction of CO_2 to CH_4 in gas phase. J. CO2 Util., 2016. **16**: p. 450-457.

210. Khazalpour, S., et al., Electrochemical synthesis of pillared layer mixed ligand metal–organic framework: DMOF-1–Zn. RSC Adv., 2015. **5**(46): p. 36547-36551.

211. Sun, M., et al., Enhancement of visible-light-driven CO_2 reduction performance using an amine-functionalized zirconium metal–organic framework. Dalton Trans., 2018. **47**(3): p. 909-915.

212. Chen, E.X., et al., Acid and Base Resistant Zirconium Polyphenolate-Metalloporphyrin Scaffolds for Efficient CO_2 Photoreduction. Adv. Mater., 2018. **30**(2): p. 1704388.

213. Wang, C.-C. and J.Y. Ying, Sol−gel synthesis and hydrothermal processing of anatase and rutile titania nanocrystals. Chem. Mater., 1999. **11**(11): p. 3113-3120.

214. Halper, S.R., et al., Topological control in heterometallic metal−organic frameworks by anion templating and metalloligand design. J. Am. Chem. Soc., 2006. **128**(47): p. 15255-15268.

215. Du, M., C.-P. Li, and X.-J. Zhao, Metal-controlled assembly of coordination polymers with the flexible building block 4-pyridylacetic acid (Hpya). Cryst. Growth Des., 2006. **6**(1): p. 335-341.

216. Yoo, Y., V. Varela-Guerrero, and H.-K. Jeong, Isoreticular metal− organic frameworks and their membranes with enhanced crack resistance and moisture stability by surfactant-assisted drying. Langmuir, 2011. **27**(6): p. 2652-2657.

217. Park, S.-E., et al., Supramolecular interactions and morphology control in microwave synthesis of nanoporous materials. Catal. Surv. Asia, 2004. **8**(2): p. 91-110.

218. Hindelang, K., et al., Tandem post-synthetic modification for functionalized metal–organic frameworks via epoxidation and subsequent epoxide ring-opening. Chem. Commun., 2012. **48**(23): p. 2888-2890.

219. Jhung, S.H., et al., Selective formation of SAPO-5 and SAPO-34 molecular sieves with microwave irradiation and hydrothermal heating. Microporous Mesoporous Mater., 2003. **64**(1-3): p. 33-39.

220. Jhung, S.H., et al., Selective crystallization of CoAPO-34 and VAPO-5 molecular sieves under microwave irradiation in an alkaline or neutral condition. Microporous Mesoporous Mater., 2005. **80**(1-3): p. 147-152.

221. Kang, K.-K., C.-H. Park, and W.-S. Ahn, Microwave preparation of a titanium-substituted mesoporous molecular sieve. Catal. Lett., 1999. **59**(1): p. 45-49.

222. Hwang, Y.K., et al., Microwave fabrication of MFI zeolite crystals with a fibrous morphology and their applications. Angew. Chem. Int. Ed., 2005. **44**(4): p. 556-560.

223. Jhung, S.H., et al., Crystal morphology control of AFI type molecular sieves with microwave irradiation. J. Mater. Chem., 2004. **14**(2): p. 280-285.

224. Martinez Joaristi, A., et al., Electrochemical synthesis of some archetypical Zn^{2+}, Cu^{2+}, and Al^{3+} metal organic frameworks. Cryst. Growth Des., 2012. **12**(7): p. 3489-3498.

225. Stock, N. and S. Biswas, Synthesis of metal-organic frameworks (MOFs): routes to various MOF topologies, morphologies, and composites. Chem. Rev., 2012. **112**(2): p. 933-969.

226. Gedanken, A., Using sonochemistry for the fabrication of nanomaterials. Ultrason. Sonochem., 2004. **11**(2): p. 47-55.

227. Suslick, K.S., et al., Sonochemical synthesis of amorphous iron. Nature, 1991. **353**(6343): p. 414-416.

228. Suslick, K.S., D.A. Hammerton, and R.E. Cline, Sonochemical hot spot. J. Am. Chem. Soc., 1986. **108**(18): p. 5641-5642.

229. Liu, Q., et al., ZIF-8/Zn_2 GeO_4 nanorods with an enhanced CO_2 adsorption property in an aqueous medium for photocatalytic synthesis of liquid fuel. J. Mater. Chem. A, 2013. **1**(38): p. 11563-11569.

230. Friščić, T., et al., Real-time and in situ monitoring of mechanochemical milling reactions. Nat. Chem., 2013. **5**(1): p. 66.

231. Do, J.-L. and T. Friščić, Mechanochemistry: a force of synthesis. ACS Cent. Sci., 2017. **3**(1): p. 13-19.

232. Klinowski, J., et al., Microwave-assisted synthesis of metal–organic frameworks. Dalton Trans., 2011. **40**(2): p. 321-330.

233. Al-Kutubi, H., et al., Electrosynthesis of metal–organic frameworks: challenges and opportunities. ChemElectroChem, 2015. **2**(4): p. 462-474.

234. Zhang, H., et al., Efficient Visible-Light-Driven Carbon Dioxide Reduction by a Single-Atom Implanted Metal–Organic Framework. Angew. Chem. Int. Ed., 2016. **55**(46): p. 14310-14314.

235. Xu, H.-Q., et al., Visible-light photoreduction of CO_2 in a metal–organic framework: boosting electron–hole separation via electron trap states. J. Am. Chem. Soc., 2015. **137**(42): p. 13440-13443.

236. Cavka, J.H., et al., A new zirconium inorganic building brick forming metal organic frameworks with exceptional stability. J. Am. Chem. Soc., 2008. **130**(42): p. 13850-13851.

237. Deria, P., et al., Topology-dependent emissive properties of zirconium-based porphyrin MOFs. Chem. Commun., 2016. **52**(88): p. 13031-13034.

238. Deria, P., et al., Framework-topology-dependent catalytic activity of zirconium-based (porphinato) zinc(II) MOFs. J. Am. Chem. Soc., 2016. **138**(43): p. 14449-14457.

239. Lam, S.-M., J.-C. Sin, and A.R. Mohamed, A newly emerging visible light-responsive $BiFeO_3$ perovskite for photocatalytic applications: a mini review. Mater. Res. Bull., 2017. **90**: p. 15-30.

240. Laurier, K.G., et al., Iron(III)-based metal–organic frameworks as visible light photocatalysts. J. Am. Chem. Soc., 2013. **135**(39): p. 14488-14491.

241. Prolongo, S., et al., Heat dissipation on electrical conductor composites by combination of carbon nanotubes and graphene nanoplatelets. J. Coat. Technol. Res., 2019. **16**(2): p. 491-498.

242. Dou, Y., et al., Visible-light responsive MOF encapsulation of noble-metal-sensitized semiconductors for high-performance photoelectrochemical water splitting. J. Mater. Chem. A, 2017. **5**(36): p. 19491-19498.

243. Kou, Y., et al., Direct detection of key reaction intermediates in photochemical CO_2 reduction sensitized by a rhenium bipyridine complex. J. Am. Chem. Soc., 2014. **136**(16): p. 6021-6030.

244. Cabrero-Antonino, M., et al., Design of cost-efficient and photocatalytically active Zn-based MOFs decorated with Cu_2O nanoparticles for CO_2 methanation. Chem. Commun., 2019. **55**(73): p. 10932-10935.

245. Li, N., et al., Adenine Components in Biomimetic Metal–Organic Frameworks for Efficient CO_2 Photoconversion. Angew. Chem., 2019. **131**(16): p. 5280-5285.

246. Hu, J., J. Ding, and Q. Zhong, In situ fabrication of amorphous TiO_2/NH_2-MIL-125(Ti) for enhanced photocatalytic CO_2 into CH_4 with H_2O under visible-light irradiation. J. Colloid Interface Sci., 2020. **560**: p. 857-865.

247. Wang, Y., et al., Hydroxide ligands cooperate with catalytic centers in metal–organic frameworks for efficient photocatalytic CO_2 reduction. J. Am. Chem. Soc., 2018. **140**(1): p. 38-41.

248. Chambers, M.B., et al., Photocatalytic Carbon Dioxide Reduction with Rhodium-based Catalysts in Solution and Heterogenized within Metal–Organic Frameworks. ChemSusChem, 2015. **8**(4): p. 603-608.

249. Wang, S. and X. Wang, Photocatalytic CO_2 reduction by CdS promoted with a zeolitic imidazolate framework. Angew. Chem. Int. Ed., 2015. **162**: p. 494-500.

250. Wang, S., et al., Cobalt imidazolate metal–organic frameworks photosplit CO_2 under mild reaction conditions. Angew. Chem. Int. Ed., 2014. **53**(4): p. 1034-1038.

251. Wang, C., et al., Doping metal–organic frameworks for water oxidation, carbon dioxide reduction, and organic photocatalysis. J. Am. Chem. Soc., 2011. **133**(34): p. 13445-13454.

252. Lee, Y., et al., Photocatalytic CO_2 reduction by a mixed metal (Zr/Ti), mixed ligand metal–organic framework under visible light irradiation. Chem. Commun., 2015. **51**(26): p. 5735-5738.

253. Masoomi, M.Y., et al., Mixed-Metal MOFs: Unique Opportunities in Metal–Organic Framework (MOF) Functionality and Design. Angew. Chem. Int. Ed., 2019. **58**(43): p. 15188-15205.

254. Han, B., et al., Nickel Metal–Organic Framework Monolayers for Photoreduction of Diluted CO_2: Metal-Node-Dependent Activity and Selectivity. Angew. Chem. Int. Ed., 2018. **57**(51): p. 16811-16815.

255. Sun, D., et al., Introduction of a mediator for enhancing photocatalytic performance via post-synthetic metal exchange in metal–organic frameworks (MOFs). Chem. Commun., 2015. **51**(11): p. 2056-2059.

256. Wan, S., et al., Perovskite-type $CsPbBr_3$ quantum dots/UiO-66 (NH_2) nanojunction as efficient visible-light-driven photocatalyst for CO_2 reduction. Chem. Eng. J., 2019. **358**: p. 1287-1295.

257. Chen, L., et al., N-CND modified NH_2-UiO-66 for photocatalytic CO_2 conversion under visible light by a photo-induced electron transfer process. Chem. Commun., 2019. **55**(33): p. 4845-4848.

258. Zhao, H., et al., CdS/NH_2-UiO-66 hybrid membrane reactors for the efficient photocatalytic conversion of CO_2. J. Mater. Chem. A, 2018. **6**(41): p. 20152-20160.

259. Wang, J.W., et al., Electrocatalytic and Photocatalytic Reduction of CO_2 to CO by Cobalt (II) Tripodal Complexes: Low Overpotentials, High Efficiency and Selectivity. ChemSusChem, 2018. **11**(6): p. 1025-1031.

260. Kong, Z.-C., et al., Core@ shell $CsPbBr_3$@ Zeolitic imidazolate framework nanocomposite for efficient photocatalytic CO_2 reduction. ACS Energy Lett., 2018. **3**(11): p. 2656-2662.

261. Wang, Y., et al., Carbothermal activation synthesis of 3D porous g-C_3N_4/carbon nanosheets composite with superior performance for CO_2 photoreduction. Appl. Catal. B, 2018. **239**: p. 196-203.

262. Su, Y., et al., $Cd_{0.2}Zn_{0.8}S$@ UiO-66-NH_2 nanocomposites as efficient and stable visible-light-driven photocatalyst for H_2 evolution and CO_2 reduction. Appl. Catal. B, 2017. **200**: p. 448-457.

263. Kajiwara, T., et al., Photochemical reduction of low concentrations of CO_2 in a porous coordination polymer with a ruthenium (II)–CO complex. Angew. Chem. Int. Ed., 2016. **55**(8): p. 2697-2700.

264. Choi, K.M., et al., Plasmon-enhanced photocatalytic CO_2 conversion within metal–organic frameworks under visible light. J. Am. Chem. Soc., 2017. **139**(1): p. 356-362.

265. Zhang, S., et al., Construction of interpenetrated ruthenium metal–organic frameworks as stable photocatalysts for CO_2 reduction. Inorg. Chem., 2015. **54**(17): p. 8375-8379.

266. Zhang, S., et al., Hierarchical metal–organic framework nanoflowers for effective CO_2 transformation driven by visible light. J. Mater. Chem. A, 2015. **3**(30): p. 15764-15768.

267. Wang, S., J. Lin, and X. Wang, Semiconductor–redox catalysis promoted by metal–organic frameworks for CO_2 reduction. Phys. Chem. Chem. Phys., 2014. **16**(28): p. 14656-14660.

268.   Shen, L., et al., CdS-decorated UiO–66 (NH$_2$) nanocomposites fabricated by a facile photodeposition process: an efficient and stable visible-light-driven photocatalyst for selective oxidation of alcohols. J. Mater. Chem. A, 2013. **1**(37): p. 11473-11482.

269.   Zhu, J., et al., Titanium-based metal–organic frameworks for photocatalytic applications. Coord. Chem. Rev., 2018. **359**: p. 80-101.

270.   Zheng, Y., et al., Metal–organic frameworks for lithium–sulfur batteries. J. Mater. Chem. A, 2019. **7**(8): p. 3469-3491.

271.   Moriche, R., et al., Thermal conductivity and lap shear strength of GNP/epoxy nanocomposites adhesives. Int. J. Adhes. Adhes., 2016. **68**: p. 407-410.

272.   Hou, W. and S.B. Cronin, A review of surface plasmon resonance-enhanced photocatalysis. Adv. Funct. Mater., 2013. **23**(13): p. 1612-1619.

273.   Liu, Z., et al., Plasmon resonant enhancement of photocatalytic water splitting under visible illumination. Nano Lett., 2011. **11**(3): p. 1111-1116.

274.   Roy, P., S. Berger, and P. Schmuki, TiO$_2$ nanotubes: synthesis and applications. Angew. Chem. Int. Ed., 2011. **50**(13): p. 2904-2939.

275.   Gupta, S.M. and M. Tripathi, A review of TiO$_2$ nanoparticles. Chin. sci. bull., 2011. **56**(16): p. 1639.

276.   Cheng, M., et al., Copper-decorated TiO$_2$ nanorod thin films in optofluidic planar reactors for efficient photocatalytic reduction of CO$_2$. Int. J. Hydrog. Energy, 2017. **42**(15): p. 9722-9732.

277.   Zwilling, V., et al., Structure and physicochemistry of anodic oxide films on titanium and TA6V alloy. Surf. Interface Anal., 1999. **27**(7): p. 629-637.

278.   Khan, M.M., D. Pradhan, and Y. Sohn, Nanocomposites for visible light-induced photocatalysis. 2017: Springer.

279.   Jun, Y., J.H. Park, and M.G. Kang, The preparation of highly ordered TiO$_2$ nanotube arrays by an anodization method and their applications. ChemComm, 2012. **48**(52): p. 6456-6471.

280.   Shankar, K., et al., Highly-ordered TiO$_2$ nanotube arrays up to 220 μm in length: use in water photoelectrolysis and dye-sensitized solar cells. Nanotechnology, 2007. **18**(6): p. 065707.

281. Sim, L.C., et al., Rapid thermal reduced graphene oxide/Pt–TiO_2 nanotube arrays for enhanced visible-light-driven photocatalytic reduction of CO_2. Appl. Surf. Sci., 2015. **358**: p. 122-129.

282. Giannakopoulou, T., et al., Tailoring the energy band gap and edges' potentials of g-C_3N_4/TiO_2 composite photocatalysts for NOx removal. Chem. Eng. J., 2017. **310**: p. 571-580.

283. Martha, S., A. Nashim, and K. Parida, Facile synthesis of highly active gC_3N_4 for efficient hydrogen production under visible light. J. Mater. Chem. A, 2013. **1**(26): p. 7816-7824.

284. Sun, M., et al., Graphitic carbon nitride (gC_3N_4) coated titanium oxide nanotube arrays with enhanced photo-electrochemical performance. Dalton Trans., 2016. **45**(32): p. 12702-12709.

285. Wu, J., et al., Preparation of Al–O-Linked Porous-g-C_3N_4/TiO_2-Nanotube Z-Scheme Composites for Efficient Photocatalytic CO_2 Conversion and 2, 4-Dichlorophenol Decomposition and Mechanism. ACS Sustain. Chem. Eng., 2019. **7**(18): p. 15289-15296.

286. Elbanna, O., M. Fujitsuka, and T. Majima, g-C_3N_4/TiO_2 mesocrystals composite for H_2 evolution under visible-light irradiation and its charge carrier dynamics. ACS Appl. Mater. Interfaces, 2017. **9**(40): p. 34844-34854.

287. Yang, C., et al., Rational design of carbon-doped TiO_2 modified g-C_3N_4 via in-situ heat treatment for drastically improved photocatalytic hydrogen with excellent photostability. Nano Energy, 2017. **41**: p. 1-9.

288. Dehkordi, A.B., et al., Preparation of hierarchical g-C_3N_4@ TiO_2 hollow spheres for enhanced visible-light induced catalytic CO_2 reduction. Solar Energy, 2020. **205**: p. 465-473.

289. Yu, J., et al., Enhanced photocatalytic performance of direct Z-scheme g-C_3N_4–TiO_2 photocatalysts for the decomposition of formaldehyde in air. Phys. Chem. Chem. Phys., 2013. **15**(39): p. 16883-16890.

290. Wallace, P.R., The band theory of graphite. Phys. Rev. B, 1947. **71**(9): p. 622.

291. Kumar, R., et al., Graphene/metal oxide–based nanocomposite as photocatalyst for degradation of water pollutants, in Graphene-Based Nanotechnologies for Energy and Environment. 2019, Elsevier. p. 221-240.

292.   Wang, Y., et al., Hydrogen production with ultrahigh efficiency under visible light by graphene well-wrapped UiO-66-NH$_2$ octahedrons. J. Mater. Chem., 2017. **5**(38): p. 20136-20140.

293.   Lee, J.S., K.H. You, and C.B. Park, Highly photoactive, low bandgap TiO$_2$ nanoparticles wrapped by graphene. Adv. Mater., 2012. **24**(8): p. 1084-1088.

294.   Drewniak, S.E., et al., Studies of physicochemical properties of graphite oxide and thermally exfoliated/reduced graphene oxide. Pol. J. Chem. Technol, 2015. **17**(4): p. 109-114.

295.   Cao, X., et al., Hybrid micro-/nano-structures derived from metal–organic frameworks: preparation and applications in energy storage and conversion. Chem. Soc. Rev., 2017. **46**(10): p. 2660-2677.

296.   Wang, Z., et al., Metal–organic frameworks and their derivatives with graphene composites: preparation and applications in electrocatalysis and photocatalysis. J. Mater. Chem., 2020. **8**(6): p. 2934-2961.

297.   Rahmani, A., et al., Synthesis and characterization of CdS/MIL-125(Ti) as a photocatalyst for water splitting. Mater. Sci. Semicond. Process., 2018. **80**: p. 44-51.

298.   Han, X., et al., Boosting visible light photocatalytic activity via impregnation-induced RhB-sensitized MIL-125(Ti). Chem. Eng. Res. Des., 2019. **143**: p. 90-99.

299.   Wang, H., et al., In situ synthesis of In$_2$S$_3$@ MIL-125 (Ti) core–shell microparticle for the removal of tetracycline from wastewater by integrated adsorption and visible-light-driven photocatalysis. Appl. Catal. B, 2016. **186**: p. 19-29.

300.   Yang, Z., et al., Construction of heterostructured MIL-125/Ag/g-C$_3$N$_4$ nanocomposite as an efficient bifunctional visible light photocatalyst for the organic oxidation and reduction reactions. Appl. Catal. B, 2017. **205**: p. 42-54.

301.   Zhao, Y., et al., A Highly Efficient Composite Catalyst Constructed From NH$_2$-MIL-125(Ti) and Reduced Graphene Oxide for CO$_2$ Photoreduction. Front. Chem., 2019. **7**: p. 789.

302.   Kim, S.-N., et al., Adsorption/catalytic properties of MIL-125 and NH$_2$-MIL-125. Catal. Today, 2013. **204**: p. 85-93.

303.   Li, X., et al., Graphene oxide enhanced amine-functionalized titanium metal organic framework for visible-light-driven photocatalytic oxidation of gaseous pollutants. Appl. Catal. B, 2018. **236**: p. 501-508.

304.   Bai, Y., et al., Enhanced photocatalytic performance of direct Z-scheme BiOCl–gC$_3$N$_4$ photocatalysts. RSC Adv., 2014. **4**(37): p. 19456-19461.

305.   Liu, J., et al., Simple pyrolysis of urea into graphitic carbon nitride with recyclable adsorption and photocatalytic activity. J. Mater. Chem., 2011. **21**(38): p. 14398-14401.

306.   Sun, J.-X., et al., Fabrication of composite photocatalyst gC$_3$N$_4$–ZnO and enhancement of photocatalytic activity under visible light. Dalton Trans., 2012. **41**(22): p. 6756-6763.

307.   Kuilla, T., et al., Recent advances in graphene based polymer composites. Prog. Polym. Sci., 2010. **35**(11): p. 1350-1375.

308.   Cao, N. and Y. Zhang, Study of reduced graphene oxide preparation by Hummers' method and related characterization. J. Nanomater., 2015. **2015**.

309.   Kumar, S., et al., Ag nanoparticles–anchored reduced graphene oxide catalyst for oxygen electrode reaction in aqueous electrolytes and also a non-aqueous electrolyte for Li–O$_2$ cells. Phys. Chem. Chem. Phys., 2014. **16**(41): p. 22830-22840.

310.   Kumar, A., A.M. Sadanandhan, and S.L. Jain, Silver doped reduced graphene oxide as a promising plasmonic photocatalyst for oxidative coupling of benzylamines under visible light irradiation. New J Chem, 2019. **43**(23): p. 9116-9122.

311.   Dervishi, E., et al., Large-scale graphene production by RF-cCVD method. ChemComm, 2009(27): p. 4061-4063.

312.   Hu, S., et al., Solvothermal synthesis of NH$_2$-MIL-125(Ti) from circular plate to octahedron. CrystEngComm, 2014. **16**(41): p. 9645-9650.

313.   Otal, E., et al., A panchromatic modification of the light absorption spectra of metal–organic frameworks. ChemComm, 2016. **52**(40): p. 6665-6668.

314.   Karthik, P., et al., π–π interaction between metal–organic framework and reduced graphene oxide for visible-light photocatalytic H$_2$ production. ACS Appl. Energy Mater., 2018. **1**(5): p. 1913-1923.

315.   Hlophe, P.V., L.C. Mahlalela, and L.N. Dlamini, A composite of platelet-like orientated $BiVO_4$ fused with MIL-125 (Ti): Synthesis and characterization. Sci. Rep, 2019. **9**(1): p. 1-12.

316.   Hu, S., et al., Simultaneous nanostructure and heterojunction engineering of graphitic carbon nitride via in situ Ag doping for enhanced photoelectrochemical activity. Appl. Catal. B, 2015. **163**: p. 611-622.

317.   Hou, Y., et al., Constructing 2D porous graphitic C_3N_4 nanosheets/nitrogen-doped graphene/layered MoS_2 ternary nanojunction with enhanced photoelectrochemical activity. Adv. Mater., 2013. **25**(43): p. 6291-6297.

318.   Zhang, Z., et al., Visible-light neural stimulation on graphitic-carbon nitride/graphene photocatalytic fibers. ACS Appl. Mater. Interfaces, 2017. **9**(40): p. 34736-34743.

319.   Raghu, M., et al., Adsorption and antimicrobial studies of chemically bonded magnetic graphene oxide-Fe_3O_4 nanocomposite for water purification. J. Water Process. Eng., 2017. **17**: p. 22-31.

320.   Wang, H., et al., Facile synthesis of amino-functionalized titanium metal-organic frameworks and their superior visible-light photocatalytic activity for Cr (VI) reduction. J. Hazard. Mater., 2015. **286**: p. 187-194.

321.   Rodríguez, N.A., et al., Facile synthesis of potassium poly (heptazine imide)(PHIK)/Ti-based metal–organic framework (MIL-125-NH2) composites for photocatalytic applications. ACS applied materials & interfaces, 2017. **9**(27): p. 22941-22949.

322.   Li, X., et al., Preparation and characterization of graphitic carbon nitride through pyrolysis of melamine. Appl. Phys. A, 2009. **94**(2): p. 387-392.

323.   Li, X., et al., Synergistic effect of efficient adsorption g-C_3N_4/ZnO composite for photocatalytic property. J Phys Chem Solids, 2014. **75**(3): p. 441-446.

324.   Hu, S., et al., Properties and photocatalytic performance of polypyrrole and polythiophene modified gC_3N_4 nanocomposites. RSC Adv., 2015. **5**(40): p. 31947-31953.

325.   Song, H., et al., Fabrication of NH2-MIL-125 (Ti) incorporated TiO_2 nanotube arrays composite anodes for highly efficient PEC water splitting. Sep. Purif. Technol., 2019. **228**: p. 115764.

326. Tahir, B., M. Tahir, and M.G. Mohd Nawawi, Well-Designed 3D/2D/2D WO_3/Bt/g-C_3N_4 Z-Scheme Heterojunction for Tailoring Photocatalytic CO_2 Methanation with 2D-Layered Bentonite-Clay as the Electron Moderator under Visible Light. Energy Fuels, 2020. **34**(11): p. 14400-14418.

327. Liao, G., et al., Graphene oxide modified gC_3N_4 hybrid with enhanced photocatalytic capability under visible light irradiation. J. Mater. Chem., 2012. **22**(6): p. 2721-2726.

328. Li, W., et al., Size dependence of thermal stability of TiO_2 nanoparticles. J. Appl. Phys., 2004. **96**(11): p. 6663-6668.

329. Dai, K., et al., Sonication assisted preparation of graphene oxide/graphitic-C_3N_4 nanosheet hybrid with reinforced photocurrent for photocatalyst applications. Dalton Trans., 2014. **43**(17): p. 6295-6299.

330. Zhang, Y., et al., Synthesis and visible-light photocatalytic property of Ag/GO/g-C_3N_4 ternary composite. Mater. Sci. Eng. B, 2017. **221**: p. 1-9.

331. Xiang, Q., J. Yu, and M. Jaroniec, Preparation and enhanced visible-light photocatalytic H_2-production activity of graphene/C_3N_4 composites. J. Phys. Chem. C, 2011. **115**(15): p. 7355-7363.

332. Li, J., et al., Ultrasonic-microwave assisted synthesis of GO/g-C_3N_4 composites for efficient photocatalytic H_2 evolution. Solid State Sci., 2019. **97**: p. 105990.

333. Ikreedeegh, R.R. and M. Tahir, A critical review in recent developments of metal-organic-frameworks (MOFs) with band engineering alteration for photocatalytic CO_2 reduction to solar fuels. J. CO2 Util. **43**: p. 101381.

334. Pruna, A., et al., Effect of reduced graphene oxide on photocatalytic properties of electrodeposited ZnO. Appl. Phys. A, 2017. **123**(12): p. 792.

335. Ye, J., et al., Effect of reduced graphene oxide doping on photocatalytic reduction of Cr (VI) and photocatalytic oxidation of tetracycline by ZnAlTi layered double oxides under visible light. Chemosphere, 2019. **227**: p. 505-513.

336. Ong, W.-J., et al., Surface charge modification via protonation of graphitic carbon nitride (g-C_3N_4) for electrostatic self-assembly construction of 2D/2D reduced graphene oxide (rGO)/g-C_3N_4 nanostructures toward enhanced photocatalytic reduction of carbon dioxide to methane. Nano Energy, 2015. **13**: p. 757-770.

337.   Oh, J., et al., Graphene oxide-assisted production of carbon nitrides using a solution process and their photocatalytic activity. Carbon, 2014. **66**: p. 119-125.

338.   Trinh, T.H.T., Membrane reactor systems for photocatalytic degradation using TiO_2 nanoparticles/submitted by Thi Huyen Trang Trinh. 2016, Universität Linz.

339.   Ibrahim, Y.O., et al., Laser-assisted synthesis of Z-scheme TiO_2/rGO/g-C_3N_4 nanocomposites for highly enhanced photocatalytic hydrogen evolution. Appl. Surf. Sci., 2020. **534**: p. 147578.

340.   Li, Y., et al., Cross-Linked g-C_3N_4/rGO Nanocomposites with Tunable Band Structure and Enhanced Visible Light Photocatalytic Activity. Small, 2013. **9**(19): p. 3336-3344.

341.   Tseng, I.-H., W.-C. Chang, and J.C. Wu, Photoreduction of CO_2 using sol–gel derived titania and titania-supported copper catalysts. Appl. Catal. B, 2002. **37**(1): p. 37-48.

342.   Wu, J.C., H.-M. Lin, and C.-L. Lai, Photo reduction of CO_2 to methanol using optical-fiber photoreactor. Appl. Catal. A, 2005. **296**(2): p. 194-200.

343.   Pelaez, M., et al., A review on the visible light active titanium dioxide photocatalysts for environmental applications. Appl. Catal. B, 2012. **125**: p. 331-349.

344.   Phromma, S., et al., Effect of Calcination Temperature on Photocatalytic Activity of Synthesized TiO_2 Nanoparticles via Wet Ball Milling Sol-Gel Method. Appl. Sci., 2020. **10**(3): p. 993.

345.   Liu, L., et al., Photocatalytic CO_2 reduction with H_2O on TiO_2 nanocrystals: Comparison of anatase, rutile, and brookite polymorphs and exploration of surface chemistry. ACS Catal., 2012. **2**(8): p. 1817-1828.

346.   Kar, P., et al., High rate CO_2 photoreduction using flame annealed TiO_2 nanotubes. Appl. Catal. B, 2019. **243**: p. 522-536.

347.   Appadurai, T., et al., Electrochemical performance of nitrogen-doped TiO_2 nanotubes as electrode material for supercapacitor and Li-ion battery. Molecules, 2019. **24**(16): p. 2952.

348.   Wu, J., et al., Efficient photocatalytic CO_2 reduction by P–O linked g-C_3N_4/TiO_2-nanotubes Z-scheme composites. Energy, 2019. **178**: p. 168-175.

349. Zubair, M., et al., Solar spectrum photocatalytic conversion of CO_2 to CH_4 utilizing TiO_2 nanotube arrays embedded with graphene quantum dots. J CO2 Util., 2018. **26**: p. 70-79.

350. Low, J., et al., Direct evidence and enhancement of surface plasmon resonance effect on Ag-loaded TiO_2 nanotube arrays for photocatalytic CO_2 reduction. Appl. Surf. Sci., 2018. **434**: p. 423-432.

351. Li, Y., et al., Octahedral Cu_2O-modified TiO_2 nanotube arrays for efficient photocatalytic reduction of CO_2. Chin. J. Catal., 2015. **36**(12): p. 2229-2236.

352. Li, Q., et al., Reprint of "Photocatalytic reduction of CO_2 on MgO/TiO_2 nanotube films". Appl. Surf. Sci., 2014. **319**: p. 16-20.

353. Razzaq, A. and S.-I. In, TiO_2 based nanostructures for photocatalytic CO_2 conversion to valuable chemicals. Micromachines, 2019. **10**(5): p. 326.

354. Nguyen, T.P., et al., Recent Advances in TiO_2-Based Photocatalysts for Reduction of CO_2 to Fuels. Nanomaterials, 2020. **10**(2): p. 337.

355. Al Jitan, S., G. Palmisano, and C. Garlisi, Synthesis and surface modification of TiO_2-based photocatalysts for the conversion of CO_2. Catalysts, 2020. **10**(2): p. 227.

356. Pan, H., et al., Enhanced Photocatalytic CO_2 Reduction with Defective TiO_2 Nanotubes Modified by Single-Atom Binary Metal Components. 2020.

357. Razzaq, A., C.A. Grimes, and S.-I. In, Facile fabrication of a noble metal-free photocatalyst: TiO_2 nanotube arrays covered with reduced graphene oxide. Carbon, 2016. **98**: p. 537-544.

358. Ru, Y., et al., Photoelectrocatalytic reduction of CO_2 on titania nanotube arrays modified by Pd and RGO. J. Mater. Sci., 2018. **53**(14): p. 10351-10362.

359. Perini, J.A.L., et al., Ag/polydopamine-modified Ti/TiO_2 nanotube arrays: A platform for enhanced CO_2 photoelectroreduction to methanol. J CO2 Util., 2019. **34**: p. 596-605.

LIST OF PUBLICATIONS

Papers Published

1.   Ikreedeegh, R.R. and M. Tahir, A critical review in recent developments of metal-organic-frameworks (MOFs) with band engineering alteration for photocatalytic CO_2 reduction to solar fuels. J. CO2 Util. 43: p. 101381.

2.   Ikreedeegh, R.R. and M. Tahir, Indirect Z-scheme heterojunction of NH_2-MIL-125(Ti)/g-C_3N_4 nanocomposite with RGO solid electron mediator for efficient photocatalytic CO_2 reduction to CO and CH_4. J. Environ. Chem.

Papers in Consideration

1.   Ikreedeegh, R.R. and M. Tahir, Well-designed 2D/2D/1D heterojunction system of g-C_3N_4/RGO/TNTAs-A/R with synergetic effect of anatase/rutile with GO moderator for efficient photocatalytic CO_2 reduction to CO/CH_4. J. CO2 Util: Under review.

2.   Ikreedeegh, R.R. and M. Tahir, Facile fabrication of well-designed 2D/2D porous g-C_3N_4–GO nanocomposite for photocatalytic methane reforming (DRM) with CO_2 (DRM) towards enhanced syngas production under visible light. Fuel: Under review.